EPFL

Thèse n° 7466

Establishing a Ternary System for Optical Monitoring of DNA–Protein Interactions with Single-Walled Carbon Nanotubes

Présentée le 20 novembre 2020

à la Faculté des sciences de base
Laboratoire de nanobiotechnologie
Programme doctoral en chimie et génie chimique

pour l'obtention du grade de Docteur ès Sciences

par

Shang-Jung WU

Acceptée sur proposition du jury

Dr H. Pick, président du jury
Prof. A. A. Boghossian, directrice de thèse
Prof. V. Davis, rapporteuse
Prof. M. Merkx, rapporteur
Prof. B. Fierz, rapporteur

École polytechnique fédérale de Lausanne

2020

What we call the present
is given shape by an accumulation of the past.
— Haruki Murakami, 1Q84

To the world.

Acknowledgements

My thesis is not simply a work of mine, but also an accumulation of the supports from everyone who ever participated this journey with me. Definitely, this story would not begin without my supervisor Professor **Ardemis Boghossian** and the financial support of SNSF. Arde always encourages me to explore the world of science without doubting my ability. Her open mind has largely shaped the working culture of LNB, which plays a crucial role in my study and influences me a lot. I would definitely miss those discussions during meetings where we debated over things. If one day I have my own group, the culture Arde has built in LNB will for sure be inherited.

I would like to thank my committee members: Professor **Virginia Davis**, Professor **Maarten Merkx**, and Professor **Beat Fierz**. Their critical comments definitely helped me to complete this thesis genuinely. I am also grateful to Dr. **Pick Horst** for being the jury president, who also generously provided supports for me in many ways.

I would like to acknowledge all my LNB lab mates. I cannot imagine a five-year PhD study without their support. I am so lucky to have them taking care me this grumpy baby, and I am thankful to all my lab mates for tolerating me being cynical and sarcastic all the time. I am very much grateful to **Nils Schergers**. He greatly influenced my mindset of doing science and approaching the truth. Moreover, his great attitude to people and his lifestyle expanded my imaginations, which I adopt and wish to share to others.

I would also like to thank the LNB first generation kids, **Alessandra Antonucci** and **Vitalijs Zubkovs**. We shared those high and low points of our studies together. Without their kind mind helping me integrating into the group, I believe I would have suffered more. I would also miss a lot of those bets with **Benjamin Lambert** and **Mohammed Mouhib**. Those random but meaningful discussions we had are one of the best spices in my life. I am grateful to **Alice Gillen**, **Melania Reggente**, and **Mary Wood**. They cared about me and accompanied with me during my tough periods, and that definitely comforted my fragile spirit. Additionally, I am thankful to Mary, Alice, Benjamin, and Mohammed for proof reading my thesis and giving me valuable advices.

I am thankful to work with **Amirmostafa Amirjani**, **Sayyed Hashem Sajjadi**, and **Arash Ramedani**. It has been my pleasure to do projects together with them. Also special thanks to our first secretary **Christine Kupper**, who kindly helped me to initiate my stay in Switzerland.

And of course, many others who ever shared memories together in the corridor of CH H3, those memories would be deeply cherished in my mind.

My life abroad would be so pale without my friends. Those hiking trips, coffee breaks, board game nights, and sport hangouts. We have experienced these moments together in a long distance away from our hometown, making these times even more exceptional. I want to thank **Yuan-Peng Du** and **Che Yang** for accompanying with me for the whole study in the five years. The trash talks refreshed my mind and assisted me capable of going farther. I am grateful for those board game nights and dinners with **Kun-Han Lin**, **Yi-Wen Lee**, **Jian-Lin Huang**, **Hsin-Tse Chen**, **Chun Lam Chan**, and **Ying Mao**. I was too fortunate to share the same hobby with them and enjoy those moments. Especially, I want to express my gratitude to Kun-Han and Jian-Lin. I believe my study may not be completed without them. Their generous support and encouragement fuel me back on track, and their kind mind would be my goal to achieve.

Finally, I would like to thank my family. There were so many tough changes in my family during these five years, and they never complained a word to me for not being there. Particularly to my sister, **Wan-Yu**. I am really grateful for having her taking care of our parents and family. And to my love **Yi-Ting Liou**. Being your partner is the luckiest thing I could imagine in my lifetime. Your lovely imaginations and kindness make my life colorful and meaningful. Thank you.

Morges, 04 November 2020 S.-J. Wu

Abstract

DNA–protein interactions lie at the crux of life's essential processes. As such, various technologies have been developed to characterize these interactions. The distinct advantages of these technologies can be leveraged to study different facets of these interactions. In this thesis, we aim to establish a ternary system for optical monitoring of DNA–protein interactions. Single-walled carbon nanotubes (SWCNTs) are especially good for optical detection because of their photostable near-infrared (NIR) fluorescence, but so far it has been limited for use as binary systems. These systems are used to detect biomolecule interaction with only DNA or only protein, but unable to examine more complex systems that include DNA–protein interactions.

This thesis overcomes this limitation by developing a ternary system consisting of immobilized DNA and protein on nanotubes. We demonstrate the applicability of this system as a new platform for studying protein binding and activity on DNA. Additionally, our biocompatible system serves as a novel bioconjugative approach for protein immobilization on SWCNTs, where we aim to combine the reactivity and orthogonality of DNA, the target selectivity of proteins, and the sensitive NIR fluorescence of SWCNTs, which is not achievable in any state-of-the-art biosensors.

In this context, this thesis was divided into three stages: (1) resolving the DNA-SWCNT structure, (2) applications of DNA-protein-SWCNT and (3) improving the ternary hybrid for fluorescence detection. First, we elucidated the structure-function relationship of double-stranded DNA (dsDNA)-SWCNT. Previously, the duplex structure of DNA on SWCNTs was debatable. We performed a restriction enzyme (RE)-based electrophoretic assay on DNA-SWCNT hybrids with various DNA sequences. Combined with the results of fluorescence spectroscopy and molecular dynamics (MD) simulations, we used this to suggest a model with B-DNA lying on the SWCNT along the long axis of the SWCNT. Additionally, we developed an analytical assay based on DNA-specific fluorescence dyes and single-stranded DNA (ssDNA)-specific nuclease, enabling the analysis at higher throughput and providing a universal method for routine analysis. Overall, we successfully validated the Watson–Crick base pairing of dsDNA on SWCNTs for the first time.

Secondly, we showcased the sensing applications of DNA-protein-SWCNT in two different configurations: (1) DNA–protein conjugates and (2) DNA–protein interactions. In the first

case, we bridged proteins to SWCNTs via dsDNA bridges, which was verified by fluorescence microscopy. We developed a facile approach to construct new materials for specific analyte detection, as we showed in an example of DNA-horseradish peroxidase (HRP)-SWCNT, which detects hydrogen peroxide. In the second case, we found that both RE and Cas9 remain enzymatically active and are able to digest specific sequences on SWCNTs. Correspondingly, we suggested a potential application of DNA–protein interactions within sensors based on SWCNT NIR fluorescence.

Finally, we demonstrated that by protein library screening and protein engineering we were able to fine-tune the interaction between proteins and ssDNA-SWCNTs. In particular, we were able to identify the electrostatic interactions and solvent-exposed Asp to be the deterministic factor of non-specific adsorption. With proper amplifier designing by incorporating sp^3-defects on SWCNTs, we envision that the detection of DNA–protein interactions via SWCNT NIR fluorescence can be accomplished in vitro and in vivo.

Key words: single-walled carbon nanotube (SWCNT), near-infrared (NIR) fluorescence, hybrid material, biosensor, DNA, DNA conformation, protein, DNA–protein interaction

Résumé

Les interactions entre protéines et ADN sont au cœur des processus essentiels à la vie. En conséquence, diverses techniques ont été développées afin de caractériser ces interactions. Les avantages distincts de ces technologies peuvent être mis à profit afin d'étudier les différentes facettes de ces interactions. Dans cette thèse, nous visons à établir un système ternaire pour le suivi optique des interactions entre ADN et protéines. Les nanotubes de carbone monoparoi (SWCNTs) sont particulièrement indiqués pour une détection optique en raison de leur fluorescence stable dans le proche infrarouge (NIR. Malheureusement, jusqu'à présent leur utilisation n'a été limitée qu'à des systèmes binaires. Ces systèmes sont utilisés pour détecter l'interaction de biomolécules avec soit de l'ADN ou des protéines uniquement, mais ne peuvent pas permettre d'examiner des systèmes plus complexes incluant des interactions ADN–protéines.

Dans cette thèse, cette difficulté est surmontée avec le développement d'un système ternaire composé d'ADN et de protéines sur des nanotubes. Nous démontrons la pertinence de ce système en tant que nouvelle plateforme pour l'étude des liaisons et de l'activité des protéines avec l'ADN. En outre, notre système biocompatible sert de nouvelle approche bioconjugative pour l'immobilisation de protéines sur des SWCNTs, dans laquelle sont combinées la réactivité et l'orthogonalité de l'ADN, la sélectivité des protéines, et la fluorescence NIR des SWCNTs, ce qui n'est actuellement le cas d'aucun autre biosenseur.

Dans ce contexte, cette thèse a été divisée en trois parties : (1) résolution de la structure de l'ADN-SWCNT, (2) applications du système ADN-protéine-SWCNT et (3) amélioration de l'hybride ternaire pour la détection en fluorescence. Tout d'abord, nous avons élucidé la relation entre structure et fonction pour l'ADN double brin (ADNdb) - SWCNT. Par la passé, la structure de l'ADN sur les SWCNT n'était pas clairement définie. Nous avons créé un test basé sur l'action d'enzymes de restriction (ER) sur des hybrides ADN-SWCNT avec diverses séquences d'ADN et la caractérisation électrophorétique de cette intéraction. Nous avons proposé un modèle dans lequel l'ADN B se trouve le long de l'axe longitudinal du SWCNT. De plus, nous avons mis au point un test analytique basé sur des fluorophores spécifiques à l'ADN et sur une nucléase spécifique à l'ADN simple brin (ADNsb), permettant une analyse plus performante et offrant une méthode universelle pour les analyses de routine. Dans l'ensemble, nous avons réussi à valider pour la première fois l'existence de paires de bases Watson-Crick

pour l'ADNdb immobilisé sur les SWCNTs.

Dans un second temps, nous avons présenté les applications du système ternaire ADN-protéines-SWCNTs dans deux configurations différentes : (1) les conjugués ADN–protéines et (2) les interactions ADN–protéines. Dans le premier cas, nous avons connecté les protéines aux SWCNTs via des ponts d'ADNdb, ce qui a été vérifié par microscopie à fluorescence. Cela résulte en une approche facile pour la construction de nouveaux matériaux pour la détection de molécules spécifiques. Ainsi, nous montrons l'exemple du système ADN-peroxydase de raifort (HRP)-SWCNT, permettant la détection du peroxyde d'hydrogène. Dans le second cas, nous avons constaté que l'ER et l'enzyme CRISPR Cas9 restent tous deux actifs sur le plan enzymatique et sont capables de digérer des séquences spécifiques sur les SWCNTs. En conséquence, nous avons suggéré une application potentielle aux interactions ADN–protéines pour des capteurs basés sur la fluorescence NIR des SWCNTs.

Enfin, nous avons démontré que l'observation de bibliothèques de protéines et l'ingénierie des protéines nous permettaient d'affiner l'interaction entre les protéines et les ADNs-SWCNTs. En particulier, nous avons pu identifier les interactions électrostatiques ainsi que les Asp exposés sur la surface des protéines comme étant les facteurs déterministes d'une adsorption non spécifique. De plus, en incorporant des défauts sp^3 dans la structure des SWCNTs afin d'amplifier le signal, nous envisageons que la détection des interactions ADN–protéines par fluorescence NIR des SWCNTs puisse être réalisée in vitro et in vivo.

Mots clefs : nanotubes de carbone monoparoi (SWCNT), fluorescence dans le proche infrarouge (NIR), matériau hybride, biocapteur, ADN, conformation de l'ADN, protéine, interaction ADN–protéine

Zusammenfassung

DNA-Protein-Wechselwirkungen sind der Dreh- und Angelpunkt der lebenswichtigen Prozesse. Daher wurden verschiedene Technologien entwickelt, um diese Interaktionen zu charakterisieren. Die klaren Vorteile dieser Technologien können genutzt werden, um verschiedene Facetten dieser Interaktionen zu untersuchen. In dieser Arbeit wollen wir ein ternäres System zur optischen Überwachung von DNA-Protein-Wechselwirkungen etablieren. Einwandige Kohlenstoff-Nanoröhrchen (SWCNTs) eignen sich aufgrund ihrer photostabilen Nahinfrarot-Fluoreszenz (NIR) besonders gut für die optische Detektion, waren aber bisher für den Einsatz als binäre Systeme begrenzt. Diese Systeme werden zum Nachweis von Biomolekül-Wechselwirkungen nur mit DNA oder nur mit Proteinen verwendet, sind aber nicht in der Lage, komplexere Systeme zu untersuchen, die DNA-Protein-Wechselwirkungen beinhalten.

Die vorliegende Arbeit überwindet diese Einschränkung durch die Entwicklung eines ternären Systems, das aus immobilisierter DNA und Protein auf Nanoröhren besteht. Wir zeigen die Anwendbarkeit dieses Systems als neue Plattform zur Untersuchung der Proteinbindung und -aktivität auf DNA. Darüber hinaus dient unser biokompatibles System als ein neuartiger biokonjugativer Ansatz für die Proteinimmobilisierung auf SWCNTs, bei dem wir die Reaktivität und Orthogonalität der DNA, die Zielselektivität von Proteinen und die empfindliche NIR-Fluoreszenz von SWCNTs kombinieren wollen, was mit keinem der modernsten Biosensoren möglich ist.

In diesem Zusammenhang wurde diese Arbeit in drei Stufen unterteilt: (1) Auflösen der DNA-SWCNT-Struktur, (2) Anwendungen von DNA-Protein-SWCNT und (3) Verbesserung des ternären Hybrids für die Fluoreszenzdetektion. Zunächst haben wir die Struktur-Funktions-Beziehung der doppelsträngigen DNA (dsDNA)-SWCNT ermittelt. Zuvor war die Duplex-Struktur der DNA auf SWCNTs umstritten. Wir führten einen auf Restriktionsenzymen (RE) basierenden elektrophoretischen Assay an DNA-SWCNT-Hybriden mit verschiedenen DNA-Sequenzen durch. Bei dem die B-DNA auf dem SWCNT entlang dessen Längsachse liegt. Zusätzlich entwickelten wir einen analytischen Assay basierend auf DNA-spezifischen Fluoreszenzfarbstoffen und einzelsträngiger DNA (ssDNA)-spezifischer Nuklease, der die Analyse bei höherem Durchsatz ermöglicht und eine universelle Methode für Routineanalyse bietet. Insgesamt haben wir die Watson-Crick-Basenpaarung von dsDNA auf SWCNTs zum

ersten Mal erfolgreich validiert.

Zweitens demonstrierten wir die Anwendungen von DNA-Protein-SWCNT in zwei verschiedenen Konfigurationen: (1) DNA-Protein-Konjugate und (2) DNA-Protein-Interaktionen. Im ersten Fall überbrückten wir Proteine über dsDNA-Brücken zu SWCNTs, was durch Fluoreszenzmikroskopie verifiziert wurde. Wir entwickelten einen einfachen Ansatz zur Konstruktion neuer Materialien für spezifischen Nachweis von Analyten, wie wir am Beispiel von DNA-Meerrettichperoxidase (HRP)-SWCNT für die Detektion von Wasserstoffperoxid zeigten. Im zweiten Fall stellten wir fest, dass sowohl RE als auch Cas9 enzymatisch aktiv bleiben und in der Lage sind, spezifische Sequenzen auf SWCNTs zu verdauen. Dementsprechend schlugen wir eine mögliche Anwendung von DNA-Protein-Interaktionen innerhalb von Sensoren vor, die auf der SWCNT-NIR-Fluoreszenz basieren.

Schließlich zeigten wir, dass wir durch Screening einer Proteinbibliothek und Protein-Engineering in der Lage waren, die Interaktion zwischen Proteinen und ssDNA-SWCNTs fein abzustimmen. Insbesondere waren wir in der Lage elektrostatische Wechselwirkungen und die oberflächenexponierte Asparagine als die Hauptfaktoren der unspezifischen Adsorption zu identifizieren. Wir halten die Detektion von DNA-Protein-Interaktionen über SWCNT-NIR-Fluoreszenz in vitro und in vivo , unter Einbeziehung von sp^3-Defekten auf SWCNTs im Amplifikator design, in Zukunft für möglich.

Stichwörter: einwandiges Kohlenstoff-Nanoröhrchen (SWCNT), Nah-Infrarot-Fluoreszenz (NIR), Hybridmaterial, Biosensor, DNA, DNA-Konformation, Protein, DNA–Protein-Interaktion

Contents

List of Figures

List of Tables

1 Introduction

Portion of this Chapter is adapted from a review article published in:
Shang-Jung Wu and Ardemis A. Boghossian. Analytical Approaches for Monitoring DNA–Protein Interactions. *Chimia* **2019**, 73, 283–287

1.1 Analytical Approaches of DNA–Protein Interaction

DNA–protein interactions lie at the core of essential biological processes such as replication, transcription, and DNA repair.[1] Mechanistic knowledge of these interactions offers insight into cell regulation, which holds the key to unlocking therapeutic targets for diseases such as cancer. DNA–protein interactions are often classified as either non-specific or specific interactions, depending on the DNA sequence specificity. Since it is unlikely that the first collision between DNA and protein finds the binding site, typically non-specific interaction initially governs the interaction.[2] Long range electrostatic forces and van der Waals (vdw) forces dominate in such interactions. The polyelectrolyte effect, which leads to an increase of the entropic term, also promotes non-specific interactions.[3] After diffusion such that protein binding pocket reaches the proximity of DNA recognition site, an additional water exclusion causes extra entropic gain (i.e., hydrophobic effect), resulting in the specific binding.

The sugar-phosphate backbone of DNA non-specifically interacts with proteins via electrostatic forces. In contrast, since an arranged orientation promotes hydrogen bonds and stabilizes binding, proteins recognize specific DNA sequences with particular structural motifs. Bidentate and complex interaction modes are thus often observed for sequence recognition.[4] For example, the DNA major groove binds to protein surface residues through hydrogen bonding for sequence specificity, where guanine preferably interacts with Arg, Lys, Ser and His. In addition to hydrogen bonding, vdw contacts also contribute to binding specificity. As an example, rings of Phe and Pro favorably stack with adenine and thymine. Non-canonical motifs were also observed in DNA–protein interactions due to the aforementioned complex interaction mode.[5] The cation–π/H-bond stair is a classic case, of which protein residue forms (1) a cation–π interaction with a base of DNA, and (2) a hydrogen bond with an adjacent

base.

As such, several analytical approaches for monitoring DNA–protein interactions have been developed. One common approach for identifying DNA sequence(s) that bind a particular protein-of-interest (POI) is based on a pull-down assay. Pull-down assays, such as chromatin immunoprecipitation (ChIP, Figure 1.1a),[6] can identify the specific region(s) of the genome that associates with a POI. In this assay, DNA-bound proteins are sheared into shorter DNA fragments by either sonication or digestion, and the POI, along with its associated DNA, are selectively immunoprecipitated from the mixture using a protein-specific antibody. The captured DNA sequence(s) is subsequently analyzed in a high-throughput manner by either DNA microarray (ChIP-on-chip) or by next-generation sequencing (ChIP-seq). Alternatively, systematic evolution of ligands by exponential enrichment (SELEX)[7–9] screens a DNA sequence library for sequences that preferentially bind with a POI. Bound sequences are eluted and amplified for additional rounds of screening with increasingly stringent elution requirements. After iterative selection, the DNA sequence(s) with the strongest binding affinity is retained and identified.

In contrast to ChIP or SELEX, which aim to identify the DNA target(s) of a POI, alternative strategies focus on identifying the particular protein(s) that binds to a specific DNA sequence of interest. Yeast-one-hybrid (Y1H, Figure 1.1b) fuses a protein library (referred to as the 'prey' protein) to the activation domain of a transcription factor.[10] Once a protein specifically binds to the sequence of interest (referred to as the 'bait' DNA) that is located upstream of a gene for a reporter protein (e.g. luciferase), the binding brings the transcription factor in close proximity to the promoter element of the gene, activating transcription and triggering protein expression. The reporter protein expression can thus be used to signal protein binding to a given DNA sequence. Alternatively, a non-specific assay can be followed by 2D gel electrophoresis or mass spectroscopy (MS) to identify the protein(s) interacting with a specific DNA.[6]

Once a DNA–protein complex has been identified, it can be further studied using the analytical tools listed in Table 1.1. In the following sections, we will discuss some of these methods in greater detail, highlighting their advantages as well as limitations. We primarily focus on characterization of the binding event, whereas methods for studying enzymatic interactions between DNA and proteins are discussed elsewhere.[6]

1.1.1 Characterizing Known DNA–Protein Interactions

Common characterization techniques focus on obtaining information on the bound DNA–protein structure, thermodynamic and kinetic parameters, and spatiotemporal mapping of binding events. The structure of the DNA–protein complex can be used to elucidate the nature of the dominant binding force, such as electrostatic and/or hydrophobic interactions. Crystal structures of purified complexes can be obtained using X-ray diffraction (XRD, Figure 1.1c), nuclear magnetic resonance (NMR),[11] or cryogenic electron microscopy (cryo-EM). The DNA-binding domain of the protein can be mutated and crosslinked to covalently attach the

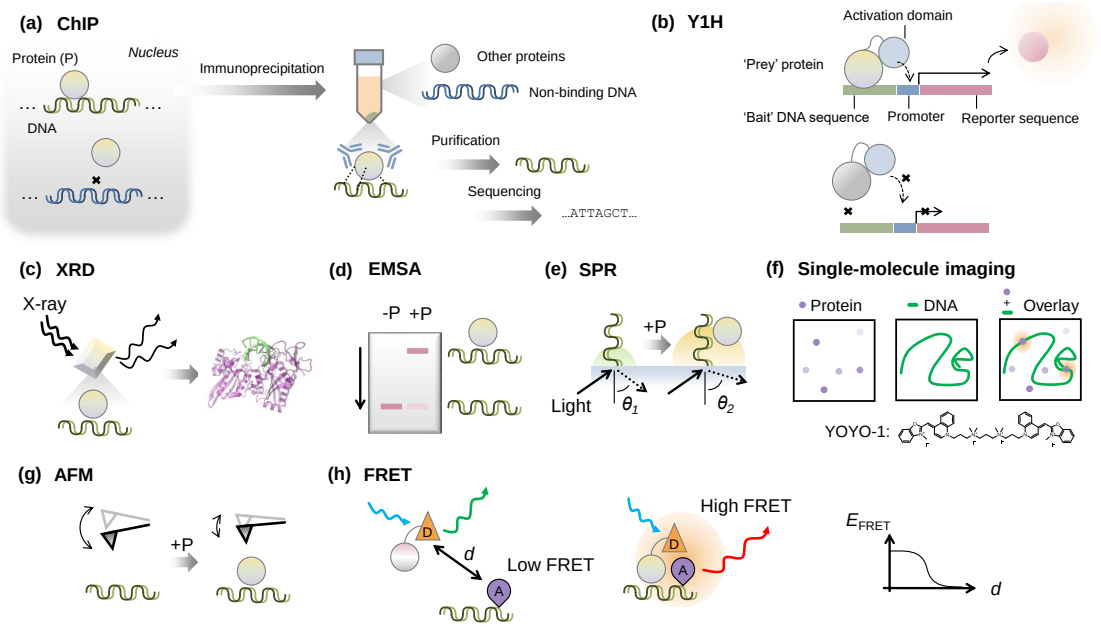

Figure 1.1 – Working principle of different methods for studying DNA–protein interactions. (a) Chromatin immunoprecipitation (ChIP) is used to identify the sequence(s) that bind to a certain protein (P), while (b) yeast-one-hybrid (Y1H) conversely identifies proteins that bind to a certain 'bait' DNA sequence. (c) X-ray diffraction (XRD) determines the crystal structure of complex. (d) Electrophoretic mobility shift assay (EMSA) can be used to determine thermodynamic parameters such as K_d, while (e) surface plasmon resonance (SPR) can further determine kinetic parameters such as k_{on} and k_{off}. (f) Single-molecule imaging and (g) atomic force microscopy (AFM) investigate binding through imaging. (h) Förster resonance energy transfer (FRET) is used for both sensing and imaging applications in vitro and in vivo.

DNA to the interacting residues. The crosslinked complex can be analyzed through MS to map the proximity of certain residues[12] and identify contributions from post-translational modifications.

The binding interaction is typically quantified by the thermodynamic (e.g. dissociation constant, K_d) and kinetic (e.g. binding on/off rate, k_{on} and k_{off}) parameters of the system. The K_d can be determined using an electrophoretic gel-based method.[13, 26] For example, in the electrophoretic mobility shift assay (EMSA, Figure 1.1d), electrophoretic movement of DNA is compared between free DNA (in the absence of protein) and DNA in the presence of the binding protein. Since DNA movement is hindered when bound to a protein(s), the bound DNA shows a distinct mobility band compared to the free DNA, and the ratio of the two bands can be used to calculate the apparent affinity of the DNA–protein complex when the stoichiometry and starting concentrations of the DNA and protein(s) are known.[13] In addition, the DNA–protein complex can be separated from free DNA and visualized with radiolabelled reagents, and the K_d can be determined through titration. Surface plasmon resonance (SPR, Figure 1.1e) is an alternative, label-free method for quantifying affinity using

Table 1.1 – Summary of common methods for studying DNA–protein interactions.

Method	Purpose of application[†]	Requirement[‡]	Sensitivity	ref
X-ray diffraction	S	P	-	-
Nuclear magnetic resonance	S	P/L	0.1-1 mM	[11]
Cryogenic electron microscope	S	P	-	-
Cross-linked mass spectrometry	S/D	-	10-100 nM	[12]
Filter-binding assay	D [T]	L	0.1 nM	[6]
Electrophoretic mobility shift assay	D [T]	L	0.1 nM	[13]
DNA footprint	D	L	0.1 nM	[14]
Southwestern blotting	D	L	0.1 nM	[6]
Fluorescence anisotropy	D	P/L	1-10 nM	[15]
Microscale thermophoresis	D	L	1-10 nM	[16]
Isothermal calorimetry	D	P	1-10 uM	[6]
Quartz crystal microbalance	D	P/I	100 uM	[17]
Analytical ultracentrifuge	D	L	~1 nM	[18]
Field effect transistor	D [T]	P/I	Single molecule	[19]
Electrochemical method	D [T]	I	Single molecule	[20]
Surface plasmon resonance	D [T]	I	1 nM	[21]
Protein induced fluorescence enhancement	D [T/Im]	P/L	Single molecule	[22]
Single-molecule imaging	D [T/Im]/Iv	I/L	Single molecule	[23]
Atomic force microscope	D [T/Im]	P/I	Single molecule	[24]
FRET-based	D [T/Im]/Iv	L	Single molecule	[25]

[†]S: structure, D: in vitro detection [T: time-resolved, Im: imaging], Iv: In vivo sensing/imaging.
[‡]P: purification, I: immobilization, L: labelling.

optical measurements.[21] In SPR, a metallic surface is modified with DNA, and the refractive index of the surface becomes altered when protein binds to the DNA. This binding modifies the surface plasmon and evanescent field, which can be optically probed using a total-reflection configuration. Unlike gel-based methods, SPR can not only be used to determine K_d, but it can also be used for real-time analysis (k_{on} and k_{off}) in complex fluids. Other methods like fluorescence polarization (FP)[15] and microscale thermoelectrophoresis (MST)[16] can also optically detect DNA–protein interactions, though these methods require additional fluorophore labelling (see Table 1.1 for comparison). More information on other methods, such as isothermal calorimetry (ITC)[6] and electrochemical techniques,[20] which are summarized in Table 1.1, are discussed elsewhere.

Though the thermodynamic and kinetic parameters offer a glimpse into the overall behavior of the system, the binding dynamics of the DNA–protein complex is critical for determining the detailed mechanism. Single-molecule imaging in particular is capable of tracking individual proteins and/or DNA targets as they are translocated or diffuse towards one another (Figure 1.1f). In a DNA-curtain assay,[23] DNA molecules stained by YOYO1 (structure is shown in Figure 1.1f) were fixed in a lipid bilayer on a cover slip, and RNA polymerase (RNAP) was fused to green fluorescence protein (GFP). Through total internal reflection fluorescence microscopy (TIRFM), the diffusion of RNAP along the DNA was monitored at the single-molecule level. In addition to optical techniques, high-speed atomic force microscope (AFM, Figure 1.1g) offers an alternative imaging approach for studying dynamics.[24] Though the

superior spatial resolution of this technique can offer a preliminary look into the detailed DNA–protein conformations, the throughput and temporal resolution are limited.

Since the majority of the aforementioned methods require sample purification, real-time detection of DNA–protein interactions in vivo remains challenging. Though methods like SPR can use crude extract for measurements, in vivo measurements often result in noisy background and low signal-to-noise ratios. A simple way to overcome this limitation is to label DNA and/or protein with fluorophores and use the colocalization of the different fluorescence emissions to monitor the interaction in vivo (Figure 1.1f). Advancements in microscopy have also pushed the limits of feasibility in the field. For example, super resolution microscopy has allowed researchers to overcome the imaging diffraction limit. One such setup based on photoactivated localization microscopy (PALM) uses a photoactivable fluorescent protein to label a POI for tracking.[27] DNA polymerase and ligase are fused to photoactivable mCherry to track the mechanism of DNA repair, and the delayed protein diffusion is reflective of the site searching mechanism.

Techniques based on Förster resonance energy transfer (FRET, Figure 1.1h) are flexible with the type and purity of samples that can be used for measurement.[6] In this system, one fluorophore behaves as a donor that absorbs a photon to achieve an excited state. Before it radiatively relaxes to the ground state, the excited donor non-radiatively transfers the energy to a neighboring fluorophore that behaves as an acceptor. This acceptor emits radiatively as it relaxes to its ground state. The FRET efficiency correlates with the distance between two fluorophores, particularly when the fluorophores are in the range of 2–10 nm. This distance-dependent efficiency has been exploited in studies that seek information on DNA–protein proximity. In one example, GFP that was fused to a POI served as a donor to nucleic acids that were stained with Sytox orange, which behaved as the acceptor.[25] When single-molecule FRET is coupled with a fluorescence lifetime imaging microscope (FLIM), the DNA–protein FRET interaction can be probed independent of local concentration.

1.1.2 Optical Monitoring of DNA–Protein Interactions Using Single-Walled Carbon Nanotubes (SWCNTs)

We recently developed a novel optical platform for investigating DNA–protein interactions using SWCNTs. SWCNTs can be conceptualized as rolled-up graphene sheets (Figure 1.2a). The wrapping direction determines the (n,m) chirality indices of a particular nanotube, and the chirality ultimately governs the optoelectronic properties of a particular SWCNT, which can be either metallic or semiconducting.[28] The semiconducting SWCNTs with diameters of 0.7–1.0 nm (Figure 1.2b) can be excited by light between 400 nm and 800 nm (i.e. E_{22} van Hove transition). The emitted fluorescence occurs at near-infrared (NIR) wavelengths between 900 nm and 1400 nm (i.e., relaxation at E_{11} van Hove transition). The characteristic excitation and emission wavelengths of a particular SWCNT is specific to the (n,m) chirality, which determines the bandgap. For example, a (6,5) SWCNT is excited around 570 nm, and the peak

fluorescence emission is around 990 nm.

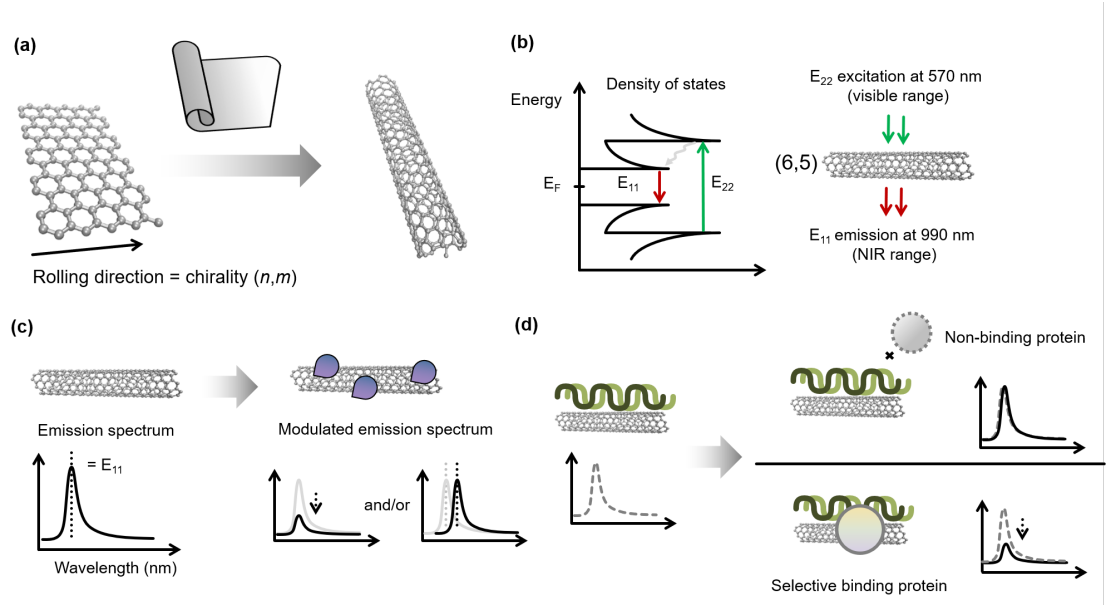

Figure 1.2 – Single-walled carbon nanotubes (SWCNTs) as optical DNA–protein biosensors. (a) A SWCNT is conceptualized as a rolled-up graphene sheet, and the rolling direction determines the (n,m) chirality. (b) For semiconducting SWCNTs like the (6,5) nanotube, the energy diagram and optical properties are characteristic of the van Hove singularities (E_{22} and E_{11} transitions). (c) The SWCNT fluorescence spectrum is modulated by the surface chemistry. (d) The surface of the SWCNT is functionalized with dsDNA, which can interact with selective binding proteins that yield a change in SWCNT fluorescence (bottom). SWCNTs that lack the target DNA sequence or solutions that lack the binding protein (top) contribute to minimal interaction and negligible fluorescence change.

These optical properties are influenced by the polarizability in the vicinity of SWCNT sidewall.[28] In other words, molecules that adsorb or interact with the surface of the SWCNT can change its NIR fluorescence spectrum (Figure 1.2c). These interactions can change the fluorescence intensity and/or shift the peak position. In the past, this sensitivity has been exploited to detect different bio-analytes. For example, small molecules such as neurotransmitters[14] and nitric oxide[29] have been detected by monitoring their effects on SWCNT fluorescence. In addition to small molecules, SWCNTs have also been used to detect aptamer-binding proteins that interact with DNA-aptamers immobilized onto the SWCNT surface.[30]

Analogous approaches can be developed for optically detecting specific DNA–protein interactions. For example, DNA can be non-covalently immobilized onto the nanotube surface (Figure 1.2d).[29–31] As demonstrated in our previous work, we anchored double-stranded DNA (dsDNA) onto SWCNTs with the help of a short single-stranded DNA (ssDNA) overhang.[31] Even when anchored to the SWCNT surface, the dsDNA remained accessible to restriction enzyme binding and cutting, as confirmed through gel electrophoresis. The sustained targeted enzyme activity on the immobilized surface confirmed (1) that the dsDNA

retained its native conformation (B-DNA) in the vicinity of the SWCNT and (2) the specificity of the restriction enzyme towards its target sequence. This technique was applied to different DNA sequences with distinct enzyme recognition sites, demonstrating the versatility of this approach for various DNA targets.

1.1.3 Conclusions and Outlook

In summary, we briefly reviewed analytical methods for investigating DNA–protein interactions, discussing approaches for identifying unknown interactions to characterizing thermodynamic and kinetic parameters for known interactions. We also discussed imaging techniques for single-molecule tracking and in vivo applications. Finally, we proposed a novel approach based on the single-molecule sensitivity of NIR SWCNT fluorescence. Though, to the best of our knowledge, this approach has yet to be used to analyze protein activity on DNA, it may offer several advantages for optical DNA–protein imaging. First, the platform benefits from a label-free approach with a facile immobilization procedure based on autonomous DNA adsorption. Also, unlike EMSA and most pull-down assays, this platform uses a non-destructive analytical method that can be extended to real-time monitoring of single-molecule events.[29, 30] Thus, both transient and equilibrium interactions can be studied, and the binding affinity can also be determined after appropriate calibration.[32] The indefinite photostability of the SWCNT fluorescence further allows continuous, long-term monitoring. Additionally, the different nanotube chiralities offer distinct fluorescence signals for detecting multiple targets simultaneously, without the need for orthogonal bioconjugative procedures. This platform can therefore be extended for use in high throughput, single-molecule measurements of multiple DNA–protein interactions.

Furthermore, the NIR emissions of the SWCNT is also conducive to in vivo applications. These emissions are minimally absorbed by biological fluids, tissue, and other biomolecules that typically absorb and/or fluoresce in the visible region of the optical spectrum. Cellular uptake of SWCNTs have already been shown in living cells through endocytosis with minimum cytotoxicity.[33] Combined with the aforementioned advantages, this technology lays the foundation in achieving the coveted single-molecule, long-term, continuous, and non-destructive monitoring of DNA–protein interactions.

1.2 Objective and Outline

The objective of this thesis is to explore the potential of SWCNTs as biosensor for detecting DNA–protein interactions. A general overview of this thesis is depicted in Figure 1.3. First, background of this ternary nano-bio hybrid, DNA-protein-SWCNT, is provided in Chapter 2. Then, we examine the structural perspective of DNA-SWCNT by developing two complementary assays (Chapter 3 and Chapter 4) for resolving structure-function relationship. Based on these findings, we then showcase the potential applications of the DNA-protein-SWCNT ternary hybrids (Chapter 5), and disclose some of the challenges that have been encountered

with this system. Next, we tackle these challenges by two different approaches (Chapter 6 and Chapter 7). Finally, a conclusion remark and future outlook will be given (Chapter 7). More details of each Chapter are provided below.

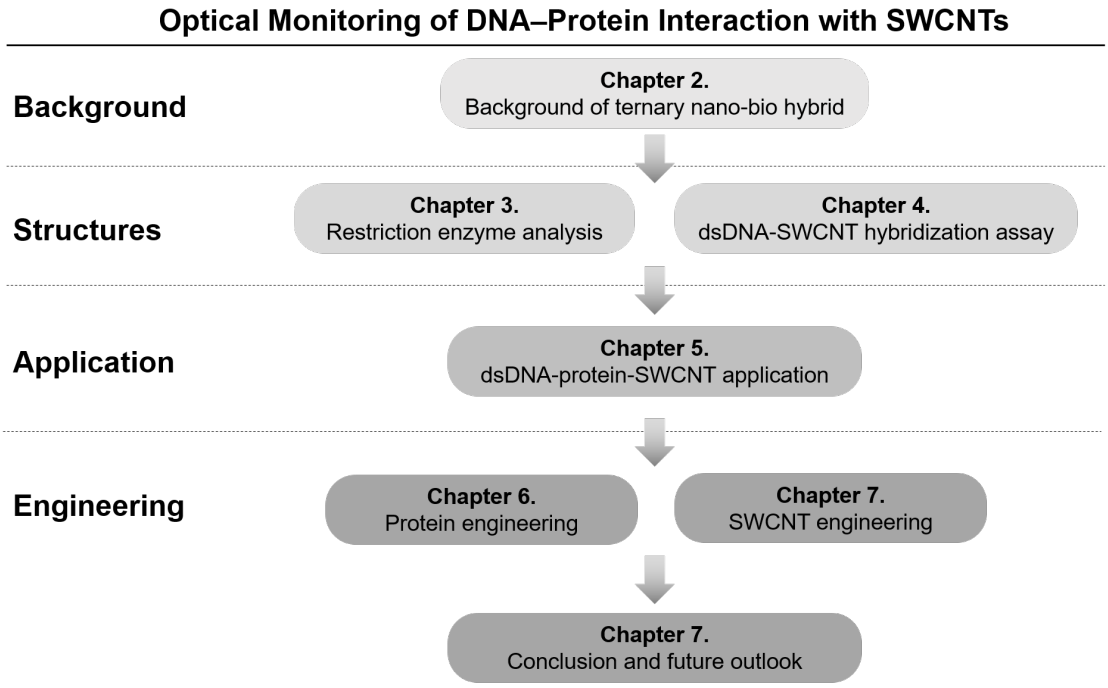

Figure 1.3 – Outline of the thesis.

The use of double-stranded DNA (dsDNA) is imperative to allow for specific binding to proteins with DNA-binding domains and/or benefit from DNA hybridization. Therefore, in Chapter 3, we systematically analyzed DNA conformations on the surface of SWCNTs by investigating whether the dsDNA fragment remains native in this system. We developed a biochemical assay based on the defined digestion of the restriction enzyme (RE), which specifically cuts dsDNA with B conformation. Fragment analysis by gel electrophoresis shows DNA on SWCNTs is shortened in the presence of RE. However, the low RE activity indicates a limited DNA-accessibility when it is bound to the SWCNT. We sought to address this problem by introducing a non-ionic surfactant, Triton X-100, to change the accessibility of the DNA on SWCNT, and demonstrated that this approach led to a 2.8-fold enhancement in the RE activity. By systematically testing a series of DNA sequences, we propose a model with B-DNA lying on the SWCNT parallel to the long axis of the SWCNT. This was further supported by the results of fluorescence spectroscopy and molecular dynamics (MD) simulations. This work revealed, for the first time, the DNA base pairing structure in the vicinity of SWCNT. Additionally, this study confirms that the DNA–protein interaction is preserved on SWCNTs, enabling the applications of dsDNA-SWCNT presented in Chapter 5.

However, comprehensive exploration of all DNA sequences remains largely unachieved by the approach in Chapter 3, limited by the sequence requirement and the assay throughput.

In Chapter 4, we expanded our toolbox by designing a generic fluorescence assay for characterization of dsDNA on SWCNTs. By using DNA-specific fluorescence dyes to probe the properly hybridized dsDNA-SWCNT, this assay performs at higher throughput and provides a widely applicable generic method. We demonstrate for the first time that the DNA hybridization on SWCNT is specific to Watson-Crick base pairing, which has never previously been supported by direct experimental evidence. Additionally, we identified the determining factors controlling the strength of DNA hybridization on SWCNTs. The understanding and optimization of these factors is critically fundamental for the applications presented in Chapter 5.

Next, in Chapter 5, we showcased the potential of DNA-protein-SWCNT ternary nano-bio hybrids with a series of applications. Two model configurations were demonstrated: (1) ssDNA-SWCNT/complementary DNA (cDNA)-protein, and (2) DNA-SWCNT/protein. In the first case, proteins are immobilized on SWCNTs via a dsDNA bridge (i.e., proteins linked to cDNA is subsequently hybridized to ssDNA-SWCNT). We used fluorescence microscopy to study the co-localization of the protein (labeled with visible fluorescence dye) and the SWCNT (with intrinsic NIR fluorescence). We demonstrated this platform with a functional enzyme (i.e., horseradish peroxidase) enabling specific analyte detection (i.e., hydrogen peroxide). In the second case, we found that Cas9 remains enzymatically active and is capable of digesting specific sequences bound to SWCNTs. Altogether, the results presented in Chapter 5 demonstrate the potential of DNA-protein-SWCNT hybrids in applications such as analyte detection or protein screening.

However, in Chapter 5, we noticed that SWCNT NIR fluorescence is barely able to distinguish the specific interaction of DNA-SWCNT/protein from non-specific interactions, limiting its applicability. We attributed this to two possibilities: (1) strong non-specific interactions between DNA-SWCNT/protein, and (2) the similar dielectric constant of DNA and protein, which leads to comparable exciton screening effect and therefore a same trend in PL modulation.

We aim to solve the problems separately with different approaches. In Chapter 6, we used a diverse set of proteins ranging from naturally occurring proteins to computationally designed proteins to characterize the attributes of non-specific interactions found in the hybrid of ssDNA-SWCNT/protein. By measuring the modulation of the intrinsic SWCNT fluorescence and using this as an estimate of interaction strength, we found electrostatic interactions are the primary interaction mode in ssDNA-SWCNT/protein, while the structural factors of proteins are also deterministic. In particular, for a library of designed proteins, we found that the overall helical propensities and the presence of solvent-exposed Asp largely determine the interaction strength. This indicates a complex cooperative interaction involving hydrogen bonds that also contribute to the interaction. Finally, we applied site-mutagenesis on the surface of a designed protein, successfully enhancing the fluorescence response of SWCNTs. In combination with protein library screening and rational design, our approach provides a guideline for tuning interaction strengths between proteins and ssDNA-SWCNT, tailoring the requirement for diverse applications.

We conclude the entire thesis in Chapter 7. We also offer the future outlook for this DNA-protein-SWCNT hybrid. Furthermore, a potential solution for the second challenge by using SWCNT-modification will be briefly discussed. We believe this study will become the foundation for future application of this type of material.

2 Background

2.1 Overview: Nano-Bio Hybrid Material and Ternary System

In Nature, in order to adapt to varying external challenges, even the simplest organism has a complex structure comprised of multiple subunits serving distinctive functions. As an analogy in material science, hybrid materials are referred to as the combination of two or more components to obtain multiple functions within the same unit. A classic application of this concept is a battery, in which a 'cell' of the battery comprises electrodes as the 'power house' and an electrolyte as 'refilling fuel.'

Over the past few decades, advances in nanotechnology have successfully achieved nanomaterials where at least one dimension is 1–100 nm. In comparison to the bulk material, it generally possesses distinctive properties due to the effects of quantum confinement. Inspired by the concept of hybrid materials, the interfacing of synthetic nanomaterials and biomolecules at the nanoscale, as nano-bio hybrid, enables unique applications with extreme sensitivity and selectivity simultaneously. For example, localized surface plasmonic resonance (LSPR) attains high antibody specificity, and the binding readout is amplified by metallic nanoparticles thanks to the evanescent field. Fluorescent and photostable quantum dots are another example, which are often decorated with DNA or proteins to enable target specificity and/or reducing cytotoxicity in in vivo imaging applications.

In this thesis, we are specifically interested in the nano-bio hybrid consisting of biomacromolecules and single-walled carbon nanotubes (SWCNTs). SWCNTs are often conceptualized as rolled-up graphene sheets, which form a sp^2 sidewall with a typical diameter of a few nanometers and a length that is sub-micrometer. The intrinsic Van Hove singularities[28] were extensively exploited in optoelectronic applications. However, the large surface area of hydrophobic SWCNT-sidewall dramatically induces self-aggregation and cytotoxicity, limiting potential applicability. Consequently, SWCNTs are often functionalized with other biomacromolecules, such as DNA or protein, to retrieve biocompatibility and dispersibility.[34, 35] These biomacromolecules in hybrid also provide the functionality and selectivity SWCNTs inherently lack.

Beyond the typical binary cases, ternary nano-bio hybrids of SWCNTs further expand the functional domain to explore complicated functionalities modularized within a single unit. In this thesis, we are primarily concerned with a special case: DNA, protein and SWCNTs. This tripartite combination allows one to simultaneously exploit the modality and tunability of DNA, the selectivity of protein and the distinctive optical properties of SWCNTs. However, poor understanding of the structure-function relationship and the interaction mode between components on the SWCNT complicates the assembly, as well as limiting the ultimate applications. To address these problems, here we are seeking to resolve the interaction and applications of such ternary nano-bio hybrids.

This Chapter 2 provides a contextual background by describing individual components included in the ternary nano-bio hybrids (namely, DNA, protein and SWCNTs) and subsequently detailing the assembled scenarios. We begin by reviewing the chemical composition, basic properties and synthesis of individual components. In particular, the structure-function relationship and their applications in biotechnology and/or material science will be highlighted, as the motive behind composing the hybrid. Next, the binary combinations will be discussed, shedding light on their interaction mode and structure-function perspective. Lastly, we will revisit existing ternary nano-bio hybrid cases, further disclosing the challenges we are facing in such systems.

2.2 Individual Components

2.2.1 DNA

2.2.1.1 Basic Properties

In the late nineteenth century, deoxyribonucleic acid (DNA) was first extracted and characterized by Miescher, and it was later considered as a fundamental ingredient of living organisms. As a biopolymer, DNA is a combination of four canonical nucleotides as monomers (Figure 2.1a): adenylate (dA), guanylate (dG), cytidylate (dC), and thymidylate (dT). By forming phosphodiester linkage between the 5'-phosphate group and the 3'-hydroxyl group of two adjacent ribose units, the genetic information was encoded in DNA sequence and later transcribed into RNA and translated into proteins for the function needed in living organisms.

It was only in the 1950s that the DNA structure was revealed by X-ray crystallography. Two antiparallel strands of DNA were shown to form into right-handed double helices with 10.5 bases per turn, a structure known as B-DNA (Figure 2.1b). The structure is stabilized by classical Watson-Crick base pairing between two strands (A=T and G≡C) with hydrogen bonds. Ring stacking between neighboring bases also contributes to the stability, which was observed in hypochromicity in the UV and is well-described by the nearest-neighbor model.[36] Importantly, the structure is stable due to the high specific pairing of two strands. This largely enables sequence orthogonality and variability, which have been exploited in many applications, including polymerase chain reaction (PCR).

So far, DNA has been discovered to adapt several distinct conformations under different conditions (Figure 2.1b). For example, closely packed and tilted right-handed double helices (A-DNA) are favored in dehydrated environments. On the other hand, in the presence of mercury cations or extremely high salt concentrations, the GC-rich region of DNA transits into left-handed double helices, known as Z-DNA.[37]

In addition to environmental factors, the sequence pattern of DNA greatly governs the tertiary structure. For example, a partial self-complementary sequence (i.e., palindrome-like) has the potential to form hairpin structures. Another example, non-canonical Hoogsteen base pairing, occurs in the polypurine/polypyrimidine region as a parallel duplex at low pH.[38] Hoogsteen pairs can also be found in triplex (H-DNA), where a third strand is intervening into the major groove of an antiparallel duplex. Other secondary structures include the quadruplex, which is stable as a G-quadruplex for a G-rich sequence (Figure 2.1b) and as an i-motif[39] for a C-rich sequence. All these non-canonical secondary structures were exploited to build the DNA aptamer for specific binding applications.

2.2.1.2 Synthesis and Applications

Nowadays, DNA oligonucleotides are prepared by solid phase synthesis and are commercially available. This accelerates the maturation of cloning and PCR amplification, allowing simple modification and replication of the gene. Long sequences or plasmid can be further prepared from Golden Gate assembly or Gibson assembly methods. Other amplification techniques, such as toehold-mediate strand displacement, enable the DNA to be amplified in tunable conditions. More recently, genomic modifications using transcription activator-like effector nuclease (TALEN) or clustered regularly interspaced short palindromic repeats (CRISPR)[43] systems also became accessible. The characterization of DNA sequences can be accomplished by Sanger sequencing and the recently-developed next-generation sequencing (NGS) technology.

In addition to information storage in vivo, DNA has been widely utilized in bioengineering and material science (Figure 2.1c). The high specificity of DNA hybridization and the ability of amplification is beneficial in applications such as diagnostic DNA microarrays and fluorescence in situ hybridization (FISH).[44] Additionally, owing to the orthogonality and the variability of sequences, DNA hybridization has been further used in in vivo imaging, such as signal amplification by exchange reaction (SABER), where the 10–20 nucleotides (nt) DNA sequence was used to barcode a specific target.[40] Similarly, DNA origami exploits these orthogonal DNA 'staples' for constructing different nanostructures.[41] Analogous to RNA-systematic evolution of ligands by exponential enrichment (SELEX), DNA-SELEX screens the secondary structure of DNA sequence and enables specific target binding.[9] Using DNA to build a program has also been of great interest. For example, the conversion of DNA 4-letter codes into other programming languages or information storage were explored.[45, 46] Also, the displacing strands mechanism and the dynamic behavior of DNA strands makes the DNA circuit possible.[42]

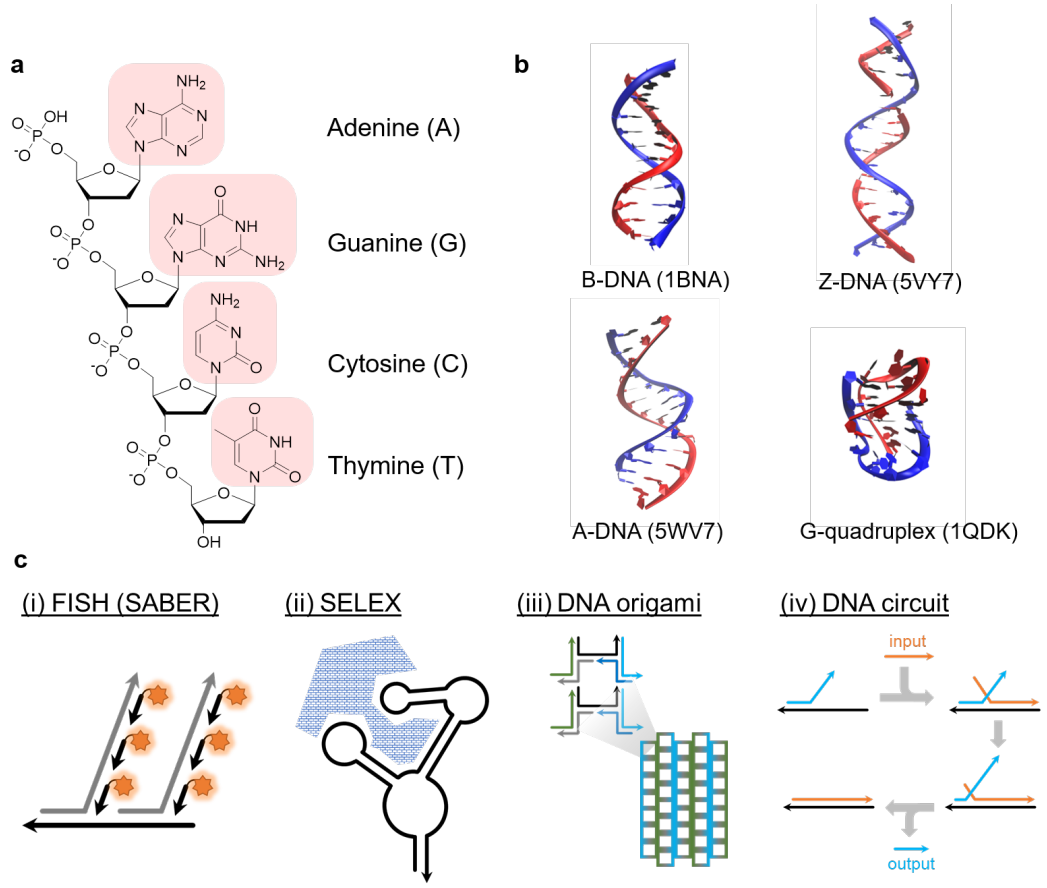

Figure 2.1 – DNA properties and its applications. (a) Chemical structure of the four canonical nucleotides. Bases are highlighted in pink and labeled respectively. (b) Typical crystal structures of DNA. Registered codes of the different structures are labeled in parenthesis. (c) Four applications of DNA. (i) FISH (SABER)[40]: target sequence (black) is hybridized with complementary strand (gray) by strand exchange, and the signal is amplified by a fluorophore (orange). (ii) SELEX[9]: DNA tertiary structure (black) is screened and selected for specific binding to a target molecule (blue). (iii) DNA origami[41]: well-defined nanostructure is constructed by DNA hybridization between distinct staple strands. (iv) DNA circuit[42]: logic gates are designed using the DNA displacement mechanism. In a simple case, input strand (orange) replaces a shorter strand (blue) on the template strand (black), releasing the blue strand as an output. Note the arrow indicates the direction of DNA from the 5'-phosphate group to the 3'-hydroxyl group. Cartoon of applications are adapted from references.

2.2.2 Protein

2.2.2.1 Basic Properties

Proteins are one of the most versatile materials: to date, according to the Structural Classification of Proteins (SCOP), more than 560,000 protein structures have been registered, and more than 47,000 non-redundant protein domains have been identified. Since the function

of a protein is encoded in its 3-dimensional structure, it is crucial to elucidate this from the building block of a protein, L-form of amino acid (a.a.). Amino acids have an enantiomeric center (C_α) that links to an amino group, a carboxyl group and a side chain (Figure 2.2a). The individual characteristics of an a.a. are determined by 20 common side chains, which are often classified as charged, polar or hydrophobic, according to Taylor's classification. A polypeptide is formed by condensation of the carboxyl group and the amino group from the adjacent a.a. into an amide bond. With the steric hindrance of the side chain, the primary structure of a polypeptide is constrained by dihedral angles, as depicted in Ramachandran plots.

Short-range and long-range interactions between a.a. in a polypeptide chain creates a local structure between protein residues, known as the secondary structure. Based on the regularity of the backbone interaction between residues, three types of secondary structural elements have been categorized: helix, sheet and loop. The α-helix is characterized by a right-handed spiral with 3.6 residues per turn (Figure 2.2). This conformation is stabilized by hydrogen bonding and electrostatic forces between the residues of neighboring turns. Alternatively, the zigzag backbone of polypeptide chain may be stabilized by hydrogen bonds in long range with adjacent segment, forming a β-sheet. These secondary structures can further fold and complex with others, resulting in the tertiary structure. As a subunit, the tertiary structure may even assemble with other cognate polypeptide chain(s), to yield the quaternary structure. Figure 2.2b shows an example of yeast RNA polymerase, which is composed of multiple subunits with distinct tertiary structures.

2.2.2.2 Synthesis and Applications

Proteins are exploited to broadly cover biological functions required for the living system or are further engineered for many applications needed in the upcoming era, including catalysis, imaging, sensing and diagnosis. The development of protein engineering, either through rational design or directed evolution, extensively expands the toolbox of proteins beyond the natural protein reservoir. Molecular cloning of plasmids allows overexpression of engineered proteins in heterologous organisms, while solid state synthesis is often used for short peptides instead. Various protein tagging methods and column chromatography purifications yield high levels of protein purity.

One of the most promising uses of proteins is that they can be engineered to bind to a specific target or to catalyze substrates that are naturally unreactive (Figure 2.2c). For example, enzymes, like P450 cytochrome, can be modified to catalyze silicon-carbon bond formation[48] or asymmetric benzylic C-H alkylation.[47] $(\beta/\alpha)_8$-barrel is another structural motif that can potentially be engineered for binding to a specific small molecule.[49] Recently, CRISPR-associated proteins (Cas), a genome editing tool, has been extensively engineered in order to expand the protospacer adjacent motif (PAM)[50–52] or to reduce the off-target effect.[53–55] Another widely used approach is protein fusion. By constructing a fluorescent protein fused to a target protein, in vivo imaging can visually localize certain organelles. This is further extended for specific applications. As an example, optogenetics exploits engineered

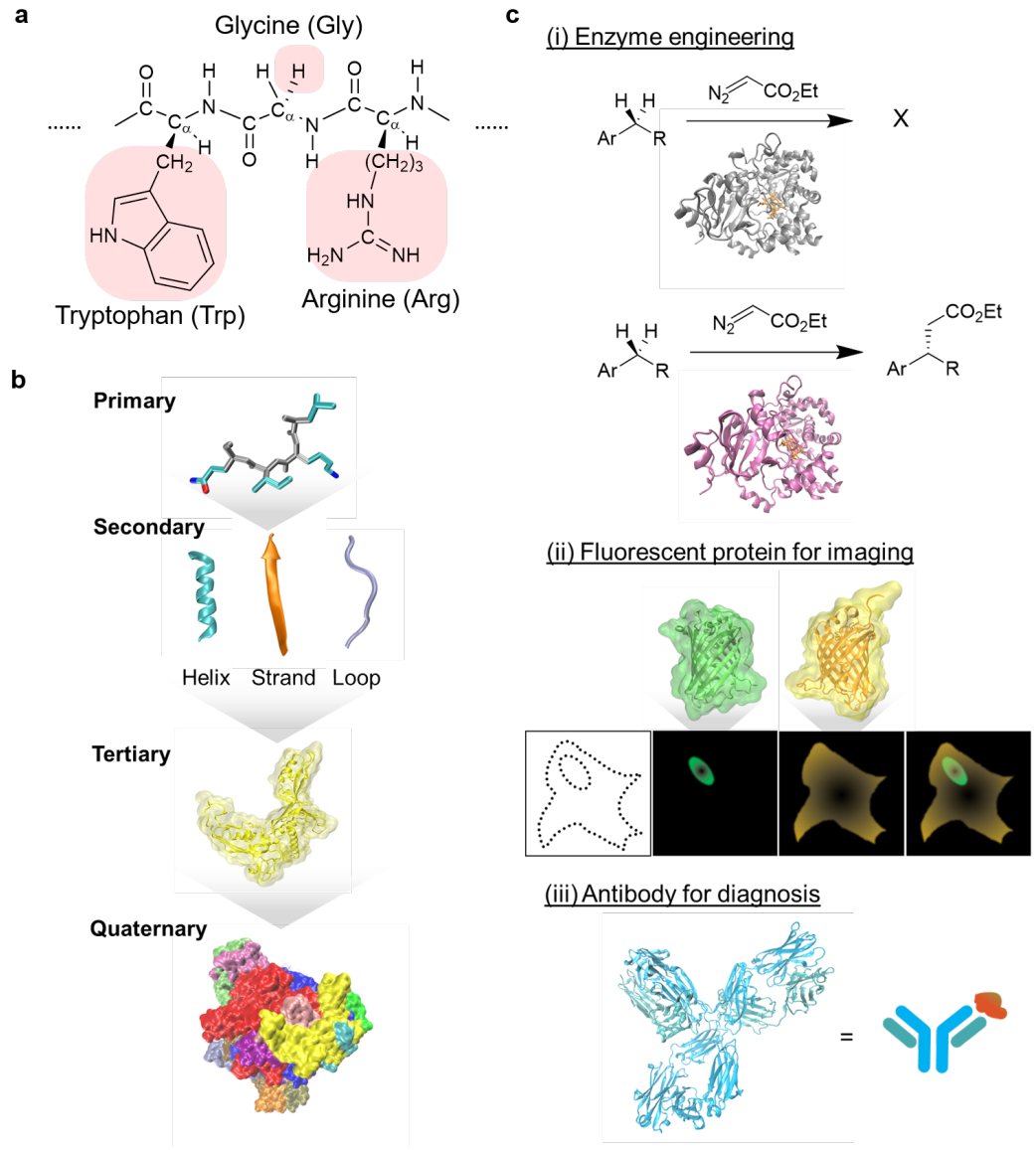

Figure 2.2 – Protein properties and its applications. (a) Chemical structure of protein, with examples of side chains. (b) Four levels of protein structure. Yeast RNA polymerase (5FJA), which has 13 subunits (different colors), is shown as an example. (c) Three applications of proteins: (i) Enzyme engineering[47]: asymmetric C-H alkylation is naturally forbidden by wild-type P450 cytochrome (1W0E, gray), but it can be achieved by using an engineered enzyme (violet). Schemes are adapted from reference. (ii) Fluorescent protein for imaging: different fluorescent proteins (2Y0G for green, 3V3D for yellow) are tagged to distinct organelles for localization. (iii) Antibody for diagnosis: antibody (5DK3, cyan for heavy chain, turquoise for light chain) can be engineered to selectively bind to a specific antigen (orange).

rhodopsin as voltage sensor in neurons.[56, 57] Finally, proteins are largely used for diagnosis (e.g., immunoassay) and medical treatment. Drugs and antigens have been derived from the design of cyclic peptides and small proteins using a combination of docking simulation and

library screening.

2.2.3 SWCNTs

2.2.3.1 Basic Properties

As a hollow cylinder with single layer sidewall, a single-walled carbon nanotube (SWCNT) is often conceptualized as a rolled-up graphene sheet exhibiting sp^2 hybridization. The periodic boundary condition limits the circumference of a nanotube (i.e., the 'rolling direction') to be the chiral vector (n **u**, m **v**), where **u** and **v** are the basis vectors of the graphene lattice and n and m are non-negative integers. The chirality of a SWCNT is thus defined as (n,m) (Figure 2.3a of SWCNT), and the diameter (d) can then be calculated by the equation below:

$$d = \frac{a}{\pi}\sqrt{n^2 + nm + m^2} \tag{2.1}$$

where a is the lattice constant. Depending on the synthesis scheme, the SWCNT diameter spans between 0.5 and 2.0 nm, while the length of the SWCNT along the tube axis varies within a range of 100–1000 nm. In particular, in this study, we mainly used HiPCO and CoMoCAT (as discussed below), which have an average diameter of 0.7–1.3 nm and a sub-micrometer length. The geometry of SWCNTs makes them a high aspect ratio and a high surface area nanomaterial.

Given a long enough SWCNT (i.e., infinite approximation), the optoelectronic properties are mainly determined by the chirality of the SWCNT. By applying a zone-folding approximation to the Brillouin zone of graphene, the electronic band structure is constrained by the boundary condition of circumference and the symmetry of the SWCNT. As a result, SWCNTs are categorized as either metallic if $m-n = 3l$, or semiconducting if $m-n = 3l \pm 1$, where l is an integer. For example, (12,0)-SWCNTs (zigzag) and (6,6)-SWCNTs (armchair) are both metallic, while (7,5)-SWCNTs (chiral) are semiconducting. The density of states (DOS) of SWCNTs can be further derived from the dispersion relations, and the Van Hove singularities (VHS) are found where the energy level has a higher DOS (i.e., the spikes).

The optical spectrum is dominated by the energy transitions between VHS (Figure 2.3b). The transitions, E_{ii} ($i = 1,2,3$.....) are limited by the selection rule imposed by the conservation of angular momentum ($\Delta q = 0$) due to the quenching of the depolarization field.[58, 59] At higher order transition (E_{22}, E_{33}.....), the exciton may radiatively relax to a lower energy VHS state in the valence band, resulting in photoluminescence (PL) with a significant Stokes shift.[60] For example, the suspension of (6,5)-SWCNTs in water can be excited at the E_{22} transition (2.19 eV), which falls in the visible light range (566 nm), and fluoresces at the E_{11} transition (1.27 eV), which falls in near-infrared (NIR) range (976 nm).

Since the external screening affects the Coulombic interaction in exciton binding, the optical transitions of SWCNTs, such as absorption and PL, highly depend on the dielectric

environment. For example, the E_{11} and E_{22} transitions of SWCNTs in air ($\epsilon \approx 1$) were found to be 40–55 and 24–48 meV larger than in water-surfactant ($\epsilon \approx 2$).[61] Similarly, Choi and Strano reported solvatochroism of SWCNTs with different solvents and adsorption of molecules (Figure 2.3c).[62] As a result, such sensitivity to environment is utilized in many applications, which will be discussed later in this Chapter.

We primarily focus on the work of pristine SWCNTs in this thesis. However, other factors including the length of SWCNTs[63] and the sp^3 defect density[63, 64] can alter the exciton dynamics and optical transitions. It is possible to control the length of SWCNTs by sorting[65] and the defect density by sp^3-modification[64], respectively. Discussion of other characteristics of SWCNTs such as mechanical and transport properties can also be found elsewhere.[28]

2.2.3.2 Synthesis and Applications

Since the first discovery of SWCNTs by Iijima in 1993,[66] the synthesis of SWCNTs has held the key to many fundamental experiments and potential applications. Different synthetic approaches produce SWCNTs at various levels of purity, chirality distribution, yield and production rate. For example, arc charge yields large diameter SWCNTs with fewer defects, while laser ablation produces high purity SWCNTs at a lower production rate. On the other hand, several commercially available SWCNTs are synthesized by catalytic chemical vapor deposition (CCVD). Two examples, cobalt-molybdenum catalyzed process (CoMoCAT) and high-pressure carbon monoxide process (HiPCO), both produce SWCNTs with a diameter around 0.7–1.3 nm and a length around 1 um. Notably, substantial amounts of catalyst are retained in the SWCNT bundles, which should be purified post-synthesis. In this thesis, CoMoCAT and HiPCO are the two major SWCNT resources used.

SWCNTs have been widely used in many bioapplications both in vitro and in vivo.[67] Exciton dynamics in SWCNTs are sensitive to the dielectric environment,[61] pH[68, 69] and electron transfer between SWCNTs and surrounding molecules.[70] This has often been exploited to detect a certain event (e.g., nucleic acid hybridization[71, 72], redox reaction[73]) or analyte (e.g., nitric oxide[29], dopamine[14]). Importantly, since SWCNTs are electron-rich, they are photostable with negligible phototoxicity under laser illumination, which makes them a good candidate for long-term continuous experiments. Also, the NIR fluorescence of SWCNTs ideally falls in the tissue-transparent window, which is preferential for in vivo imaging applications. On the other hand, the high surface area of SWCNTs provides a platform for cargo delivery into the cell, as realized in applications including drug delivery,[74] gene transfection[75, 76] and nanoparticle uptake.[77] Last but not least, the well-defined electronic structure of SWCNTs can be taken advantages of in the fabrication of high-performance electrical devices, including single-junction field-effect transistors.[78–80]

Despite these unique properties and potential applications, SWCNTs are hardly used in pristine form. The hydrophobicity of their large surface area induces inter-tube aggregation, which causes fluorescence quenching, diminishes the reproducibility and limits the general

use. Therefore, similarly to other nanoparticles, SWCNTs require proper decoration to improve the suspension stability and functionality (e.g., selectivity). To address this challenge, in Section 2.3.1 and Section 2.3.2, we will briefly review how biomolecules can be used to disperse SWCNTs and provide functionality in the hybrid. Two special cases will be highlighted: DNA-SWCNT and protein-SWCNT. However, it should be noted that other materials can also be processed with SWCNTs, such as surfactants,[60, 81] lipids,[77] polymers[82–85] and sugars.[86, 87]

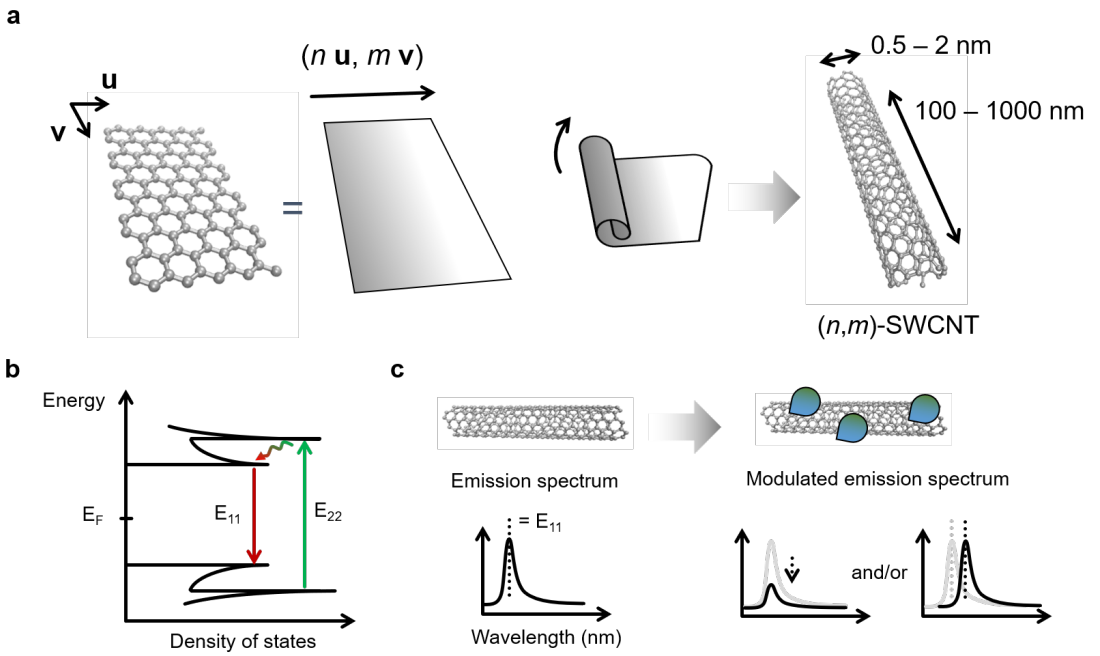

Figure 2.3 – SWCNT properties and its applications. (a) Chemical structure of a SWCNT where carbon is represented as a gray ball. **u** and **v** represent the basis vector of graphene sheet, while (n **u**, m **v**) is the chiral vector of a SWCNT. (b) Band diagram of a semiconducting SWCNT. Green and red arrows are the allowed optical transition of E_{22} and E_{11}, respectively. (c) Sensing application of SWCNTs using NIR fluorescence. The emission spectrum of SWCNTs is modulated as an adsorbent (blue droplet) interacting with the SWCNT surface.

2.3 Binary Hybrid of SWCNT

In this section, we will discuss the binary combinations of each of the two components of DNA, proteins and SWCNTs. A brief summary of the potential applications of binary hybrids will be provided, and we will focus more on how the two components interact with each other and their corresponding structure. Preparation, functionalization and purification approaches of binary hybrids will not be included, but extensive discussion can be found elsewhere.[34, 35] We also exclude nanoparticles which are not SWCNTs, since it is beyond the scope of this thesis.

2.3.1 DNA-SWCNT Interaction

Since the pioneering work of Zheng et al. in 2003,[88] DNA has been widely used to disperse pristine SWCNTs. The easily processed biopolymer has an amphiphilic and biocompatible nature, making it a stable dispersant of SWCNTs in aqueous solution or biological media. Moreover, the conformation of DNA bound to SWCNT is sequence dependent, providing the potential for tuning the functionality, such as the selectivity toward different analytes (Figure 2.4a). Though the sequence-structure-function relationship of DNA-SWCNT remains mostly unresolved, directed evolution,[89–91] library screening[14] and machine learning[92] has recently been applied to improve the performance of these binary hybrids. The subtle structural differences of DNA sequences bound to SWCNTs even have potential applications in SWCNT chirality separation. On the other hand, well-defined structures can be achieved with the use of DNA hybridization and DNA origami technology (Figure 2.4b). Recently, a single-junction field-effect transistors (FETs) based on DNA-SWCNT perfectly demonstrated the manipulation of nano-bio hybrids in nanofabrication.[79, 80] In this section, we will review how DNA interacts with SWCNTs. We separate the section into two parts: single-stranded DNA (ssDNA) and double-stranded DNA (dsDNA). DNA conformations when bound to SWCNTs will be specifically highlighted, since it is the key to the functionality.

2.3.1.1 ssDNA-SWCNT and Corresponding Secondary Structures

The main interaction between ssDNA and a SWCNT is $\pi-\pi$ stacking between the nucleobases and the sp^2-hybridized graphene structure. Similarly to base stacking in dsDNA, hypochromicity in the UV regime with respect to free ssDNA experimentally confirms the $\pi-\pi^*$ transition in ssDNA-SWCNT.[93] This agrees with the prediction of density functional theory (DFT), which suggests a redistribution of the net charge as a nucleoside adsorbs to a SWCNT.[94] Also, the binding energy was found to differ between nucleosides. Purine generally has a higher affinity for SWCNTs than pyrimidine does because of an additional $\pi-\pi$ stacking contributed by its imidazole ring. However, this sequence dependence may differ significantly in the case of oligonucleotides on SWCNTs, where the steric hindrance from neighboring bases and the curvature of the SWCNT are also deterministic factors.[95, 96] In contrast to nucleosides, the hydrophilic sugar-phosphate backbone of DNA has less vdw contact with uncharged SWCNTs.[97] However, it majorly determines the secondary structure of DNA bound to SWCNTs, which will be discussed below.

The conformation of ssDNA bound to SWCNT was originally believed to be dependent on ssDNA sequence and length, as inferred by ssDNA-SWCNT application in chemical sensing[14] and chirality separation.[92] Periodic height profiles of ssDNA-SWCNT in AFM imaging implied that the ssDNA adopted a helical wrapping on the surface of SWCNTs.[98] Molecular dynamics (MD) simulation further elucidated that ssDNA spontaneously helically wraps around SWCNTs within 10 ns.[97] Both right-handed and left-handed wrapping were found to be stable. Interestingly, in contradiction with a proposed structure by Zheng et al.,[88, 98] the conformation is not stabilized by the hydrogen bond between bases due to the curved surface

of the SWCNT and steric hindrance. Instead, the helical wrapping is driven by the torsional force in the sugar-phosphate backbone and the electrostatic force.[97] It was thus believed that the helical structure is sequence independent.

In additional to helical wrapping, other DNA structures have been found to be energetically stable on the surface of SWCNTs. Johnson et al. applied replica-exchange molecular dynamics (REMD) to sample the energy landscape of $(GT)_7$-SWCNTs, and six different conformations were found to be energetically favorable, including three loop-like non-helical structures.[99] Roxbury et al. suggested $(GT)_n$ ssDNA forms into β-sheets and β-barrel motifs on SWCNTs.[100] Recent work by Beyene et al.[101] and Alizadehmojarad et al.[102] also identified a ring-like structure of 12 nt long ssDNA on (9,4)-SWCNTs. Notably, these structures may not be distinguishable by experimental techniques due to the limitation of microscope resolution. Despite these advancements, the exact sequence-structure relationship of ssDNA-SWCNT remains vague. Consequently, library screening,[14] directed evolution[89, 90] or machine learning[92] was utilized to guide the ssDNA-SWCNT design.

Furthermore, intrinsic ssDNA secondary structures on SWCNTs are of great interest due to their sensing capability. For example, Richert et al.[103] and Hain et al.[104] both suggested that the hairpin DNA structure is preserved, as the loop region preferably adsorbs on SWCNTs. Alternatively, DNA aptamers were also successfully anchored on SWCNT through a 5'-overhang,[30] and the protein-binding ability of DNA aptamer remained intact, indicating a preservation of secondary structure. Post-modification of various DNA aptamers on ssDNA-SWCNT was also achieved by click chemistry whereby different molecules were targeted.[105] Similarly, G-quadruplex was brought to the vicinity of the SWCNT surface without deformation.[106] All these studies suggest the application of DNA secondary structures on SWCNTs as sensors is practically feasible.

2.3.1.2 dsDNA-SWCNT

dsDNA-SWCNT interactions are considered to be weaker than ssDNA-SWCNT. Because the hydrophobic nucleobases of DNA are buried inside the phosphate-sugar backbone, $\pi-\pi$ stacking with SWCNT is forbidden, except for the end-group where nucleobases are exposed. Therefore, unless dsDNA unwinds, only short-range weak vdw interactions are available for dsDNA-binding.

dsDNA-SWCNT can potentially provide more well-defined applications than ssDNA-SWCNT due to the specificity and orthogonality of DNA, as mentioned in Section 2.2.1. Nevertheless, the structure-function relationship of dsDNA-SWCNT has been debated regarding: (1) the position and orientation of the dsDNA with respect to the SWCNT, and (2) the conformation of dsDNA in the vicinity of SWCNT. It has been suggested that vdw between dsDNA and SWCNT surface are too weak to stabilize the binding and only the end group of dsDNA adsorbs onto the SWCNT by $\pi-\pi$ stacking (i.e., the long axes of dsDNA and SWCNT are perpendicular to each other).[107] In support of the theory concerning exposure to nucleobases for $\pi-\pi$

stacking, transmission electron microscope (TEM) imaging suggested that the double-helices structure of genomic DNA is gradually disrupted on SWCNTs.[108] Shiraki et al. used MD simulations and absorption spectroscopy to further probe this interaction, proposing that oligonucleotide DNA forms a partially destabilized duplex on the surface of SWCNTs.[109] Alternatively, Bascom et al. have suggested that there is a conformational change of B-to-A DNA without $\pi - \pi$ stacking when the dsDNA is in proximity to the nanotube.[110] It should be noted that many factors may lead to these mixed conclusions, including the hybrid preparation method, DNA length and DNA sequence and initial configuration of DNA in simulation. This topic is further discussed in Chapter 3.

2.3.2 Protein-SWCNT Interaction

Protein-SWCNT offers broad functionality and good selectivity.[111] Many endogenous proteins are capable of dispersing SWCNTs, as demonstrated by the early systematic studies of Nepal and Geckeler.[112] By attaching an antibody or enzyme, target specificity is introduced to the SWCNT. For example, glucose-binding proteins and glucose oxidase (GOx) have been successfully used to decorate the SWCNT surface, resulting in a SWCNT fluorescence selectively responding to glucose (Figure 2.4c).[113, 114] On the other hand, de novo protein design enables ordered assembly of protein-SWCNT structures that can be used for nanoparticle manipulation (Figure 2.4d).[115]

However, interactions between proteins (or peptides) and SWCNTs are complicated as a result of different affinities for 20 a.a. with SWCNTs and the high-order structure of proteins. We thus begin with elucidating the interaction of individual a.a. and SWCNTs, followed by short peptide-SWCNT and protein-SWCNT. Notably, in this Section, we only focus on systems without any assisting agents like DNA, surfactant or lipids, which can be found in Section 2.4.3.

2.3.2.1 Amino Acid and Short Peptide-SWCNT

Amino acids which are able to have π–interactions have a high binding affinity to the SWCNT surface, as confirmed theoretically[117] and experimentally.[118, 119] This includes $\pi - \pi$ stacking (Trp, Tyr, Phe, His, and Arg) and cation—π interactions (Arg). Aliphatic residues also preferentially bind to SWCNTs due to hydrophobic interactions, though exceptions have been predicted for a.a. such as Ala.[117]

In 3D space, the cooperative interactions between high affinity residues should be considered. Similarly to DNA, the primary sequence of protein determines its structure and thus contributes to the binding affinity to SWCNTs. Previously, Heller et al. used natural occurring peptides, such as bombolitin, to suspend SWCNTs without further engineering.[120] Though they found a secondary structure forming at the surface of SWCNTs, peptide-SWCNT interactions at a molecular level are still elusive.

Designing SWCNT-binding peptides based on structural considerations has been shown

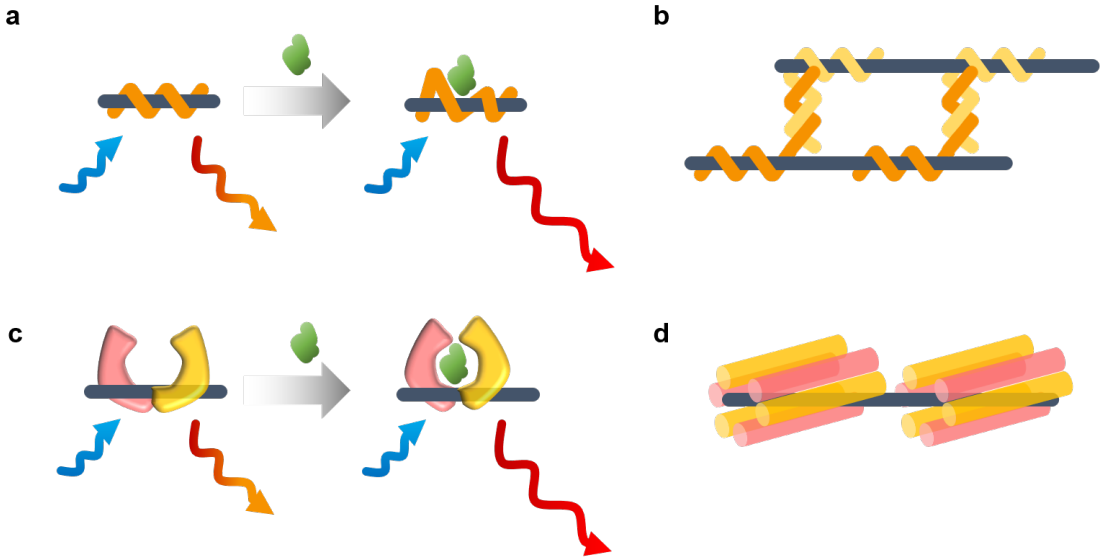

Figure 2.4 – Applications of SWCNT binary hybrids. (a) DNA-SWCNT for sensing: DNA (orange) is helically wrapped around a SWCNT (black). While interacting with an analyte (green), the conformation of DNA changes, modulating the NIR fluorescence of the SWCNT.[14] (b) DNA-SWCNT for well-defined structure: individual DNA-SWCNTs can be bridged together using complementary DNA sequences (orange and yellow).[116] (c) Protein-SWCNT for sensing: the conformation of a protein (pink and yellow) adsorbed onto a SWCNT changes upon binding to an analyte (green), causing a change of SWCNT NIR fluorescence.[113] (d) Protein-SWCNT for well-defined structure: a designed protein (pink and yellow) self-assembles with tunable orientation and positioning on the SWCNT.[115]

to be an effective approach. In order to increase the vdw contact of peptide-SWCNT, aliphatic residues (i.e., Ala) are aligned in a de novo designed α-helix peptide, which forms a motif similar to Leu zipper.[115, 121] By using a sodium dodecylbenzenesulfonate (SDBS)-displacing assay, the affinity of such peptides was proved as strong as ssDNA to the SWCNT surface, while sequences without Ala alignment are not capable of dispersing SWCNTs. Likewise, Mann et al. incorporated de novo designed α-helical coiled-coil barrels to suspend SWCNTs.[122] They were able to modulate the SWCNT suspension yield by simply changing the pore size of the protein barrel.

In contrast to rational design, directed evolution has been extensively applied to screen and to identify SWCNT-binding peptide sequences. Wang et al.[123] pioneered an approach using phage display and suggested His and Trp are highly enriched in several selected SWCNT-binding sequences. Subsequently, a possible SWCNT-binding motif, SXWWXXW, was identified by Zheng et al.,[124] and they hypothesized that all Trp (W) may position on the same side of peptide. Using a similar approach, Yu et al.[125] identified peptide sequences that exhibited a preference for large diameter chiralities. Even though most of the structures of SWCNT-binding peptides have not been fully characterized, such peptides have been tagged

onto proteins (e.g., carbonic anhydrase), which improved their binding affinity to SWCNTs.

2.3.2.2 Protein-SWCNT

In addition to chemical features found predominantly in protein-SWCNT interactions, the secondary and tertiary structures of proteins also serve as determinants.[35] For example, proteins with hydrophobic pockets may strongly interact with the hydrophobic surface of SWCNTs, as shown in the case of bovine serum albumin (BSA)-SWCNT hybrids.[126] Similarly, a flanking interaction mechanism was illustrated by MD docking in recombinant lamin B1-SWCNT hybrids.[74] Structural changes of proteins originating from protein-SWCNT interactions can also be inferred from protein activity in the presence of SWCNTs. Horseradish peroxidase (HRP) loses activity in HRP-SWCNT hybrids within 5 days, indicating a structural denaturation of the protein by SWCNTs.[127] In contrast, a moderate protein-SWCNT interaction is found in glucose oxidase (GOx)-SWCNT, which shows retention of GOx activity and a suspension stability of over 36 days.[128] However, a comprehensive rule of how protein structure affects protein-SWCNT interactions is still missing.

Another challenge is the intrinsically low affinity of some proteins for SWCNTs, which may not possess the surface residues necessary for binding.[112] Curvature of the nanotube also reduces the vdw contact between proteins and SWCNTs.[129] Even for proteins like BSA, which was identified as a good SWCNT binder, dynamic adsorption-desorption behavior of BSA-SWCNT implies a general lower affinity compared to ssDNA.[130] As a result, specific linker or SWCNT modification may be necessary to increase affinity or to control the orientation of the protein with respect to the SWCNT.[131, 132] Previous attempts to address this limitation by Chen et al. involved fusing a SWCNT-binding sequence (LLADTTHHRPWT, found using phage display) with carbonic anhydrase to immobilize the protein.[133] The authors found that using this approach the tagged protein showed intact enzymatic activity following adsorption onto the SWCNT. Alternative chemical modifications for preparing protein-SWCNT hybrids will be discussed further in Section 2.4.3 and in Chapter 5. Overall, precise control of protein affinity towards SWCNTs while maintaining the structural and functional integrity of protein is still an ongoing field of research.

2.4 Ternary Hybrid of SWCNT

In this section, we will discuss ternary nano-bio hybrids composed of nanoparticles and macromolecules, with particularly focus on hybrids of DNA-protein-SWCNT. We mainly investigated two special cases: DNA-SWCNT/protein and protein-SWCNT/DNA. In such ternary hybrids, all the interactions previously mentioned in Section 2.3 are involved (Table 2.1) and hence elevate the level of complexity. Other ternary cases will also be briefly discussed.

Table 2.1 – Short duplex DNA oligomers used to wrap SWCNTs.

Binary pair	Interaction	Example of motif structure
DNA/protein	• Vdw interaction • Columbic interaction • Polyelectrolyte effect • Hydrophobic interaction	• Leucine zipper • Cation–π/H-bond stair
ssDNA/SWCNT	• Vdw interaction – $\pi-\pi$ interaction	• Helical wrapping • Loop/ring motif
dsDNA/SWCNT	• Vdw interaction – $\pi-\pi$ interaction (end group)	• Native dsDNA • A-DNA • Denatured ssDNA
Protein/SWCNT	• Vdw interaction – $\pi-\pi$ interaction – Cation–π interaction	• Random coil • Alanine coiled-coil • Native protein structure

2.4.1 Special Case 1: DNA-SWCNT/Protein Interaction

2.4.1.1 Non-Specific Interactions

Non-specific adsorption of a single type of proteins on DNA-SWCNT was considered to be a good model system in ternary hybrids. Early work by Bisker et al. screened different non-covalent functionalizations of SWCNTs, including ssDNA and lipids, to select the best interacting molecules with fibrinogen.[32] They concluded that the binding is related to the relative surface coverage of the species on the SWCNT, while independent of other parameters such as isoelectric point (IEP) and molecular weight (MW) of a protein. As a result, the protein binding is determined by how the functionalized molecules form their secondary structure on the SWCNT,[144] while such binding events are absent without SWCNTs. Recently, by using time-resolved fluorescence spectroscopy to study protein adsorption-desorption dynamics on ssDNA-SWCNT, Pinals et al. found that the short ssDNA sequence $(GT)_6$ desorbs from the SWCNT surface upon protein binding.[135] In addition, fibrinogen was found to have a higher binding affinity than albumin to both $(GT)_6$ and $(GT)_{15}$ wrappings. This protein dependency is in contrast with the findings of Bisker et al.[32] Thus, so far, no conclusive

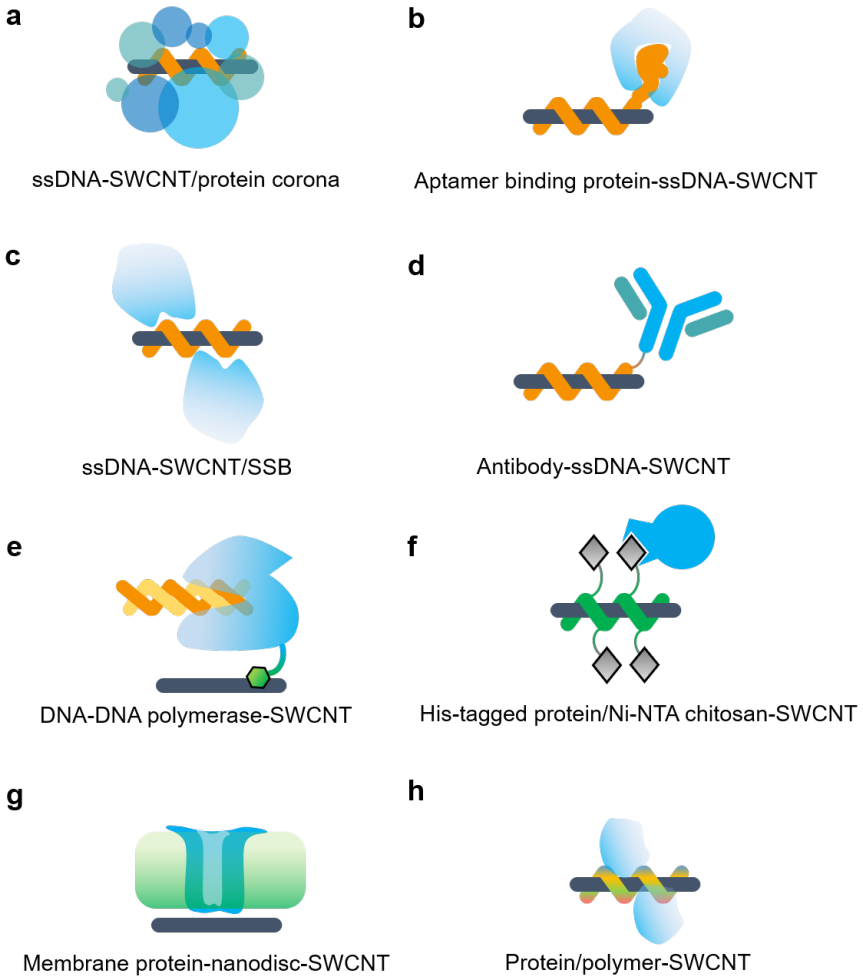

Figure 2.5 – Ternary nano-bio hybrids of SWCNTs. General cartoon representations: DNA (orange or yellow), protein (blue), SWCNT (black). In serum, non-specific adsorption can be found in the case of (a) ssDNA-SWCNT/protein corona.[134, 135] Specific interactions of ssDNA-SWCNT and protein requires considered design, such as (b) aptamer-binding protein-ssDNA-SWCNT,[30] (c) ssDNA-SWCNT/SSB,[136] and (d) antibody-ssDNA-SWCNT.[137] Note that the antibody and the DNA are attached by a covalent bond. For proteins with a low affinity to SWCNTs, intermediates can be introduced between the protein and the SWCNT to facilitate binding. (e) DNA-DNA polymerase-SWCNT[138]: with pyrene (green hexagon) as linker. (f) His-tagged protein/Ni-NTA chitosan-SWCNT[139, 140]: chitosan (green) is modified with Ni-NTA as a side chain (gray rhombus). (g) Membrane protein-nanodisc-SWCNT[141, 142]: lipid nanodisc (green block) embeds membrane protein. (h) Protein/polymer-SWCNT[83, 143]: polymer with multiple side chains (as various colors). All illustrations are adapted from references.

understanding on the mechanism of interaction has been outlined that accounts for the protein's structure. More discussions are provided in Chapter 6. Despite this gap in the knowledge, non-specific interactions between DNA-SWCNT and proteins have been already

exploited in various applications. For example, Williams et al. used BSA to non-specifically passivate the hydrophobic surface of functionalized SWCNTs, in order to enhance the response of the sensor toward an antigen biomarker in serum.[145]

Additional complexities arise when DNA-SWCNT are used in a complex fluid (like serum containing hundreds of proteins or cell culture).[134, 135, 146] Gong et al. pioneered the use of shotgun proteomics by mass spectrometry to investigate the interactome between ssDNA-SWCNT and fetal bovine serum (FBS) (Figure 2.5a).[134] They found that protein adsorption on ssDNA-SWCNT depends on the properties of a protein: MW, amount of hydrophobic a.a., and amount of charged a.a. The conclusion of Gong et al. reveals the system to be similar to protein-SWCNT interactions,[112, 117] where hydrophobic and charged a.a. are believe to predominantly contribute to the protein adsorption on SWCNTs (see also Section 2.3.2). Furthermore, proteins form a corona phase on the surface of nanoparticles in the medium.[135, 147] In the case of DNA-SWCNT/protein, two protein layers can be differentiated by proteomic approaches in combination with small-angle X-ray scattering (SAXS): an inner protein corona driven by hydrophobic interactions, and an outer protein corona which is stabilized by the shielding of electrostatic forces provided by the inner corona.

2.4.1.2 Specific Interactions

Controlling specific DNA–protein interactions in DNA-protein-SWCNT ternary hybrids is even more challenging. Steric hindrance caused by SWCNTs may reduce the probability of specific DNA–protein binding (i.e., limiting the ability of the protein to locate specific sites after non-specific binding). Recently, Landry et al. designed a ssDNA aptamer-SWCNT system with a spacer (PEG_3) incorporated in the ssDNA sequence to interact with aptamer-binding protein (Figure 2.5b).[30] They observed SWCNT fluorescence changes when the corresponding binding protein was introduced, indicating the steric hindrance from SWCNT had been overcome and specific DNA–protein binding had occurred. On the other hand, Nii et al. incubated ssDNA-SWCNT with single-stranded binding proteins (SSB), and AFM images showed adsorption of SSB on ssDNA-SWCNT (Figure 2.5c).[136] Notably, in both cases, it remains unknown whether the specific binding originates from the endogenous protein binding domain of the DNA or is due to an alternative effect.

Alternatively, covalently linked DNA–protein conjugates have gained significant interest since they provide a controllable approach for protein immobilization onto SWCNTs. In this case, proteins that lack a DNA-binding domain can also be engineered once an accessible conjugation site is incorporated (Figure 2.5d). Click chemistry has been used to conjugate proteins site-specifically to the ssDNA on SWCNTs, including EDC-NHS chemistry,[137] thiol-ene chemistry[148] and DBCO-azide conjugation.[149] Nonetheless, when compared with other protein immobilization methods (e.g., direct sonication), such approaches provide a lower yield due to fewer reaction sites on SWCNTs. More detail will be discussed in Chapter 5.

2.4.2 Special Case 2: Protein-SWCNT/DNA

In general, protein-SWCNT/DNA interactions remain largely unexplored. As mentioned in Section 2.3.2, protein-SWCNT interactions are weak, and the DNA-binding domain should be kept available for DNA while avoiding binding to SWCNTs. Thus, how to properly orient the DNA-interacting protein on the SWCNT is the key to accessing applications of this hybridized configuration. One example is SWCNTs decorated with pyrene-modified DNA-polymerase (Figure 2.5e).[138] Olsen et al. fabricated FET based on the hybrid, and they observed two states of electrical current (open and closed) in single molecule measurements when both the dsDNA template and dNTP were introduced into the system. Consequently, they were able to resolve replication events on a sub-millisecond timescale.

2.4.3 Other Ternary Cases

Intermediate materials are designed to immobilize low binding affinity proteins/peptides on SWCNTs. The third component, which is used to functionalize SWCNTs, can introduce specific interactions with proteins and acts as a bridge between SWCNTs and proteins. For example, nickel-nitrilotriacetic acid (Ni-NTA) modified chitosan was used to wrap SWCNTs and to bind His-tagged proteins (Figure 2.5f).[139, 140] Lipid nanodiscs were also exploited to assemble SWCNTs and membrane proteins (Figure 2.5g), such as cytochrome c[141] and olfactory receptors.[142] On the other hand, for those cases with unknown interacting modes, library screening of wrapping molecules has been utilized to find proper bridging materials. For example, Bisker et al. screened a library composed of DNA and lipids searching for the best intermediate of fibrinogen binding.[32] Combining screening with semi-rational polymer design, Budhathoki-Uprety et al. synthesized polymers whose side chains have varying levels of hydrophobicities to select a suitable intermediate for albumin binding to SWCNTs (Figure 2.5h).[83] Similarly, Chio et al. screened a peptoid library with segments that have different affinities for lectin protein binding on SWCNTs.[143] These approaches allow low-binding proteins to be functionalized on SWCNTs, which in turn further expands the possible applications of these hybrid systems.

2.4.4 Summary of Ternary Hybrids

A summary of the interactions possible in the DNA-protein-SWCNT system are summarized in the interaction diagram presented in Figure 2.6. In general, DNA-SWCNT has strong interactions (as solid line), while protein-SWCNT has weak interactions (as dashed line). DNA–protein interactions can contribute at different strengths, depending on the specificity of binding (either solid or dashed line). It should be noted that the interactions between individual components are highly dependent on their structures. For example, the conformation of DNA on the SWCNT would affect the protein binding. Therefore, understanding the structure-interaction relationship in the system is critical for its widespread application.

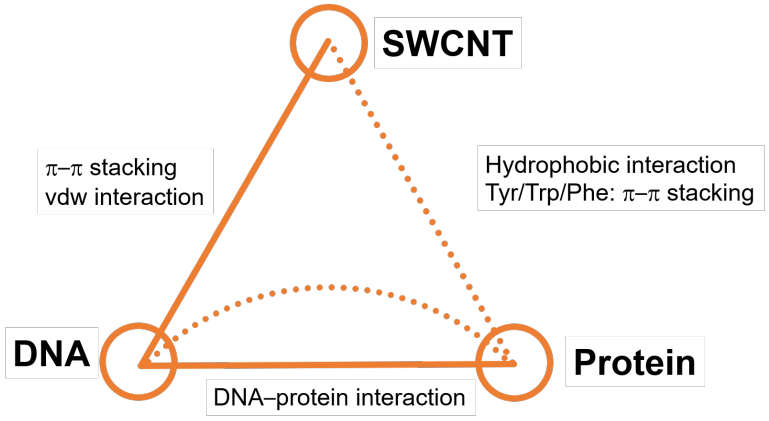

Figure 2.6 – Summary of interactions in ternary nano-bio hybrids.

3 Restriction Enzyme Analysis of dsDNA on Pristine SWCNTs

This Chapter is published as:
Shang-Jung Wu, Nils Schuergers, Kun-Han Lin, Alice J. Gillen, Clémence Corminboeuf, and Ardemis A. Boghossian. Restriction Enzyme Analysis of Double-Stranded DNA on Pristine Single-Walled Carbon Nanotubes. *ACS Appl. Mater. Interfaces.* **2018**, 10, 37386–37395

3.1 Introduction

The discovery of the helical structure of double-stranded DNA (dsDNA) incited technologies that have since shaped modern molecular biology. The omnipresence of DNA in most basic life processes has motivated its incorporation into gene delivery, imaging, and sensing technologies that exploit its biocompatibility, versatile molecular structure, and specificity.[150–153] When coupled to nanoparticle and fluorescent probes, dsDNA provides a scaffold for studying fundamental processes, such as replication, hybridization, and transcription, as well as bioengineering techniques, such as gene delivery and genome editing.[154, 155]

Single-walled carbon nanotubes (SWCNTs) are among the most studied nanoparticle probes because of their near-infrared fluorescence, indefinite photostability, and single-molecule detection limits. These beneficial properties are particularly advantageous for both in vivo and in vitro imaging and sensing applications.[72, 74, 77, 156, 157] The noncovalent functionalization of SWCNTs with DNA not only keeps these optoelectronic properties intact, but also increases the solubility and biocompatibility of SWCNTs and bestows biochemical accessibility for further functionalization.[34, 88, 158] In addition, DNA binding affinity and surface coverage of SWCNTs are length- and nucleotide-specific,[159] allowing nanotube chirality separation.[160] The wrapped DNA can further hybridize with complementary sequences or form aptamer structures that bind target molecules with high affinity and specificity, incentivizing its use for optical SWCNT sensing applications. In addition, SWCNTs have been shown to protect DNA from degradation[161] (see Figure S3.1 and discussion in Section 3.5), a critical consideration for gene delivery applications.

Although DNA is the most commonly used polymer for suspending SWCNTs, the majority of SWCNT-based applications rely on noncovalent functionalization with single-stranded DNA (ssDNA) of 20–40 nucleotides (nt).[88, 158] The ssDNA oligonucleotides possess a strong affinity to the SWCNTs that is attributed mainly to $\pi - \pi$ stacking between nucleobases and the SWCNT sidewall.[162] In contrast, dsDNA has received less attention as it does not efficiently suspend SWCNTs unless sonicated vigorously.[88] To circumvent the low binding affinity and functionalize SWCNTs with dsDNA sequences, previous studies have designed hybrid configurations such as dsDNA containing an ssDNA overhang[116, 163] or ssDNA-based hairpin structures.[103] These studies demonstrated that the hybrids can be employed successfully in optical sensing and nanostructure design applications.

A lack of uniform and precise techniques for dsDNA-SWCNT characterization has yielded several seemingly conflicting models on the interaction of dsDNA with SWCNTs (Table 3.1). The weak binding of dsDNA to the SWCNT is believed to emanate from the low affinity between the hydrophilic dsDNA backbone and the hydrophobic SWCNT surface. However, some studies have suggested that van der Waals forces are sufficient to facilitate dsDNA adsorption to the SWCNT surface.[107, 164, 165] Nii et al. demonstrated that ssDNA-binding proteins do not bind to conjugates of chromosomal dsDNA and SWCNTs, while they readily interact with ssDNA-functionalized SWCNTs,[136] thereby validating the preservation of the double-stranded structure on SWCNTs. On the other hand, Cathcart et al. investigated SWCNTs suspended with chromosomal DNA from salmon sperm by electron microscopy and circular dichroism analysis.[108] They concluded that following sonication, nanotubes are initially stabilized by dangling ssDNA ends from which the dsDNA slowly denatures to form an ordered ssDNA coating around the SWCNT within 20–50 days.

Similar disparities have been reported for the hybridization of complementary sequences to ssDNA on the surface of SWCNTs.[71, 72, 166, 167] For example, on the basis of electrophoresis and molecular dynamics (MD) simulation results, Jung et al. suggested that 17 base pairs (bp) dsDNA duplexes formed by hybridization desorb from the nanotube surface.[167] On the other hand, Jeng et al. used atomic force microscopy (AFM) imaging to show that a random 24 bp dsDNA will remain adsorbed on a nanotube surface after duplex formation.[71] However, AFM imaging did not allow the authors to distinguish whether the dsDNA duplex adopts a canonical B-type conformation or some non-natural conformation on the SWCNT surface.

Differences in sequences, observed time scales, varying degrees of charge screening by counter ions, and other factors in these studies may contribute to the observed variation in the dsDNA-SWCNT behavior. The field thus currently lacks a fundamental understanding of the nature of the dsDNA-SWCNT interaction, the preservation of the dsDNA structure, and its accessibility while wrapped on SWCNTs. In this work, we study the structure of dsDNA strands on SWCNTs by analyzing the interaction of dsDNA-modifying type-II restriction enzymes (REs) with DNA-SWCNT hybrids. Type-II REs recognize short palindromic dsDNA sequences and cleave the phosphodiester bond of the DNA backbone within their respective recognition sites.[170] Type-II RE-mediated DNA cleavage is widely used in different tech-

Table 3.1 – Summary of previous proposed models and methods.

DNA-SWCNT preparation method	DNA type	Methodology	Buffer	Duplex/ Unwinding	Adsorption/ Desorption	Reference
Sonication	Chromosomal DNA	CD, HRTEM	Water	Duplex ⟶ Unwinding	A	[108]
Sonication	Chromosomal DNA	SSB and AFM	Assay condition: NaCl + $MgCl_2$	-	A	[136]
Sonication	Chromosomal DNA	dsDNA-specific fluorescence assay	Tris-EDTA buffer	Duplex	A	[165]
Sonication	A_{20}-T_{20}	SEC-HPLC	Tris-EDTA buffer	Duplex	A	[164]
Sonication	7, 20, 60 bp with overhang	AFM	TAE with Mg^{2+}	Duplex	D	[116]
Sonication	23 bp with hairpin	Fluorescence assay	Phosphate buffer	Duplex	D	[103]
Hybridization	A_{30}-T_{30}	Absorption spectrum	Water	-	D	[166]
Hybridization	17 bp	Transistor, gel electrophoresis, MD simulation	Experiment: PBS buffer	Duplex	D	[167]
Hybridization	23 bp with $(GT)_{15}$	PL, MD	SSC buffer	Duplex	D	[72]
Hybridization	24 bp	AFM	Tris buffer	Duplex	A	[71]
Adsorbent exchange	A20-T20	Absorption spectrum, MD simulation	Phosphate buffer	Duplex	A	[109]
Simulation	12 bp	MD	NaCl	Duplex	A (end group)	[107]
Simulation	9, 27, 51 bp	MD	Na^+ as counterion	9 bp: unwind; 27, 51 bp: duplex	A	[168]
Simulation	20 bp	MD	NaCl	Duplex	A	[169]

niques, such as restriction fragment length polymorphism, single nucleotide polymorphism, and post-modification analysis as the cleavage activity can be easily investigated by gel electrophoresis. Importantly, these enzymes are mostly specific for dsDNA in the native B-DNA conformation.[171, 172] We take advantage of this conformational specificity to understand the structure and stability of DNA duplexes in the vicinity of the SWCNT surface. Additional Förster resonance electron transfer (FRET) measurements and MD simulation results show that short dsDNA strands can retain their native conformation in the proximity of a SWCNT surface.

3.2 Results and Discussion

The enzymatic digestion assay developed in this study (Figure 3.1) allows us to quantify the amount of accessible native dsDNA on the nanotube surface. HiPCO SWCNTs were functionalized with short ($\leqslant$30 bp) dsDNA sequences containing an endonuclease recognition site and a single-stranded $(GT)_{10}$ overhang on either one or both strands (Figure 3.1a, Table 3.2; see Table 3.3 for exact sequences). DNA-SWCNT hybrids were prepared by a sodium cholate (SC)-exchange method adopted from Shiraki et al.,[109] as this method minimizes SWCNT damage and increases yields of native dsDNA on SWCNTs (see conclusion and discussion in Section 3.5 for a comparison of DNA-SWCNT hybrids prepared by different methods). Free DNA was thoroughly removed (Figure S3.2), and the suspension (around 1 mg/L of SWCNT) was incubated with the BamHI restriction enzyme to cleave native dsDNA into smaller fragments. Total DNA was subsequently purified from the SWCNT suspension by phenol-chloroform-isoamyl alcohol extraction (Figure S3.3), concentrated, and analyzed by denaturing gel-electrophoresis (Figure 3.1b). Because BamHI is specific to DNA in the B-conformation,[171] the enzyme activity is directly related to the amount of accessible DNA in its native configuration.

This protocol was first applied to SWCNTs wrapped with dsDNA containing a single 5'-overhang and a GC content of 53% (BH13-5). Enzymatic digestion (Figure 3.1c) leads to the appearance of two extra bands around 33 and 15 nt, which correspond to the lengths of the expected fragments c and d_{1-3}, as shown in Figure 3.1d. These bands resulted from the specific restriction at the single BamHI site of sequence BH13-5, as no cutting was observed for single-stranded sequences or a hybrid sequence without a BamHI recognition site (Figure S3.4). In contrast, the uncut bands shown as fragments a and b may represent uncut dsDNA as well as any adsorbed ssDNA strands that may have remained following annealing. To eliminate the possibility that free oligonucleotides detaching from the SWCNTs contribute to the observed cutting, we independently analyzed DNA fragments extracted from the SWCNT-containing pellet and the supernatant of an ultra-filtrated solution directly following enzymatic restriction (Figure 3.1e). Fragments a, b, and c were only found in the pellet fraction containing the SWCNTs, and no desorbed DNA was detected in the supernatant, confirming that restriction occurred at the SWCNT surface. We noted that despite the observed surface-bound activity, dsDNA restriction was not complete, and enzyme activity was notably decreased when

Table 3.2 – Short duplex DNA oligomers used to wrap SWCNTs.

DNA[a]	Cutting site[b]	Site-to-end distance[c]	dsDNA length	GC content of ds-DNA segment	Overhang configuration[d]
ERV13-5	EcoRV	13 bp	30 bp	47%	5'
ERV13-53	EcoRV	13 bp	30 bp	47%	5' + 3'
ERV13-55	EcoRV	13 bp	30 bp	47%	5' + 5'
BH13-5	BamHI	13 bp	30 bp	53%	5'
BH13-53	BamHI	13 bp	30 bp	53%	5' + 3'
BH13-55	BamHI	13 bp	30 bp	53%	5' + 5'
BHH13-5	BamHI	13 bp	30 bp	70%	5'
BHL13-5	BamHI	13 bp	30 bp	30%	5'
BH10-5	BamHI	10 bp	27 bp	52%	5'
BH7-5	BamHI	7 bp	24 bp	50%	5'
BH4-5	BamHI	4 bp	21 bp	53%	5'
BH2-5	BamHI	2 bp	19 bp	53%	5'

[a]DNA sequences are named based on the RE cutting site, site-to-end distance, and configuration, consecutively. [b]The 6-bp recognition site for BamHI (5'-GGATCC-3') or EcoRV (5'-GATATC-3') is included in the dsDNA sequence. [c]The site-to-end distance is defined as the length between cutting site and the closest overhanging end. [d]The overhang configuration is defined as the position(s) where a $(GT)_{10}$ overhang is added to one or both complementary strands.

compared to the restriction rate of free DNA (Figure S3.5).

In order to quantify the number of cutting events, we examined the relative enzyme activity (A_{rel}). We define this variable as the cut ratio (CR) of DNA in the SWCNT hybrid normalized to the CR of free DNA with the same sequence.

$$A_{rel} = \frac{\mathrm{CR}_{\mathrm{DNA-SWCNT}}}{\mathrm{CR}_{\mathrm{freeDNA}}} \tag{3.1}$$

This normalization therefore accounts for contributions from any unwanted ssDNA which may still be present during the digestion assay. The CR was calculated from the fluorescence intensity observed for bands a and c in the PAGE gel (I_a and I_c) normalized with respect to the corresponding DNA length (L_a and L_c), assuming that fluorescence intensity is proportional to DNA length.

$$\mathrm{CR} = \frac{\dfrac{I_c}{L_c}}{\dfrac{I_a}{L_a} + \dfrac{I_c}{L_c}} \tag{3.2}$$

The relative activity of BamHI on BH13-5 SWCNT hybrids was calculated to be $A_{rel} = 0.26$, indicating a strong negative impact on enzymatic DNA cleavage due to the presence of SWCNTs.

Cleavage of DNA by type-II REs consists of three general mechanistic steps: first, the enzyme nonspecifically binds to DNA; second, it slides or hops along the DNA helix until it

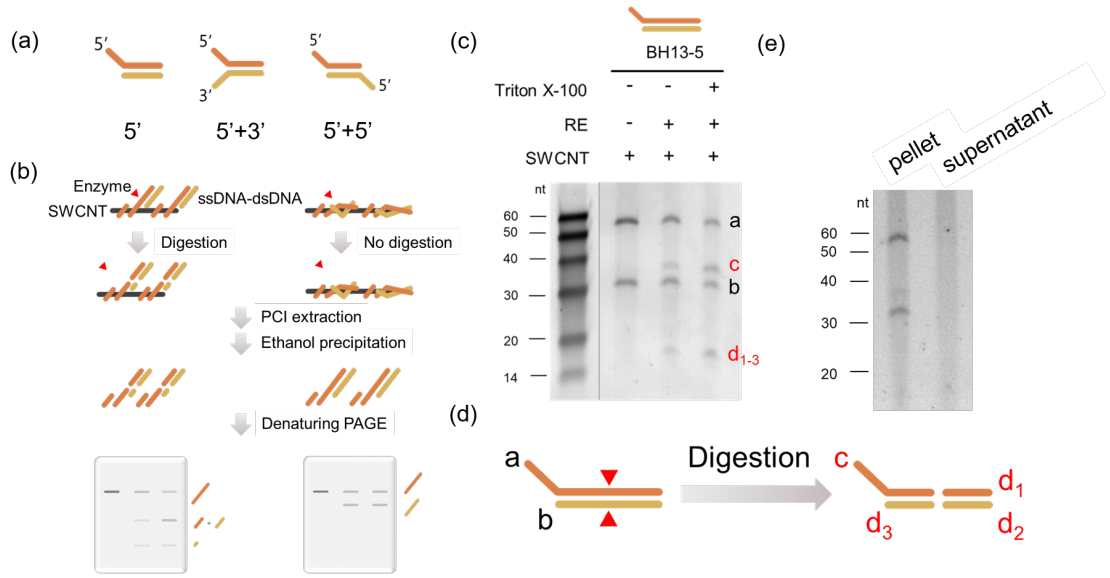

Figure 3.1 – Digestion assay showing dsDNA restriction on the surface of SWCNTs, which is enhanced in the presence of Triton X-100. (a) Schematic of DNA configurations differing in the position of the single-stranded $(GT)_{10}$ overhang(s). (b) Cartoon of the digestion assay. DNA -SWCNTs were incubated with the corresponding REs whose activities depend on the conformation of the dsDNA on the SWCNT surface.Restriction was followed by phenol-chloroform-isoamyl alcohol extraction and ethanol precipitation to purify DNA from SWCNTs. Recovered DNA fragments were analyzed by denaturing PAGE, and the ratio of different fragments was calculated to determine enzyme activity and dsDNA conformation. (c) BH13-5 DNA extracted from HiPCO SWCNTs was separated on a 12% denaturing PAGE. Restriction products c (33 nt) and d_{1-3} (15 nt) were only observed when DNA-SWCNTs were incubated with BamHI. (d) Cartoon showing all possible digestion products. (e) Denaturing PAGE showing DNA recovered from the DNA-SWCNT pellet (i.e., DNA on the SWCNT surface) and from the supernatant (i.e., desorbed DNA) after the digestion reaction.

encounters a specific recognition site; and third, the enzyme cleaves the phosphate-sugar backbone and diffuses from the DNA. Reduced enzyme activity on DNA-SWCNT hybrids is likely caused by either (i) competing adsorption of the enzyme on the SWCNT surface or (ii) hindered DNA accessibility for the enzyme due to the presence of the SWCNT. We explored enzyme adsorption (case (i)) by mixing free DNA and BamHI in the presence of SWCNTs suspended in 0.02 wt% SC. Although the SC concentration was deliberately chosen to not fully cover the SWCNT[173] and allow BamHI to adsorb on the surface, the presence of SWCNTs in the reaction mix did not significantly influence the yield of cleavage products as 96% BamHI activity was retained (Figure S3.6). This finding indicates that enzyme adsorption is not limiting DNA cleavage.

Next, we investigated if close proximity of the dsDNA to the SWCNT surface leads to steric hindrance or induces conformational changes on the DNA-helix (case (ii)). The accessibility of the dsDNA was studied by tuning the strength of the dsDNA-SWCNT interaction through

surfactant addition. This approach is based on work by Harvey et al.,[72] who showed that certain surfactants can be used to weaken the interaction of DNA - RNA duplexes with the SWCNT surface. Our measurements showed that the addition of 0.002 wt% Triton X-100, a nonionic surfactant that does not denature proteins at low concentrations,[174] leads to an 8 nm blue shift of the DNA - SWCNT photoluminescence (Figure S3.7). This blue-shifting was attributed to altered dsDNA binding to the SWCNT without desorbing ssDNA from the surface.[72] In addition, the presence of Triton X-100 in the BH13-5-SWCNT digestion assay boosted the relative activity of the BamHI digestion by 2.3-fold to 0.60 compared to the case without surfactant (Figure 3.1c).

The influence of Triton X-100 was further studied by measuring the reaction kinetics of DNA cleavage (Figure 3.2a). The initial linear rate of DNA cleavage (r_i) in DNA-SWCNT hybrids is 0.0034 min^{-1}, which is 10 times lower than the r_i for free DNA (0.033 min^{-1}). By introducing Triton X-100 to the system, r_i was increased 2.8-fold (0.0091 min^{-1}), implying that enzyme kinetics were negatively affected by reduced DNA accessibility on the SWCNT surface. The addition of Triton X-100 can thus enhance DNA accessibility and facilitate binding and/or cutting by BamHI.

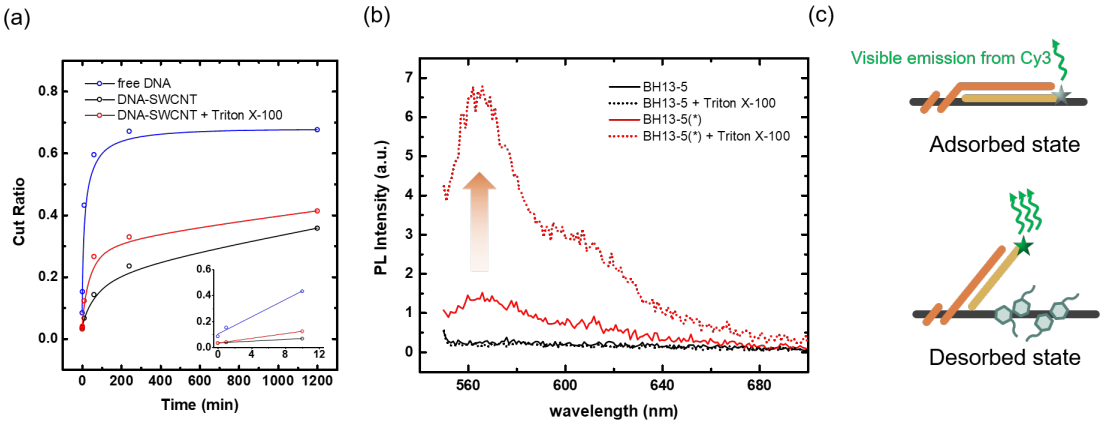

Figure 3.2 – Triton X-100 enhances BamHI activity by increasing the mean distance between dsDNA and SWCNT. (a) BamHI digestion kinetics for free DNA, DNA-SWCNTs, and DNA-SWCNTs with Triton X-100. The inset shows the initial slopes fitted by linear regression. (b) FRET assay to monitor the dsDNA-SWCNT distance. DNA-SWCNT hybrids of BH13-5 or BH13-5(*), which has a Cy3 fluorophore attached at the opposite end of the $(GT)_{10}$ overhang, were excited at 532 nm. Emission spectra are shown before (solid lines) and after (dash lines) the addition of 0.002 wt% Triton X-100. (c) Cartoon depiction of adsorbed and desorbed states of DNA on the SWCNT surface. Triton X-100 (hexagons) stabilizes the SWCNT surface that is exposed to water, allowing the dsDNA fragment to desorb from the SWCNT surface.

On the basis of these findings, we hypothesize that the amphiphilic Triton X-100 destabilizes the dsDNA-SWCNT interaction by preferentially binding to the hydrophobic SWCNT surface. Consequently, native dsDNA is displaced from the nanotube surface to promote accessibility by BamHI. To verify dsDNA displacement by Triton X-100, we employed FRET

analysis. FRET has previously been used to study ssDNA and/or RNA hybridization events with fluorophore-labeled ssDNA-SWCNTs.[14, 72] The enhanced fluorescence intensity on the addition of complementary sequences was attributed to an increased mean distance between the dye and the SWCNT surface. Here, we functionalized SWCNTs with DNA containing an overhang in the 5 configuration and a Cy3 fluorophore attached to the opposite 5'-end of the complementary strand (BH13-5(*); Table 3.3). We excited SWCNT-BH13-5(*) conjugates at 532 nm and collected visible-range fluorescence spectra to measure changes in energy transfer. While Triton X-100 had a minimal effect on Cy3 fluorescence for free BH13-5(*) (Figure S3.8), it yielded a 6-fold fluorescence increase when the DNA was conjugated to the SWCNT (Figure 3.2b). Because FRET efficiency (E) is inversely related to the distance according to the equation

$$E = \frac{1}{1 + (\frac{r}{R_0})^6} \tag{3.3}$$

where r is the distance between the emitter and the quencher and R_0 is the Förster distance, the 6-fold decrease in efficiency in the presence of surfactant suggests an increase in the mean distance between the 5'-Cy3 and the SWCNT. Assuming the change of FRET efficiency is proportional to the change of fluorescence, $r \approx 9.9$ nm (the length of the dsDNA) in the presence of surfactants, and $r \approx 0.8$ nm in the absence of surfactants (i.e., hydrodynamic radius of Cy3),[175] we predicted the R_0 of Cy3 and SWCNT is on the order of ~8 nm. This value falls within the range of previously reported values of R_0 of Cy3 coupled with a nanoparticle.[176] The close agreement between the predicted and reported values of R_0 thus confirms that the ssDNA anchor remains attached, while the dsDNA strand is displaced.

The effects of the DNA sequence and configuration on enzyme activity were also studied. specifically, we varied the recognition site-to-end distance, GC content, and the configuration of the $(GT)_{10}$ overhang(s), as summarized in Figure 3.3. First, we tested five different variants with restriction site-to-end spacings varying from 2 to 13 bp. In the absence of Triton X-100, the relative activity of BamHI was significantly decreased only when the recognition site was within 2 bp from the anchoring $(GT)_{10}$ overhang (i.e., BH2-5) (Figure 3.3a), whereas placing the cut site more than 4 bp from the overhang (i.e., BH4-5 to BH13-5) leads to a 3 - 4-fold increase in relative activity. This finding shows that the SWCNT has a substantial negative impact on enzyme activity when the recognition site is in close proximity to the wrapping anchor. This observation is in agreement with the results of Shiraki et al.,[109] who predicted that dsDNA termini can be partially disrupted by the short- lived exchange of favorable base pairings with $\pi - \pi$ interactions along the SWCNT surface, a phenomenon that has been described as "fraying" in another study.[108] As our results imply that this loss of the native conformation is restricted to the first few bp near the ssDNA anchor, we find that positioning sequence elements at least 4 bp into the dsDNA region is crucial for optimizing applications relying on protein-dsDNA interactions. Similarly, Landry et al. previously confirmed that a spacer of at least six units of ethyleneglycol between the anchoring DNA and the aptamer is necessary to achieve protein-aptamer binding on an SWCNT surface.[30]

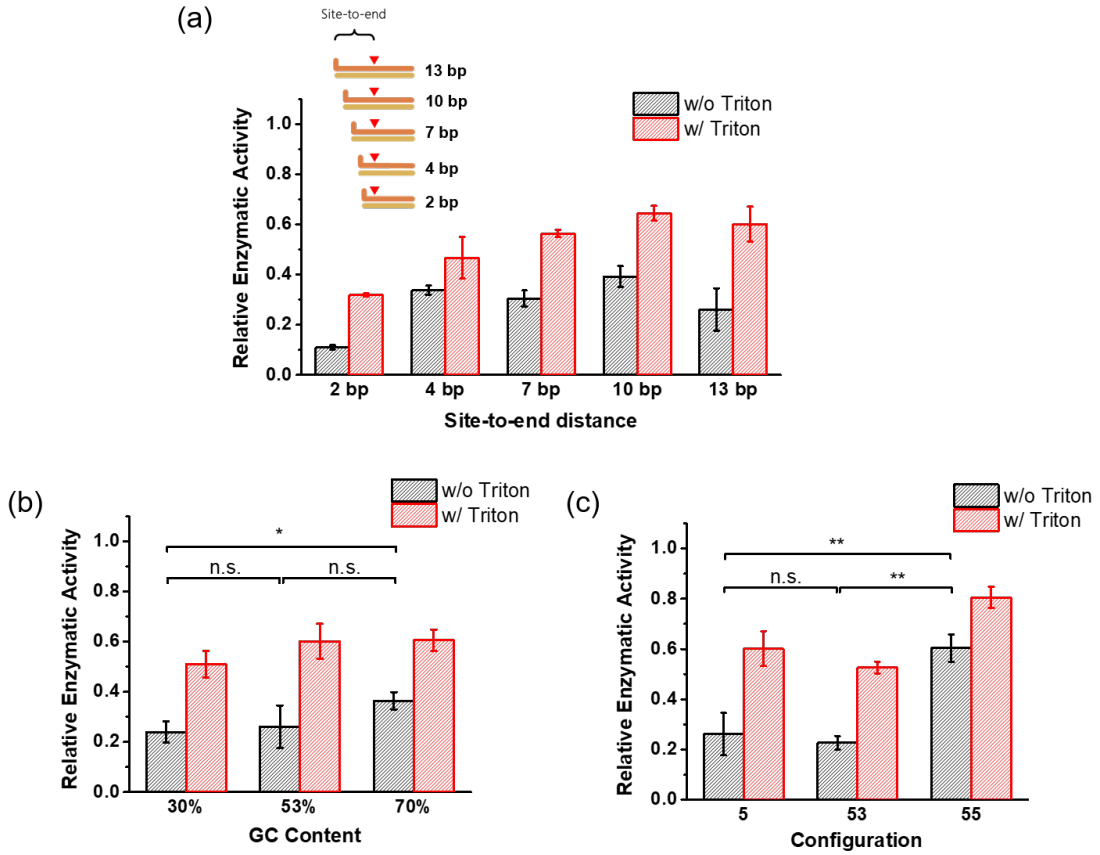

Figure 3.3 – RE activity depends on the sequence and configuration of DNA wrapped on SWCNTs. Fragment analysis by denaturing PAGE was used to quantify the relative enzyme activity, as defined in Equation 3.2 and plotted against (a) site-to-end distance, (b) GC content of the dsDNA sequence, and (c) configuration of $(GT)_{10}$ overhang. All results are mean values of independent triplicates, with the error bar representing 1 S.D. Significance was evaluated by a two-sample t-test (* = $p < 0.05$, ** = $p < 0.01$).

The addition of Triton X-100 increased BamHI activity for all restriction site-to-end distances tested. The effect was especially pronounced in the case of BH2-5 (site-to-end distance of 2 bp, as shown in Figure 3.3a) where BamHI showed a 3-fold increase in activity in the presence of surfactants. This corroborates the idea that Triton X-100, by shielding the SWCNT surface, weakens dsDNA-nanotube interactions and allows dsDNA to move away from the SWCNT. Conversely, in the absence of surfactants, the increased steric hindrance of the SWCNT is shown to disrupt enzyme activity. Moreover, a strong positive correlation between the site-to-end distance and relative enzyme activity was observed (Spearman correlation = 0.81, with $p < 0.001$). As in the case of surfactant addition, the increased distance from the SWCNT surface is believed to promote enzyme activity through increased dsDNA accessibility.

The stability of dsDNA can be improved by increasing the number of GC pairs, which form an additional third hydrogen bond and have a more favorable base stacking energy

compared to AT pairs. Nonetheless, GC content showed only a minor influence on relative BamHI activity when comparing SWCNTs wrapped with 30% GC dsDNA sequences (BHL13-5) to 70% GC sequences (BHH13-5) (Figure 3.3b). The addition of Triton X-100 increased BamHI activity for all GC variants tested to an extent that negated the small differences seen in the absence of the surfactant. Independent of their GC content, the 30 bp DNA duplexes used in this study are sufficiently stable to prevent DNA dehybridization in favor of competitive SWCNT interactions. Accordingly, dsDNA stability is unlikely to be the limiting factor for BamHI activity.

In contrast to GC content, the configuration of the tested DNA hybrids had a strong impact on enzyme activity (Figure 3.3c). While there was little difference in relative enzyme activity between DNA with a single (BH13-5) or double (BH13-53) overhang at the same terminus, activity increased markedly when two overhangs were added at different DNA termini (BH13-55). The two overhangs are capable of either binding on the surface of the same nanotube or the surfaces of two distinct nanotubes. Han et al. showed that the majority of SWCNTs suspended with DNA containing two overhangs in a similar 55 configuration assume the latter arrangement, allowing dsDNA bridging between two distinct nanotubes.[116] Such bridging would introduce an additional tensile strain on the dsDNA strands that could displace them from the nanotube surface and facilitate dsDNA cleavage by BamHI. Although wrapping of the BH13-55 on the same nanotube could negatively impact enzyme activity, our results indicate that this effect could be outweighed by the majority of nanotubes that are expected to show a relative increase from the dsDNA bridging. Again, relative activity of all configurations was promoted by the addition of Triton X-100.

Furthermore, we compared the activity of different digestion enzymes on dsDNA-SWCNT hybrids (Figure 3.4a). BamHI and EcoRV are REs with comparable DNA-binding constants (EcoRV: 10.0 μM and BamHI: 11.0 μM for nonspecific DNA).[177] The relative activity of EcoRV was similar to BamHI for dsDNA-SWCNTs with duplexes in the 5 and 53 configurations (Figure 3.4b). As with BamHI, EcoRV showed enhanced activity with duplexes in the 55 configuration compared to the 5 and 53 configurations, in agreement with the hypothesis that the favored bridging conformation may contribute to increased DNA accessibility. However, this enhancement was less pronounced than that observed with BamHI, and we consequently observed a significant difference between the enzymes' activities with this dsDNA configuration ($p < 0.0001$). A comparison of the crystal structures of the enzymes (BamHI: 1ESG; EcoRV: 1RVB) bound to non-cognate DNA shows that EcoRV occupies a larger interaction surface area (2448 Å^2) than BamHI (631 Å^2) (PDBePISA[178]), though both enzymes are smaller than the ca. 10 nm distance that is predicted between the bridged nanotubes.[116] Moreover, upon binding to its recognition sequence, EcoRV needs to bend the DNA in a 50° kink[179, 180] to correctly position the phosphodiester bonds for DNA cleavage. This bending could be hampered more by the torsional strain from the DNA bridge compared to BamHI.[181] Consequently, this torsional strain, combined with the increased interaction surface, may therefore account for the diminished EcoRV enhancement compared to BamHI.

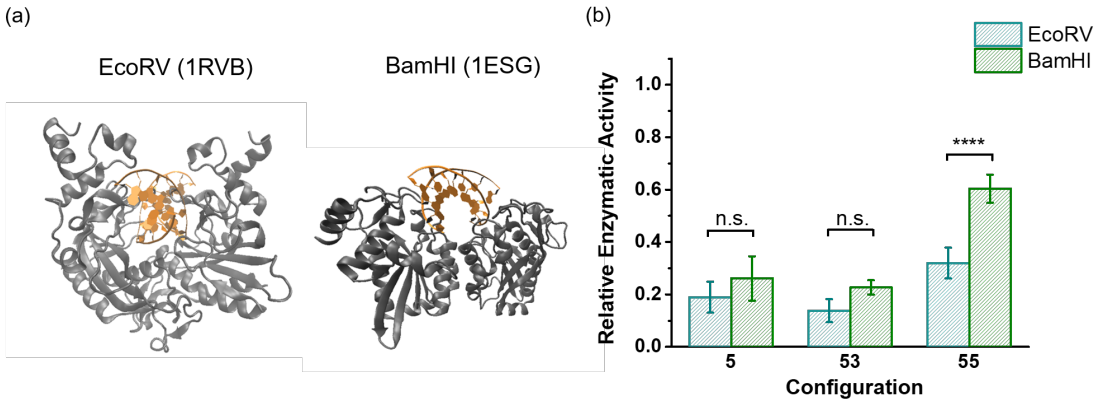

Figure 3.4 – Different enzymes exhibit distinct restriction kinetics toward dsDNA of varying overhang configurations. (a) Crystal structure of EcoRV (PDB: 1RVB)[179] and BamHI (PDB: 1ESG)[182] binding to DNA (orange). (b) Comparison of EcoRV and BamHI activity on dsDNA-SWCNT with different $(GT)_{10}$ overhang configurations. Denaturing PAGE fragment analysis was used to quantify RE activity. Significance was evaluated by a two-sample t-test (**** = $p <$ 0.0001).

Lastly, we used classical MD simulations (see Section 3.5 for details) to understand the stability and conformation of different regions of dsDNA (BH7-5) on the SWCNT surface (Figure 3.5a). Ghosh and co-workers have shown that inevitable double-stranded oligonucleotide unzipping is affected by factors such as type of oligonucleotide, salt concentration, and temperature.[183] Greater base-pair stability has been reported for dsDNA compared to other oligonucleotides, such as siRNA, and for longer sequence lengths.[107, 168] For the experimental conditions used in our study, we observe that dsDNA remains hybridized. In line with this, we did not observe unwinding of the 24 bp duplex over the time scale used in our simulation (Supporting Information video S1). This stability was attributed to the stable canonical Watson-Crick base pairs in the simulated sequence (Figure 3.5b). The duplex region was shown to largely retain the theoretical 60 hydrogen bonds throughout the simulation for a hydrogen bond pairing cutoff of 0.35 nm and 30°.[168] The observed stability of the DNA duplex along the SWCNT is in agreement with previously published MD simulations for DNA sequences >12 bp.[72, 107, 168, 169]

A comparison of the distance (d) between the SWCNT surface and the center of mass of each of the bp of the dsDNA over time showed that the bp closest to the ssDNA anchoring point conveys bimodal displacement with d oscillating between 1.1 and 1.5 nm (Figure 3.5c). In the state where the bp was close to the SWCNT, the nucleobases formed canonical H-bonds (inset of Figure 3.5d). However, as the first bp has lower stability because of less neighboring bases,[36] the Watson-Crick pairing can be temporally broken, and the fluctuating residue leads to an increase in d. This binding disruption is in agreement with the "fraying" phenomenon previously reported in the literature[108, 109] and in the discussion above for cut sites within 2 bp of the nanotube surface. In contrast, the central and last bp of the

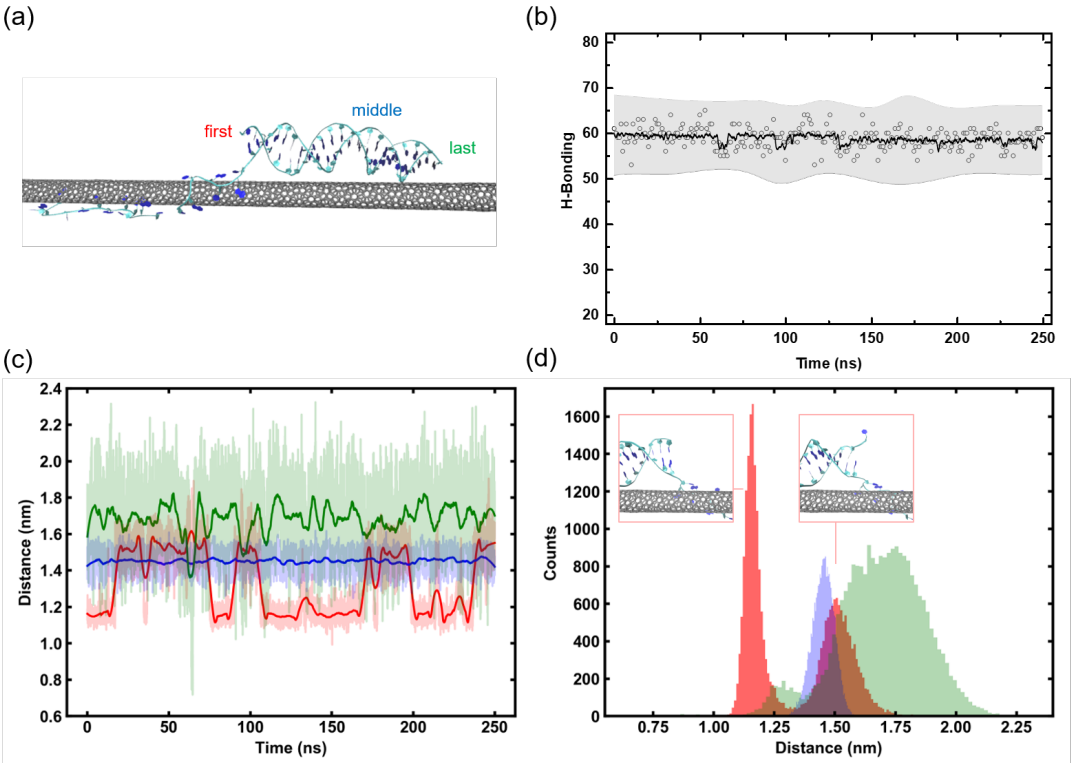

Figure 3.5 – MD simulation of a DNA-SWCNT complex predicts stable dsDNA pairing while adsorbed on an SWCNT surface. (a) Final structure after 250 ns production run showing the dsDNA aligned along the SWCNT. (b) Number of hydrogen bonds formed over time calculated with a threshold of 0.35 nm and 30°. (c) Distance between the SWCNT surface and the center of mass for the first (3' end of antisense strand, in red), middle (blue), and the last (5' end of antisense strand, in green) bp shows minimal variance over time. (d) Histogram of the bp-SWCNT distance. The insets depict snapshots of the first bp in the far (at d = 1.5 nm) state and the near (at d = 1.1 nm) state, showing the temporary disruption of the Watson-Crick pairing in the far state.

dsDNA segment remained in a relatively constant position with $d = 1.5 \pm 0.05$ and 1.7 ± 0.2 nm, respectively. Although the large standard deviation of d implies that the last bp has the highest tendency to desorb from the SWCNT surface, it stayed within 2.2 nm throughout the simulation. As all MD simulations previously mentioned neglected the polarization contribution (i.e., a nonpolarizable force field was used, see Section 3.5), the attractive force between dsDNA and SWCNT is typically underestimated.[107] Therefore, the adsorption of dsDNA on SWCNTs is likely even more favorable than predicted.

These observations can be reconciled with the observations of Jung et al.,[167] who suggested that the energy released by a 17 bp duplex formation is enough to facilitate desorption of the dsDNA. The values estimated by the authors predict that the 24 bp dsDNA used in our simulation would have a desorption energy of around 56 kcal/mol, which is 2 orders of

magnitude larger than thermal fluctuation at ambient conditions. In addition, Harvey et al. also reported adsorption of an unanchored 23 bp dsDNA along the surface of the SWCNT.[72] Accordingly, these findings suggest that pre-hybridized dsDNA remains within the vicinity of the SWCNT surface under ambient conditions. This observation corroborates the results in Figure 3.3a, which show comparable enzyme activity in the absence of surfactants for cut sites between 2 and 13 bp from the anchoring $(GT)_{10}$, suggesting that the loci of the cut sites are all close to the SWCNT surface.

3.3 Conclusions

This study presents a systematic investigation of enzyme activity on unmodified DNA strands wrapped on pristine SWCNTs. Whereas previous work on SWCNT-based DNA–protein interactions has focused on the binding activity of proteins to aptamers[30] or on single-strand DNA-binding proteins,[136] our findings uniquely explore the effects of enzyme activity, specifically the cutting of the phosphodiester backbone of dsDNA on the SWCNT surface. To the best of our knowledge, this study offers the first experimental verification of a native dsDNA conformation on an SWCNT surface by DNA–protein interaction. Our results show that the DNA–protein interaction strongly depends on DNA accessibility, which can be enhanced through the addition of nonionic surfactants. FRET analysis shows that the surfactant is able to partially displace the dsDNA by diminishing DNA-SWCNT affinity. In addition to DNA-SWCNT affinity, variation in the activities of different enzymes suggests that geometric constraints based on the interaction area and enzyme mechanism may also affect DNA accessibility. Although the precise mode of action of REs on SWCNT-adsorbed dsDNA has not yet been studied, previous studies have explored enzyme behavior in the presence of a competitive DNA-bound protein. Jeltsch et al. showed that REs helically scan along DNA and pause when encountering a bound ligand.[184] We propose a similar mechanism for the dsDNA-SWCNT system, where the enzyme helically scans along the dsDNA until it encounters the SWCNT, blocking enzyme sliding and thereby slowing binding-site recognition.

Alternative models on the interaction of dsDNA with SWCNTs have been reported in the literature (Table 3.1). Differences in the predicted behaviors can be attributed to the range of experimental conditions, including varying buffer systems and component concentrations that are expected to modulate the dsDNA-SWCNT interaction markedly. Our restriction enzyme digestion assay provides a universal method applicable under varying conditions to evaluate the conformation of dsDNA interacting with SWCNTs. For example, we applied the assay to compare enzyme activity on dsDNA-SWCNT hybrids prepared using different methods (Figures S3.9 and S3.10, and discussion in Section 3.5). While the assay confirmed that all the tested methods generate native and accessible dsDNA, the yield varied considerably, with the SC-exchange method adopted in this study showing the highest yields. We also applied the assay to monitor the long-term stability of dsDNA in the nanotube hybrid (Figure S3.11), and we observed negligible denaturation of the dsDNA within 3 months at 4 °C. In addition to its applicability in different conditions, this technique is insensitive to GC content, offering

great versatility for studying dsDNA-SWCNT hybrids and applications over a wide range of sequence compositions.

While previous efforts to explore and enhance the interaction between SWCNTs and dsDNA have relied on carboxylated-SWCNTs[185] or pyrene-modified biomolecules,[138, 149, 186] these approaches show limited application for high-throughput screening or optical sensing. The added flexibility in using pristine SWCNTs, which are specifically capable of auto fluorescence, offers a promising prospect for the label-free optical detection of protein-dsDNA interactions. Future applications of this platform therefore include not only exploring other DNA-binding proteins, such as transferases and topoisomerases, but also exploiting the preserved NIR SWCNT fluorescence to optically detect a broad range of enzymatic DNA–protein interactions in vitro and/or in vivo. Such in vivo applications can exploit the temperate properties of Triton X-100, which has been shown to increase nanoparticle uptake and permeabilize cell membranes at low concentrations without curtailing cell viability.[181, 187] Alternatively, the system can benefit from the natural salt concentration gradient that exists across the outer cell membrane to trigger DNA release for gene delivery applications, as described by Ghosh et al.[183] Thus, by carefully choosing an appropriate DNA configuration, suspension method, and reagent conditions for tuning dsDNA-SWCNT interactions, this platform can enable new dsDNA optical measurements for both fundamental and applied studies.

3.4 Methods and Experiments

Materials. Purified SWCNTs were purchased from NanoIntegris (HiPCO, batch HP26-019 and HP29-064). BamHI-HF (E163A/E167T), EcoRV-HF (D19A/E27A), and reaction buffer NEBuffer 4 (50 mM potassium acetate, 20 mM Tris-acetate, 10 mM magnesium acetate, 1 mM DTT, pH 7.9) were purchased from New England Biolabs. Unless otherwise noted, all chemicals were purchased from Sigma-Aldrich.

All DNA were purchased from Microsynth. The sequences each contain one specific cutting site for one of the type-II REs, either BamHI (GGATCC) or EcoRV (GATATC). In order to non-covalently anchor dsDNA on the SWCNT surface, three different configurations were designed, as shown in Figure 3.1a. Cy3-modified DNA was purified by PAGE by the manufacturer. Complementary DNA sequences were annealed in ddH_2O by incubation at 95 °C for 5 min followed by slow cooling to room temperature (~2 h).

Preparation of dsDNA-SWCNT. We prepared ssDNA-dsDNA-SWCNT hybrids according to the method described by Shiraki et al. with some modifications (summarized in Section 3.5). In brief, the SC concentration of the SC-suspended SWCNT was adjusted by dialyzing against 0.5 mM SC. The resulting SWCNT suspension was incubated with thermally annealed dsDNA in excess at room temperature for at least 3 days in order to reach equilibrium. Replaced SC and free DNA were removed with Amicon Ultra-2 mL centrifugalfilters (Millipore, MWCO = 100 kDa) washing 6 times with 1 mL of ddH_2O (see Section 3.5). The filtered solutions were collected and centrifuged at 21 130g for 10 min to remove unwanted SWCNT bundles.

The dsDNA-SWCNT solutions were stored at 4 °C, where they can remain stable for months. The concentration of SWCNTs was estimated from the absorption spectrum, taking ϵ_{910nm} of 0.02554 L mg^{-1} cm^{-1} .[188] Details on photoluminescence and AFM characterization of hybrids can be found in Section 3.5.

Digestion assay. We developed an endonuclease assay to study conformations of dsDNA on SWCNTs. The scheme is shown in Figure 3.1b. In a typical experiment, 0.5 mg/L of DNA-SWCNTs was incubated with 20 U of BamHI-HF or EcoRV-HF in NEBuffer 4 (1×) in a total volume of 30 μL in 1.5 mL Eppendorf tubes, at 22 °C and shaking with 300 rpm. Aliquots supplemented with Triton X-100 were incubated with the desired Triton X-100 concentration for 2 h at 22 °C before mixing with the enzyme and buffer. After 16 h of incubation, the reaction solutions were diluted to 300 μL with ddH_2O before being stopped by adding an equal volume of phenol-chloroform-isoamyl alcohol extraction reagent (Sigma-Aldrich, 25:24:1). After centrifugation for 5 min at 16 000g at room temperature, the aqueous phase was collected, and the DNA was precipitated according to literature using ethanol supplemented with glycogen (Carl Roth).[189] The pellet was washed with 70% ethanol and resuspended in denaturing gel loading buffer containing 95% formamide. Samples were heat-denatured for 3 min at 95 °C and immediately quenched on ice before separation on a denaturing 12% urea-polyacrylamide gel in 1× Tris-boric acid-EDTA buffer at 250 V for 45 min. The DNA was stained with SYBR Gold (Thermo Fisher) for ~25 min and visualized on a blue-light gel imager. The amount of DNA was quantified using ImageJ. All experiments were conducted in triplicate.

Fluorescence Measurements. Twenty microliter sample aliquots were placed in a flat-bottom 384-well plate (Nunc MaxiSorp). Visible-range emission spectra were recorded using a Varioskan microplate reader.

MD Simulation. For the initial condition, we conjugated the dsDNA segment of BH7-5 aligned along the nanotube axis to an equilibrium conformation of $(GT)_{10}$ on the (9,4)-SWCNT, which was modeled by Harvey et al.[72] The surrounding aqueous solution contained 30 mM sodium and 10 mM magnesium ions. After 100 ns equilibration, the simulation was subsequently run for 250 ns. The final equilibrated snapshot is shown in Figure 3.5a. Additional details on the simulation can be found in Section 3.5

3.5 Supporting Information

DNase I assay. The DNase I reaction was carried out similar to the Type-II RE reactions with 1.2 ug/uL of DNase I (Sigma-Aldrich, DN25) in a reaction buffer containing 100 mM Tris-Cl (pH 7.6), 25 mM $MgCl_2$, and 5 mM CaCl2. The DNA was extracted, precipitated, and analyzed using the same procedure described in the main text (Figure S3.1).

Removal of free DNA. To verify that free DNA is successfully removed after wrapping SWCNTs via adsorbent exchange we analyzed the flow-through following ultrafiltration on denaturing PAGE (Figure S3.2). DNA was gradually removed, and after six washing steps, no

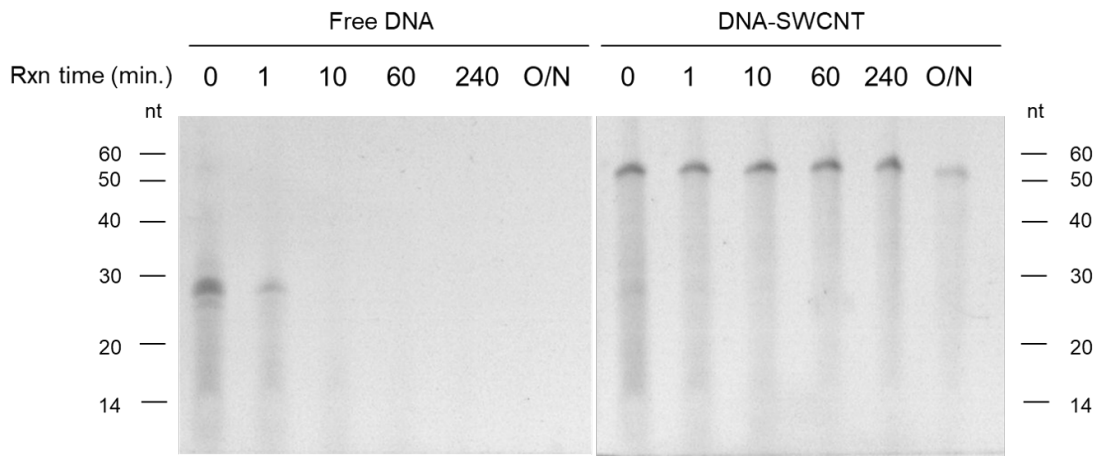

Figure S3.1 – Denaturing PAGE was used to monitor the kinetics of DNase I on different substrates. While free BH13-55 is degraded within minutes, BH13-55 immobilized on SWCNTs is protected from non-specific digestion by DNase I for an extended period of time.

DNA was visible in the PAGE gel (FigureS3.2b). Accounting for the sensitivity of the staining dye, we estimate the concentration of free DNA in the complex solution to be less than 2.5 pg/uL. Compared to the total amount of DNA in the complex (around 7.8 ng/uL, as estimated by comparing to the ladder intensity), and given that the amount of DNA on SWCNT is around 3 ug per ug of SWCNT, which is in agreement with previous findings, these measurements suggest that any trace amount of free DNA does not significantly contribute to the results of the digestion assay.

Verification of surfactant displacement by DNA. We measured the photoluminescence (PL) of the purified DNA-SWCNT complex in the near-infrared (NIR) region to verify surfactant displacement. Compared to SC-suspended SWCNT, the resulting DNA-SWCNT solution has a red-shifted spectrum that is expected for DNA-covered SWCNTs (Figure S3.2c). The red-shift is attributed to increased water accessibility due to the decreased SWCNT surface coverage compared to SC.[109] We also used AFM to image the complex, and we observed SWCNTs with the expected ~1 nm height and ~700 nm length (Figure S3.2d).

DNA extraction by phenol-chloroform-isoamyl alcohol extraction (PCI). In the digestion assay, we used PCI extraction to recover DNA from SWCNTs. To investigate whether all DNA molecules are removed from SWCNTs, we compared the amount of DNA recovered after PCI extraction to the DNA recovery using the SDBS-exchange method[190] by denaturing PAGE (Figure S3.3). No significant difference between the recovery efficiency of the two methods was observed (two-sample t-test, $p = 0.19$). As a result, we have concluded that the DNA is sufficiently removed from the SWCNTs by PCI extraction.

Comparison of alternative DNA-SWCNT preparation methods. The preparation method of the DNA-SWCNT hybrid complexes might lead to differences in the interaction of dsDNA with the nanotube. We thus determined the efficiency of different preparation methods in forming

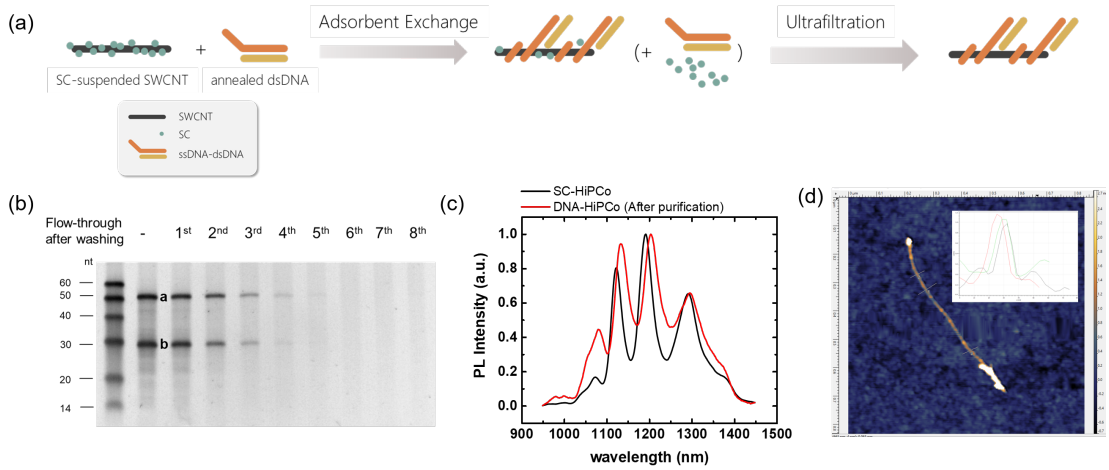

Figure S3.2 – Preparation and characterization of DNA-SWCNTs. (a) Cartoon of the surfactant exchange method. (b) 12% denaturing PAGE showing the removal of free DNA by ultrafiltration. The two bands, a and b, correspond to the sequence in Figure 3.1d. The lane numbering corresponds to the times the sample was washed by ultrafiltration. No DNA was detected in the flow-through after the sixth washing. (c) PL spectrum of DNA-SWCNTs after purification exhibits a red-shifted spectrum compared to SC-SWCNTs. (d) AFM image of HiPCO-BH7-5.

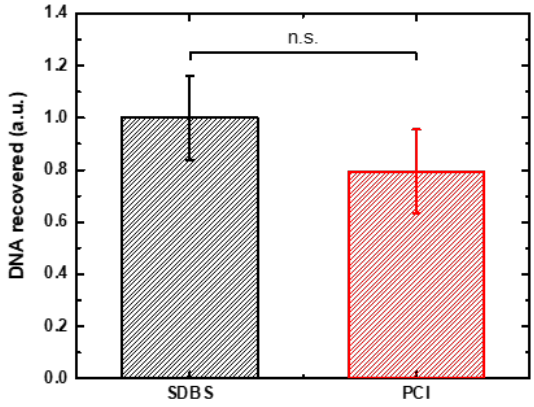

Figure S3.3 – DNA recovery using two different methods: SDBS-exchange[190] and PCI extraction (this work). $(GT)_{15}$ -suspended SWCNTs were used. The amount of DNA recovered was analyzed using 12% denaturing PAGE. All results are mean values of independent triplicates, with the error bar representing 1 S.D. No significant difference between the methods was observed (two sample t-test, $p = 0.19$).

accessible dsDNA on SWCNTs. Three methods have been reportedly used to generate dsDNA-SWCNT conjugates: i) the surfactant exchange method we adopted in this study,[109] ii) direct sonication of SWCNTs with dsDNA (Figure S3.9a),[108] and iii) the addition of complementary strands to ssDNA-suspended SWCNT (Figure S3.9b).[72] Although different techniques have

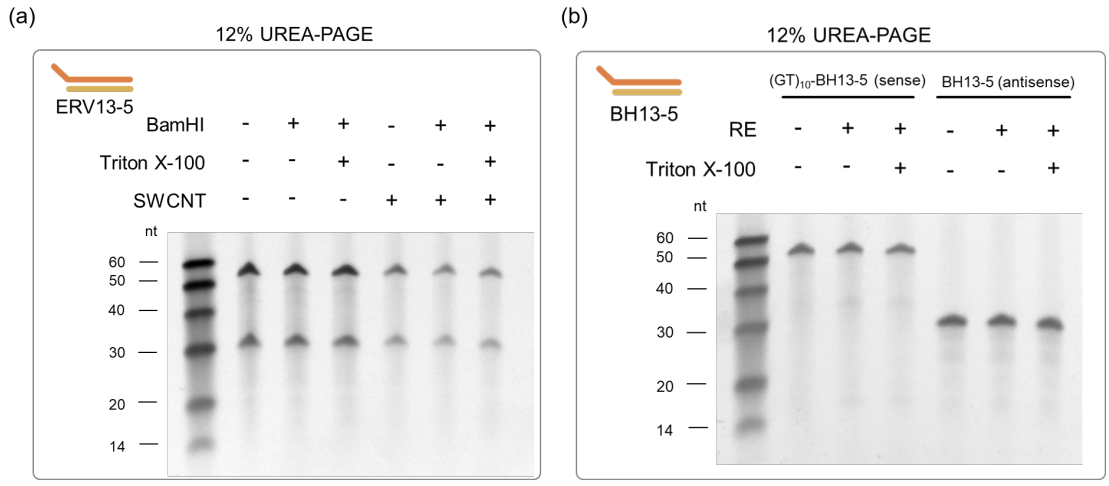

Figure S3.4 – DNA fragment analysis by 12% denaturing PAGE. (a) BamHI is not active on ERV13-5, which does not contain a recognition site. (b) No restriction fragments are detected when the two complementary strands each containing the BamHI recognition sequence are separately incubated with BamHI.

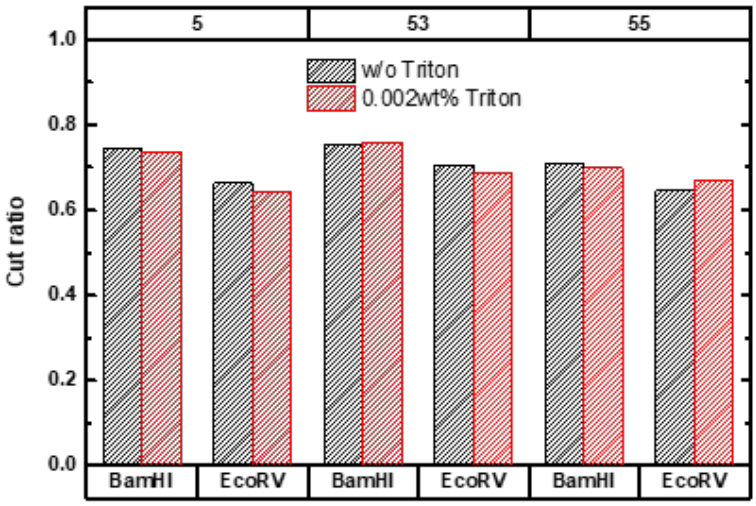

Figure S3.5 – Cut ratio of BamHI and EcoRV on free dsDNA quantified by denaturing PAGE fragment analysis. The lower panel indicates the corresponding cutting site of the RE on the DNA, and the upper panel shows the overhang configuration of $(GT)_{10}$. Addition of Triton X-100 (in red) does not alter RE activity.

been used to exclude the denatured dsDNA during the wrapping procedure or to validate the presence of dsDNA on the SWCNTs,[136, 165] there is no direct confirmation that the dsDNA retains its native conformation. Here, we employed RE-fragment analysis to evaluate the DNA conformation when dsDNA-SWCNTs were prepared accordingly (see below for details on the

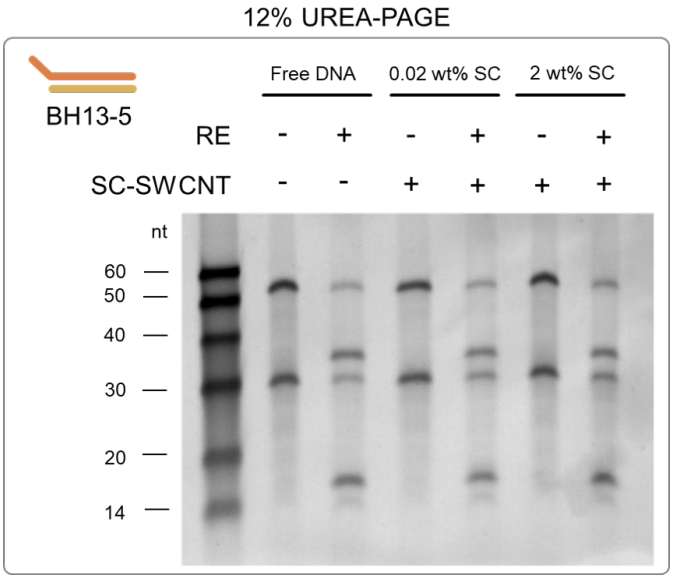

Figure S3.6 – Fragment analysis of DNA digested by REs in the absence or presence of SC-suspended SWCNTs. 12% Denaturing PAGE was used to quantify the cut ratio and enzymatic activity. RE activity on DNA in the presence of SWCNTs suspended with 0.02 or 2 wt% SC (A_{rel} = 0.96 and 0.92, respectively) is comparable to that of free DNA in the absence of SC-SWCNTs.

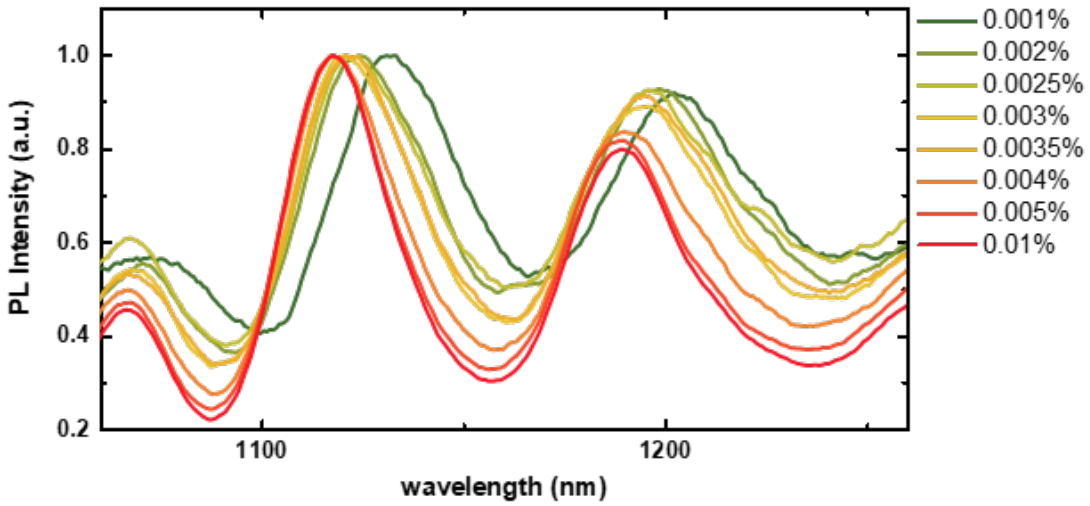

Figure S3.7 – Blue-shift of BH13-55-SWCNT PL spectrum excited at λ_{max}= 730 nm after addition of Triton X-100. The extent of the wavelength shift depends on the Triton X-100 concentration. The PL spectrum is blue-shifted by 16 nm when 0.005 wt% of Triton X-100 is added to the DNA-SWCNT complex. The incomplete blue-shift in the 0.002 wt% Triton X-100 spectrum indicates that the SWCNT surface is not fully covered by the surfactant and that the surfactant has not completely replaced the DNA wrapping.

preparation).

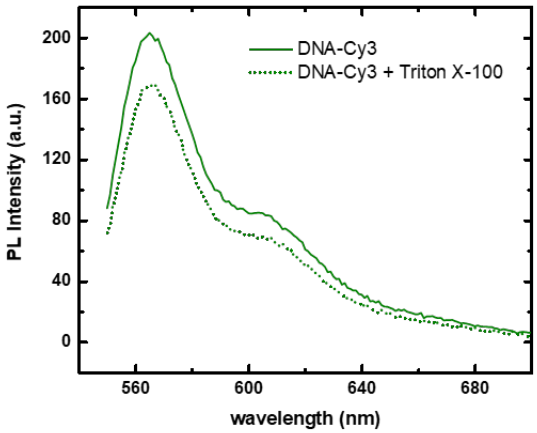

Figure S3.8 – Fluorescence spectrum of BH13-5(*) which contains a Cy3 fluorophore at the opposite end of $(GT)_{10}$. Emission spectra were collected in the visible range using excitation at 532 nm. Cy3 fluorescence at 565 nm is decreased by the addition of 0.002 wt% Triton X-100.

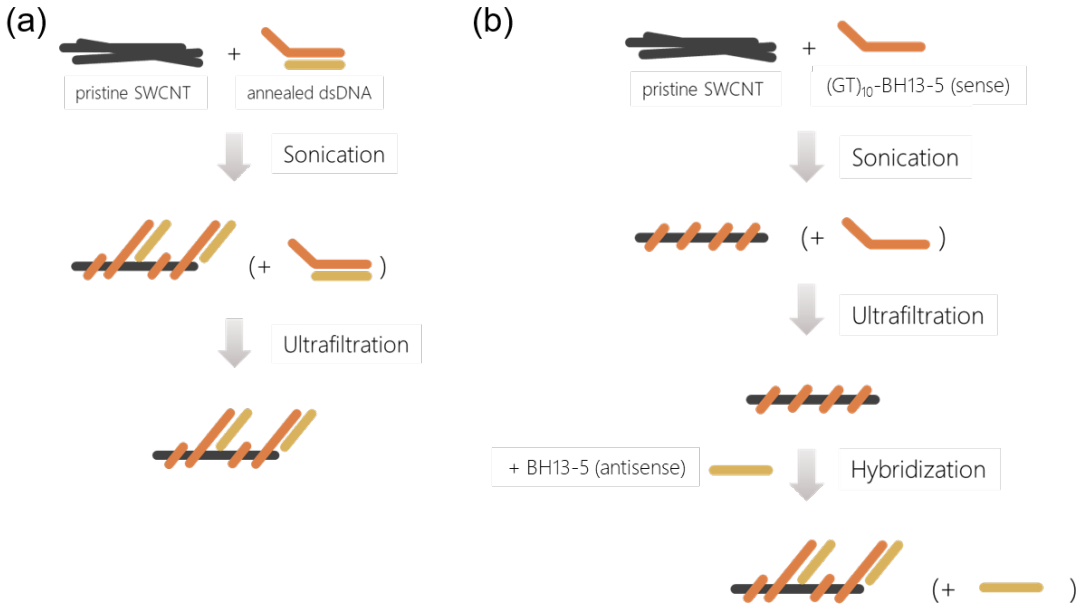

Figure S3.9 – Schematic cartoon of two different preparation methods for the DNA-SWCNT complex. (a) Direct sonication: thermally annealed dsDNA was mixed with SWCNT powder, sonicated, and purified by ultrafiltration. (b) Hybridization: $(GT)_{10}$-BH13-5 (sense) was sonicated with SWCNT powder and purified by ultrafiltration. BH13-5 (antisense) was introduced to the hybrid and allowed to hybridize for 2 hours at room temperature.

Figure S3.10 shows the restriction fragment analysis of BamHI on dsDNA-SWCNT conjugates prepared by direct sonication. In the presence of Triton X-100, the enzyme activity (A_{rel} = 0.39) on complexes assembled through sonication is reduced by 35% compared to the

sample prepared using the surfactant exchange method. This implies that a lower amount of dsDNA maintains its accessible native conformation even though the steric hindrance is reduced by Triton X-100. We think sonication partially unwinds dsDNA and leads to a mixture of ssDNA and dsDNA interacting with the SWCNT surface. We observed a larger cut ratio after digesting DNA-SWCNT hybrids prepared via the hybridization method (Figure S3.10b) when comparing to direct sonication method. However, compared to the surfactant exchange method, the cut ratio is reduced by 50% (A_{rel} = 0.13 and 0.32, without and with Triton X-100, respectively), indicating that a smaller fraction of bound DNA forms accessible dsDNA.

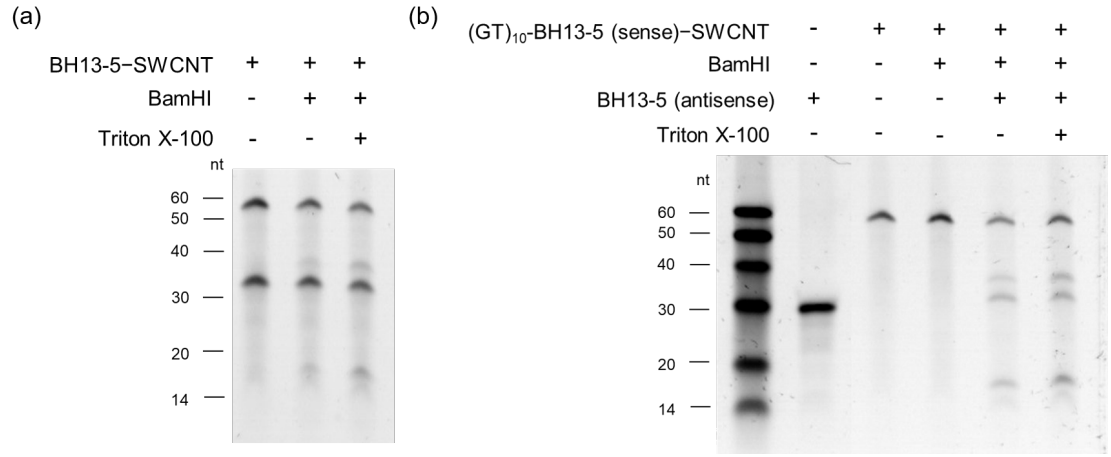

Figure S3.10 – Comparison of dsDNA accessibility for DNA-SWCNT complexes prepared by different methods. Fragment analysis of BamHI digestion by denaturing PAGE on hybrids prepared by (a) direct sonication of dsDNA (BH13-5) with SWCNTs and (b) hybridization of ssDNA-suspended SWCNTs $(GT)_{10}$-BH13-5 (sense) with a complementary strand (BH13-5 (antisense)). Low enzymatic activity in systems prepared by sonication (without and with Triton X-100: A_{rel} = 0.29 and 0.39, respectively) and hybridization (without and with Triton X-100: A_{rel} = 0.13 and 0.32, respectively) implies a low amount of native dsDNA on the SWCNT.

Direct Sonication (Figure S3.9a and Figure S3.10a.) BH13-5 was hybridized by heating to 95°C for 5 min followed by a gradual cooling down to room temperature over 2 hr in ddH_2O. The DNA was then mixed with SWCNTs in a DNA:SWCNT weight ratio of 1:2. Samples were sonicated and purified using the same procedure described above.

Hybridization (Figure S3.9b and Figure S3.10b.) $(GT)_{10}$-BH13-5 (sense) was mixed with SWCNTs in a DNA:SWCNT weight ratio of 1:2 in ddH_2O. The samples were subsequently sonicated in a cup horn sonicator for 30 minutes at 4 °C, and the supernatant was collected after centrifugation at 21130 g for 3 hours at room temperature. Free DNA was removed from the resulting solution by using an Amicon Ultra-2 mL (MWCO = 100 kDa) filter. An excess of BH13-5 (antisense) was introduced to the sample and incubated for 2 hours before digestion.

Long-term stability of dsDNA-SWCNT complexes. Though single-stranded DNA-binding protein (SSB) has previously been shown not to interact with a dsDNA-SWCNT complex,[136] this finding does not corroborate the native conformation of the DNA duplex. Cathcart et

al.[108] observed a complete rearrangement of dsDNA into helically wrapped ssDNA strands during a slow transition process over 3 months. We speculate that this process is negligible if no partial denaturation of the dsDNA due to sonication occurs, as we could still observe native duplexes on dsDNA-SWCNTs prepared by adsorbent exchange when samples were stored for 3 months at 4 °C (Figure S3.11).

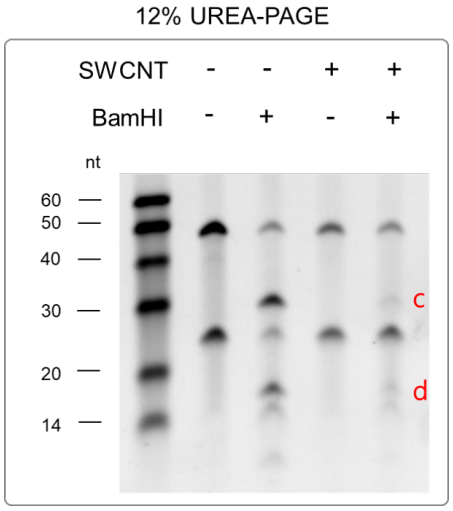

Figure S3.11 – The dsDNA is not fully denatured on SWCNT three months after preparation. The intensity of restricted products, c and d, is similar to the ones from the fresh samples (see BH7-5 digestion in Figure 3.3a in the main text).

Table 3.3 – Sequences used in Chapter 3.

dsDNA	ssDNA for hybridization	Sequence (5' to 3')	
BH2-5	GTBHMain2	GTG TGT GTG TGT GTG TGT GTG GGA TCC GTT AGT TCA TGC	
	BHCom2	GCA TGA ACT AAC GGA TCC C	
BH4-5	GTBHMain4	GTG TGT GTG TGT GTG TGT GTA GGG GAT CCG TTA GTT CAT GC	
	BHCom4	GCA TGA ACT AAC GGA TCC CCT	
BH7-5	GTBHMain7	GTG TGT GTG TGT GTG TGT GTG ATA GGG GAT CCG TTA GTT CAT GC	
	BHCom7	GCA TGA ACT AAC GGA TCC CCT ATC	
BH10-5	GTBHMain10	GTG TGT GTG TGT GTG TGT GTC CTG ATA GGG GAT CCG TTA GTT CAT GC	
	BHCom10	GCA TGA ACT AAC GGA TCC CCT ATC AGG	
BH13-5	GTBHMain13	GTG TGT GTG TGT GTG TGT GTC GTC CTG ATA GGG GAT CCG TTA GTT CAT GC	
	BHCom13	GCA TGA ACT AAC GGA TCC CCT ATC AGG ACG	
BH13-53	GTBHMain13	GTG TGT GTG TGT GTG TGT GTC GTC CTG ATA GGG GAT CCG TTA GTT CAT GC	
	BHCom13GT	GCA TGA ACT AAC GGA TCC CCT ATC AGG ACG GTG TGT GTG TGT GTG TGT GT	
BH13-55	GTBHMain13	GTG TGT GTG TGT GTG TGT GTC GTC CTG ATA GGG GAT CCG TTA GTT CAT GC	
	GTBHCom13	GTG TGT GTG TGT GTG TGT GTG CAT GAA CTA ACG GAT CCC CTA TCA GGA CG	
BHH13-5	GTBHMain13HighGC	GTG TGT GTG TGT GTG TGT GTG TTG GAC GCT CTG GAT CCT CCC TCG GGG CG	
	BHCom13HighGC	CGC CCC GAG GGA GGA TCC AGA GCG TCC AA	
BHL13-5	GTBHMain13LowGC	GTG TGT GTG TGT GTG TGT GTG TAA CAT AAC TTG GAT CCT TAT TGA TAT TG	
	BHCom13LowGC	CAA TAT CAA TAA GGA TCC AAG TTA TGT TAC	
BH13-5-Cy3	GTBHMain13	GTG TGT GTG TGT GTG TGT GTC GTC CTG ATA GGG GAT CCG TTA GTT CAT GC	
	BHCom13Cy3	GCA TGA ACT AAC GGA TCC CCT ATC AGG ACG	5' Cy3
ERV13-5	GTERVMain13	GTG TGT GTG TGT GTG TGT GTC GTC CTG ATA GGG ATA TCG TTA GTT CAT GC	
	ERVCom13	GCA TGA ACT AAC GAT ATC CCT ATC AGG ACG	
ERV13-53	GTERVMain13	GTG TGT GTG TGT GTG TGT GTC GTC CTG ATA GGG ATA TCG TTA GTT CAT GC	
	ERVCom13GT	GCA TGA ACT AAC GAT ATC CCT ATC AGG ACG GTG TGT GTG TGT GTG TGT GT	
ERV13-55	GTERVMain13	GTG TGT GTG TGT GTG TGT GTC GTC CTG ATA GGG ATA TCG TTA GTT CAT GC	
	GTERVCom13	GTG TGT GTG TGT GTG TGT GTG CAT GAA CTA ACG ATA TCC CTA TCA GGA CG	

Molecular dynamics (MD) simulations The full MD simulation box consists of a (9,4) SWCNT, a single-stranded $(GT)_{10}$ linked to a double-stranded BH7, and counterions solvated in explicit water. In order to have a reasonable conformation of ssDNA adsorbed on CNT, we

first started with the $(GT)_{10}$ on (9,4)-SWCNT structure provided by Harvey et al.[72] using a replica-exchange based method.[191, 192] The dsDNA sequences of BH7 were connected to the 3'-terminus of $(GT)_{10}$ on SWCNT by PyMol, and the dsDNA was placed parallel to the nanotube axis at a distance of 1.4 nm.

The hybrid structure was then centered in the simulation box (10.65 nm × 10.65 nm × 19.54 nm) with 13 Mg^{2+} (9.7 mM), 40 Na^{+} counterions (29.8 mM), and 72000 water molecules randomly added in the box using Packmol.[193] The as-prepared full system was followed by a 100 ps equilibration in an NVT (T = 300 K) ensemble where the number of water molecules were fine-tuned to make the average pressure approximately equivalent to atmospheric pressure, leading to approximately 71300 water molecules in the simulation box. Further equilibration was performed for 100 ns in the NVT (T = 300 K) ensemble with a subsequent 250 ns production run. Analysis and video were based on the final production run.

The simulations were performed under periodic boundary conditions using the GROMACS (v. 5.1) package.[194–196] The Charmm36/TIP3P force field[108] was used to describe DNA, counterions, and water molecules. Carbon atoms in the SWCNT were modeled as uncharged Lennard-Jones particles[107, 162] and were kept frozen during the entire simulation. For temperature control, we used velocity rescaling with a stochastic term[197] (T = 300K, τ_T = 1.0 ps) to ensure canonical sampling. The time step used in all simulations was 2 fs. All bonds were constrained using the Linear Constraint Solver (LINCS) algorithm[198] to enable a large simulation time step. A cutoff of 1.2 nm was applied to the van der Waals interaction. For long-range electrostatic interactions, the particle mesh Ewald (PME) method was employed with a 1.2 nm real space cut-off.

4 Nuclease-Assisted Fluorescence Assay of DNA Hybridization on SWCNT

This Chapter is adapted from a manuscript prepared for submission in a journal with co-authors:
Shang-Jung Wu, Benjamin P. Lam bert, and Ardemis A. Boghossian.

4.1 Introduction

Single-walled carbon nanotubes (SWCNTs) have tunable optoelectronic properties that inspire their use in multiple electronic, electrochemical, and optical sensors.[199] These devices take advantage of the nanotube's 1D structural and quantum confinement, allowing SWCNTs to serve as unidimensional scaffolds for biomolecule immobilization as well as optoelectronic actuators that are responsive to interactions occurring on the nanotube surface citations. Such sensing devices rely on immobilized biomolecules to disperse nanotubes in aqueous solutions and to control the selectivity of the interactions.

Many of the SWCNT-based sensors rely on the extensive use of single-stranded DNA (ssDNA) as a biocompatible dispersant. Such dispersions benefit from the self-assembly of ssDNA, which occurs via $\pi - \pi$ stacking of the bases on the nanotube surface. The immobilized ssDNA further provides a means of anchoring other nanoparticles and biomolecules through additional bioconjugation. Additionally, by exploiting its sequence tunability, ssDNA can be used for SWCNT chirality separation[158, 160] as well as bioanalyte sensing.[29, 200]

In contrast to ssDNA-SWCNT, double-stranded DNA (dsDNA)-SWCNT complexes have been less explored.[78, 116, 163] These complexes provide a basis for studying DNA hybridization as well as dsDNA-biomolecule interactions on the nanotube surface. Several approaches have been developed to monitor dsDNA hybridization in the presence of SWCNTs. For example, Jeng et al.[71, 201] and Harvey et al.[72] used the near-infrared fluorescence of SWCNTs to differentiate complementary sequences from non-complementary sequences with enough sensitivity to detect single nucleotide polymorphisms. Star et al.[202] and Jung et al.[167] designed transistors for detecting DNA hybridization through variation in current. Despite

these advances, orthogonal approaches for directly validating dsDNA immobilization on the nanotube surface have been limited. The competitive base-base interactions required for hybridization and base-nanotube interactions required for solubilizing nanotubes have given rise to conflicting reports on the immobilization of dsDNA in nanotube dispersions citation.

In a recent study,[31] a new assay based on restriction enzyme (RE) analysis was used to characterize dsDNA immobilization on a nanotube surface. In this assay, the RE's activity on the dsDNA was used to confirm immobilization of dsDNA and the retention of its native conformation. Despite the lower RE activity on immobilized dsDNA compared to free dsDNA, this assay also demonstrated the accessibility of the immobilized dsDNA to enzyme activity. However, this assay is highly specific, requiring laborious purification and gel electrophoresis steps that limit the assay throughput. In addition, the assayed sequences must include a cutting site of RE, which introduces additional limitations on the sequence of the gene or oligonucleotide of interest.

The drawbacks of the RE assay could be addressed using fluorescent dyes. Organic fluorescent dyes are routinely used to determine DNA concentration as well as to label DNA for imaging and high-throughput screening. Unlike REs, these dyes have been designed to interact with dsDNA non-specifically. For example, ethidium bromide (EtBr) intercalates between nucleobases, and the dye fluorescence increases due to the resulting decrease in the number of water molecules in its vicinity.[203] Other examples include Hoechst and SybrGold, which bind to the minor groove of the dsDNA. This binding decreases the rotational degree of freedom and increases the conjugation length of the dye, resulting in a fluorescence increase.[204, 205] Although these dyes have been previously used to study free dsDNA formation in the presence of suspended SWCNTs,[206, 207] their use in studying immobilized dsDNA on SWCNTs has remained unexplored.

In this chapter, we develop a fluorescence assay for studying dsDNA formation on SWCNTs. This assay, which is based on a commercially available DNA-labelling dye, QuantiFluor (QF), obviates the need for sequence-dependent REs and subsequent electrophoresis analysis. We further exploit the throughput of this assay to explore different hybridization conditions, allowing us to optimize dsDNA formation. These optimized conditions serve as a basis for engineering dsDNA-SWCNT platforms for new sensing applications, particularly for devices that require sufficient amounts of immobilized dsDNA.

We first show the validity of our fluorescence assay based on the hybridization of ssDNA-SWCNT and its complementary DNA sequence (cDNA). The assay reveals that the base pairing on SWCNT surface is sequence specific. Furthermore, we show the hybridization kinetics to be highly dependent on ionic strength, and the hybridized dsDNA (19 bp) to be stable only 16 °C below the melting temperature (T_m). We also use the assay to determine dissociation constants (K_D) of hybridization on SWCNT, found to be 1000-fold higher than in free state. These results demonstrate the versatility and the high-throughput nature of the assay. Importantly, our assay offers new insight in the mechanism of DNA hybridization on the SWCNT surface and

the associated SWCNT fluorescence behaviors. We anticipate that this assay will boost the understandings of dsDNA-SWCNT hybrids and their application in the near future.

4.2 Results and Discussion

The dsDNA complexes were prepared by hybridizing ssDNA-SWCNTs with complementary DNA (cDNA), as shown in Figure 4.1a. The ssDNA is composed of a $(GT)_{10}$ anchoring sequence and one of several target sequences. The DNA sequences used in this study are summarized in Table 4.1. Nanotube solubilization by these ssDNA sequences was verified through absorption and near-infrared (NIR) fluorescence spectroscopy (Figure S4.1).[89]

Table 4.1 – Summary of DNA sequences used in Chapter 4. The underlined DNA bases represent the $(GT)_{10}$ anchoring sequence.

Name	Alias	Sequence (5' to 3')	cDNA
$(GT)_{10}$-A1	$(GT)_{10}$BHMain2	GTG TGT GTG TGT GTG TGT GTG GGA TCC GTT AGT TCA TGC	a1
$(GT)_{10}$-A2	$(GT)_{10}$BHMain2to7	GTG TGT GTG TGT GTG TGT GTG GTT AGT GGA TCC TCA TGC	a2
a1	BHCom2	GCA TGA ACT AAC GGA TCC C	$(GT)_{10}$-A1, A1-$(GT)_{10}$
a2	BHCom2to7	GCA TGA GGA TCC ACT AAC C	$(GT)_{10}$-A2
$(GT)_{10}$	-	GTG TGT GTG TGT GTG TGT GT	N/A
a1-3'FAM	-	GCA TGA ACT AAC GGA TCC C-FAM	$(GT)_{10}$-A1, A1-$(GT)_{10}$
A1-$(GT)_{10}$	-	GGG ATC CGT TAG TTC ATG CGT GTG TGT GTG TGT GTG TGT	a1
$(GT)_{10}$-A3	$(GT)_{10}$-handle	GTG TGT GTG TGT GTG TGT GTG TAA CGA CTC	a3
a3	handle-com	GAG TCG TTA C	$(GT)_{10}$-A3
$(GT)_{10}$-R1	-	GTG TGT GTG TGT GTG TGT GTG TCG CTT AAG GCG ATT GCT	r1
$(GT)_{10}$-R2	-	GTG TGT GTG TGT GTG TGT GTC ATT GGA TCG GTC CTG GAT	r2
r1	-	AGC AAT CGC CTT AAG CGA C	$(GT)_{10}$-R1
r2	-	ATC CAG GAC CGA TCC AAT G	$(GT)_{10}$-R2

The QF dye was used to detect dsDNA hybridization on the SWCNT surface using the assay depicted in Figure 1a. As shown in the schematic, the reaction sample was incubated with S1 nuclease prior to the addition of the dye. The introduction of S1 nuclease is used to selectively digest unbound cDNA. Since the immobilized ssDNA is inaccessible to the nuclease (Figure S4.2b and S4.2c), this steps serves to remove any contaminating fluorescence contribution from unbound cDNA (Figure S4.3).

The dsDNA hybridization on the nanotube surface was confirmed using QF fluorescence. As shown in Figure 4.1b, we observe a fluorescence peak at 530 nm in the presence of $(GT)_{10}$-A1-SWCNT incubated with cDNA (a1) (red curve). This fluorescence peak is in agreement with

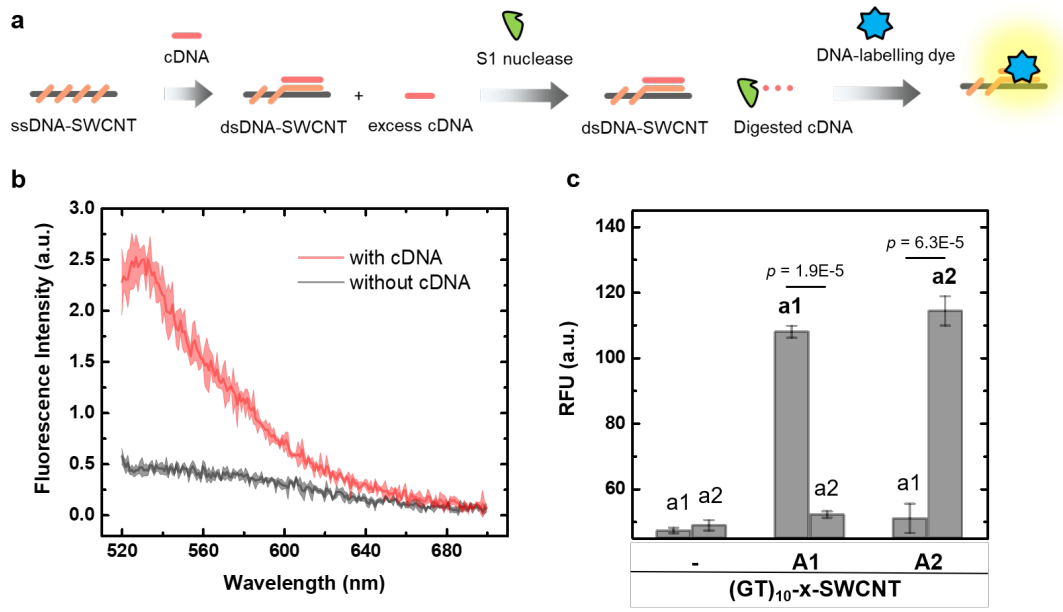

Figure 4.1 – Fluorescence characterization of immobilized dsDNA on SWCNTs. (a) Schematic of the assay. The cDNA is added to the ssDNA-SWCNT and annealed, the excess non-hybridized cDNA is digested by S1 nuclease, and the DNA-labelling dye is added to the suspension. (b) Fluorescence spectra of QF in the presence of $(GT)_{10}$-A1-SWCNT with and without cDNA. Samples were annealed at 60 °C in SSC buffer. Nuclease digestion and fluorescence measurements were performed at room temperature. (c) Comparison of fluorescence emissions in the presence of cDNA and non-complementary DNA. $(GT)_{10}$-A1-SWCNT/a1 and $(GT)_{10}$-A2-SWCNT/a2 correspond complementary combinations. The relative fluorescence unit (RFU) is defined as the integrated area under the fluorescence curve between 520 nm and 700 nm. Error bars represent standard deviation of independent triplicates. The two-sample t-test was used to verify statistical significance. All fluorescence spectra were taken at 500 nm excitation.

the QF emissions reported in manufacturer's instruction. Since the unbound ssDNA is digested by the S1 nuclease (Figure S4.4 and S4.5), this fluorescence is attributed to the formation of dsDNA, which is inaccessible for S1 nuclease digestion.[208, 209] In contrast, the baseline fluorescence emission that is observed in the absence of cDNA (black line) indicates negligible fluorescence contribution from ssDNA-SWCNTs. Furthermore, negligible fluorescence was observed on the addition of non-complementary DNA (Figure 4.1c). Whereas significant fluorescence can be seen for the $(GT)_{10}$-A1/a1 and $(GT)_{10}$-A2/a2 complementary pairs, we observed no significant fluorescence for samples in the presence of non-complementary DNA and $(GT)_{10}$ samples lacking a target sequence (Figure 4.1c and Figure S4.6). Furthermore, the fluorescence assay confirms a stronger fluorescence signal for longer hybridization sequences compared to shorter sequences, in agreement with the more favorable hybridization that is expected for longer sequences (Figure S4.7). These results suggest a minimum hybridization length required for accurate detection using this assay. Additional measurements show neg-

ligible fluorescence contributions from desorbed ssDNA (Figure S4.8a), confirming that the fluorescence increase is due to dsDNA hybridization.

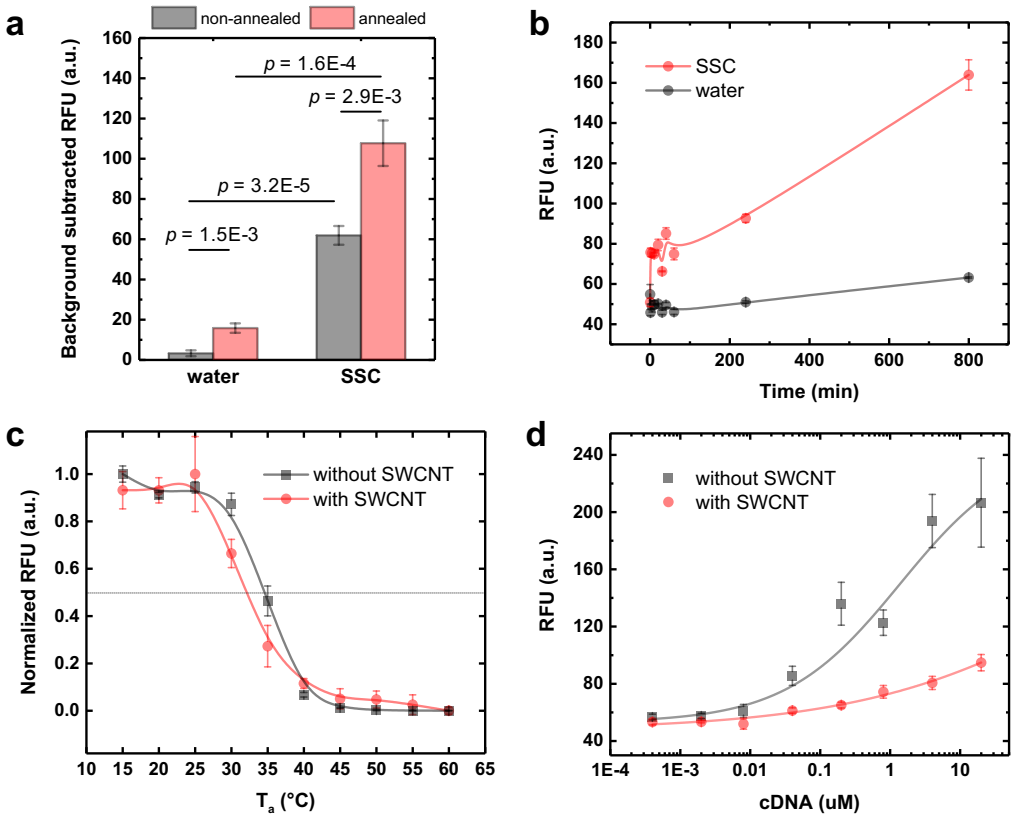

Figure 4.2 – Fluorescence analysis of DNA hybridization on SWCNTs under different conditions. (a) Comparison of annealed and non-annealed hybridization yield in different media (water vs. SSC). Background subtracted RFU was defined as ($RFU_{+\text{cDNA}} - RFU_{-\text{cDNA}}$), where $RFU_{+\text{cDNA}}$ and $RFU_{-\text{cDNA}}$ refer to the RFU in the presence and absence of cDNA, respectively. (b) Kinetic monitoring of DNA hybridization in SSC and in water. The samples were heated up to 60 °C, then quenched to 20 °C ($t = 0$) for hybridization to occur. (c) Comparison of annealing temperature (T_a) in SSC in the absence and presence of SWCNTs. In this experiment, the S1 digestion was conducted at $T = T_a$. Lines in (b) and (c) are included as visual guides. (d) Concentration dependence of cDNA in SSC in the absence and presence of SWCNTs. The lines are best fits achieved using the Hill equation.

Table 4.2 – T_h and K_D of DNA hybridization in the presence and absence of cDNA.

	T_h (°C)	K_D (μM)
Without SWCNT	34.5	1.4
With SWCNT	32.1	2200

The QF fluorescence assay was further used to probe the effects of different hybridization conditions (Figure 4.2). As shown in Figure 4.2a, thermal annealing (i.e. heating at 60 °C

followed by gradually cooling down to room temperature) results in a 1.7-fold increase in fluorescence compared to non-annealed samples in SSC buffer. Since ssDNA is shown to remain stable on SWCNTs at 60 °C (Figure S4.8a), and the S1 nuclease remains active up to 80 °C (Figure S4.8b), these results suggest that thermal annealing facilitates dsDNA formation on the SWCNT. We hypothesize that thermal annealing helps the DNA to overcome kinetically trapped metastable states and correct possible base pair mismatches.[210]

A comparison of hybridization in SSC buffer and in water shows an increase in fluorescence in SSC compared to water for both annealed and non-annealed samples (Figure 4.2a). In particular, we observe a 19-fold increase in fluorescence for SSC compared to water under annealed conditions. Based on the calibration curves presented in Figure S4.9, this enhancement suggests favorable dsDNA formation in the presence of SSC. Additionally, the SSC buffer shows more favorable hybridization kinetics compared to water (Figure 4.2b), in agreement with previous findings.[211–213] This favored hybridization is attributed to the salts screening the negative charges of ssDNA, thus reducing the repulsive force between the complementary DNA strands.

We also applied the fluorescence assay to monitor the effects of varying annealing temperatures (T_a) on dsDNA hybridization (Figure 4.2c). Samples were heated to 60 °C and cooled to $T = T_a$ for hybridization. The nuclease digestion was then performed at $T = T_a$ to stop hybridization by digesting any unbound cDNA (see Method for details). As shown in Figure 4.2c, the fluorescence signal at $T_a > 35$ °C is significantly lower than that at $T_a < 30$ °C, indicating that DNA hybridization is unstable at high T_a, as expected. Further, if we define T_h to be the temperature at which RFU = 0.5, we find that $T_h = 32.1$ °C and 34.5 °C for ssDNA-SWCNT and free DNA, respectively. Both T_h values lie below the theoretical T_m of 49.3 °C for the A1/a1 hybridization pair. In addition, the lower T_h observed for the ssDNA-SWCNT is attributed to the partial destabilization of the dsDNA in the presence of the nanotube. This hypothesis is supported by molecular dynamics simulations that show that the SWCNT partially denatures dsDNA that is within 9 bp of the anchoring strand.[168] As a consequence, a lower temperature is required to stabilize dsDNA in the vicinity of the SWCNT.

The fluorescence assay was also used to investigate the dissociation constant (K_D) of the system by varying the concentration of cDNA, as shown in (Figure 4.2d). These results show an apparent K_D of cDNA and free ssDNA of approximately 1.4 μM, in agreement with previously reported values based on isothermal titration calorimetry.[214] In contrast, we calculate a K_D of 2200 μM for cDNA in the presence SWCNTs based on the apparent concentration of immobilized ssDNA (see Figure S4.10). The significantly higher K_D observed with the SWCNTs suggests that most the ssDNA on the SWCNT is inaccessible to the cDNA, even in the presence of SSC buffer at $T_a = 60$ °C. These observations are in agreement with previous studies that have shown diminished hybridization yields for ssDNA immobilized on SWCNTs.[31] In addition, we observe a Hill coefficient of 0.24 for the ssDNA-SWCNT/cDNA system, indicating a decrease in cDNA affinity following hybridization due to charge repulsion between the free cDNA and immobilized cDNA.

The DNA hybridization was further optically studied using the near-infrared (NIR) fluorescence of SWCNTs. The NIR fluorescence of SWCNTs is sensitive to changes in the vicinity of the nanotube, and this sensitivity has been exploited for the optical detection of various binding events on the nanotube surface, including nucleic acid hybridization (Figure 4.3a).[71, 72, 201, 211] Nonetheless, no direct evidence of DNA hybridization was provided. Here, Figure 4.3b shows a NIR response red-shifting of the $(GT)_{10}$-A1-SWCNT emission on hybridization of cDNA (see Figure S4.11 for full spectrum). In contrast, no shifting was observed in the absence of cDNA or in the presence of non-complementary DNA. The de-convoluted emission spectrum shows that the dominant (7,6) chirality exhibits a 0.7–0.8 nm red-shift in the presence of complementary $(GT)_{10}$-A1/a1 and $(GT)_{10}$-A2/a2 pairs (Figure 4.3c, top) compared to negative controls in the absence of cDNA and in the presence of non-complementary DNA. This shifting is in agreement with the QF assay results shown in Figure 4.1c which show a significant QF fluorescence response for $(GT)_{10}$-A1/a1 and $(GT)_{10}$-A2/a2 hybridization pairs in the presence of SWCNTs.

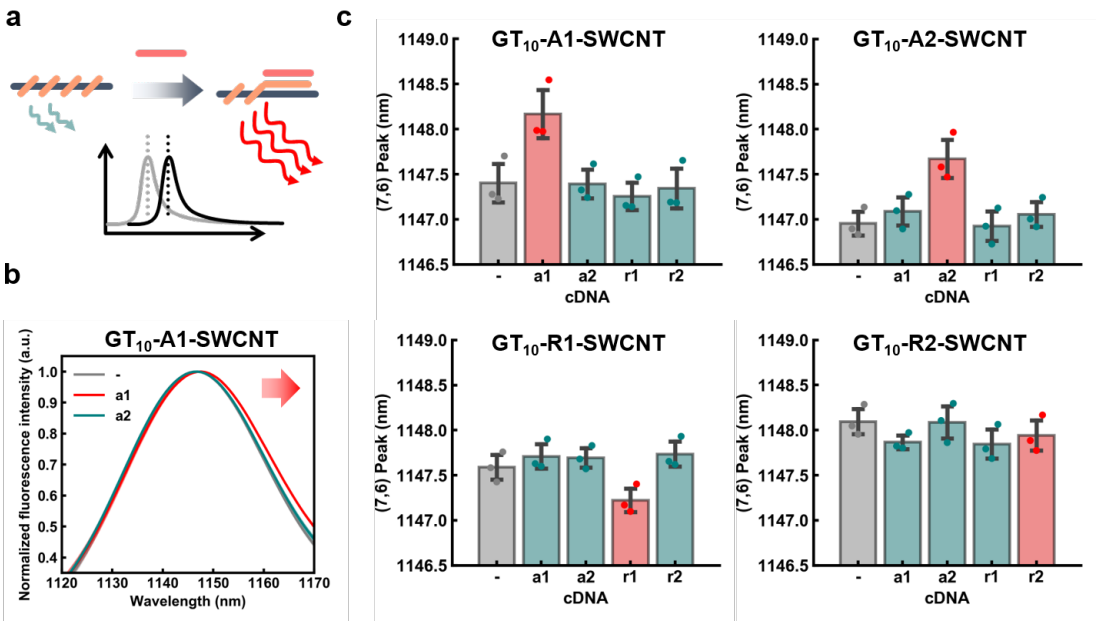

Figure 4.3 – SWCNT NIR-fluorescence responses to DNA hybridization. (a) Schematic depiction of NIR modulation upon DNA hybridization on the SWCNT surface. (b) A typical NIR fluorescence spectrum of $(GT)_{10}$-A1-SWCNT. The figure shows the peak of the dominant species (7,6). A clear red shift is observed in the presence of cDNA (a1) (red curve) compared to the case when no cDNA is present (black curve) or when non-complementary DNA (a2) is added (blue curve). The full spectrum can be found in Figure S4.11. (c) Peak maxima of the (7,6) chirality following spectral deconvolution and Lorentzian fitting. All samples were thermally annealed at 60 °C in SSC buffer. The red bar represents the fluorescence after annealing with the corresponding cDNA, the grey bar represents the fluorescence without cDNA, and the blue bars represent fluorescence with non-complementary DNA. All fluorescence spectra were recorded under 660 nm excitation. Error bars represent standard deviation of independent triplicates.

Interestingly, we observe a sequence dependence on this NIR response. Unlike the $(GT)_{10}$-A1/a1 and $(GT)_{10}$-A2/a2 pairs, the $(GT)_{10}$-R1/r1 leads to a 0.5 nm blue-shift of the (7,6) emission, while $(GT)_{10}$-R2/r2 pair exhibits no shifting compared to the negative controls (Figure 4.3c, bottom). This suggests that the SWCNT fluorescence response to hybridization (see Figure S4.12 for hybridization assays of $(GT)_{10}$-R1/r1 and $(GT)_{10}$-R2/r2 pairs) is not universal even with sequences having the same GC content and sequence length (Table 4.1). Additionally, the fluorescence response is chirality-dependent (response of (9,4) chirality shown in Figure S4.13). We hypothesize that the difference between these sequences and/or chiralities may originate from the formation of secondary structures on the SWCNT surface, which can possibly lead to a difference of reference point (see all (-) conditions in Figure 4.3c). These could be revealed by further molecular dynamics simulations in the future. Nevertheless, the results suggest that such platform could be applied for the multimodal sensing of different nucleic acid sequences.

This is the first experimental evidence directly showing that SWCNT fluorescence and DNA hybridization are not necessarily correlated. These findings are in contrast to the studies by Harvey et al.[72] and Jeng et al.,[71, 201] which report a sequence-independent blue-shifting of SWCNT fluorescence due to a decrease in negative charge or a denser DNA packing on the SWCNT following hybridization. We hypothesize that the discrepancy comes from (1) non-specific adsorption of the non-complementary DNA due to non-optimized annealing condition, and/or (2) residual of unbound ssDNA from the sample preparations.

To verify this hypothesis, we incubated a1 sequence modified by fluorescein dye at the 3'-end (a1-3'FAM) with two ssDNA-SWCNT complexes: $(GT)_{10}$-A1 and $(GT)_{10}$-R1. As the fluorescence of FAM was shown to be quenched by SWCNT,[135, 215, 216] we are able to determine whether the cDNA sequence was interacting with the SWCNT (Figure 4.4a). We used SC-suspended SWCNT as reference, which has been shown to exclude analyte at high surfactant concentration[217] (i.e. no DNA adsorption on SWCNT, no FAM quenching) labelled as "high SC", while it is able to exchange with DNA at low surfactant concentration[218] (i.e. DNA replace SC onto SWCNT, closest adsorption) labelled as "low SC". When compared with the high SC case, both $(GT)_{10}$-A1- and $(GT)_{10}$-R1-SWCNT show a quenching in the fluorescence of a1-3'FAM to a similar extent (Figure 4.4b). This decrease in fluorescence is close to the low SC case, even though $(GT)_{10}$-R1 has no specific pairing with a1-3'FAM. Since SC has insignificant influence on FAM fluorescence (Figure S4.14), we confirm that the FAM quenching is due to the adsorption of a1-3'FAM on SWCNT surface regardless of the sequence.

These results confirms a significant non-specific adsorption of DNA on SWCNT, which can further change the SWCNT fluorescence due to screening effect,[211] charges redistribution,[219] and/or increase of surface coverage.[220] Consequently, analyses and proposed mechanisms in previous studies may be biased. Moreover, as we show in Figure 4.3 and Figure S4.13, different sequences and different chiralities exhibit diverse fluorescence responses. Since no general rule is readily applicable, we therefore suggest to apply the nuclease-assisted fluorescence assay described in this work, in order to properly determine the correlation

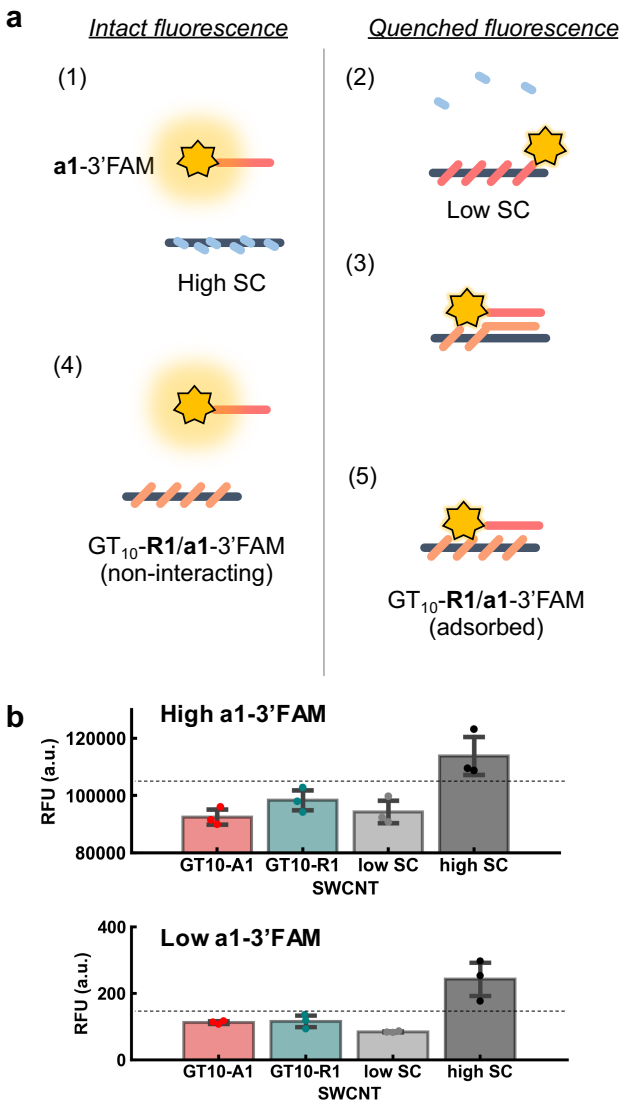

Figure 4.4 – FAM quenching experiments reveal non-specific adsorption of non-complementary DNA on ssDNA-SWCNT. (a) Cartoons of two different scenarios. For the complementary pair (A1/a1), the fluorescence of a1-3'FAM should be quenched due to close vicinity to SWCNT. For the non-complementary pair (A1/r1), if a1-3'FAM does not adsorb on ssDNA-SWCNT, the fluorescence of FAM remains unchanged (left case). However, if a1-3'FAM adsorbs on ssDNA-SWCNT, the fluorescence of FAM should be quenched. (b) Fluorescence of a1-3'FAM in the presence of different SWCNT suspensions. a1-3'FAM show similar fluorescence quenching effect in $(GT)_{10}$-A1, $(GT)_{10}$-R1, and low SC. Excitation wavelength = 480 nm. Error bars represent S.D. of independent triplicates.

between hybridization and SWCNT fluorescence for future applications.

4.3 Conclusions

Previous reports have relied on the blue-shifting of the NIR fluorescence of SWCNTs to confirm dsDNA hybridization on the nanotube surface. However, in this study, we observe a sequence-dependent NIR response of the SWCNT that has not been previously reported. In particular, whereas the R1/r1 hybridization pair confers a blue-shifting of the nanotube fluorescence, the R2/r2 hybridization pair and the A1/a1 and A2/a2 hybridization pairs show no shifting and even red-shifting responses, respectively. This sequence dependence responsivity is attributed to the non-specific adsorption of ssDNA onto the nanotube complex, which has been shown to interfere with the NIR responsivity.

In contrast to the NIR optical measurement, the S1 nuclease-assisted fluorescence assay developed in this study was used to successfully characterize dsDNA hybridization on the SWCNT. The S1 nuclease was used to digest unhybridized ssDNA to eliminate contributions from nonspecific ssDNA interactions. This assay was applied to DNA sequences that lack RE cut sites, allowing a versatile means for studying a diverse range of sequences compared to the electrophoresis assay developed in previous studies.[31] The increased throughput of this assay allowed us to probe a diverse range of hybridization conditions to optimize dsDNA immobilization onto the nanotube surface. Our result show maxmimum immobilization in the presence of a high excess of cDNA, high annealing T, and overnight incubation in the presence of high salt (e.g. SSC).

4.4 Methods and Experiments

Materials. All oligonucleotides were purchased from Microsynth. Lyophilized DNA was re-dissolved in ddH_2O as indicated by the supplier. The DNA concentration was adjusted using a Nanodrop spectrometer. The DNA sequences are summarized in Section 4.5. High-pressure carbon monoxide (HiPCO) SWCNTs were purchased from NanoIntegris (lot number: HP29-064). SWCNTs were suspended in 2 wt% sodium cholate (SigmaAldrich) as described in Section 4.5.

Suspension of SC-SWCNTs. 5 mg of SWCNTs (NanoIntegris) was mixed with 0.2 g of sodium cholate (SigmaAldrich, BioUltra) dissolved in 20 mL ddH_2O in a 50 mL Falcon tube. The mixture was homogenized at 5000 rpm for 30 min. prior to ultrasonication with a QSonica Q500 with a 6.4 mm tip at an amplitude of 40% for 30 min in ice bath. The resulting suspension was pre-centrifuged at 10000 rpm for 1 h at room temperature (Beckman, fixed angle) in order to remove the majority of the non-suspended SWCNTs and catalyst. The supernatant was collected and centrifuged once more at 30000 rpm for 1 h at room temperature (Beckman). The supernatant was collected and stored at room temperature. The resulting absorption and fluorescence spectra are shown in Figure S4.1.

Preparation of ssDNA-SWCNTs. The ssDNA-SWCNTs were prepared using a modified SC-DNA exchange method (Figure S4.1a for scheme).[89] Briefly, a 2 wt% SC-SWCNT suspension

was prepared (see Section 4.5 for details) and mixed with ssDNA and methanol in a 1:1:3 volume ration with a total volume of 1 mL. A 10-fold excess of ssDNA was added to a 8 mg/L solution of SWCNTs to ensure SWCNT solubilization. The mixture was incubated in a 1.5 mL Eppendorf tube for 1 h at room temperature. The solution was then transferred to a 15 mL Falcon tube with the addition of 400 mM NaCl and 5 mL cold ethanol and incubated at -20 °C for 30 min. to pellet the ssDNA-SWCNT. The pellet was collected by centrifugation at 3220 rcf for 10 minutes at 4 °C and resuspended in 1 mL of 70% ethanol in a 1.5 mL Eppendorf tube. After centrifugation at 21130 rcf for 1 min at room temperature, the solution was decanted and the pellet was dried for 30 min under ambient conditions. The resulting ssDNA-SWCNT pellet was resuspended in 500 μL ddH_2O and stored at 4 °C. The concentration of SWCNTs was adjusted to 40 mg/L with ϵ_{632} = 0.036 L mg^{-1} cm^{-1}.

Purification of ssDNA-SWCNTs. S1 nuclease (ThermoFisher, EN0321) was used to digest free DNA in the reaction solution. 50 U of S1 nuclease was introduced to ssDNA-SWCNTs in 0.5× reaction buffer (20 mM sodium acetate (pH 4.5 at 25 °C), 150 mM NaCl and 1 mM $ZnSO_4$). EDTA (5 mM, pH 8) was used to quench the reaction after incubating at room temperature for 90 minutes. The reaction was subsequently ultrafiltrated with an Amicon Ultra-0.5 (MWCO = 100 kDa) at 4000 rcf for 2 min at room temperature and resuspended with ddH_2O to a final volume of 500 μL. This washing step was repeated 6 times. The resulting ssDNA-SWCNT sample was resuspended in ddH_2O and characterized with absorption and NIR fluorescence spectroscopies (see Section 4.5 for additional details.)

S1-assisted fluorescence assay pre-treatment. Starting reaction solutions had a volume of 50 μL and a SWCNT concentration of 0.4–0.5 mg/L. The reaction solutions were mixed in either 1.5 mL Eppendorf tubes or PCR tubes. The temperature was controlled by a thermal cycler (GE Healthcare or Eppendorf).

For the pre-treatment of kinetic experiment shown in Figure 4.2b, all reaction solutions were heated to 60 °C for 5 min and quenched to 20 °C for hybridization. The hybridization was stopped by introducing S1 nuclease after t min, and the sample was digested for 30 min in the presence of the nuclease. The QF fluorescence assay was performed following digestion.

For the pre-treatment of annealing temperature experiments shown in Figure 4.2c, all reactions were heated to 60 °C for 5 min. The reaction solutions were then cooled to the selected annealing temperature (T_a) and incubated for 10 min. The S1 nuclease (50 U) was then introduced at $T = T_a$, and the reaction was incubated for 30 min. The reaction was then brought to room temperature to perform the QF fluorescence assay.

S1-assisted fluorescence assay. The general scheme of the assay is depicted in Figure 4.1a. Following the specific treatments described above to remove free DNA and to stop hybridization, 50 μL of the reaction mixture was incubated with 50 U of the S1 nuclease (Thermo Fisher EN 0321) for 30 min at room temperature in 1x reaction buffer (40 mM sodium acetate (pH 4.5 at 25 °C), 300 mM NaCl and 2 mM $ZnSO_4$) in a total volume of 100 μL. The mixture was then transferred to a 96-well plate (Corning EIA/RIA), and 10 μL of 1:200 diluted QuantiFluor

(Promega, E2671) in 1× TE buffer was introduced and mixed by pipetting. After 5 min of incubation at room temperature, the fluorescence of dye was measured using a Varioskan under top-reading mode (exc. 500 nm, bandwidth = 5 nm). The RFU was defined as the integrated area under the curve spanning from 520 to 700 nm using OriginPro software.

NIR fluorescence and analysis. The ssDNA-SWCNT/cDNA samples were thermally annealed under the optimized conditions (i.e. annealed at 60 °C followed by gradually cooling down to room temperature) with a final cDNA concentration of 36 uM and SWCNT concentration of 3 mg/L. The SWCNT fluorescence was measured using a custom-built inverted Nikon Eclipse Ti-E microscope (Nikon AG Instruments) described previously.[114] In brief, 40 μL of the mixture was placed in a flat-bottomed, 384-well plate (ThermoFisher, Nunc Maxisorp). The samples were excited at 660 or 730 nm (NKT SuperK with VARIA grating) with a 10 nm bandwidth and 5 s exposure time. The NIR epifluorescence was directed through a long-pass filter (Semrock, LP 830 nm), dispersed by a spectrometer (Princeton Instruments, grating: 70 lines mm^{-1}), and collected by an InGaAs camera (Princeton Instruments, NIRvana 640) for wavelengths spanning from 898 to 1399 nm. A custom Python script was then used for data processing. The transmittance-corrected spectrum was smoothed using the Savitzky-Golay algorithm and deconvoluted with eight Lorentzian peaks.

FAM quenching experiment. The SWCNT suspension (SWCNT: 8 mg/L) was mixed with a1-3'FAM (high: 15.8 μM, low: 15.8 nM) in 1× SSC (ThermoFisher). High and low concentrations of SC-SWCNTs were prepared with SC concentrations of 46 mM and 2 mM, respectively. The mixtures were thermally annealed at 60 °C for 5 min, followed by gradual cooling to room temperature and overnight incubation. The fluorescence of the FAM was measured with a plate reader (Varioskan LUX, Thermo Scientific) in top-reading mode (exc. 480 nm, bandwidth = 5 nm). The RFU was defined as the integrated area under the curve between 510 and 700 nm using OriginPro software.

4.5 Supporting Information

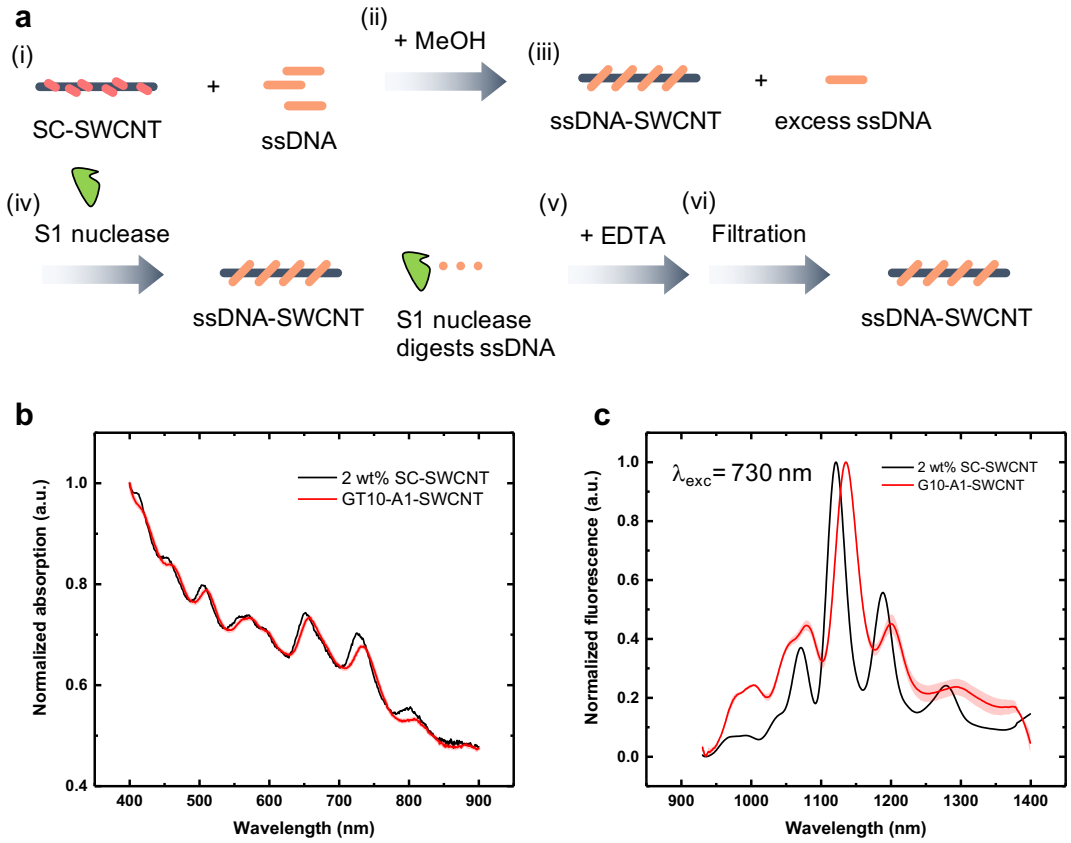

Figure S4.1 – ssDNA-SWCNT preparation by SC-DNA exchange method. (a) Scheme of the method. (i) The SC-SWCNTs mixed with ssDNA. (ii) Upon addition of methanol, (iii) the ssDNA replaces the SC on the SWCNT surface. (iv) The introduction of S1 nuclease is used to digest the excess unbound ssDNA. (v) EDTA is added to quench the nuclease activity. (vi) The mixture was then filtrated to remove the nuclease and digested ssDNA. (b) Visible-NIR absorption spectrum. The black curve represents the SC-SWCNTs (before exchange) and the red curve represents the $(GT)_{10}$-A1-SWCNTs (after exchange). (c) Normalized NIR fluorescence spectrum under 730 nm excitation. The black curve represents the SC-SWCNTs (before exchange) and the red curve represents the $(GT)_{10}$-A1-SWCNTs (after exchange).

To estimate the DNA degradation and its amount on SWCNT, SDBS was used to replace all ssDNA on SWCNT. The amount of ssDNA was then calculated based on the calibration curve (RFU (a.u.)= 7.2E4 [ssDNA] (uM) + 1.1E2) in Figure S4.10.

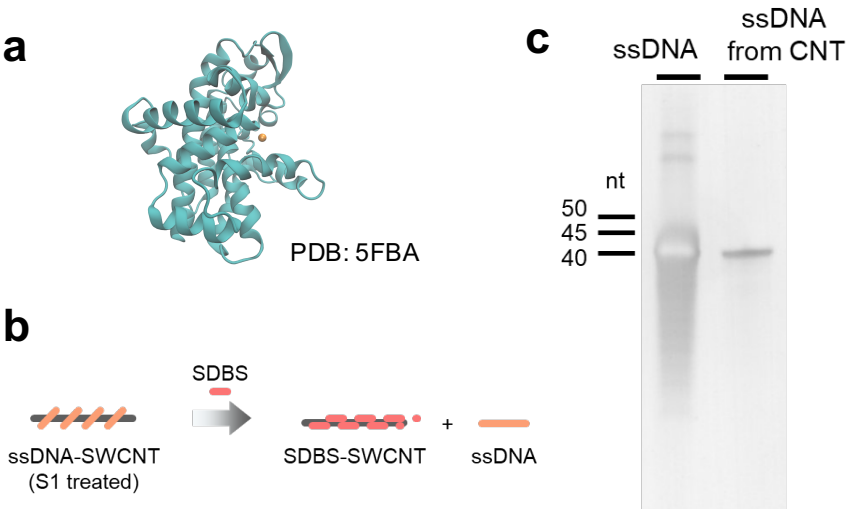

Figure S4.2 – (a) Structure of S1 nuclease (pdb: 5FBA) includes a central zinc cation colored in orange. (b) Scheme for SDBS replacement experiment. The replacement is used to recover the ssDNA from SWCNT for gel characterization. (c) 12% Denaturing-PAGE shows ssDNA ($(GT)_{10}$-A1, 39 nt) extracted from SWCNT remains intact after interaction between ssDNA-SWCNT and S1 nuclease.

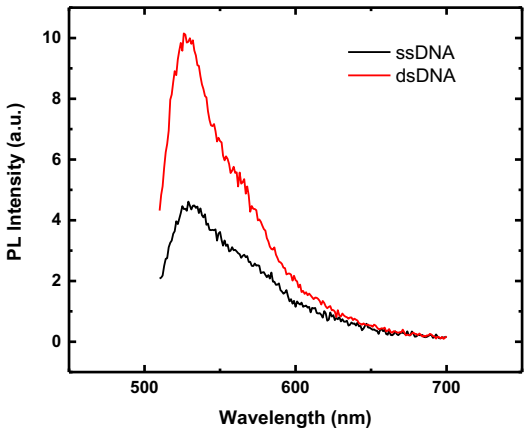

Figure S4.3 – Visible fluorescence spectrum shows that the QF fluorescence dye also binds to ssDNA at 140 nM.

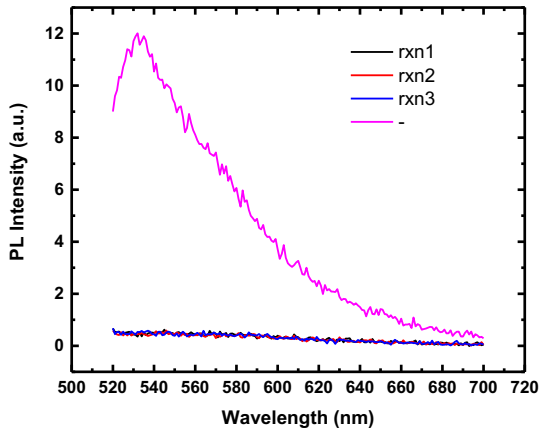

Figure S4.4 – Fluorescence spectrum shows no signal from cDNA after digestion by S1 nuclease. The QF fluorescence is shown in the presence of cDNA without S1 nuclease (pink curve) or after digestion by S1 nuclease (black, red, blue curves) after 30 min. Initial concentration of cDNA = 9.6 uM. Excitation wavelength = 500 nm.

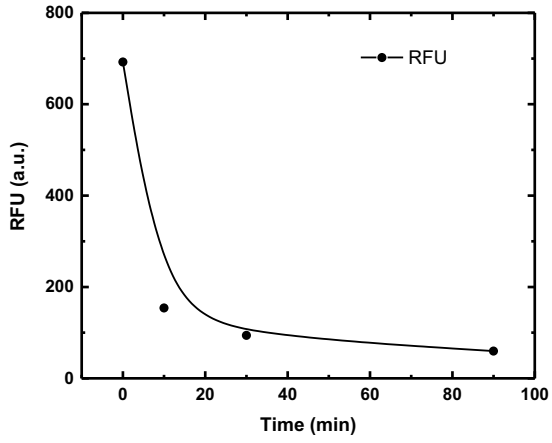

Figure S4.5 – DNA (a1) is 92% digested by S1 nuclease in SSC buffer at room temperature in the presence of SWCNT.

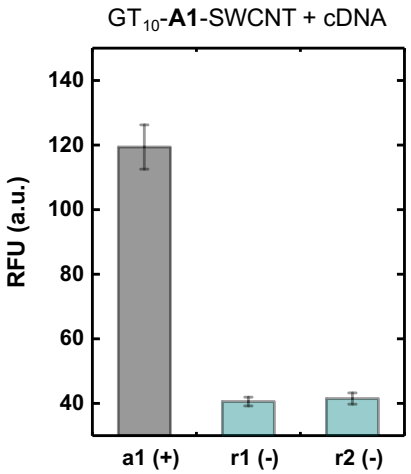

Figure S4.6 – The DNA hybridization of sequences of $(GT)_{10}$-A1-SWCNT is specific to the complementary a1 sequence and cannot hybridize with r1 nor r2 (see Table 4.1), which show no fluorescence in comparison with positive control (a1).

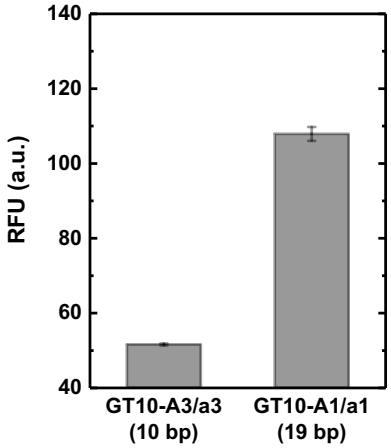

Figure S4.7 – Short sequences show significantly lower fluorescence in the assay.

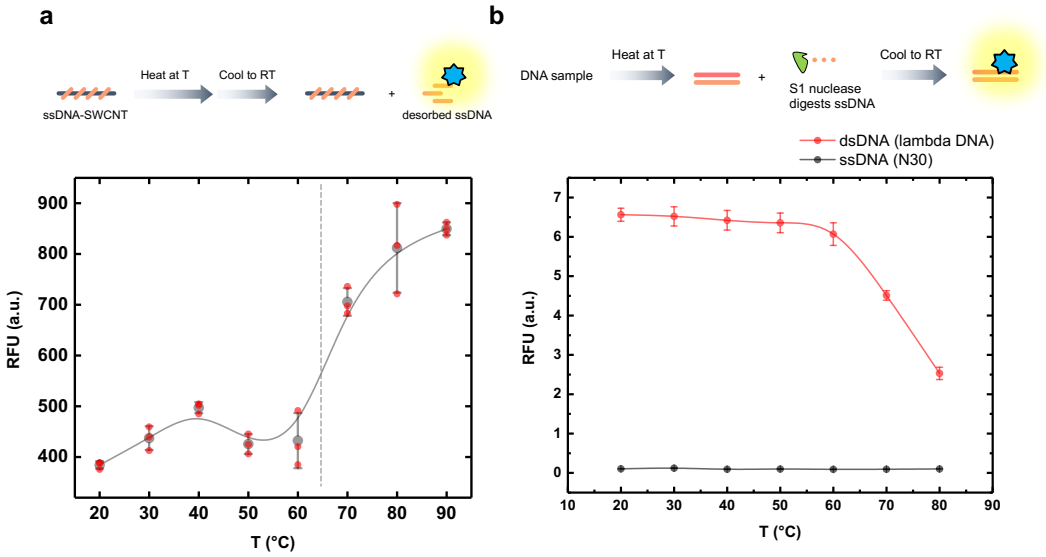

Figure S4.8 – Thermal stability of the assay. (a) ssDNA does not desorb from the SWCNT below 60 °C. The ssDNA-SWCNT is heated between 20 to 90°C and the QF fluorescence is considered proportional to the presence of concentration of ssDNA. (b) The S1 nuclease remains active up to 80 °C. The DNA sample (lambda dsDNA or N30 ssDNA) is heated between 20 and 80 °C and digested by S1 nuclease before the amount of dsDNA is assayed by the QF fluorescence.

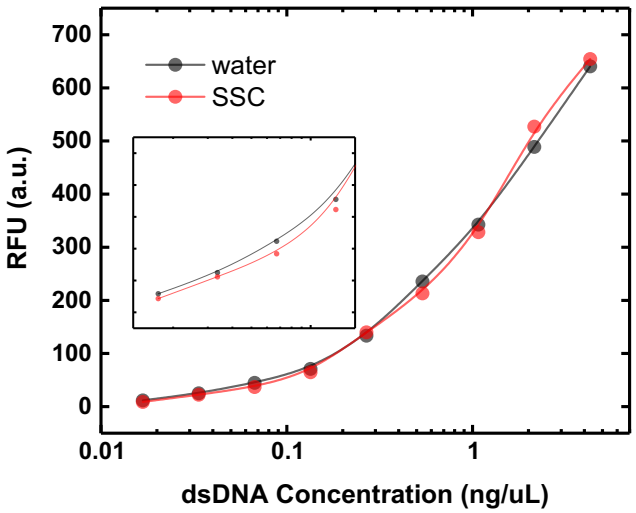

Figure S4.9 – Calibration curve of QF dye in different solutions. Lambda DNA (Sigma-Aldrich) was used as the dsDNA standard.

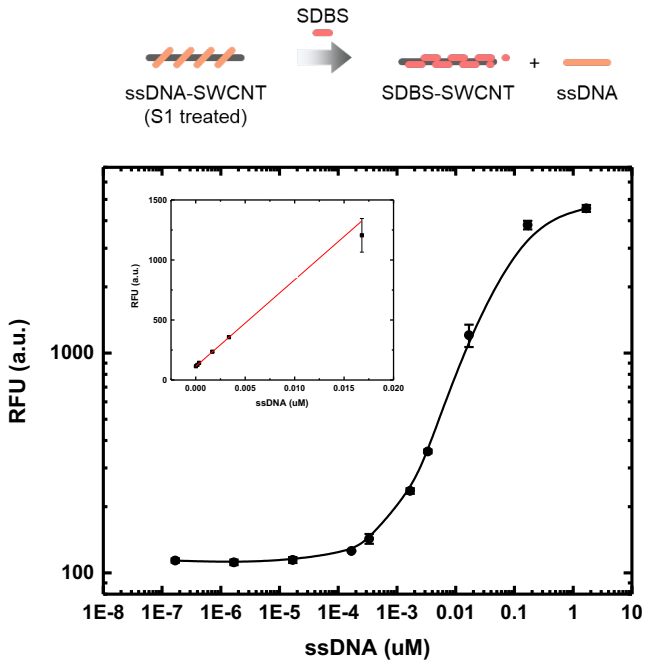

Figure S4.10 – Calibration curve of ssDNA was used to estimate the amount of ssDNA on the SWCNTs.

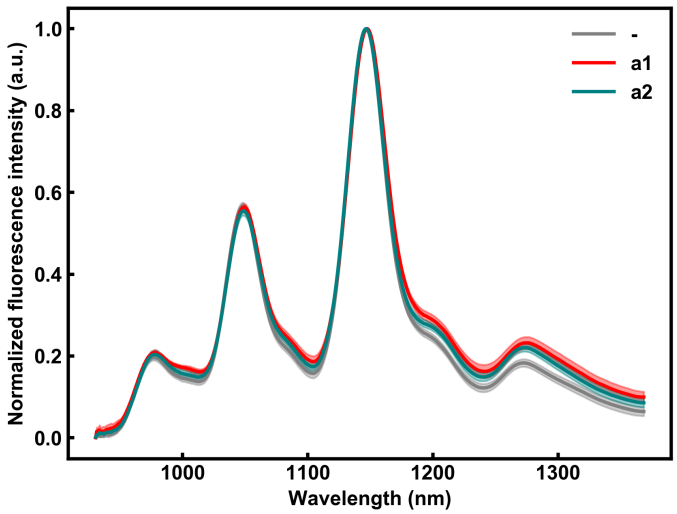

Figure S4.11 – Fluorescence spectra of $(GT)_{10}$-A1-SWCNT excited at 660 nm in the presence of a1 (red), a2 (blue) and no (gray) added DNA.

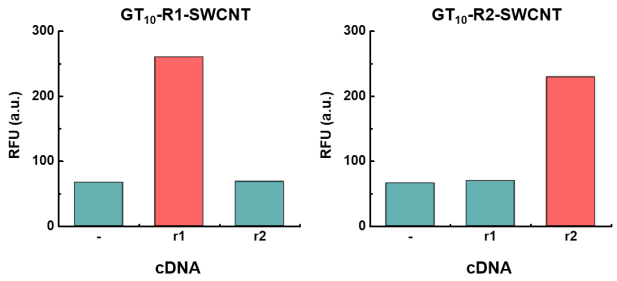

Figure S4.12 – DNA hybridization of $(GT)_{10}$-R1/r1 and $(GT)_{10}$-R2/r2 pairs are sequence specific. The relative fluorescence unit (RFU) is defined as the integrated area under the fluorescence curve between 520 nm and 700 nm. All fluorescence spectra were taken at 500 nm excitation.

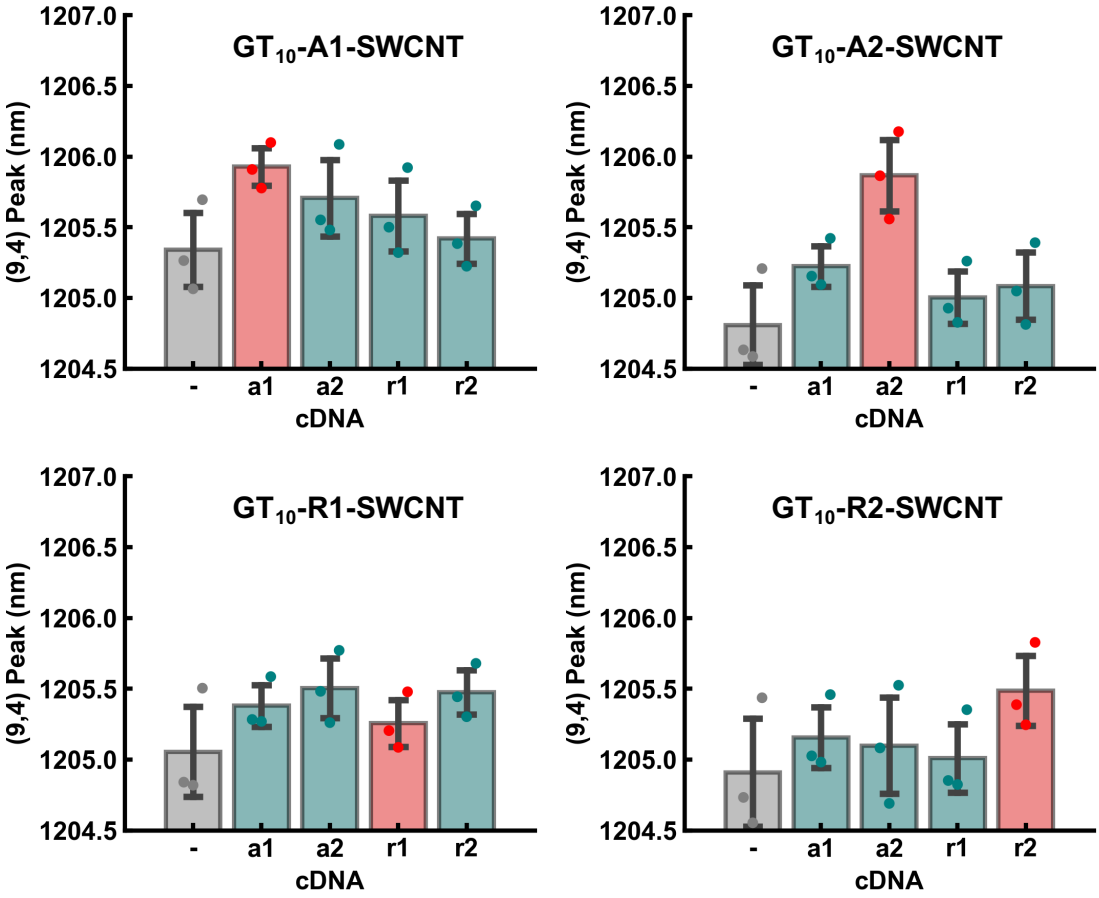

Figure S4.13 – Peak maxima of (9,4) chirality at 730 nm excitation.

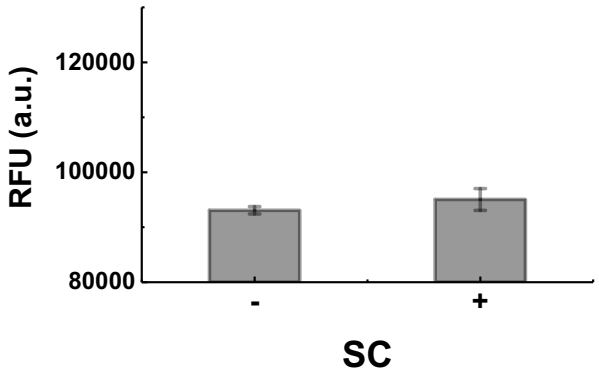

Figure S4.14 – SC does not contribute to FAM fluorescence change.

5 A Ternary System Based on Protein-dsDNA-SWCNT Interactions

This Chapter is adapted from a manuscript prepared for submission in a journal with co-authors:
Shang-Jung Wu and Ardemis A. Boghossian.

5.1 Introduction

Proteins play a key role in life's essential processes. Both commercial and academic advancements have therefore focused on developing a slew of techniques focused on probing protein behavior,[6, 221] understanding their mechanisms,[6, 221] and exploiting their activities in a wide range of biomedical technologies.[222] Optical techniques in particular benefit from high-throughput measurements, non-invasive and remote probing, as well as multi-modal capabilities that allow one to detect multiple proteins or activities simultaneously using different wavelengths of light.

The fluorescence emissions of single-walled carbon nanotubes (SWCNTs) offer a powerful optical platform for probing protein behavior and interactions.[199, 221] SWCNTs emit near-infrared fluorescence that can optically penetrate biological tissue and fluids that are otherwise opaque to visible light. This penetrability makes SWCNTs not only useful for deep-tissue optical imaging and sensing applications in vivo but also for optically characterizing autofluorescent proteins. Furthermore, the emission wavelengths vary with the nanotube's diameter, enabling multi-modal optical measurements using nanotubes of different diameters simultaneously. Since these fluorescence emissions are sensitive to even the slightest perturbations in the immediate environment of the nanotube, the nanotube serves as a necessary scaffold for controlling the specificity of the biomolecular interactions occurring on its surface. The specificity and selectivity of these interactions is typically achieved through the appropriate immobilization of biomolecules.

Various strategies have been developed for immobilizing different proteins onto the surface of SWCNTs.[35, 86, 112, 114, 137, 138, 148, 223, 224] These strategies often take advantage

of the high protein selectivity and biocompatibility, as well as non-covalent functionalization approaches that preserve the SWCNT fluorescence, to create selective optical sensors.[86, 114] Most strategies rely on the non-specific adsorption of proteins onto the nanotube surface. Though this approach provides a simple, scalable means of immobilizing proteins,[112, 114] it suffers from poor long-term suspension stability and susceptibility to protein denaturation. Furthermore, this approach yields a heterogeneous mixture of protein orientations on the nanotube surface that often compromises applications that require controlled protein orientation. Alternative strategies have focused on site-directed protein conjugation either to a linker or biopolymer such as single-stranded DNA (ssDNA) that is non-covalently adsorbed onto the nanotube surface[137, 148, 223] or to a functional group on the nanotube that preserves the SWCNT fluorescence.[224]

In this study, we develop a ternary nano-biohybrid system for conjugating proteins and probing their interactions on the nanotube surface using double-stranded DNA (dsDNA) (Figure 1a). The protein-dsDNA interactions play a critical role in vital cell processes such as DNA replication, cell division, and gene expression, as well as biotechnological advancements such as Cas9 genome editing based on clustered regularly interspaced short palindromic repeats (CRISPR).[225, 226] Expanding on our previous efforts focused on immobilizing dsDNA onto SWCNTs,[31] we herein propose two approaches for protein immobilization based on DNA hybridization (Figure 1b) and dsDNA protein binding (Figure 1c). In the first approach, we demonstrate immobilization of an enzymatically active protein, horseradish peroxidase, in a sequence-dependent manner via hybridization of a ssDNA tether with complementary ssDNA immobilized onto a nanotube surface. In the second approach, we demonstrate directed protein binding of a restriction enzyme, BamHI, and Cas9 to a target dsDNA sequence immobilized onto the nanotube surface. These immobilization strategies not only offer a multiplexed approach to conjugating various and even multiple enzymes, which is useful for optical nanotube sensors that rely on enzyme specificity and activity, but also an unprecedented optical nanotube platform for studying protein-dsDNA interactions.

5.2 Results and Discussion

We prepared the dsDNA-SWCNT/protein complex by hybridizing ssDNA-SWCNTs with a complementary DNA (cDNA)-protein conjugate as shown in Figure 5.2a. The preparation of ssDNA-SWCNT complex and additional details on the DNA sequences used are provided in Chapter 4 and the Section 5.5. 5'-biotin-cDNA conjugated with streptavidin-Cy3 (SA-Cy3) was selected as a model system for the cDNA-protein complex. Following assembly, we performed an electrophoretic mobility shift assay (EMSA) to examine whether the cDNA-protein complex was formed. The reduced mobility of the cDNA-biotin in the presence of SA indicated successful conjugation (Figure 5.2b), while no significant perturbation was observed for cDNA without biotin indicating that it was not impacted by the presence of SA. Notably, the cDNA-biotin-SA ran slightly faster than isolated SA, which we attributed to the negative charge of the cDNA.[227] As no non-conjugated residual cDNA-biotin was detected by EMSA

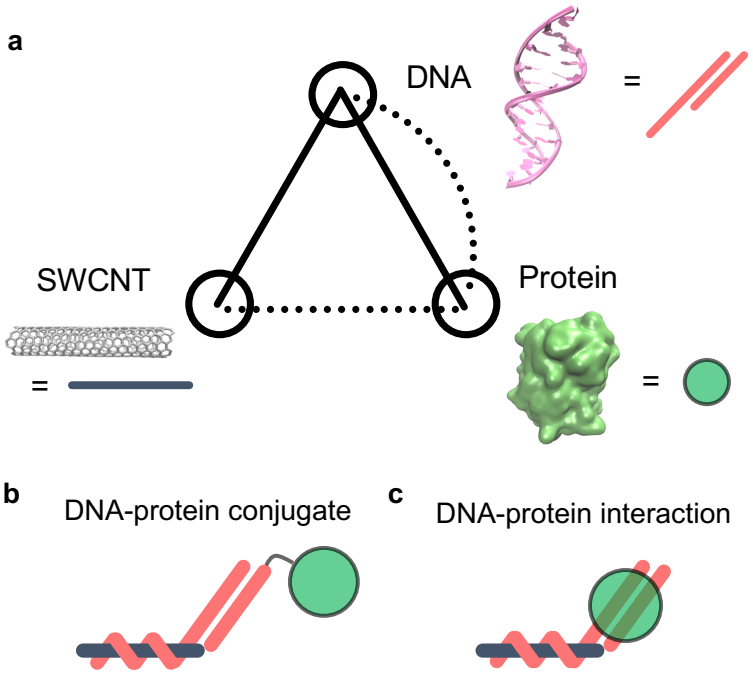

Figure 5.1 – (a) Scheme of the DNA-protein-SWCNT ternary hybrid system. Solid lines indicate a strong, specific interaction while dashed lines indicate a weak, non-specific interaction. The DNA and SWCNT interact via $\pi - \pi$ stacking of a ssDNA overhang and the sp^2 hybridized SWCNT surface. The protein–DNA interaction may either occur via (b) hybridization of ssDNA with a complementary strand that is bioconjugated to a protein or (c) via binding of protein to a targeted dsDNA sequence.

following incubation, conjugates for hybridization with ssDNA-SWCNT were used without further purification.

We performed a co-localization fluorescence assay to estimate the yield of dsDNA-SWCNT/SA-Cy3 hybrids. Using a custom-built fluorescence microscope,[228] SWCNTs were imaged in the NIR, while the position of SA was determined using the visible fluorescence of the Cy3 dye. Hybrids were constructed using the optimized conditions previously outlined in Chapter 4. Following hybridization, the dsDNA-SWCNT/SA-Cy3 sample was concentrated and washed using biotin-functionalized magnetic beads (Figure 5.2c). The beads were subsequently immobilized onto SA-functionalized coverslips for visualization.

As shown in Figure 5.2d, we observe co-localization of the SWCNT and SA-Cy3 fluorescence signals for GT10-A1/a1, which is able to form dsDNA as we previously showed (Chapter 4). On the contrary, samples incapable of forming dsDNA (GT10-R2/a1) show reduced levels of colocalization. To quantitatively assess these results, we further calculated the Manders co-localization coefficient (MCC)[229, 230] for the images with respect to the NIR

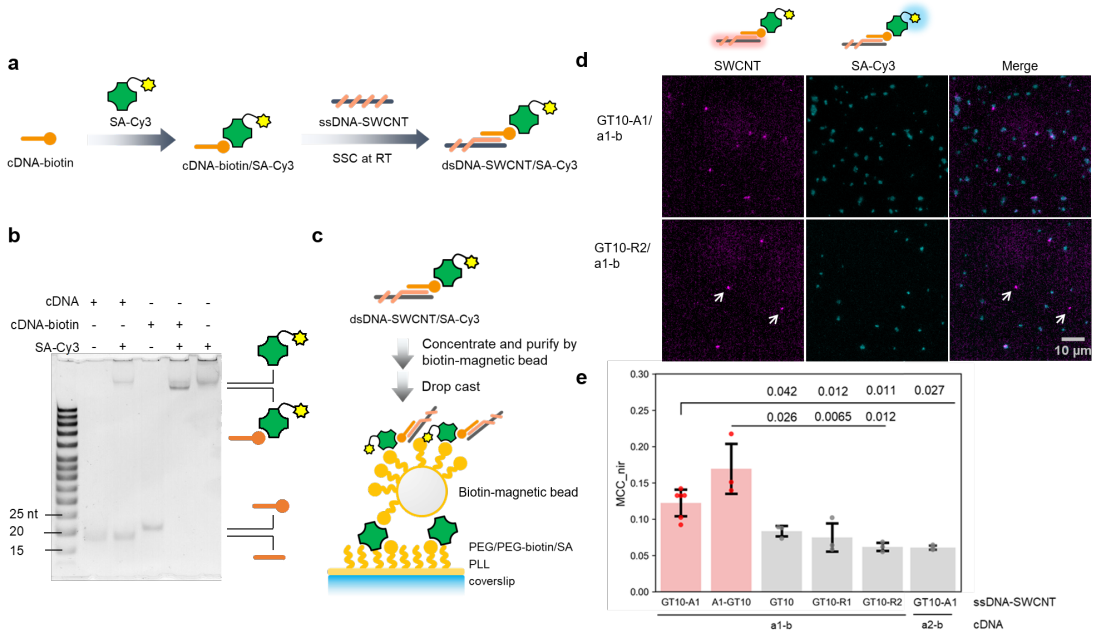

Figure 5.2 – dsDNA is used for bridging protein and SWCNT. (a) Schematic cartoon of the method. The cDNA is conjugated to the streptavidin-Cy3 (SA-Cy3) protein complex by biotin-SA interaction. The cDNA is then hybridized to the ssDNA-SWCNT complexes. (b) 12% native-PAGE reveals the conjugation of cDNA-biotin and SA-Cy3. (c) Scheme of the sample preparation prior to microscopy measurements. (d) Fluorescence microscope shows the co-localization of SA-Cy3 and SWCNT emissions if dsDNA is present. The arrows highlight where co-localization do not occur. (e) Image analysis shows the co-localization is sequence specific. The y-axis represents the Manders co-localization coefficient with respect to near-infrared signal from SWCNT (MCC_{NIR}) as defined in Equation 5.1. The numbers above each bar represent the p values of two-sample t-test.

signal of the SWCNTs, defined as

$$MCC_{NIR} = \frac{\sum_i NIR_{i,\,vis}}{\sum_i NIR_i} \tag{5.1}$$

where

$$NIR_{i,\,vis} = \begin{cases} NIR_i, & vis_i > 0 \\ 0, & vis_i = 0 \end{cases} \tag{5.2}$$

and NIR_i and vis_i is the intensity of pixel i above a predefined threshold (additional details are provided in Section 5.4). Although there may be non-specific adsorption of SA on ssDNA-SWCNT, (Figure S5.1), significantly higher MCC_{NIR} values were obtained for DNA pairs capable of forming dsDNA hybrids compared to the non-complementary pairs (Figure 5.2e). This observation suggests that the dsDNA greatly aids the specific immobilization of the SA onto the SWCNT, resulting in a significantly improved yield of immobilized protein.

To further probe whether the co-localization was a result of specific or non-specific binding, we compared the fluorescence emission distributions of SA-Cy3 and SWCNTs before and after the addition of urea. Urea is a denaturant of dsDNA (i.e., can separate the DNA bridge) however does not impact the streptavidin-biotin interaction.[231] Following the introduction of urea (5 M) the ssDNA-SWCNT is released, due to the denaturation of the linker, while the SA-Cy3 remains attached to biotin-magnetic bead and immobilized on the glass slide thanks to the streptavidin-biotin interaction (Figure 5.3a). This results in a significant decrease in the SWCNT fluorescence, while the Cy3 signal remains relatively constant (Figure 5.3b). As urea itself greatly enhances the fluorescence of ssDNA-SWCNTs (Figure S5.2), we can attribute the observed signal loss to the disruption of dsDNA and displacement of the ssDNA-SWCNT (Figure 5.3b). This further verifies that the conjugation of SA-Cy3 onto ssDNA-SWCNTs occurs via the formation of a dsDNA-bridge and is not simply the result of non-specific adsorption.

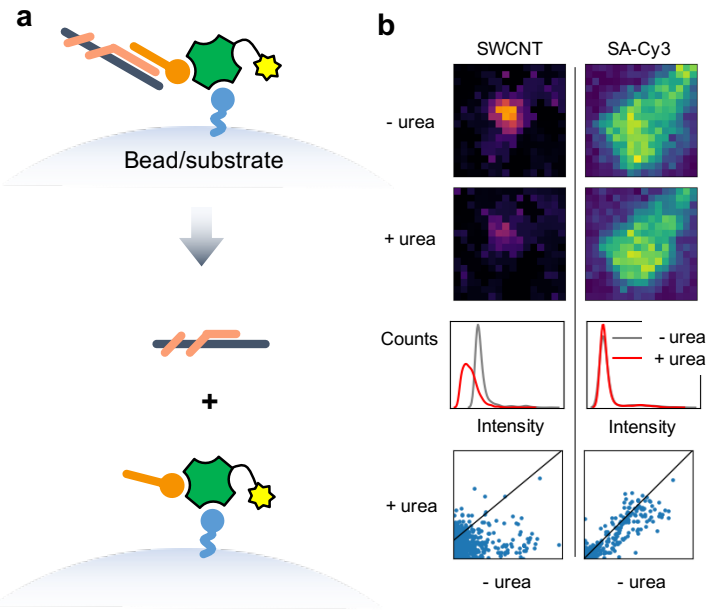

Figure 5.3 – (a) Urea denatures dsDNA and release SWCNT from immobilized SA-Cy3/biotin. (b) Single particle images (3.2 um × 3.2 um) and histogram of whole-field both show that SWCNT signal diminishes in the presence of urea. Before addition of urea: - urea. After addition of urea: + urea.

Based on these findings and to test the versatility of this platform, we sought to examine whether a nanosensor could be rationally designed to selectively detect a target analyte using a similar construction process. Horseradish peroxidase (HRP, Figure 5.4a), a heme-containing enzyme, was selected as a model system due to its ability to selectivity detect hydrogen peroxide (H_2O_2), an important reactive oxygen species (ROS). HRP specifically reduces H_2O_2 to water and oxidizes a substrate (Equation 5.3) with high turnover rate.

$$H_2O_2 + \text{substrate} \xrightarrow{\text{HRP}} H_2O + \text{substrate}^* \tag{5.3}$$

To assemble our sensor, we used SA-HRP to conjugate the protein to cDNA-biotin and subsequently hybridized this complex with the ssDNA-SWCNT (Figure 5.4a). The enzymatic activity of HRP was preserved in the vicinity of SWCNT, as confirmed by ABTS (2,2'-Azinobis(3-ethylbenzthiazoline-6-sulfonic acid)) assay (Figure 5.4b, see Section 5.4 for more detail).

We subsequently examined the hybrid's performance for H_2O_2 detection using fluorescent imaging. We first noticed that 1.5 uM of H_2O_2 generally quenches NIR fluorescence of ssDNA-SWCNT (Figure S5.3 for representative images). As incorporation of cDNA-biotin (hereon referred to as cDNA) and SA-HRP to the ssDNA-SWCNTs, we observed an enhancement of NIR fluorescence after addition of H_2O_2, contrary to the quenching observed for ssDNA-SWCNTs. Figure 5.4c shows the intensity distribution of the NIR fluorescence (violin plot) and average intensity (dot) over time for the four different combinations. While the ssDNA-SWCNT/cDNA-SA-HRP becomes significantly brighter following the addition of H_2O_2 (p = 4.9E-12 at t = 9 min), in the absence of either cDNA and/or SA-HRP the fluorescence intensity is quenched or remains unchanged. Similar trends were observed in independent replicates (Figure S5.4). Furthermore, only the ssDNA-SWCNT/cDNA-SA-HRP complex exhibited an enhanced normalized intensity both on average (Figure 5.4d) and in individual single molecule analysis (Figure 5.4e), further indicating that the successful assembly of the hybrid is required for the selective detection of H_2O_2.

While many dyes have been synthesized for tracking H_2O_2 in vivo, including several polymer functionalized-SWCNTs,[87, 232–235] our rationally designed hybrid is the first turn-on H_2O_2 SWCNT-sensor, which is beneficial for in vivo tracking. We believe that the fluorescence modulation of the SWCNT complexes following H_2O_2 addition can be attributed to two possible interaction mechanisms detailed further below.

Firstly, it is important to note that average fluorescence intensity of the cDNA-SA-HRP hybrid is initially about 60% lower compared to the control hybrid (Figure 5.4c, at t = 0). This decrease is attributed to the heme cofactor in the HRP, which contains a ferric cation (Fe^{3+}) capable of quenching SWCNT fluorescence (Figure S5.5). Similar quenching effects have been observed for other transition metals.[236] In accordance with this hypothesis, the addition of EDTA, to chelate the Fe^{3+} from the HRP, resulted in the successful recovery of the SWCNT fluorescence (Figure S5.6). In the presence of H_2O_2, HRP activity may result in a conformational change of the protein itself,[237–239] which in turn causes a change in its distance to the surface of the SWCNT. Due to the heme cofactor, as the protein moves away from the surface of the nanotube, so does the ferric cation. As a result, the SWCNT fluorescence could become less quenched, leading to the apparent increase in intensity.

The other possible mechanism is electron transfer, since it has been shown that slightly doped SWCNT has brighter fluorescence.[64] The electron rich SWCNT can possibly act as the substrate of HRP and be oxidized:

$$H_2O_2 + \text{SWCNT} \xrightarrow{\text{HRP}} H_2O + \text{SWCNT}^+ \tag{5.4}$$

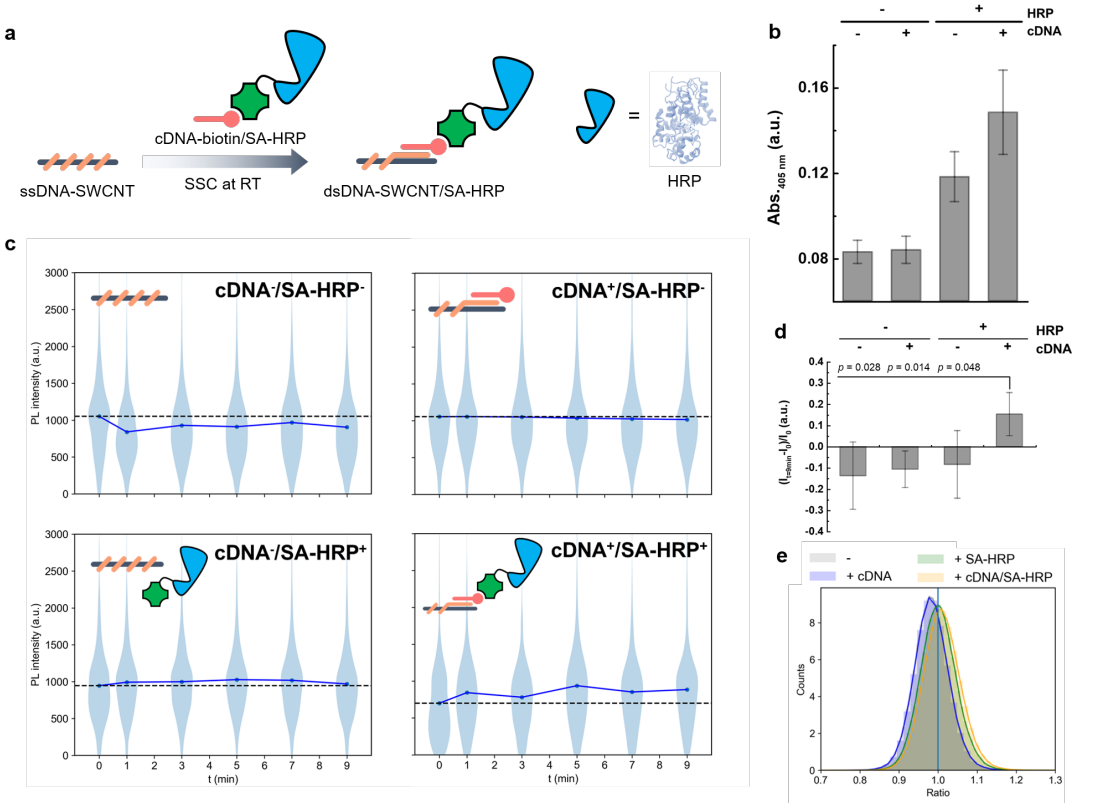

Figure 5.4 – Sensing applications of HRP immobilized on SWCNT through dsDNA. (a) Scheme of hybrid preparation. Crystal structure of HRP (PDB: 1GWU) is shown. A heme is embedded at the center of the protein. (b) ABTS assay confirms the activity of HRP remains intact in the presence of SWCNT. (c) Average of images over time. (d) Normalized intensity of t = 9 min. (e) Single molecule distribution at t = 9 min. Ratio is defined as $\frac{NIR_{i,t=9min}}{NIR_{i,t=0min}}$ for each pixel i.

The reduction potential of HRP intermediate (known as compound II, an oxoferryl species with Fe^{4+}) back to ferric state is +0.950 V,[240] while the oxidation potential of SWCNT (for chiralities in HiPCO) is around +0.4–0.6 V.[241] This indicates electron transfer in Equation 5.4 is thermodynamically favorable. However, Allen et al. found that HRP is not able to oxidize SWCNT even in the presence of 80 uM of H_2O_2 for 10 days.[242] They attributed to the non-desired orientation of HRP on pristine SWCNT leading to a distant HRP active site from SWCNT, as shown by MD simulation. Since HRP is linked to SWCNT by dsDNA in our hybrid, the enzyme has more degree of freedom in comparison with the case of pristine SWCNT. Therefore, dequenching effect and electron transfer are both plausible mechanisms in enhancing NIR fluorescence.

This work demonstrates the feasibility and widespread potential of dsDNA bridges to obtain such ternary hybrids. Importantly, our platform can also be used for enzymes that are not typically stable in the vicinity of SWCNTs. For example, in previous studies HRP was found to degrade on SWCNTs within 5 days.[127] However, using our method we were able to hybridize the enzyme before use and keep the enzyme viable in the hybrid system for extended

periods of time, which is not achievable by other protein-modification methods. Moreover, by choosing highly specific enzymes, these sensors bypass the extensive screening step that is often required for developing selective SWCNT sensors. However, we note that additional measurements are required to fully characterize the hybrid system and further elucidate the mechanism (e.g., pH dependence, H_2O_2 concentration dependence).

Finally, we demonstrated the use of dsDNA-SWCNTs as a sensor for monitoring DNA–protein interactions (depicted in Figure 5.1c).[221] As detailed in Chapter 3, our previous work has shown that a RE can cut dsDNA adsorbed onto the surface of SWCNTs, indicating that the DNA–protein interaction was not destroyed due to the presence of the SWCNT.[31] As shown in Figure 5.5, incubation of BamHI with a dsDNA-SWCNT hybrid containing the appropriate recognition dsDNA sequence (GT10-A2/a2-b) resulted in a decrease in the NIR fluorescence intensity (Figure 5.5a). Similarly to what was observed following the addition of urea (Figure 5.3a), we attributed this decrease in intensity to the release of the SWCNTs from the substrate (bead) due to the disruption of the dsDNA by the BamHI. In agreement with this hypothesis, the NIR fluorescence was preserved for the non-cognate sequence (GT10-R1/r1-b) with the slight increase ascribed to the reducing agent present in the storage buffer of BamHI.

There is additional interest in studying the dsDNA-protein interaction with Cas9 and so we sought to investigate the applicability of our platform for this purpose. The CRISPR-Cas system has been extensively studied over the past decade due to its potential for precisely controlled genomic modification.[43] One variants, Cas9, is a single-turnover endonuclease that targets and cuts at specific DNA loci determined by the sequence of an accompanying scaffold guide RNA (sgRNA). Importantly, a protospacer adjacent motif (PAM) upstream in the DNA sequence is required to initiate Cas9-sgRNA binding.[243]

Figure 5.5b shows the working principle of the proposed Cas9-platform. The non-target strand (NT) was anchored to the SWCNT using a $(GT)_{10}$ overhang, while the complementary target strand (T) was hybridized through the annealing protocol described in the previous section. As shown in Figure 5.5b, the PAM site was designed closer to the anchoring sequence $(GT)_{10}$. Two other sequences, a scrambled sequence (R) and a target sequence without the PAM site (NT-nP), were used as control sequences. Further sequence information is provided in Table 5.2. The sgRNA for the target dsDNA (NT/T) was transcribed in vitro using the cloned plasmid as described in the Supplementary Information (Figure S5.7). The resulting sgRNA was capable of complexing with Cas9 and successfully cut the specific dsDNA in the absence of SWCNTs (Figure S5.8). As shown in Figure S8a, all the resulting cut products have the correct sizes, while the negative controls (R and NT-nP) do not exhibit any cutting events. Notably, despite excess Cas9-sgRNA complex, we noticed a lower endonuclease activity for the oligonucleotides compared to genomic DNA and plasmid DNA, which we attributed to the reduced binding probabilities for Cas9-sgRNA on short oligonucleotide sequences.[225]

Limited activity was observed following the introduction of Cas9-sgRNA to the dsDNA-SWCNT hybrid (Figure S5.9). We attribute this to the lower accessibility of dsDNA in the vicinity

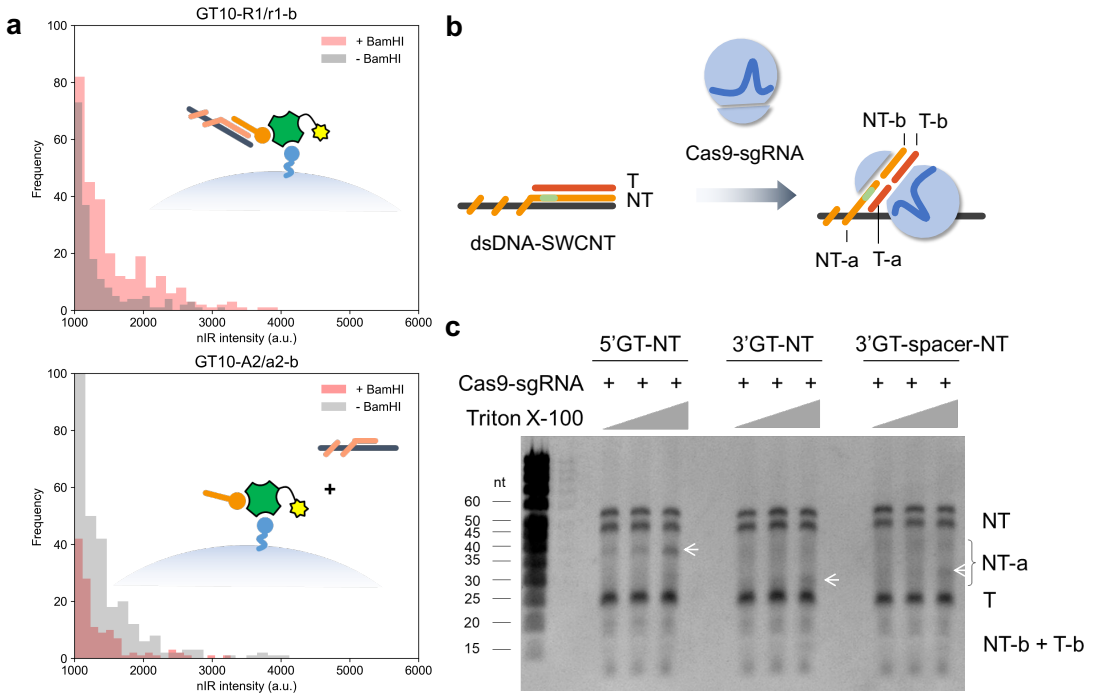

Figure 5.5 – DNA-protein interaction is preserved in the proximity of SWCNT on SWCNT. (a) Restriction enzyme, BamHI specifically cuts A2/a2. (b) Scheme of interaction of dsDNA-SWCNT and Cas9-sgRNA. T: target strand, NT: non-target strand, NT-a, NT-b, T-a, and T-b: cut products. The green bar represents PAM sequence. (c) 12% denaturing-PAGE shows that Cas9 cuts dsDNA on SWCNT in the presence of Triton X-100.

of SWCNT. To overcome this problem, we introduced Triton X-100, which is a surfactant known to enhance the dsDNA accessibility (as discussed in Chapter 3).[31] The addition of Triton X-100 resulted in enhanced cutting efficiency for all sequences (Figure 5.5c and Figure S5.10). Interestingly, the 3'-GT-spacer-NT had a similar cutting efficiency independent of whether the Triton X-100 was present, implying that the spacer may have a similar effect to the addition of the surfactant. Moreover, amongst all sequences, 5'-GT-NT had the highest activity in the presence of Triton X-100. Since the 5'-GT-NT has a PAM site located at the opposite end to the anchoring sequence, we suggest that the increase in cutting efficiency is due to increased accessibility of the dsDNA to Cas9-sgRNA, which in turn means the nuclease activity can be more easily initiated. This further confirms that the steric hindrance imposed by the presence of the SWCNT critically impacts the activity of the enzyme and needs to be accounted when designing systems for similar applications.

Recently, CRISPR-Cas systems have been combined with gold nanoparticles,[244] graphene,[245] and hydrogels[246] for diagnostic purposes. To the best of our knowledge, the results presented herein represent the first demonstration that Cas9 activity can be preserved close to the SWCNT surface. We anticipate that this dsDNA-SWCNT platform can be utilized for protein interaction analysis both optically and electrically. Importantly, despite the preservation of

Cas9 activity we observed no correlation between the cutting event and the fluorescence response of the SWCNTs (Figure S5.11). Control systems (i.e., those containing the scrambled sequence (R) or the sequence without the PAM (NT-nP)) showed a comparable NIR PL redshift to samples constructed with the specific sequence (NT and spacer-NT). We attribute this to the strong non-specific interaction of the Cas9-sgRNA with the dsDNA-SWCNT, as has previously been reported for DNA-SWCNT and other high molecular weight proteins such as fibrinogen.[134] To address this issue, future work will aim to reduce this effect by engineering the protein surface residues which are responsible for the non-specific interaction or re-wire the system using a Cas9 mutant (e.g., dCas9 or Cas13a).

5.3 Conclusions

In this work we demonstrate the applicability of a DNA-protein-SWCNT ternary hybrid in different configurations. We show that dsDNA bridge formation can be used to immobilize protein onto SWCNTs in a controllable manner by manipulating the cDNA sequence and optimizing dsDNA hybridization. This strategy was further used to attach HRP onto SWCNT, and these sensors was further demonstrated for the selective detection of H_2O_2. Furthermore, our method provides a rational approach for constructing functional materials without a need to screen large combinatorial libraries, which is also easy to perform and does not compromise hybrid stability. Additionally, we show how similar nano-bio hybrids can be used for studying the interaction of specific enzymes, including Cas9, with the dsDNA-SWCNT complex. This platform offers a versatile approach for a range of applications (Figure S5.12 for depiction), such as examining the proximity effects of multiple enzymes, creating temperature responsive materials, and designing multimodal sensing devices.

5.4 Methods and Experiments

Material. All oligonucleotides were purchased from Microsynth. Lyophilized DNA was re-dissolved in ddH2O as indicated by the supplier. The DNA concentration was adjusted by Nanodrop. DNA sequences were summarized in Supporting Information. Proteins were purchased from GEHealthcare, NEB, or Sigma-Aldrich, as indicated. High-pressure carbon monoxide (HiPCO) SWCNT was purchased from NanoIntegris for high purity (lot number: HP29-064). SWCNT was suspended in 2 wt% sodium cholate (Sigma-Aldrich) as described in SI. ssDNA-SWCNTs were prepared by SC-DNA exchange method as described in Chapter 4 without S1 nuclease purification step.

cDNA-protein conjugate. SA-Cy3 (GEHealthcare, GEPA43001, 0.1 mg/mL) or SA-HRP (ThermoFisher, SA10001, stock concentration) was incubated with of cDNA with 5'-end biotin (1 uM) in HEPES (10 mM, pH 7) with a final volume of 100 μL. The mixture was incubated at RT for at least 2 h and stored at 4 °C. For cDNA-SA-Cy3, the yield of conjugation was assayed by 12 % native PAGE in 1× Tris-boric acid-EDTA (TBE) (300 V, 20 min). SybrGold (ThermoFisher)

was used for DNA staining. The conjugate was used without further purification.

Protein immobilization: SA-dsDNA-SWCNT. The immobilization of SA on SWCNT follows the optimized method found by the fluorescence assay with the supplement of bovine serum albumin (BSA) to prevent non-specific adsorption of SA. Briefly, ssDNA-SWCNT (2 mg/L of SWCNT) was mixed with 1× SSC (ThermoFisher) and BSA (1 mg/mL, Sigma-Aldrich, A7906) and incubated for more than 30 minutes. Subsequently, cDNA-SA-Cy3 (10 nM of cDNA) was added to the mixture and thermal-annealed at 60 °C for 5 min, then gradualy cooled to RT and left overnight.

Coverslip treatment. Coverslips attached at the bottom of petri dishes (Mattek, P35G-1.5-14-C) were treated with 60 μL of PLL-g-PEG-biotin (susos, PLL(20)-g[3.5]-PEG(2)/PEG(3.4)-biotin(20%), dissolves in 1 mg/mL in 100 mM HEPES, pH 6.7). After 1 h at RT, the surface was thoroughly washed with HEPES (100 mM, pH 6.7). The coverslips were always freshly modified before sample coating. For co-localization experiments, the coverslips were further treated with 20 μL SA (15 uM in 0.5x PBS, Sigma-Aldrich, S4762), incubated 30 min at RT, then washed thoroughly with HEPES. Other experiments were used without SA coating.

Sample preparation for imaging. Biotin magnetic beads (RayBiotech) were used to concentrate the samples and for colocalization analysis. The beads were extensively washed with HEPES supplemented with BSA (1 mg/mL) to saturate the surface. Afterwards, bead suspension was mixed with SA-dsDNA-SWCNT, incubated for 1 h with 1000 rpm shaking for better immersion. The beads were washed with HEPES-BSA to remove unbound SWCNT. Then, the beads were resuspended in HEPES and coated on coverslip.

Wide-field fluorescence microscope. A custom-built fluorescence microscope (Nikon Eclipse Ti-E microscope) with software Nikon NIS-Elements was used to image the protein-dsDNA-SWCNT complex.[228] Briefly, sample-coated coverslip was mounted on a TIRF Apo 100 × 1.49 NA oil immersion objective (Nikon Instruments). For SWCNT, NIR epifluorescence was excited by a continuous wave laser at 780 nm (Triline Laser Bank, Cairn Research), collected through a 980 nm long-pass filter (BLP01-980R-25, Semrock), and detected by a cooled indium gallium arsenide (InGaAs) camera (NIRvana 640 ST, Princeton Instruments). Additional bright field image of NIRvana channel without filter was recorded for image registration (see detail below). For Cy3, fluorescence at visible range was excited by 555 ± 7.5 nm (Spectra X, lumencor), filtered through a 570-613 nm band-pass filter (67-006, Semrock), and detected by a CCD camera (Andor DU-888). NIR and visible fluorescence images were acquired for 5 s and 100 ms, respectively. Three arbitrary regions of interest (ROI) were recorded for each sample.

Image analysis. Custom-built Python code were used for image pre-processing. In brief, dead pixels were first removed from NIR fluorescence images by closing (skimage.morphology). Gaussian blurred image (σ = 50) was then used to remove background. Next, image registration was performed using ImageJ (ver.1.51j): visible image was transformed based on NIRvana bright field image by least square algorithm with affine method (Landmark Correspondences

plugin), then the transformation was applied to NIR fluorescence image. After thresholding the top 5% brightest pixels, MCC_{NIR} was then calculated based on Equation 5.1. For urea experiment (Figure 5.3), top 1% brightest pixels was selected for calculation. For H_2O_2 (Figure 5.4) and BamHI (Figure 5.5a) experiments, pixels with absolute intensity of NIR PL > 1000 was selected.

NIR Fluorescence Spectroscopy. NIR fluorescence spectrum was measured by a custom-built inverted Nikon Eclipse Ti-E microscope (Nikon AG Instruments). In brief, reaction was in flat-bottom 384-well plate (ThermoFisher, Nunc Maxisorp). The samples was excited by laser (NKT SuperK with VARIA grating) at 660 or 730 nm with a bandwidth = 10 nm for 5 s exposure time. The NIR epifluorescence was directed through long pass filter (Semrock, LP 830 nm), dispersed by spectrometer (Princeton Instruments, grating: 70 lines mm^{-1}), and collected by InGaAs camera (Princeton Instruments, NIRvana 640) from 898 to 1399 nm. Custom Python script was then used for data processing. The transmittance-corrected spectrum was smoothed with Savitzky-Golay algorithm.

H_2O_2 detection. SWCNT hybrid was coated on coverslip as described above. After thoroughly washed with HEPES, the surface was immersed in 190 μL of HEPES (100 mM, pH 6.7). To initiate the redox reaction, 10 μL of H_2O_2 (30 uM) was introduced to and thoroughly mixed by pipetting. NIR fluorescence of SWCNT was then recorded by wide-field fluorescence microscope.

ABTS assay. The colorimetric assay of HRP activity is based on the reaction:

$$H_2O_2 + \text{ABTS} \xrightarrow{\text{HRP}} H_2O + \text{ABTS}^{\bullet+} \tag{5.5}$$

Redox reaction is catalyzed by HRP and turns ABTS (colorless) into radical $\text{ABTS}^{\bullet+}$ (dark green). Here, SWCNT solution was mixed with 4 mM of ABTS (BioChemica) and 6 uM of H_2O_2 for a total volume of 100 μL in 96-well plate (Corning EIA/RIA). After 5 min of incubation, absorption at 405 nm was recorded by multiwell-plate reader (Varioskan).

RE detection. ssDNA-SWCNT/cDNA-SA-Cy3 hybrid was incubated with 10 U of BamHI-HF (R3136S, NEB) in NEBuffer 4 (NEB) for a volume of 100 μL. SWCNT concentration was set to be 0.2 mg/L. After incubation overnight at RT, the reaction was concentrated with biotin magnetic bead and coated on PLL-g-PEG-biotin (susos) treated coverslip as described above.

Cas9-sgRNA digestion with SWCNT. First, dsDNA-SWCNT was incubated with 0.1 mg/mL of BSA in 1× reaction buffer (NEBuffer 3.1, NEB) for 1 h at RT. SWCNT concentration was fixed to be 0.4 mg/L, while Triton X-100 concentration 0.002 v% and 0.005 v%. Meanwhile, Cas9 (M0386T, NEB) was assembled with sgRNA in 1× reaction buffer for 10 minutes at RT. Afterwards, 40 ug mL of heparin (H5515, Sigma-Aldrich) was introduced to prevent non-specific interaction. The ratio of Cas9:sgRNA:dsDNA is fixed to be 1:5:0.05, where the dsDNA concentration is estimated by the SDBS exchange method as described in Chapter 4. The

total volume was fixed to be 20 μL. After digestion in 1.5 mL tube overnight at RT, additional Triton X-100 (0.4 v%) was introduced to desorb all DNA and proteins on SWCNT for analysis. Then the mixture was heated up to 95°C for 10 minutes, then digested by 5 ng/μL RNase A and 5 ng/μL Proteinase K at 50 °C, each for 10 minutes, sequentially. DNA was then ethanol precipitated with glycogen, and analyzed with 12% denaturing-PAGE in 1× TBE (250 V, 40 min). DNA was stained by SybrGold.

5.5 Supporting Information

Table 5.1 – DNA sequences used in Chapter 5.

Name	Alias	Sequence (5' to 3')	cDNA
GT10-A1	GT10BHMain2	GTG TGT GTG TGT GTG TGT GTG GGA TCC GTT AGT TCA TGC	a1
GT10-A2	GT10BHMain2to7	GTG TGT GTG TGT GTG TGT GTG GTT AGT GGA TCC TCA TGC	a2
a1	BHCom2	GCA TGA ACT AAC GGA TCC C	GT10-A1, A1-GT10
a2	BHCom2to7	GCA TGA GGA TCC ACT AAC C	GT10-A2
GT10	-	GTG TGT GTG TGT GTG TGT GT	N/A
a1-b	-	biotin-GCA TGA ACT AAC GGA TCC C	GT10-A1, A1-GT10
a2-b	-	biotin-GCA TGA GGA TCC ACT AAC C	GT10-A2
A1-GT10	-	GGG ATC CGT TAG TTC ATG CGT GTG TGT GTG TGT GTG TGT	a1
GT10-A3	GT10-handle	GTG TGT GTG TGT GTG TGT GTG TAA CGA CTC	a3
a3	handle-com	GAG TCG TTA C	GT10-A3
GT10-R1	-	GTG TGT GTG TGT GTG TGT GTG TCG CTT AAG GCG ATT GCT	r1
GT10-R2	-	GTG TGT GTG TGT GTG TGT GTC ATT GGA TCG GTC CTG GAT	r2
r1	-	AGC AAT CGC CTT AAG CGA C	GT10-R1
r2	-	ATC CAG GAC CGA TCC AAT G	GT10-R2
r1-b	-	biotin-AGC AAT CGC CTT AAG CGA C	GT10-R1
r2-b	-	biotin-ATC CAG GAC CGA TCC AAT G	GT10-R2

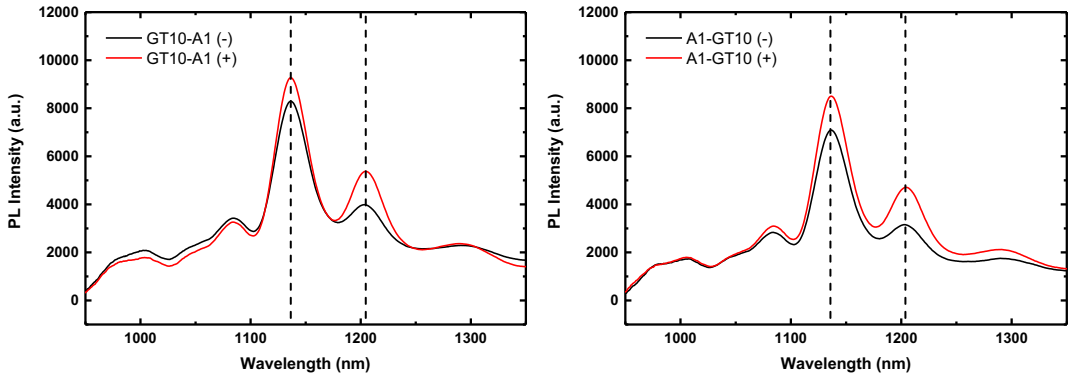

Figure S5.1 – NIR fluorescence spectra of ssDNA-SWCNTs (2 mg/L of SWCNT) with (+) and without (-) streptavidin. The presence of streptavidin (750 nM in PBS) increases the SWCNT fluorescence for both ssDNA sequences (GT10-A1 and A1-GT10) in comparison with the control experiment (addition of PBS). This increase in fluorescence intensity indicates that the SA can non-specifically interact with the DNA-SWCNT complex. The buffer used contains 10 mM HEPES (pH = 6.7) supplemented with 1 mg/mL of BSA. Spectra were recorded after 3 h of incubation at RT.

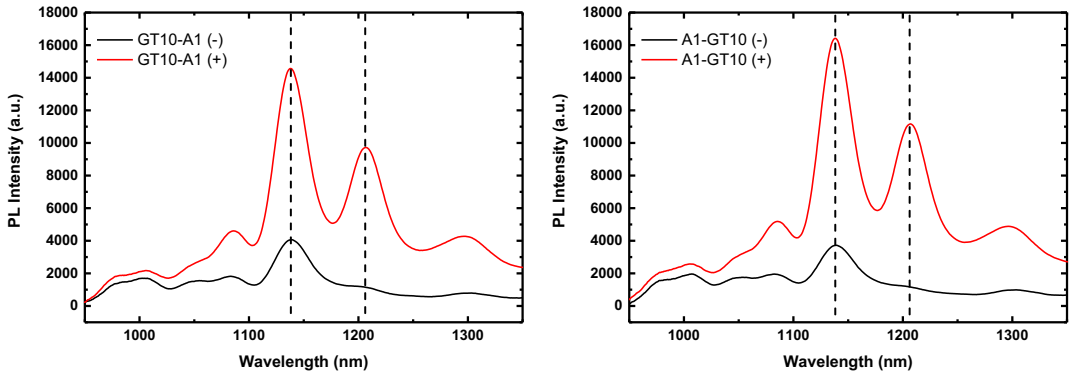

Figure S5.2 – NIR fluorescence spectra of ssDNA-SWCNTs (2 mg/L of SWCNT) with (+) and without (-) urea. The presence of 5 M urea significantly increases SWCNT fluorescence in both ssDNA sequences (GT10-A1 and A1-GT10). The buffer used contains 10 mM HEPES (pH = 6.7) supplemented with 1 mg/mL of BSA. Spectra were recorded after 3 h of incubation at RT.

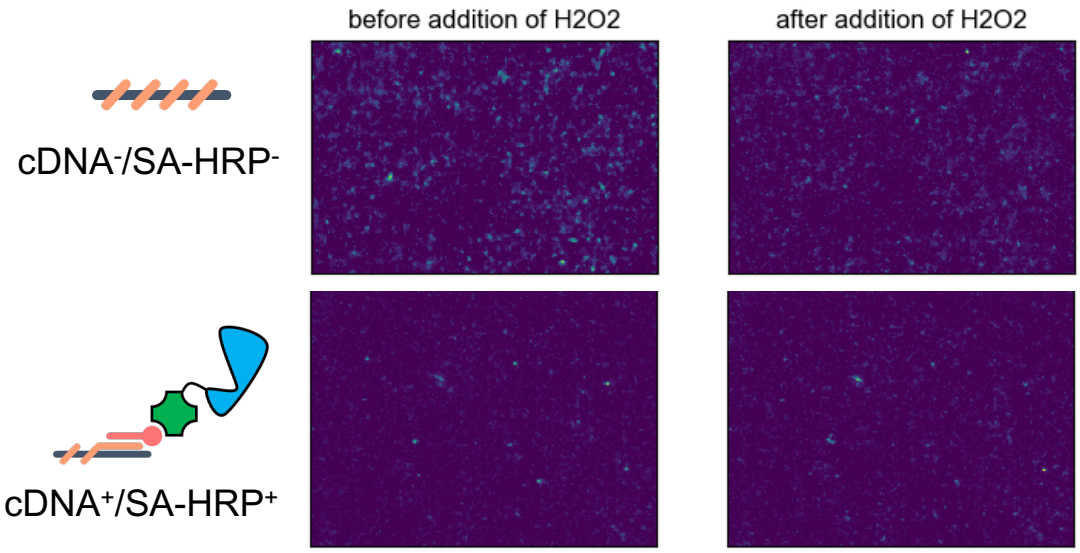

Figure S5.3 – Wide-field NIR fluorescence images of the SWCNT hybrids.

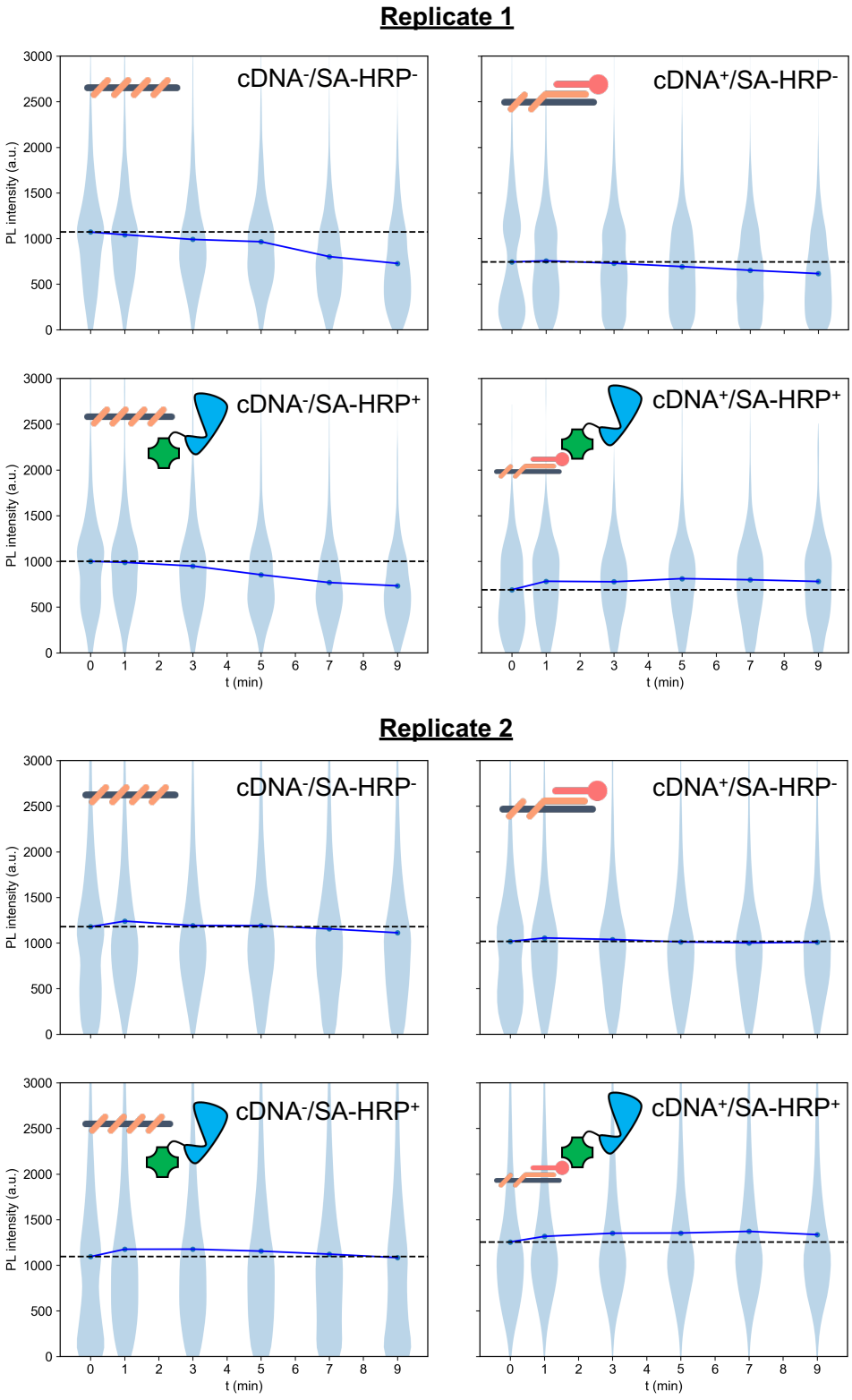

Figure S5.4 – Additional replicates of the H_2O_2 detection experiment.

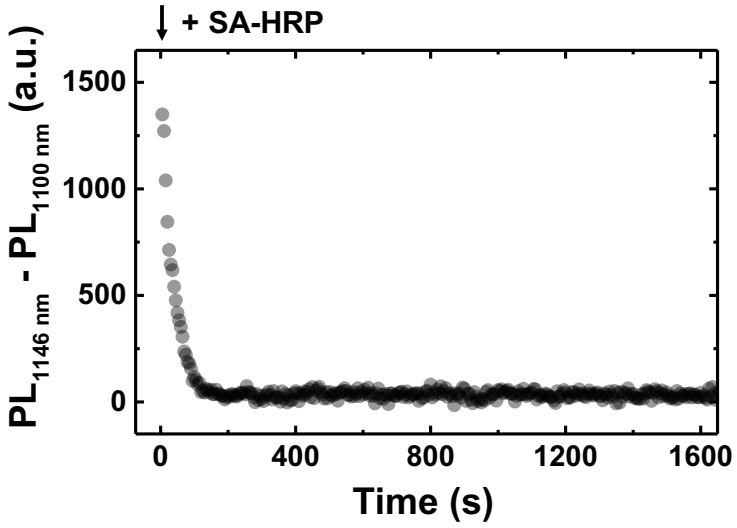

Figure S5.5 – The addition of SA-HRP to ssDNA-SWCNTs significantly quenches the SWCNT NIR fluorescence. The y-axis represents the height of SWCNT fluorescence peak.

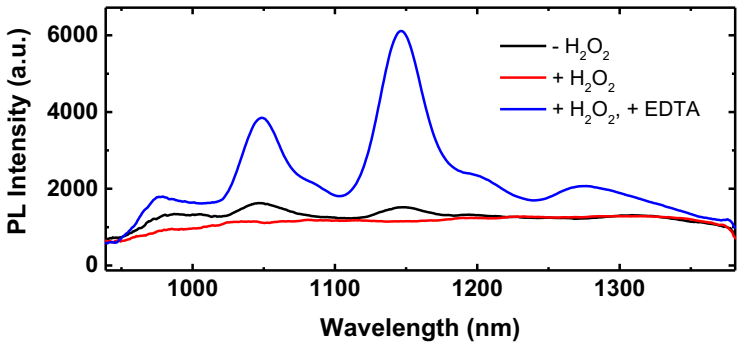

Figure S5.6 – The addition of EDTA recovers the NIR fluorescence of ssDNA-SWCNT/SA-HRP by removing the ferric cation from the heme.

Table 5.2 – DNA sequences of Cas9-related section in Chapter 5.

sgRNA cloning			
Name	**Alias**	**Sequence (5' to 3')**	**cDNA**
Forward primer	-	TAA TAC GAC TCA CTA TAG GAC	-
ssDNA target sequence	RNATempTarget4	TAA TAC GAC TCA CTA TAG GGC ACC GGG ATT CTC CAG GGG TTT TAG AGC TAG A	-
Scaffold sequence	-	AAA AGC ACC GAC TCG GTG CCA CTT TTT CAA GTT GAT AAC GGA CTA GCC TTA TTT TAA CTT GCT ATT TCT AGC TCT AAA AC	-
reverse primer	-	AAA AGC ACC GAC TCG GTG	-
dsDNA template	-	TAA TAC GAC TCA CTA TAG GGC ACC GGG ATT CTC CAG GGG TTT TAG AGC TAG AAA TAG CAA GTT AAA ATA AGG CTA GTC CGT TAT CAA CTT GAA AAA GTG GCA CCG AGT CGG TGC TTT T	-
sgRNA transcript	-	GGG CAC CGG GAU UCU CCA GGG GUU UUA GAG CUA GAA AUA GCA AGU UAA AAU AAG GCU AGU CCG UUA UCA ACU UGA AAA AGU GGC ACC GAG UCG GUG CUU UU	T
DNA-wrapping			
Name	**Alias**	**Sequence (5' to 3')**	**cDNA**
5'-GT-NT	GT10NTStrandT4	GTG TGT GTG TGT GTG TGT GTG GCA CCG GGA TTC TCC AGG GCG GCC	T
3'-GT-NT	NTStrandT4GT10	GGC ACC GGG ATT CTC CAG GGC GGC CGT GTG TGT GTG TGT GTG TGT	T
3'-GT-spacer-NT	NTStrandT4-s-GT10	GGC ACC GGG ATT CTC CAG GGC GGC C–(PEG)6–GT GTG TGT GTG TGT GTG TGT	T
T	TStrandT4	GGC CGC CCT GGA GAA TCC CGG TGC C	5'-GT-NT, 3'-NT-GT, 3'-GT-spacer-NT
NT-nP	NTStrandT4GT10-noPAM	GGC ACC GGG ATT CTC CAG GGC AAC CGT GTG TGT GTG TGT GTG TGT	T-nP
T-nP	TStrandT4-noPAM	GGT TGC CCT GGA GAA TCC CGG TGC C	NT-nP
R-NT	R1GT10	GAC TGT GTA ACT CGA TGA GCT ACT GGT GTG TGT GTG TGT GTG TGT	R-T
R-T	r1	CAG TAG CTC ATC GAG TTA CAC AGT C	R-NT

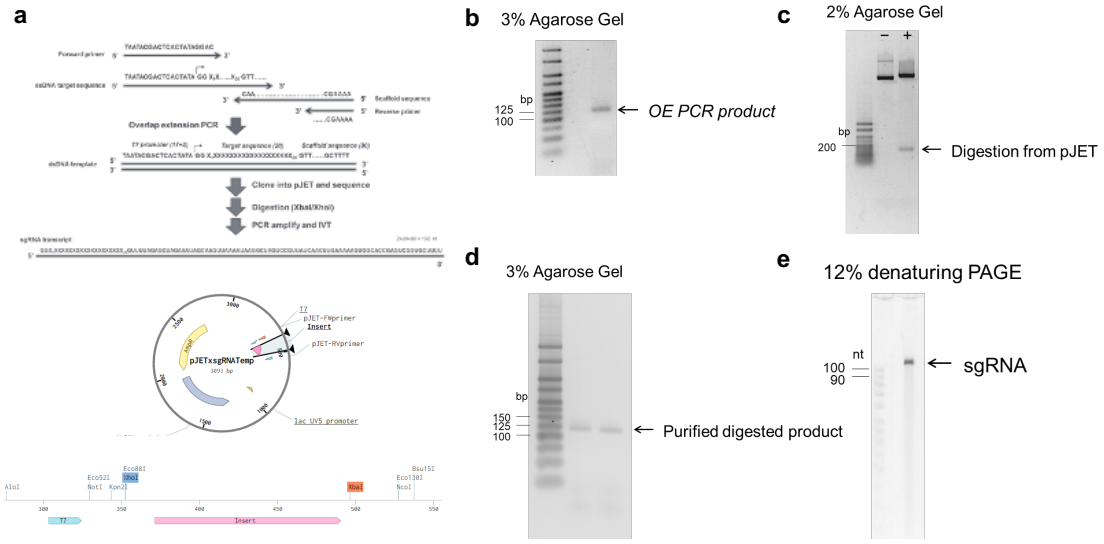

Figure S5.7 – sgRNA cloning and in vitro transcription.

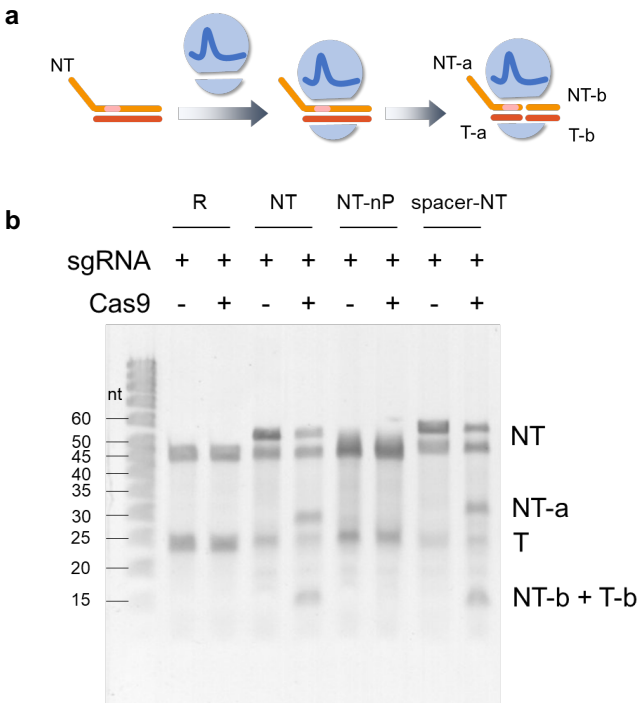

Figure S5.8 – Cas9 digestion in the absence of SWCNTs (3'GT-series).

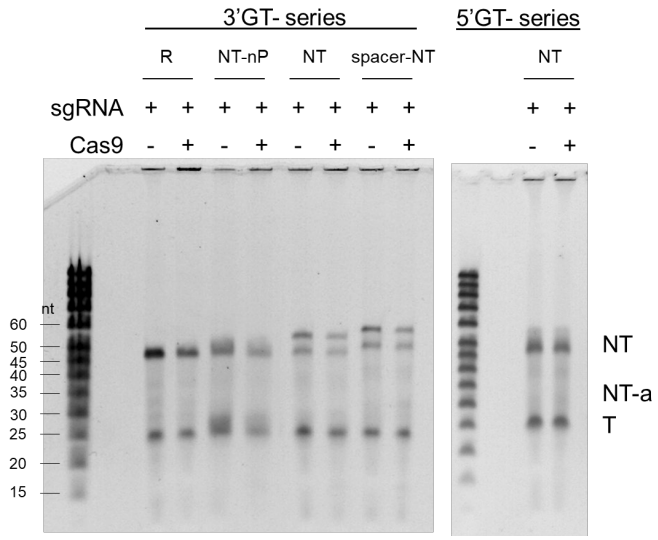

Figure S5.9 – Cas9 digestion in the presence of SWCNTs and absence of Triton X-100.

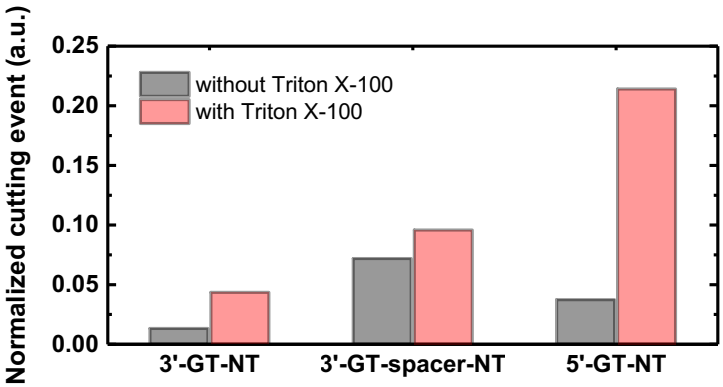

Figure S5.10 – Fragment analysis of Cas9-sgRNA digestion efficiency from the results of Figure 5.5c.

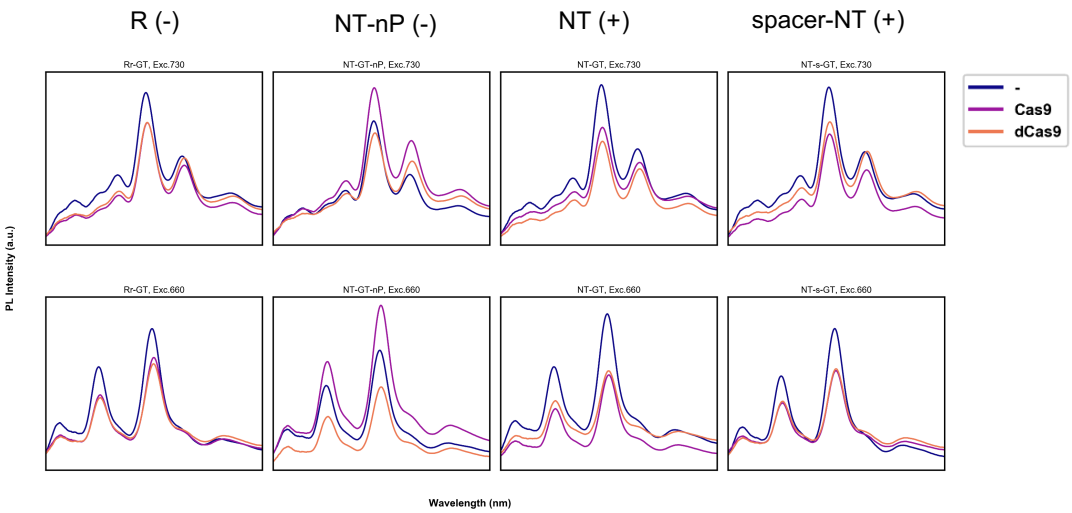

Figure S5.11 – NIR fluorescence of dsDNA-SWCNT in the absence and presence of Cas9 or dCas9. Limited difference between non-cognate sequences and cognate sequences was observed.

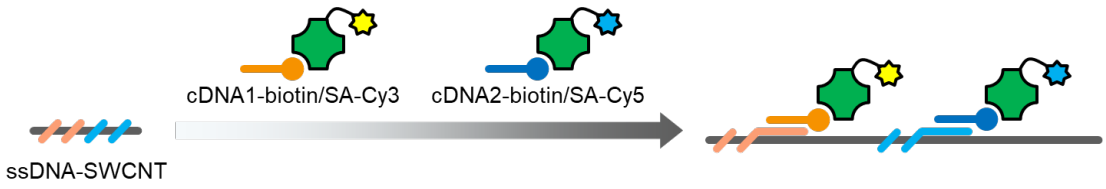

Figure S5.12 – Cartoon of multimodal decoration.

6 Chemical Determinants of DNA-SWCNT/Protein Interaction

This Chapter is adapted from a manuscript prepared for submission in a journal with co-authors:
Shang-Jung Wu, Che Yang, Mohammed Mouhib, Bruno Correia, and Ardemis A. Boghossian.

6.1 Introduction

Non-specific protein adsorption is one of the most critical issues in bio-applications. Due to diverse surface residues, proteins may adsorb on the surface of testing tubes, well-plates, filter membranes, or glass slides. Consequently, production yield, purity, reactivity, and sensitivity are reduced. Diminishing the non-specific interaction while maintaining the integrity of specific interaction is the key to methodology development. For example, enzyme-linked immunosorbent assay (ELISA) requires an incubation of bovine serum albumin (BSA) in well-plate to passivate the surface, in order to decrease false positive signal. Similar approach can be found in surface plasmon resonance (SPR) analysis and Western blotting while analyzing in a complex media, where surface passivation was accomplished by BSA or milk powder.

One bio-application of great interest in the recent years is nano-bio hybrid, which potentially combines advantages of multiple components. Nanoparticles often offer well-defined and controllable distinguish properties, such as high quantum yield fluorescence, large surface area for cargo delivery, thermal resistance, and photostability. However, nanoparticles amplify the challenge of non-specific interaction at the interface of material science and biology. As an example, the coating on nanoparticle induces zeta potential, and the large surface area leads to unwanted aggregation and cytotoxicity. Meanwhile, hydrophobic nature of some systems denatures protein, and nanoparticle competitively binds to ligand binding pocket, limiting the protein activity.

Among nano-bio hybrids, composites of DNA and single-walled carbon nanotubes (SWCNTs) have been extensively studied due to the potential in multiple applications. It combines the versatility, which is offered by the vast amount of possible DNA sequences, and the sensi-

tivity of near-infrared (NIR) fluorescence, which is originated from SWCNT distinguish band diagram. However, similar to other nano-bio hybrid applications, protein non-specific adsorption limits the application, especially in a crowded environment like cellular or complex media. Of which application requires specific protein binding (e.g., DNA–protein interaction),[221] significant effort is needed to reduce protein non-specific interaction. In other words, understanding how protein interacts with ssDNA-SWCNT becomes the premise of advance applications.

Despite the complexity of natural interaction between ssDNA-SWCNT/protein, previous efforts have been invested on characterization of the physicochemical properties contributed to the formation of nano-bio interface. Gong et al. pioneered using mass spectrometry-based (MS) proteomics approach to identify the properties of protein which contributes to non-specific adsorption.[134] The hydrophobic and charged residues and molecular weight (MW) of a protein were found important, while isoelectric point (IEP) was surprisingly found less significant. Subsequently, Pinals et al. categorized the adsorption 'protein corona' into two layers by exploiting 2D-polyacrylamide gel electrophoresis (2D PAGE), MS and small-angle X-ray scattering (SAXS).[135] They concluded that the first shell of protein layer in close contact with SWCNT is more hydrophobic, while the second shell of protein layer has more charged residues.

Although hydrophobic interaction and electrostatic force are both considered critical, it is unclear what residues are crucial for cooperative interaction in complex fluid. This bulk adsorption behavior cannot be resolved on individual protein. The dynamic behavior of protein adsorption also implies a replacing mechanism may exist (i.e., strong association protein replaces weak association ones).[130, 135] Furthermore, surface passivation approach, similar to ELISA and SPR, has been applied but cannot work universally (see Chapter 5). A general approach for avoiding non-specific adsorption and a structure-interaction relationship are still lacking and needed to be established.

Here, we described the detailed structural and chemical features accounts for interaction of ssDNA-SWCNT/protein hybrid by analyzing NIR fluorescence of SWCNT. Protein adsorption on ssDNA-SWCNT triggers substantial fluorescence shift and/or intensity change which has been attributed to water exclusion and/or ssDNA secondary structure change. Assuming a monotonic correlation, we thus infer the strength of interaction in ssDNA-SWCNT/protein from NIR fluorescence spectrum. Beginning with a natural protein repertoire, we explored the effects of ionic strength on non-specific interaction in the hybrid. Inhibitor experiments were used to confirm the major interaction types in the hybrid to be electrostatic interaction. We next employed correlation test, and we identify IEP is the most critical factor. Moreover, we screened a de novo protein library composing of similar IEP and MW to identify crucial structural propensities and surface residues. We particularly found aspartate (Asp) and the overall percentage of α-helix determines the strength of ssDNA-SWCNT/protein interaction. This is further verified by site-directed mutagenesis on one of the designed proteins. Altogether, the general screening and protein engineering approach can be used to guide the optimization

of the protein components in nano-bio hybrid.

6.2 Results and Discussion

First, we prepared ssDNA-SWCNT by surfactant-DNA exchange from sodium cholate (SC)-suspended SWCNT, as described in our previous studies.[89] Here, we primarily used SWCNT synthesized by CoMoCAT process, which has chirality enrichment of (6,5)-SWCNT. In order to eliminate the contribution of sequence-dependence, four different oligonucleotides with 30 nt were prepared and used in the study (see Table S1 for sequences). Then, we performed NIR fluorescence of SWCNT using custom-built fluorescence microscope (see Section 6.4). Figure S6.1 shows a typical fluorescence spectrum of $(GT)_{15}$-SWCNT (black) and the corresponding fitted peak with single skewed-Lorentzian function (blue).

For testing of ssDNA-SWCNT/protein interaction, we determined the NIR fluorescence of ssDNA-SWCNT together with natural occurring proteins (Figure 6.1a). These proteins have different isoelectric point (IEP) and molecular weight (MW). Two of which, DNase I and histone H1, consist of intrinsic DNA binding domain. Proteins were mixed with ssDNA-SWCNT in HEPES buffer (pH = 8) with various ionic strength. We observed a substantial red-shift of (6,5)-SWCNT fluorescence with respect to corresponding negative control (i.e., no protein at the same salt concentration) (Figure 6.1b and Figure S6.2). For convenience, we define the peak shift ($\Delta\lambda$) as

$$\Delta\lambda = \lambda_{\text{ssDNA-SWCNT/protein}} - \lambda_{\text{ssDNA-SWCNT}} \tag{6.1}$$

and $\Delta\lambda_{(6,5)}$ is the difference of (6,5) fluorescence peak maxima. Figure 6.1b show the statistics of $\Delta\lambda_{(6,5)}$ based on four different sequences. Most proteins at low ionic strength (except for BSA) has $\Delta\lambda_{(6,5)} > 0$ (i.e., red-shifted fluorescence). However, $\Delta\lambda_{(6,5)}$ is negligible at high ionic strength, especially for proteins having lower IEP (BSA, DNase I, RNase A, Proteinase K).

We inferred the red-shift of fluorescence peak is due to protein adsorption on ssDNA-SWCNT. Protein adsorption can cause (1) ssDNA secondary structure change on SWCNT, (2) water exclusion, and/or (3) cation redistribution on SWCNT. As a result, localize dielectric environment around the hybrid is changed, leading to a modulated (6,5)-SWCNT optical band gap.[146] Moreover, lysozyme and histone have the highest $\Delta\lambda_{(6,5)}$ at pH = 8. Since lysozyme and histone are both positively charged at this pH and ssDNA-SWCNT is intrinsically negatively charged,[247] the Columbic interaction between ssDNA-SWCNT and proteins is attraction. As ionic strength increase, we observed a substantial drop of $\Delta\lambda_{(6,5)}$. We attributed to the increased shielding effect reduces Columbic interaction, which is less favored for protein association on ssDNA-SWCNT. On the other hand, proteins with lower IEP have less $\Delta\lambda_{(6,5)}$. Since these proteins are overall either neutral or negatively charged at pH = 8, the protein adsorption mainly relies on short-range van der Waals (vdW) interaction and hydrogen bond, rather than Columbic interaction. Notably, as NaCl concentration increases, the salt-out effect is generally strengthened (see Hofmeister series), reducing protein adsorption on ssDNA-

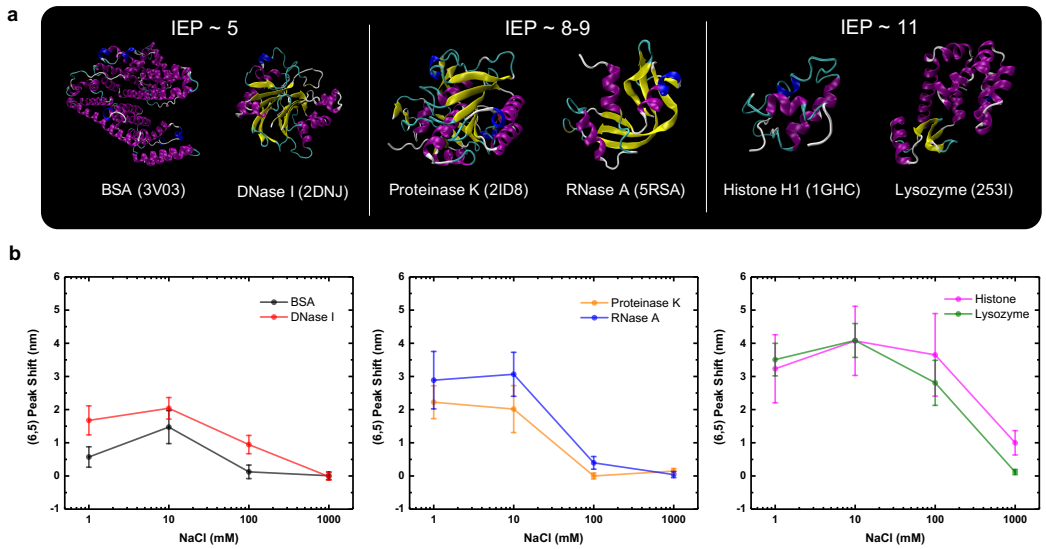

Figure 6.1 – (a) Natural protein library and their crystal structures. (b) (6,5) fluorescence peak of ssDNA-SWCNT/protein hybrid depends on the ionic strength.

SWCNT and $\Delta\lambda_{(6,5)}$.

Next, we performed inhibition experiments by introducing three different additives (Figure 6.2a): guanidium hydrochloride (GdmCl), urea, and heparin. GdmCl at pH = 8 is protonated and effectively binds to ssDNA-SWCNT surface. Of note, at 1 M, GdmCl does not denature hydrogen bonding nor the protein secondary structure.[248, 249] Urea (1 M) perturbs the hydrogen bonding without disrupting the protein secondary structure.[250] Heparin is negatively charged polysaccharide, which is often utilized to reduce electrostatic interaction by stacking on positively charged residues. The effect of the additives on the DNA-SWCNT/protein interaction was assessed using $\Delta\lambda_{(6,5)}$ (Figure 6.2b).

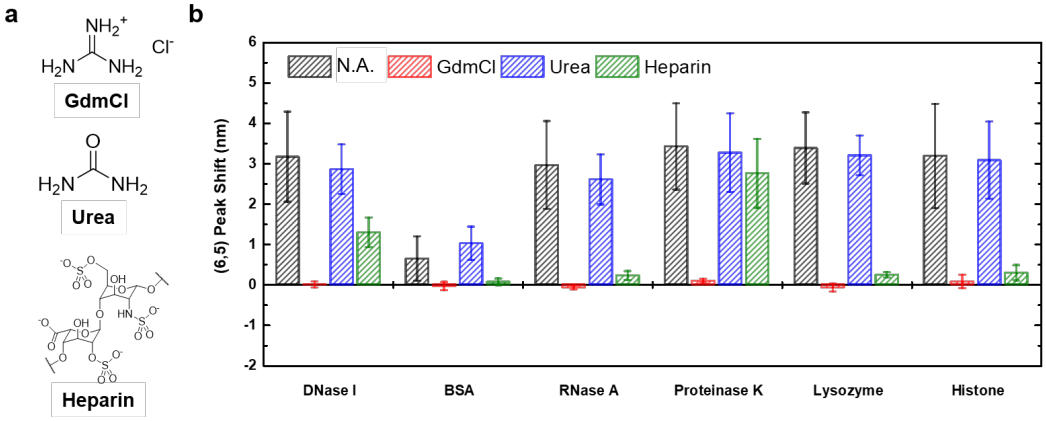

Figure 6.2 – (a) Three additives used in inhibitor experiment. (b) $\Delta\lambda_{(6,5)}$ in the presence of various inhibitors. N.A.: no additive.

We found that GdmCl significantly reduces interaction between proteins and ssDNA-SWCNT in all scenarios. The charged guanidium group adsorbing on ssDNA-SWCNT effectively prevents proteins from binding to ssDNA-SWCNT surface. However, it is also possible GdmCl replaces ssDNA on SWCNT since it has strong hydrophobic interaction and $\pi - \pi$ stacking, and this may largely determine the fluorescence changes. In sodium deoxycholate (SDC)-SWCNT (Figure S6.3), where SDC has strong binding affinity to SWCNT (i.e., high coverage of SWCNT surface), we found negligible peak shift and protein adsorption, similar to the case of ssDNA-SWCNT. We thus conclude that GdmCl blocks the electrostatic interaction between SWCNT and protein. Interestingly, despite a similar chemical structure to GdmCl, non-charged urea rarely perturbs protein adsorption. It indicates that the hydrogen bonding marginally contributes to ssDNA-SWCNT/protein interaction in this protein library.

Similar to GdmCl, heparin significantly reduces interaction in most cases, except for Proteinase K. We therefore think the electrostatic force is the major interaction. In the past, it has been shown that charged residues contributes to the protein adsorption.[134] Along with ionic strength experiment, these inhibitor experiments confirm that the protein adsorption mainly relies on electrostatic interaction. Likewise, in a competitor experiment, we demonstrated that heparin is able to recover SDC-SWCNT fluorescence in the presence of RNase A (Figure S6.4).

Next, we performed Spearmen correlation test between properties of a protein and $\Delta\lambda_{(6,5)}$ under different conditions (Figure 6.3). We include IEP, MW, fraction of secondary structure (α-helix, β-sheet, coil), and fraction of surface residues. We used the conventional relative solvent accessibility (RSA) as defined by solvent accessible surface area (SASA),

$$\mathrm{RSA} = \frac{\mathrm{SASA}_{\mathrm{X-in-protein}}}{\mathrm{SASA}_{\mathrm{Gly-X-Gly}}} \tag{6.2}$$

where X is any residue in a protein. The calculation is based on the plugin in PyMol with crystal structure in PDB (Figure 6.1a). If a residue has RSA above 20 %, we consider it is at the surface of a protein. Here, we consider the percentage of a type of amino acid at the surface of a protein (details can be found in Section 6.5). Amino acids are further grouped into nonpolar, aromatic, polar, positively charged, and negatively charged.

In this natural protein library, we found at low ionic strength, $\Delta\lambda_{(6,5)}$ is strong positively correlated to IEP of a protein but negatively correlated to MW (see also Figure S5). As we increased the ionic strength or introduced heparin, the correlation between IEP and $\Delta\lambda_{(6,5)}$ diminished. Since we fixed the experiment at pH = 8, IEP directly determined the overall charge of a protein. As we changed the pH (Figure S6.6), the protein adsorption and $\Delta\lambda_{(6,5)}$ largely varies for the same protein. This again confirms the electrostatic interaction dominates the ssDNA-SWCNT/protein interaction. Notably, since MW is negatively correlated to IEP for the protein library (ρ = -0.82), we think the observed effect of MW may be biased. Interestingly, these trends are opposite to what Gong et al. reported,[134] where they found MW is more determinant than IEP in a complex medium. The protein corona formed at the surface of ssDNA-SWCNT may largely change the shell structure and introduce shielding effect. In

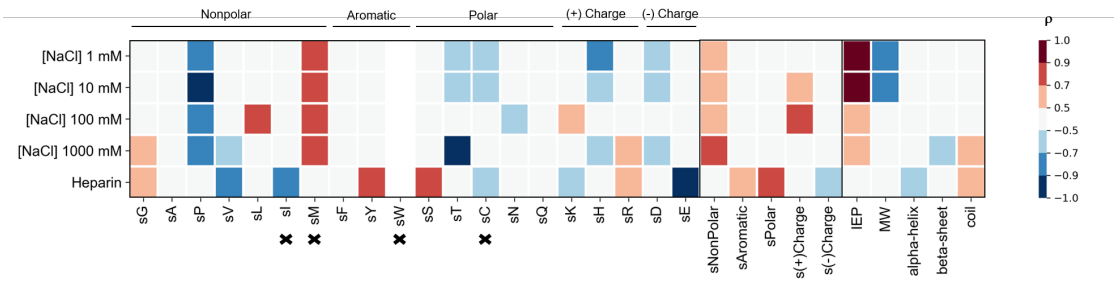

Figure 6.3 – Correlation matrix analysis of $\Delta\lambda_{(6,5)}$ with respect to properties of protein. Natural protein library (Figure 6.1a) was used in this analysis. The surface residues (x-axis, prefix denoted with s for surface, followed by one-letter code of a.a.) are calculated based on their corresponding crystal structure and RSA > 0.2. The colorbar denotes the scale of ρ in Spearman correlation test. Note amino acids which are not present at the surface of this protein library are labelled with a cross.

our case, since we investigate individual protein, the effect can be directly attributed to the interaction between a specific protein and ssDNA-SWCNT.

However, structural factors are less critical in this library. We observed only a weak correlation with fractions of secondary structure ($\rho < 0.7$). After excluding a.a. not presenting at the surface (Ile, Met, Trp, Cys), no consistent relationship was found between $\Delta\lambda_{(6,5)}$ and surface residues. We think IEP and MW is too dominant in this library, hiding other factors which could be potentially crucial.

Therefore, to eliminate the contribution of IEP and MW, we screened the previously de novo designed protein library containing ten proteins (Figure 6.4a). These proteins possess similar IEP (6.4–9.7) and MW (7.6–13.9 kDa) with various secondary structure and surface residues. Likewise, we first measured $\Delta\lambda_{(6,5)}$ of ssDNA-SWCNT in the presence of each protein (Figure 6.4b), and a wide range of results (0.9–4.5 nm) was observed.

We obtained a correlation matrix of this designed protein library with protein properties, secondary structure, and surface residues (Figure 6.4c). The SWCNT fluorescence shows positive correlation to the amount of α-helix and negative correlation to the amount of β-sheet (see also Figure S6.7), but the composition of loop region does not affect the SWCNT fluorescence significantly. We thus hypothesize that ssDNA-SWCNT mainly interacts with proteins through α-helix. The periodicity of side chain alignment in α-helix may coincide with the ssDNA secondary structure on SWCNT, promoting a cooperated interaction mode, which has been proposed previously in the case of alanine coiled-coil with bare SWCNT surface.[115, 121] In contrast, β-sheet may not have the corresponding periodicity with ssDNA secondary structure, and the close contact between residues on β-sheet may introduce additional steric hindrance and repulsion force. These hypotheses will be further verified by extended protein library, and the exact interacting mode will be resolved by molecular dynamics simulation.

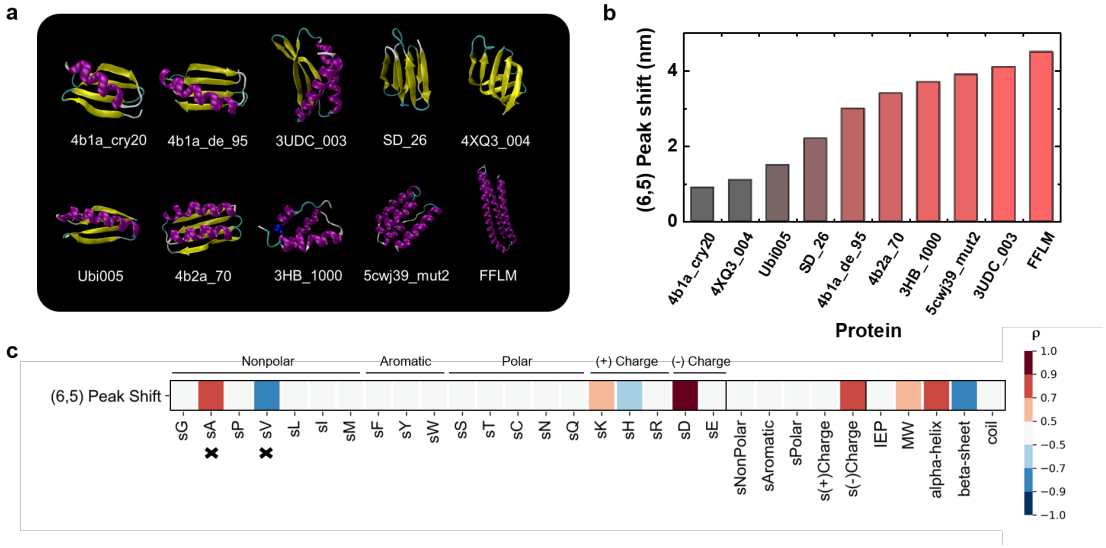

Figure 6.4 – (a) De novo designed library used in this study. (b) $\Delta\lambda_{(6,5)}$ of de novo designed protein library. The results are average of two distinct DNA sequences, GT and ERV. (c) Correlation matrix of the library. The surface residues (x-axis, prefix denoted with s for surface, followed by one-letter code of a.a.) are calculated based on their corresponding crystal structure and RSA > 0.2. The colorbar denotes the scale of ρ in Spearman correlation test. Note amino acids which are not present at the surface of this protein library are labelled with a cross.

Moreover, after excluding amino acids which do not present at the surface of all members in the library (i.e., Ala and Val), we found charge residues are mainly responsible for the interaction, especially for negatively charged Asp (ρ = 0.9, see also Figure S6.7). Interestingly, at pH = 7.4 (in PBS), negatively charged Asp should have electrostatic repulsive force with negatively charged ssDNA-SWCNT. We thus hypothesize in addition to electrostatic interaction, a cooperative interaction mode including multiple hydrogen bonds may also contribute for protein/ssDNA-SWCNT interaction in this library. Likewise, for DNA–protein interaction involving Asp, water-mediated cooperative interaction with hydrogen bonds has been shown to be critical.[5, 251]

To test whether surface Asp is critical to ssDNA-SWCNT/protein interaction, we resurfaced 4b1a_cry20, which has the least $\Delta\lambda_{(6,5)}$ in the library (i.e., the least interaction with ssDNA-SWCNT). We replaced three glutamate residues (Glu) with Asp (D40E, D54E, D55E) at the surface of α-helix (Figure 6.5a, in red). We obtained 1.0 ± 0.4 nm and 1.9 ± 0.2 nm of $\Delta\lambda_{(6,5)}$ with wild type (4b1a_cry20) and the mutant (4b1a_cry20*), respectively (Figure 6.5b). Despite a marginal difference between Asp and Glu (R = (CH_2)COOH and $(CH_2)_2$COOH), the change in interaction strength is pronounced (p = 0.0031). Although the detail of interaction mode remains unknown, we proposed the alignment of Asps at the surface of α-helix may promote a cooperated interaction.[115, 121]

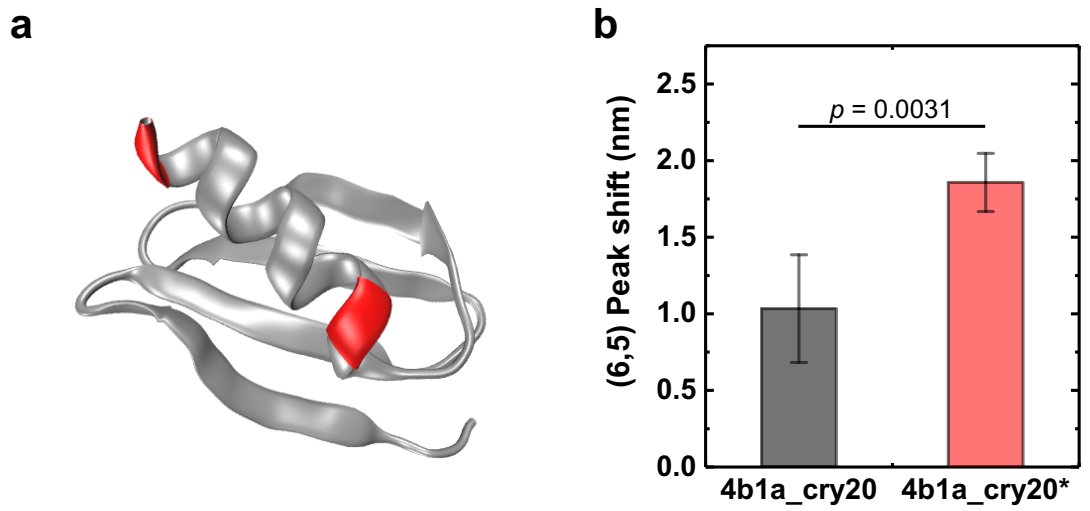

Figure 6.5 – (a) Structure of 4b1a_cry20 and the mutation site of 4b1a_cry20* (D40E, D54E, D55E). The mutation is at the surface of an α-helix. (b) (6,5)-SWCNT fluorescence peak shift of 4b1a_cry20 and mutant 4b1a_cry20*. Statistics are based on four ssDNA sequences (GT, ERV, BHL, BHH). Two sample t-test (one tailed) was used for significance test.

6.3 Conclusions

In this study, we employed two protein libraries (natural: $n = 6$, designed: $n = 10$) to identify the dominant factors of ssDNA-SWCNT/protein interaction by investigating SWCNT NIR fluorescence. While electrostatic force is found to be the most critical interaction mode, correlation matrix also identifies the protein 3-dimensional structure to be important, where possessing α-helix is more deterministic than β-sheet and loop. Moreover, surface Asp, a negatively charge residue, surprisingly enhances the ssDNA-SWCNT/protein interaction, indicating that hydrogen bonds are involved in a cooperative mode. This is the first time that structural features were found to be crucial and missing in the past.

We successfully utilized, for the first time, rationally engineering the protein surface residues to tune the affinity between protein and ssDNA-SWCNT, where the mutant (4b1a_cry20*) shifts SWCNT fluorescence 0.9 nm more than the wild type (4b1a_cry20). We envision knock-out of surface Asp can also help to reduce ssDNA-SWCNT/protein interaction. Further investigation can be applied in protein library with different IEP and MW using the same methodology.

We aim to extend such protein engineering approach for fine tuning ssDNA-SWCNT/protein interaction in in vivo application, where we are limited from including inhibitor or changing ionic strength. By simply modifying a specific gene, we can either reduce or enhance the interaction between ssDNA-SWCNT and protein. Alternatively, as shown in the past, modifying

ssDNA sequence can also change ssDNA-SWCNT/protein interaction, but one may have to compromise the sensitivity or selectivity of ssDNA-SWCNT sensor. Our approach provides a complementary method bypassing the need of re-engineering ssDNA-SWCNT.

6.4 Methods and Experiments

Materials. All DNA were bought from MicroSynth and used as received unless specified. DNA was dissolved in ddH_2O, and the concentration was measured by Nanodrop with corresponding extinction coefficient at 260 nm (as provided by supplier). DNA sequences can be found in Section 6.5. All chemicals and proteins in natural protein library were bought from either Sigma-Aldrich or Carl Roth and used without further purification. Bovine serum albumin (BSA, Sigma-Aldrich, A7906), deoxyribonuclase I (DNase I, Sigma-Aldrich, DN25), histone Type III-S (Sigma-Aldrich, H5505), proteinase K (Sigma-Aldrich, P2308), lysozyme (Sigma-Aldrich, L6876) ribonuclease A (RNase A, Carl Roth, 7156.1) were dissolve in ddH_2O, and the concentration was measured by Nanodrop with corresponding extinction coefficient at 280 nm. Single-walled carbon nanotube was purchased from CHASM (CoMoCAT, lot: SG65i-L59) and used without further washing.

Preparation of ssDNA-SWCNT. ssDNA-SWCNT was prepared by sodium cholate (SC, Sigma-Aldrich, C1254)-DNA exchange method as reported previously with some modifications. Briefly, 200 μL of 1 wt% SC-suspended SWCNT (around 60 mg/L of SWCNT) was mixed with 200 μL of ssDNA (50 μM) in a 1.5 mL Eppendorf tube. Subsequently, 600 μL methanol was added to initiate the SC-DNA exchange reaction at room temperature. After 2 h of incubation, the reaction was transferred to 15 mL Falcon tube. Followed by adding 1 mL of NaCl (400 mM) to the reaction, 5 mL of cold ethanol was introduced to precipitate ssDNA-SWCNT at -20 °C for 1 h. The pellet was collected by centrifugation at 3220 rcf for 30 min. To remove residual of methanol and SC, the pellet was resuspended with 70% ethanol and collected again by centrifugation (21300 rcf, 4 °C, 10 min). The washing step was performed twice sequentially. After decanting ethanol and drying, the pellet was resuspended in 1 mL ddH_2O. The final SWCNT concentration was around 12–14 mg/L ($\epsilon_{739} = 0.025\,\mathrm{L\,cm^{-1}\,mg^{-1}}$). Notably, in this study, unbound ssDNA was not removed by ultrafiltration nor dialysis.

Fluorescence measurements. SWCNT fluorescence was measured by a custom-built inverted Nikon Eclipse Ti-E microscope (Nikon AG Instruments) as described previously. In brief, the mixture was placed in flat-bottom 384-well plate (ThermoFisher, Nunc Maxisorp) for a total volume of 20 μL. The samples were excited by laser (NKT SuperK with VARIA grating) at 575 nm with a bandwidth = 10 nm for 10 s exposure time. The nIR epifluorescence was directed through long pass filter (Semrock, LP 830 nm), dispersed by spectrometer (Princeton Instruments, grating: 600 lines $\mathrm{mm^{-1}}$), and collected by InGaAs camera (Princeton Instruments, NIRvana 640) from 970 to 1030 nm.

Ionic strength experiment. ssDNA-SWCNT was pre-equilibrated in HEPES buffer (1 mM, pH = 8; Carl Roth, HN78.1) for a total volume of 10 μL. Subsequently, 10 μL of protein in

HEPES-NaCl was added to ssDNA-SWCNT and mixed in 384 well-plate (Thermo Fisher, flat bottom MaxiSorp). Reaction has a total volume of 20 μL. NaCl (Sigma-Aldrich, S3014) has a gradient final concentration (1 M, 100 mM, 10 mM, 1 mM), while final protein concentration is fixed at 0.1 mg/mL. Final SWCNT concentration is 6–7 mg/L.

Inhibitor experiment. ssDNA-SWCNT was pre-equilibrated in HEPES buffer (1 mM, pH = 8) for a total volume of 10 μL. Subsequently, 10 μL of protein with inhibitor in HEPES (1 mM, pH = 8) was added to ssDNA-SWCNT and mixed in 384 well-plate. Guanidium hydrochloride (GdmCl, Carl Roth, 0035.1) and urea (Sigma-Aldrich, U1250) have a final concentration of 1 M, while heparin (Sigma-Aldrich, H5515) has a final concentration of 0.125 mg/mL (1:1 weight ratio to protein). Reaction has a total volume of 20 μL. Final protein concentration is fixed at 0.125 mg/mL. Final SWCNT concentration is 6–7 mg/L.

Designed library experiment. ssDNA-SWCNT was pre-equilibrated in PBS buffer (pH = 7.4) for a total volume of 10 μL. Subsequently, 10 μL of protein in PBS was added to ssDNA-SWCNT and mixed in 384 well-plate. Reaction has a total volume of 20 μL. Final protein concentration is fixed at 0.1 mg/mL. Final SWCNT concentration is 6–7 mg/L.

Data analysis. Custom Python script was used for data processing. NIR fluorescence spectrum was transmittance-corrected and smoothed with Savitzky-Golay algorithm (scipy.signal.savgol_filter). After normalization between 0 to 1, non-linear least square algorithm (scipy.optimize.least_squares) was used to fit (6,5)-SWCNT fluorescence intensity (L) with single skewed-Lorentzian peak,[252]

$$L(\nu) = \frac{\frac{2A}{\pi\gamma}}{1 + 4[\frac{\nu - \nu_0}{\gamma}]^2} \tag{6.3}$$

where $\gamma(\nu)$ is defined as a sigmoidal function of wavelength (ν)

$$\gamma(\nu) = \frac{2\gamma_0}{1 + e^{a(\nu - \nu_0)}} \tag{6.4}$$

Full-width half-maxima (γ_0, FWHM) was bound between 1 and 100 nm, while center wavelength (ν_0) was constrained between 980 and 1010 nm. Correlation function in Pandas package (dataframe.corr) was applied for Spearman correlation in Figure 6.3 and Figure 6.4.

Protein properties calculation. IEP and MW are both given by the supplier. Protein structure is either obtained from protein databank (natural protein library, pdb code as shown in Figure 6.1) or simulated from ROSETTA (designed library, as shown in Figure 6.4). Protein visualization is performed by VMD 1.9.2. Percentage of secondary structure is estimated by Timeline plugin in VMD, while RSA is estimated by PyMol.

De novo design of protein. De novo protein library was initially designed as a demonstration of computational algorithm, of which the well-described design process was documented

in previous study.[253, 254] The proteins were selected on the basis of secondary structural composition and surface potential to diversify the overall features of individual protein for testing the interaction with DNA-SWCNT.

Protein overexpression. DNA encoded the protein sequence of de novo protein library was purchased from Twist Bioscience as DNA fragments, which were subsequently cloned into pET11b or pET21b expression vectors by Gibson cloning. For 4b1a_cry, 4b2a, SD_26, 4xq3, 3UDC, was flanked between NheI and BlpI restriction enzyme site of pET11b vector with 6× His tag attached at the N terminus. A 6× His tag was added at the C terminus of 4b1a_de, Ubi_005, 5cwj, FFLM, and 3HB designs and cloned between NheI and XhoI restriction sites of pET21b. Plasmids were transformed into *E. coli* BL21 (DE3) (Merck), and grown overnight in LB media supplemented with 100 µg/ml ampicillin. Overnight cultures were diluted to the optical density (OD_{600}) around 0.1 in TB medium and grown until the OD_{600} reached 0.6-0.8. Following with 1 mM of isopropyl β-d-1-thiogalactopyranoside (IPTG) was added for protein induction and cells were further grown for 12-16 hours at 22 °C. Collected bacterial pellet were harvested and resuspended in lysis buffer (50 mM Tris, pH 7.5, 500 mM NaCl, 5% glycerol, 1 mg/mL lysozyme, 1 mM PMSF, 1 μg/mL DNase), and lysed by sonication. The cell lysate was pelleted by centrifugation (20,000 rpm, 20 mins) and supernatant was filtered with a 0.22 µm filter before loading onto a 1 ml HisTrap HP column (GE Healthcare). Proteins bound to the column were washed with 10 column volumes of washing buffer (50 mM Tris, pH 7.5, 500 mM NaCl, 10 mM imidazole) and eluted in 5 column volumes of elution buffer (50 mM Tris, pH 7.5, 500 mM NaCl, 300 mM imidazole). Eluted proteins were further purified by size exclusion chromatography on a HiLoad 16/600 Superdex 75 pg column (GE Healthcare) in PBS buffer.

6.5 Supporting Information

Table 6.1 – DNA sequences used in Chapter 6.

Name	**Sequence (5' to 3')**
GT (or $(GT)_{15}$)	GTG TGT GTG TGT GTG TGT GTG TGT GTG TGT
ERV	GCA TGA ACT AAC GAT ATC CCT ATC AGG ACG
BHL	CAA TAT CAA TAA GGA TCC AAG TTA TGT TAC
BHH	CGC CCC GAG GGA GGA TCC AGA GCG TCC AAC
TCT	TCT CTC CTC TCT

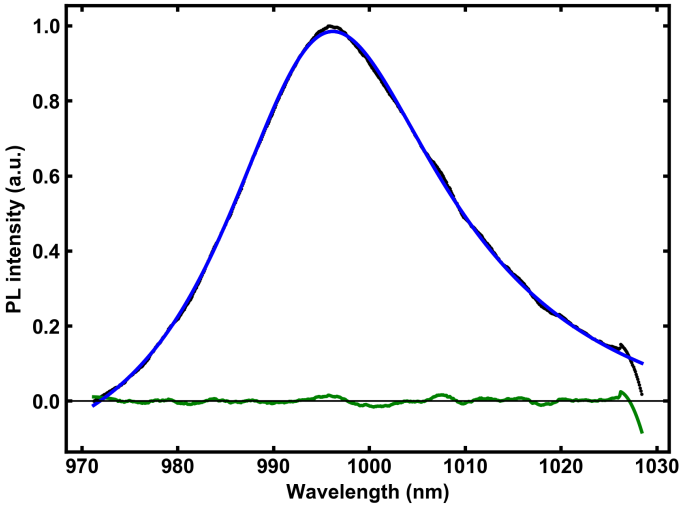

Figure S6.1 – NIR fluorescence spectrum of $(GT)_{15}$-SWCNT. The result (black) was fitted with skewed-Lorentzian function (blue), and the residual is shown in green.

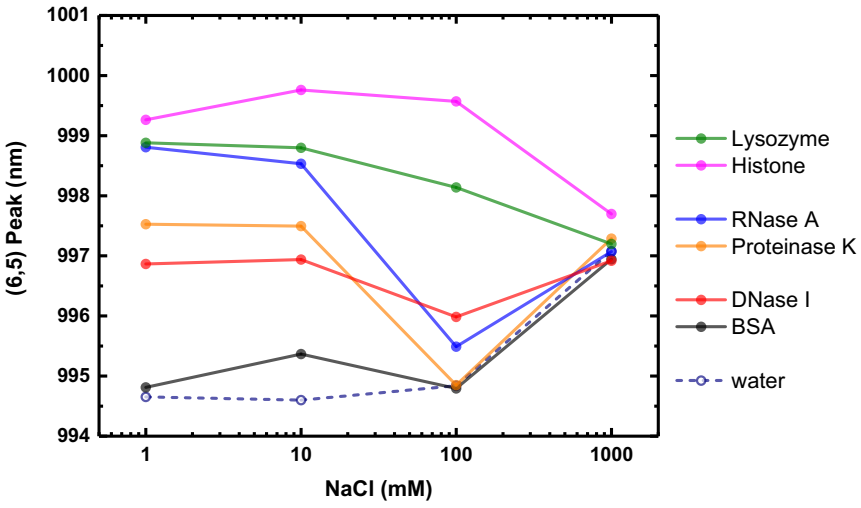

Figure S6.2 – (6,5) peak maxima of $(GT)_{15}$-SWCNT when incubating with various proteins.

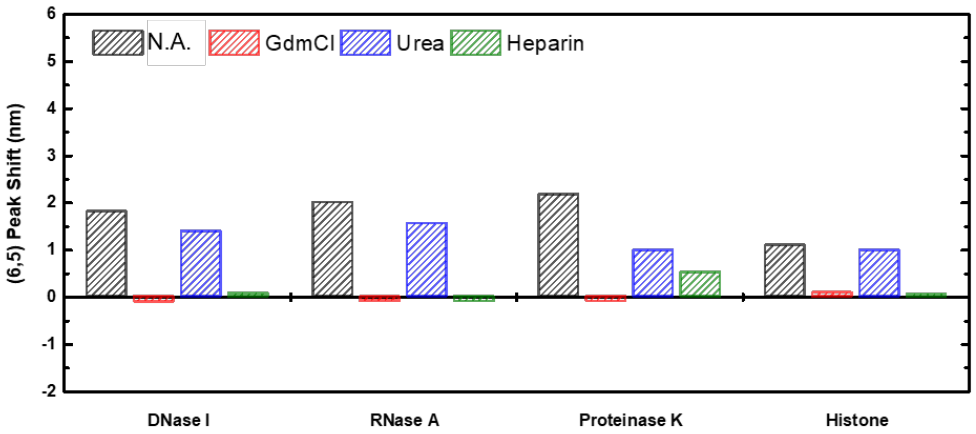

Figure S6.3 – Inhibitor experiment of SDC-SWCNT/protein. N.A.: no additive.

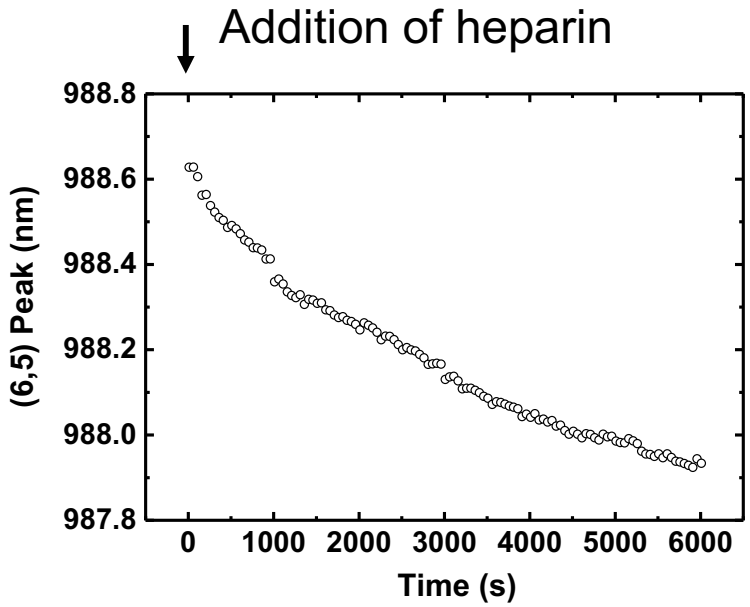

Figure S6.4 – Addition of heparin to SDC-SWCNT/RNase A causes the (6,5) fluorescence peak to shift back to characteristic maximum of SDC-SWCNT.

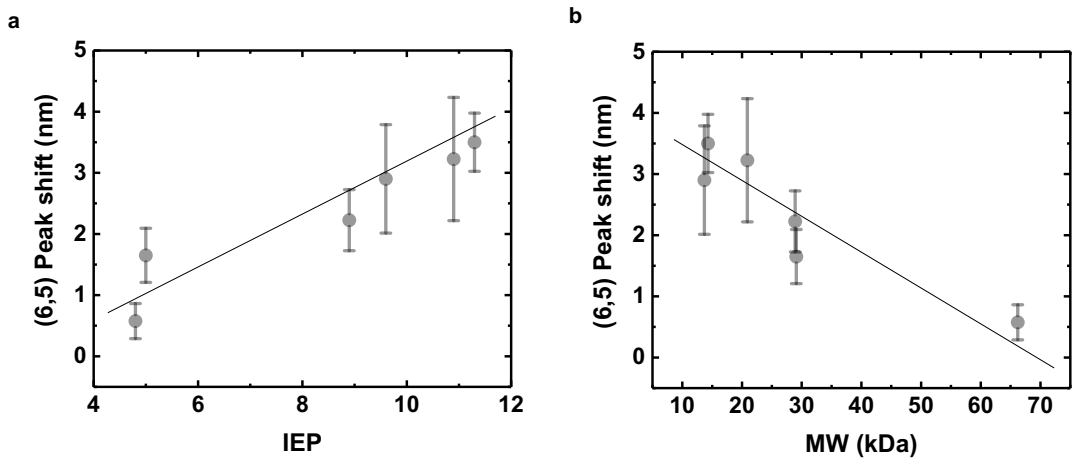

Figure S6.5 – $\Delta\lambda_{(6,5)}$ of ssDNA-SWCNT/protein at 1 mM NaCl in HEPES plotted against (a) IEP and (a) MW. Note lines are for eye guide.

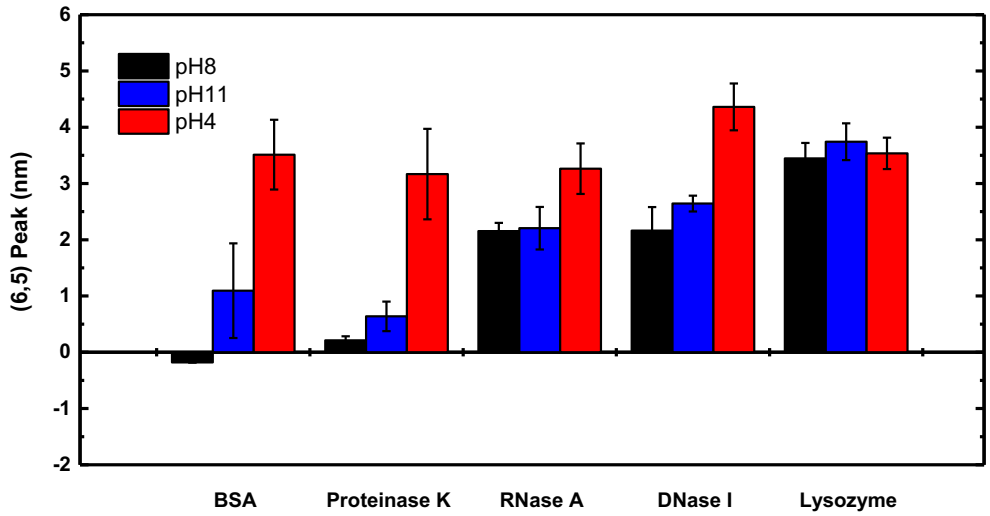

Figure S6.6 – $\Delta\lambda_{(6,5)}$ are dependent on pH. Note single sequence was used (TCT), and ssDNA-SWCNT was prepared by sonication.

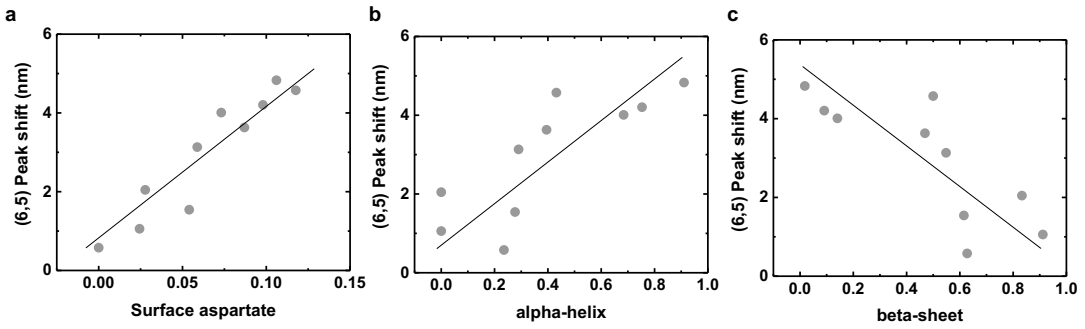

Figure S6.7 – Correlation of peak shift versus three different properties of de novo designed protein library: (a) surface Asp, (b) α-helix, and (c) β-sheet. Note lines are for eye guide instead of linear regressions.

7 General Conclusions and Outlook

In this thesis, we systematically investigated a ternary nano-bio hybrid as an optical biosensor composed of DNA, protein and SWCNT. In particular, we aim to monitor DNA–protein interaction via SWCNT NIR fluorescence. We began with developing two biochemical assays for analyzing DNA structures and DNA hybridization on SWCNTs: restriction enzyme analysis revealed the DNA conformation to be B-DNA lying on the SWCNT (Chapter 3), while nuclease-assisted fluorescence assay supported the proposition that DNA hybridization on SWCNT is a Watson-Crick specific pairing (Chapter 4). We marked the first experimental evidence of DNA duplex conformation on SWCNTs. These findings support the applicability of DNA technology when exploited within this ternary hybrid.

Next, we pioneered applying DNA-protein-SWCNT in two configurations (Chapter 5): DNA-protein conjugate and DNA-protein interaction. Using DNA-specific hybridization, we enabled conjugation of proteins to the surface of the SWCNT, including constructing DNA-HRP-SWCNTs as a turn-on NIR fluorescence sensor of H_2O_2. On the other hand, two nuclease systems, RE and Cas9, retained their enzymatic activity on SWCNTs, exhibiting a potential sensing platform for DNA-protein interactions.

Lastly, we combined protein library screening and rational protein design to reduce non-specific interactions in DNA-SWCNT/protein hybrids (Chapter 6. In addition to electrostatic interactions, we also hypothesize cooperative interactions including hydrogen bonding may be critical, especially for exposed Asp on α-helices.

Altogether, our discoveries outlined in this thesis have demonstrated the impressive potential of DNA-protein-SWCNT hybrids. Below, we highlight some future perspectives.

1) DNA technology and other potential applications

In Chapter 3 and Chapter 4, we described the development of two assays for investigating the structure-function relationship in DNA-SWCNT hybrids. However, as we mentioned in Chapter 4, the relationship of DNA hybridization and NIR fluorescence remains ambiguous. To improve this,more DNA sequences could be investigated in order to better understand the

influence of factors such as the length and the GC content of dsDNA. The design of anchoring sequences may also be reconsidered. On the other hand, the concept of our assay can be readily applied to construct assays for different systems, such as microRNA hybridization on SWCNTs in diagnostic applications.

Furthermore, our assays provide crucial parameters and allow other advanced applications to be easily characterized and optimized. For example, a nanoscale 'thermometer' can be built up based on the denaturation of DNA bound to SWCNTs. By exploiting the toehold-mediated displacement of DNA, dynamic hybridization of DNA on SWCNTs can also be applied for DNA circuit applications, where SWCNTs offer a platform for the localization of DNA that could potentially boost the reactions. Single molecule sensing on the surface substrate and electrical measurements through SWCNT FET would be easily achieved, with our presented assays serving as complementary methods for analyzing the response and for condition optimization.[255, 256]

2) DNA-Protein-SWCNT conjugation

Using DNA hybridization, we have enabled DNA-protein-SWCNT conjugation. Instead of using biotin-streptavidin, we can employ one-to-one DNA-protein conjugates to obtain a more controllable system by avoiding the formation of oligomers. Furthermore, we envision a great number of other potential applications should the range of proteins used in the hybrids be expanded. In addition to HRP, by simply using the same concept and platform, we can also implement glucose oxidase (GOx) for glucose detection, aldehyde dehydrogenase (ALDH) for aldehyde detection, or monoamine oxidase (MAO) for dopamine detection.

The distinctive characteristics of DNA can be fully exploited for advanced applications of this ternary hybrid. First, the specificity of DNA hybridization allows us to produce multimodal sensing platforms or enzyme cascades in close proximity. As an example, we can conjugate DNA sequence 1 to GOx and sequence 2 to HRP. With a ssDNA-SWCNT containing complementary sequences of both 1 and 2, we can immobilize GOx and HRP in close proximity on the same SWCNT. Upon the addition of glucose, the sequential reaction of redox reactions catalyzed by GOx and HRP can be monitored.

Secondly, DNA is a responsive material. In Chapter 5, we have shown it can release proteins from SWCNTs by DNA reacting to small molecules (urea) and restriction enzymes. Likewise, temperature response and other targets of interest can be achieved with DNA design. For example, the length and GC content of the DNA can be varied in order to tune the DNA melting temperature, while deoxyribozymes (DNAzyme) can react to metallic cations. Finally, DNA allows additional nanostructure(s) to be incorporated in the hybrid. Structure of DNA origami has been shown to be effectively preserved on SWCNTs, allowing single SWCNT positioning. As a result, an orthogonal array of proteins and SWCNTs can be generated.

3) Detection of DNA-protein interactions

As we demonstrated in Chapter 5, SWCNTs are an extremely promising material for the detection of DNA-protein interactions. To achieve this goal, in Chapter 6, we successfully applied site-directed mutagenesis on a low-response protein to enhance its fluorescence response in ssDNA-SWCNT/protein hybrids. Conversely, we believe that by knocking out Asp from high-response proteins, such as Cas9, we can reduce non-specific adsorptions that may 'cover' the SWCNT response of specific DNA-protein interactions. Unravelling how Asp strongly participates in the interaction would be of great interest. Our approach of identifying deterministic factors (i.e., protein library screening and protein engineering) can be applied for a larger library size of proteins, including different IEPs and MWs. Different DNA sequences with biological interest, such as telomere and upstream activating sequences, could be potentially included.

Another challenge when using SWCNTs for detecting DNA-protein interactions originates from the fact that the permittivity of the DNA and the protein are at the same order of magnitude ($\epsilon_{dsDNA} \approx 8$ and $\epsilon_{protein} \approx 2-4$, respectively), in comparison with water ($\epsilon_{water} \approx 80$).[257] Consequently, DNA and proteins intrinsically impose a similar level of screening on the exciton in SWCNTs, leading to a low response of SWCNT fluorescence when DNA-protein interactions occur on SWCNTs. To tackle this challenge, we aim to introduce sp^3-defects on the SWCNT sidewalls to fine tune the SWCNT optical band diagram and exciton dynamics, without diminishing the SWCNT fluorescence. Without including extra additives, sp^3-defect has been proven to be an effective strategy to immobilize macromolecules on SWCNTs and modify the fluorescence response.[64, 258] We propose the use of such sp^3-defects as 'amplifiers' of NIR fluorescence. Recently, we have successfully reacted SWCNTs with 1-azido-4-iodobenzene, 4-iodobenzyl amine, and 4-iodobenzoic acid by a simple photoactivating reaction (Figure 7.1). These functional groups (azide, carboxylic acid, amino) are useful for further Click chemistry with other molecules, such as proteins and DNA. Meanwhile, the fluorescence of SWCNT is enhanced and modified (Figure 7.1).

Finally, we foresee the combination of protein engineering and amplifier design, in order to complete an optical sensing platform for DNA-protein interactions. The NIR fluorescence would enable both in vitro and in vivo sensing applications. In the near future, epigenetic modification of DNA or post-translational modification (PTM) of proteins may both be achievable. Such new platforms can be further useful as assays for directed evolution of protein engineering. As an example, we can screen Cas9 variants with different PAM site activation or reduced off-target binding, based on the SWCNT NIR fluorescence changes.[31].

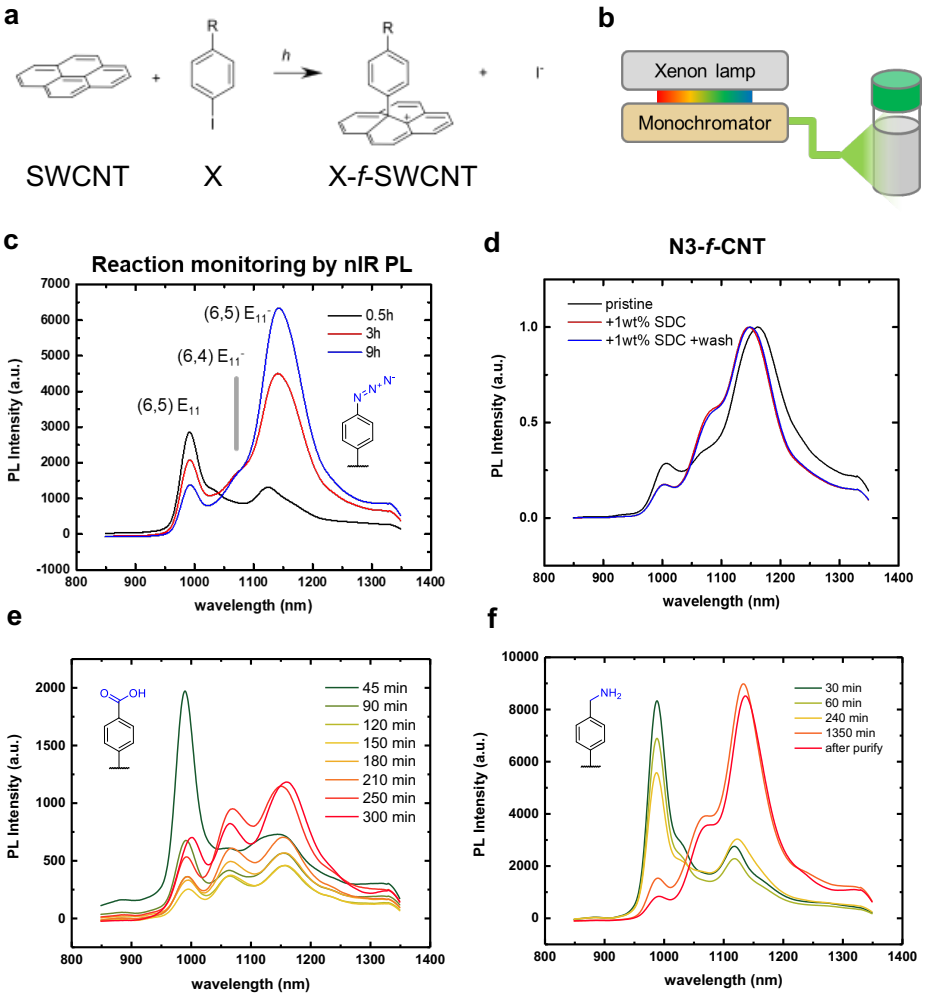

Figure 7.1 – Defect chemistry activates SWCNTs with various functional groups. (a) Reaction scheme. (b) Brief experimental setup. (c) Reaction of azido-4-iodobenzene with CoMoCAT SWCNT. The reaction is monitored using the evolution of the characteristic peak at 1150 nm. (d) N3-f-CNT as purified. (e) Reaction of 4-iodobenzoic acid. (f) Reaction of 4-iodobenzyl amine.

Bibliography

(1) Kirsanov, D. D.; Zanegina, O. N.; Aksianov, E. A.; Spirin, S. A.; Karyagina, A. S.; Alexeevski, A. V. *Nucleic Acids Research* **2013**, *41*, D517–23.

(2) Saecker, R. M. In *eLS*; American Cancer Society: 2007.

(3) Privalov, P. L.; Dragan, A. I.; Crane-Robinson, C. *Nucleic Acids Research* **2011**, *39*, 2483–91.

(4) Sathyapriya, R.; Vishveshwara, S. *Nucleic Acids Research* **2004**, *32*, 4109–4118.

(5) Luscombe, N. M.; Laskowski, R. A.; Thornton, J. M. *Nucleic Acids Research* **2001**, *29*, 2860–2874.

(6) Moss, T.; Leblanc, B., *DNA-Protein Interactions*; Tom Moss, B. L., Ed.; Methods in Molecular Biology, Vol. 543; Springer: 2009.

(7) Yuan, L.; Perry, S. E., *Plant Transcription Factors*; L. Yuan, S. E. P., Ed.; Methods in Molecular Biology, Vol. 754; Springer: 2011.

(8) Gotrik, M. R.; Feagin, T. A.; Csordas, A. T.; Nakamoto, M. A.; Soh, H. T. *Accounts of Chemical Research* **2016**, *49*, 1903–1910.

(9) Zhou, J.; Rossi, J. *Nat Rev Drug Discov* **2017**, *16*, 181–202.

(10) Ouwerkerk, P. B. F.; Meijer, A. H. *Current Protocols in Molecular Biology* **2001**, *55*, 12.12.1–12.12.12.

(11) Campagne, S.; Gervais, V.; Milon, A. *J R Soc Interface* **2011**, *8*, 1065–78.

(12) Makowski, M. M.; Grawe, C.; Foster, B. M.; Nguyen, N. V.; Bartke, T.; Vermeulen, M. *Nat Commun* **2018**, *9*, 1653.

(13) Hellman, L. M.; Fried, M. G. *Nat Protoc* **2007**, *2*, 1849–61.

(14) Kruss, S.; Landry, M. P.; Vander Ende, E.; Lima, B. M. A.; Reuel, N. F.; Zhang, J.; Nelson, J.; Mu, B.; Hilmer, A.; Strano, M. *Journal of the American Chemical Society* **2014**, *136*, 713–724.

(15) Anderson, B. J.; Larkin, C.; Guja, K.; Schildbach, J. F., *Using Fluorophore-Labeled Oligonucleotides to Measure Affinities of Protein–DNA Interactions*; Methods in Enzymology, Vol. 450, 2008.

(16) Jerabek-Willemsen, M.; André, T.; Wanner, R.; Roth, H. M.; Duhr, S.; Baaske, P.; Breitsprecher, D. *Journal of Molecular Structure* **2014**, *1077*, 101–113.

(17) Xu, J.; Liu, K. W.; Matthews, K. S.; Biswal, S. L. *Langmuir* **2011**, *27*, 4900–5.

(18) Yang, T. C.; Catalano, C. E.; Maluf, N. K., *Analytical Ultracentrifugation as a Tool to Study Nonspecific Protein-DNA Interactions*; Methods Enzymol, Vol. 562, 2015.

(19) Liu, S.; Zhang, X.; Luo, W.; Wang, Z.; Guo, X.; Steigerwald, M. L.; Fang, X. *Angewandte Chemie* **2011**, *50*, 2496–502.

(20) Nasiri Khonsari, Y.; Sun, S. *Chemical Communications* **2017**, *53*, 9042–9054.

(21) Ritzefeld, M.; Sewald, N. *J Amino Acids* **2012**, *2012*, 816032.

(22) Hwang, H.; Myong, S. *Chemical Society Reviews* **2014**, *43*, 1221–9.

(23) Collins, B. E.; Ye, L. F.; Duzdevich, D.; Greene, E. C. *Methods Cell Biol* **2014**, *123*, 217–34.

(24) Lyubchenko, Y. L.; Shlyakhtenko, L. S. *Crit Rev Eukaryot Gene Expr* **2016**, *26*, 63–96.

(25) Camborde, L.; Jauneau, A.; Briere, C.; Deslandes, L.; Dumas, B.; Gaulin, E. *Nat Protoc* **2017**, *12*, 1933–1950.

(26) Brenowitz, M.; Senear, D. F.; Kingston, R. E. *Current Protocols in Molecular Biology* **1989**, *7*, 12.4.1–12.4.16.

(27) Uphoff, S.; Reyes-Lamothe, R.; Garza de Leon, F.; Sherratt, D. J.; Kapanidis, A. N. *Proceedings of the National Academy of Sciences of the United States of America* **2013**, *110*, 8063–8.

(28) Charlier, J.-C.; Blase, X.; Roche, S. *Reviews of Modern Physics* **2007**, *79*, 677–732.

(29) Zhang, J.; Boghossian, A. A.; Barone, P. W.; Rwei, A.; Kim, J.-H.; Lin, D.; Heller, D. A.; Hilmer, A. J.; Nair, N.; Reuel, N. F.; Strano, M. S. *Journal of the American Chemical Society* **2011**, *133*, 567–581.

(30) Landry, M. P.; Ando, H.; Chen, A. Y.; Cao, J.; Kottadiel, V. I.; Chio, L.; Yang, D.; Dong, J.; Lu, T. K.; Strano, M. S. *Nature Nanotechnology* **2017**, *12*, 368–377.

(31) Wu, S.-J.; Schuergers, N.; Lin, K.-H.; Gillen, A. J.; Corminboeuf, C.; Boghossian, A. A. *ACS Appl Mater Interfaces* **2018**, *10*, 37386–37395.

(32) Bisker, G.; Dong, J.; Park, H. D.; Iverson, N. M.; Ahn, J.; Nelson, J. T.; Landry, M. P.; Kruss, S.; Strano, M. S. *Nat Commun* **2016**, *7*, 10241.

(33) Yaron, P. N.; Holt, B. D.; Short, P. A.; Lösche, M.; Islam, M. F.; Dahl, K. N. *Journal of Nanobiotechnology* **2011**, *9*, 45.

(34) Kupis-Rozmysłowicz, J.; Antonucci, A.; Boghossian, A. A. *ECS Journal of Solid State Science and Technology* **2016**, *5*, M3067–M3074.

(35) Antonucci, A.; Kupis-Rozmysłowicz, J.; Boghossian, A. A. *ACS Appl Mater Interfaces* **2017**, *9*, 11321–11331.

(36) SantaLucia, J.; Allawi, H. T.; Seneviratne, P. A. *Biochemistry* **1996**, *35*, 3555–3562.

(37) Gruenwedel, D. W. *European Journal of Biochemistry* **1994**, *219*, 491–496.

(38) Szabat, M.; Kierzek, R. *The FEBS Journal* **2017**, *284*, 3986–3998.

(39) Phan, A. T.; Leroy, J.-L. *Journal of Biomolecular Structure and Dynamics* **2000**, *17*, 245–251.

(40) Kishi, J. Y.; Lapan, S. W.; Beliveau, B. J.; West, E. R.; Zhu, A.; Sasaki, H. M.; Saka, S. K.; Wang, Y.; Cepko, C. L.; Yin, P. *Nat Methods* **2019**, *16*, 533–544.

(41) Tian, Y.; Lhermitte, J. R.; Bai, L.; Vo, T.; Xin, H. L.; Li, H.; Li, R.; Fukuto, M.; Yager, K. G.; Kahn, J. S.; Xiong, Y.; Minevich, B.; Kumar, S. K.; Gang, O. *Nature Materials* **2020**, *19*, 789–796.

(42) Zhang, D. Y.; Seelig, G. *Nature Chemistry* **2011**, *3*, 103–113.

(43) Knott, G. J.; Doudna, J. A. *Science* **2018**, *361*, 866–869.

(44) Yilmaz, L. S.; Noguera, D. R. *Applied and Environment Microbiology* **2004**, *70*, 7126–39.

(45) Church, G. M.; Gao, Y.; Kosuri, S. *Science* **2012**, *337*, 1628–1628.

(46) Koch, J.; Gantenbein, S.; Masania, K.; Stark, W. J.; Erlich, Y.; Grass, R. N. *Nature Biotechnology* **2020**, *38*, 39–43.

(47) Zhang, R. K.; Chen, K.; Huang, X.; Wohlschlager, L.; Renata, H.; Arnold, F. H. *Nature* **2019**, *565*, 67–72.

(48) Kan, S. B. J.; Lewis, R. D.; Chen, K.; Arnold, F. H. *Science* **2016**, *354*, 1048–1051.

(49) Huang, P.-S.; Feldmeier, K.; Parmeggiani, F.; Fernandez Velasco, D. A.; Höcker, B.; Baker, D. *Nature Chemical Biology* **2015**, *12*, 29.

(50) Kleinstiver, B. P.; Prew, M. S.; Tsai, S. Q.; Topkar, V. V.; Nguyen, N. T.; Zheng, Z.; Gonzales, A. P.; Li, Z.; Peterson, R. T.; Yeh, J. R.; Aryee, M. J.; Joung, J. K. *Nature* **2015**, *523*, 481–5.

(51) Hu, J. H.; Miller, S. M.; Geurts, M. H.; Tang, W.; Chen, L.; Sun, N.; Zeina, C. M.; Gao, X.; Rees, H. A.; Lin, Z.; Liu, D. R. *Nature* **2018**, *556*, 57.

(52) Miller, S. M.; Wang, T.; Randolph, P. B.; Arbab, M.; Shen, M. W.; Huang, T. P.; Matuszek, Z.; Newby, G. A.; Rees, H. A.; Liu, D. R. *Nature Biotechnology* **2020**, *38*, 471–481.

(53) Pattanayak, V.; Lin, S.; Guilinger, J. P.; Ma, E.; Doudna, J. A.; Liu, D. R. *Nat Biotech* **2013**, *31*, 839–843.

(54) Kleinstiver, B. P.; Pattanayak, V.; Prew, M. S.; Tsai, S. Q.; Nguyen, N. T.; Zheng, Z.; Joung, J. K. *Nature* **2016**, *529*, 490–495.

(55) Boyle, E. A.; Andreasson, J. O. L.; Chircus, L. M.; Sternberg, S. H.; Wu, M. J.; Guegler, C. K.; Doudna, J. A.; Greenleaf, W. J. *Proceedings of the National Academy of Sciences of the United States of America* **2017**, *114*, 5461–5466.

(56) McIsaac, R. S.; Engqvist, M. K. M.; Wannier, T.; Rosenthal, A. Z.; Herwig, L.; Flytzanis, N. C.; Imasheva, E. S.; Lanyi, J. K.; Balashov, S. P.; Gradinaru, V.; Arnold, F. H. *Proceedings of the National Academy of Sciences* **2014**, *111*, 13034–13039.

(57) Flytzanis, N. C.; Bedbrook, C. N.; Chiu, H.; Engqvist, M. K. M.; Xiao, C.; Chan, K. Y.; Sternberg, P. W.; Arnold, F. H.; Gradinaru, V. *Nature Communications* **2014**, *5*, 4894.

(58) Benedict, L. X.; Louie, S. G.; Cohen, M. L. *Phys. Rev. B* **1995**, *52*, 8541–8549.

(59) Marinopoulos, A. G.; Reining, L.; Rubio, A.; Vast, N. *Phys. Rev. Lett.* **2003**, *91*, 046402.

(60) Weisman, R. B.; Bachilo, S. M. *Nano Letters* **2003**, *3*, 1235–1238.

(61) Kiowski, O.; Lebedkin, S.; Hennrich, F.; Malik, S.; Rösner, H.; Arnold, K.; Sürgers, C.; Kappes, M. M. *Physical Review B* **2007**, *75*, 075421.

(62) Choi, J. H.; Strano, M. S. *Applied Physics Letters* **2007**, *90*, 223114.

(63) Cherukuri, T. K.; Tsyboulski, D. A.; Weisman, R. B. *ACS Nano* **2012**, *6*, 843–850.

(64) Piao, Y.; Meany, B.; Powell, L. R.; Valley, N.; Kwon, H.; Schatz, G. C.; Wang, Y. *Nat Chem* **2013**, *5*, 840.

(65) Khripin, C. Y.; Arnold-Medabalimi, N.; Zheng, M. *ACS Nano* **2011**, *5*, 8258–8266.

(66) Iijima, S.; Ichihashi, T. *Nature* **1993**, *363*, 603–605.

(67) Lu, F.; Gu, L.; Meziani, M. J.; Wang, X.; Luo, P. G.; Veca, L. M.; Cao, L.; Sun, Y.-P. *Advanced Materials* **2009**, *21*, 139–152.

(68) Blackburn, J. L.; McDonald, T. J.; Metzger, W. K.; Engtrakul, C.; Rumbles, G.; Heben, M. J. *Nano Letters* **2008**, *8*, 1047–1054.

(69) Strano, M. S.; Huffman, C. B.; Moore, V. C.; O'Connell, M. J.; Haroz, E. H.; Hubbard, J.; Miller, M.; Rialon, K.; Kittrell, C.; Ramesh, S.; Hauge, R. H.; Smalley, R. E. *The Journal of Physical Chemistry B* **2003**, *107*, 6979–6985.

(70) Barone, P. W.; Baik, S.; Heller, D. A.; Strano, M. S. *Nat Mater* **2005**, *4*, 86–92.

(71) Jeng, E. S.; Barone, P. W.; Nelson, J. D.; Strano, M. S. *Small* **2007**, *3*, 1602–1609.

(72) Harvey, J. D.; Jena, P. V.; Baker, H. A.; Zerze, G. H.; Williams, R. M.; Galassi, T. V.; Roxbury, D.; Mittal, J.; Heller, D. A. *Nature Biomedical Engineering* **2017**, *1*, 0041.

(73) Sen, F.; Boghossian, A. A.; Sen, S.; Ulissi, Z. W.; Zhang, J.; Strano, M. S. *ACS Nano* **2012**, *6*, 10632–10645.

(74) Boyer, P. D.; Ganesh, S.; Qin, Z.; Holt, B. D.; Buehler, M. J.; Islam, M. F.; Dahl, K. N. *ACS Applied Materials and Interfaces* **2016**, *8*, 3524–3534.

(75) Demirer, G. S.; Zhang, H.; Matos, J. L.; Goh, N. S.; Cunningham, F. J.; Sung, Y.; Chang, R.; Aditham, A. J.; Chio, L.; Cho, M.-J.; Staskawicz, B.; Landry, M. P. *Nature Nanotechnology* **2019**, *14*, 456–464.

(76) Demirer, G. S.; Zhang, H.; Goh, N. S.; Pinals, R. L.; Chang, R.; Landry, M. P. *Science Advances* **2020**, *6*, eaaz0495.

(77) Wong, M. H.; Misra, R. P.; Giraldo, J. P.; Kwak, S. Y.; Son, Y.; Landry, M. P.; Swan, J. W.; Blankschtein, D.; Strano, M. S. *Nano Letters* **2016**, *16*, 1161–1172.

(78) Maune, H. T.; Han, S.-p.; Barish, R. D.; Bockrath, M.; Goddard, I. I. A.; RothemundPaul, W. K.; Winfree, E. *Nat Nano* **2010**, *5*, 61–66.

(79) Sun, W. et al. *Science* **2020**, *368*, 874–877.

(80) Zhao, M.; Chen, Y.; Wang, K.; Zhang, Z.; Streit, J. K.; Fagan, J. A.; Tang, J.; Zheng, M.; Yang, C.; Zhu, Z.; Sun, W. *Science* **2020**, *368*, 878–881.

(81) Park, M.; Park, J.; Lee, J.; Ju, S.-Y. *Carbon* **2018**, *139*, 427–436.

(82) Lee, H. W. et al. *Nat Commun* **2011**, *2*, 541.

(83) Budhathoki-Uprety, J.; Shah, J.; Korsen, J. A.; Wayne, A. E.; Galassi, T. V.; Cohen, J. R.; Harvey, J. D.; Jena, P. V.; Ramanathan, L. V.; Jaimes, E. A.; Heller, D. A. *Nature Communications* **2019**, *10*, 3605.

(84) Lei, T.; Chen, X.; Pitner, G.; Wong, H.-S. P.; Bao, Z. *Journal of the American Chemical Society* **2016**, *138*, 802–805.

(85) Hasan, T.; Scardaci, V.; Tan, P.; Rozhin, A. G.; Milne, W. I.; Ferrari, A. C. *The Journal of Physical Chemistry C* **2007**, *111*, 12594–12602.

(86) Barone, P. W.; Strano, M. S. *Angewandte Chemie* **2006**, *45*, 8138–41.

(87) Jin, H.; Heller, D. A.; Kalbacova, M.; Kim, J.-H.; Zhang, J.; Boghossian, A. A.; Maheshri, N.; Strano, M. S. *Nature Nanotechnology* **2010**, *5*, 302–309.

(88) Zheng, M.; Jagota, A.; Semke, E. D.; Diner, B. A.; McLean, R. S.; Lustig, S. R.; Richardson, R. E.; Tassi, N. G. *Nature Materials* **2003**, *2*, 338–342.

(89) Lambert, B.; Gillen, A. J.; Schuergers, N.; Wu, S.-J.; Boghossian, A. A. *Chemical Communications* **2019**, *55*, 3239–3242.

(90) Lambert, B. P.; Gillen, A. J.; Boghossian, A. A. *The Journal of Physical Chemistry Letters* **2020**, *11*, 4791–4802.

(91) Jeong, S.; Yang, D.; Beyene, A. G.; Del Bonis-O'Donnell, J. T.; Gest, A. M. M.; Navarro, N.; Sun, X.; Landry, M. P. *Science Advances* **2019**, *5*, eaay3771.

(92) Yang, K. K.; Wu, Z.; Arnold, F. H. *Nature Methods* **2019**, *16*, 687–694.

(93) Hughes, M. E.; Brandin, E.; Golovchenko, J. A. *Nano Letters* **2007**, *7*, 1191–1194.

(94) Meng, S.; Maragakis, P.; Papaloukas, C.; Kaxiras, E. *Nano Letters* **2007**, *7*, 45–50.

(95) Xiao, Z.; Wang, X.; Xu, X.; Zhang, H.; Li, Y.; Wang, Y. *The Journal of Physical Chemistry C* **2011**, *115*, 21546–21558.

(96) Fernando, A.; Mary, E. H.; Jene, A. G.; Daniel, B. *Nanotechnology* **2009**, *20*, 395101.

(97) Johnson, R. R.; Johnson, A. T. C.; Klein, M. L. *Nano Letters* **2008**, *8*, 69–75.

(98) Zheng, M. *Science* **2003**, *302*, 1545–1548.

(99) Johnson, R. R.; Kohlmeyer, A.; Johnson, A. T. C.; Klein, M. L. *Nano Letters* **2009**, *9*, 537–541.

(100) Roxbury, D.; Manohar, S.; Jagota, A. *The Journal of Physical Chemistry C* **2010**, *114*, 13267–13276.

(101) Beyene, A. G.; Alizadehmojarad, A. A.; Dorlhiac, G.; Goh, N.; Streets, A. M.; Král, P.; Vuković, L.; Landry, M. P. *Nano Letters* **2018**, *18*, 6995–7003.

(102) Alizadehmojarad, A. A.; Zhou, X.; Beyene, A. G.; Chacon, K. E.; Sung, Y.; Pinals, R. L.; Landry, M. P.; Vuković, L. *Advanced Materials Interfaces* **2020**, 2000353.

(103) Müller, K.; Malik, S.; Richert, C. *ACS Nano* **2010**, *4*, 649–656.

(104) Hain, T. C.; Kroker, K.; Stich, D. G.; Hertel, T. *Soft Matter* **2012**, *8*, 2820–2823.

(105) Xu, X.; Clément, P.; Eklöf-Österberg, J.; Kelley-Loughnane, N.; Moth-Poulsen, K.; Chávez, J. L.; Palma, M. *Nano Letters* **2018**, *18*, 4130–4135.

(106) Atsumi, H.; Belcher, A. M. *ACS Nano* **2018**, *12*, 7986–7995.

(107) Zhao, X.; Johnson, J. K. *Journal of the American Chemical Society* **2007**, *129*, 10438–10445.

(108) Cathcart, H.; Nicolosi, V.; Hughes, J. M.; Blau, W. J.; Kelly, J. M.; Quinn, S. J.; Coleman, J. N. *Journal of the American Chemical Society* **2008**, *130*, 12734–12744.

(109) Shiraki, T.; Tsuzuki, A.; Toshimitsu, F.; Nakashima, N. *Chemistry- A European Journal* **2016**, *22*, 4774–4779.

(110) Bascom, G.; Andricioaei, I. *The Journal of Physical Chemistry C* **2014**, *118*, 29441–29447.

(111) Calvaresi, M.; Zerbetto, F. *Accounts of Chemical Research* **2013**, *46*, 2454–2463.

(112) Nepal, D.; Geckeler, K. E. *Small* **2007**, *3*, 1259–1265.

(113) Yoon, H.; Ahn, J. H.; Barone, P. W.; Yum, K.; Sharma, R.; Boghossian, A. A.; Han, J. H.; Strano, M. S. *Angewandte Chemie* **2011**, *50*, 1828–31.

(114) Zubkovs, V.; Schuergers, N.; Lambert, B.; Ahunbay, E.; Boghossian, A. A. *Small* **2017**, *13*, 1701654.

(115) Grigoryan, G.; Kim, Y. H.; Acharya, R.; Axelrod, K.; Jain, R. M.; Willis, L.; Drndic, M.; Kikkawa, J. M.; DeGrado, W. F. *Science* **2011**, *332*, 1071–6.

(116) Han, S.-P.; Maune, H. T.; Barish, R. D.; Bockrath, M.; Goddard, W. A. *Nano Letters* **2012**, *12*, 1129–1135.

(117) He, Z.; Zhou, J. *Carbon* **2014**, *78*, 500–509.

(118) Zorbas, V.; Smith, A. L.; Xie, H.; Ortiz-Acevedo, A.; Dalton, A. B.; Dieckmann, G. R.; Draper, R. K.; Baughman, R. H.; Musselman, I. H. *Journal of the American Chemical Society* **2005**, *127*, 12323–12328.

(119) Hirano, A.; Tanaka, T.; Kataura, H.; Kameda, T. *Chemistry* **2014**, *20*, 4922–30.

(120) Heller, D. A.; Pratt, G. W.; Zhang, J.; Nair, N.; Hansborough, A. J.; Boghossian, A. A.; Reuel, N. F.; Barone, P. W.; Strano, M. S. *Proc Natl Acad Sci U S A* **2011**, *108*, 8544–9.

(121) Roxbury, D.; Zhang, S. Q.; Mittal, J.; Degrado, W. F.; Jagota, A. *J Phys Chem C* **2013**, *117*, 26255–26261.

(122) Mann, F. A.; Horlebein, J.; Meyer, N. F.; Meyer, D.; Thomas, F.; Kruss, S. *Chemistry - A European Journal* **2018**, *24*, 12241–12245.

(123) Wang, S.; Humphreys, E. S.; Chung, S. Y.; Delduco, D. F.; Lustig, S. R.; Wang, H.; Parker, K. N.; Rizzo, N. W.; Subramoney, S.; Chiang, Y. M.; Jagota, A. *Nature Materials* **2003**, *2*, 196–200.

(124) Zheng, L.; Jain, D.; Burke, P. *The Journal of Physical Chemistry C* **2009**, *113*, 3978–3985.

(125) Yu, T.; Gong, Y.; Lu, T.; Wei, L.; Li, Y.; Mu, Y.; Chen, Y.; Liao, K. *RSC Advances* **2012**, *2*, 1466–1476.

(126) Holt, B. D.; McCorry, M. C.; Boyer, P. D.; Dahl, K. N.; Islam, M. F. *Nanoscale* **2012**, *4*, 7425–34.

(127) Palwai, N. R.; Martyn, D. E.; Neves, L. F. F.; Tan, Y.; Resasco, D. E.; Harrison, R. G. *Nanotechnology* **2007**, *18*, 235601.

(128) Tsai, T.-W.; Heckert, G.; Neves, L. F.; Tan, Y.; Kao, D.-Y.; Harrison, R. G.; Resasco, D. E.; Schmidtke, D. W. *Analytical Chemistry* **2009**, *81*, 7917–7925.

(129) Gu, Z.; Yang, Z.; Chong, Y.; Ge, C.; Weber, J. K.; Bell, D. R.; Zhou, R. *Scientific Reports* **2015**, *5*, 10886.

(130) Frise, A. E.; Edri, E.; Furó, I.; Regev, O. *J Phys Chem Lett* **2010**, *1*, 1414–1419.

(131) Thomas, S. K.; Jamieson, W. D.; Gwyther, R. E. A.; Bowen, B. J.; Beachey, A.; Worthy, H. L.; Macdonald, J. E.; Elliott, M.; Castell, O. K.; Jones, D. D. *Bioconjugate Chemistry* **2020**, *31*, 584–594.

(132) Freeley, M.; Worthy, H. L.; Ahmed, R.; Bowen, B.; Watkins, D.; Macdonald, J. E.; Zheng, M.; Jones, D. D.; Palma, M. *Journal of the American Chemical Society* **2017**, *139*, 17834–17840.

(133) Chen, X.; Wang, Y.; Wang, P. *Langmuir* **2015**, *31*, 397–403.

(134) Gong, X.; Sharma, A. K.; Strano, M. S.; Mukhopadhyay, D. *ACS Nano* **2014**, *8*, 9126–9136.

(135) Pinals, R. L.; Yang, D.; Lui, A.; Cao, W.; Landry, M. P. *Journal of the American Chemical Society* **2020**, *142*, 1254–1264.

(136) Nii, D.; Hayashida, T.; Yamaguchi, Y.; Ikawa, S.; Shibata, T.; Umemura, K. *Colloids Surf B Biointerfaces* **2014**, *121*, 325–330.

(137) Williams, R. M.; Lee, C.; Galassi, T. V.; Harvey, J. D.; Leicher, R.; Sirenko, M.; Dorso, M. A.; Shah, J.; Olvera, N.; Dao, F.; Levine, D. A.; Heller, D. A. *Science Advances* **2018**, *4*.

(138) Olsen, T. J.; Choi, Y.; Sims, P. C.; Gul, O. T.; Corso, B. L.; Dong, C.; Brown, W. A.; Collins, P. G.; Weiss, G. A. *Journal of the American Chemical Society* **2013**, *135*, 7855–7860.

(139) Ahn, J.-H.; Kim, J.-H.; Reuel, N. F.; Barone, P. W.; Boghossian, A. A.; Zhang, J.; Yoon, H.; Chang, A. C.; Hilmer, A. J.; Strano, M. S. *Nano Letters* **2011**, *11*, 2743–2752.

(140) Nelson, J. T.; Kim, S.; Reuel, N. F.; Salem, D. P.; Bisker, G.; Landry, M. P.; Kruss, S.; Barone, P. W.; Kwak, S.; Strano, M. S. *Analytical Chemistry* **2015**, *87*, 8186–8193.

(141) Ham, M.-H. et al. *Nat Chem* **2010**, *2*, 929–936.

(142) Goldsmith, B. R.; Mitala, J. J.; Josue, J.; Castro, A.; Lerner, M. B.; Bayburt, T. H.; Khamis, S. M.; Jones, R. A.; Brand, J. G.; Sligar, S. G.; Luetje, C. W.; Gelperin, A.; Rhodes, P. A.; Discher, B. M.; Johnson, A. T. C. *ACS Nano* **2011**, *5*, 5408–5416.

(143) Chio, L.; Del Bonis-O'Donnell, J. T.; Kline, M. A.; Kim, J. H.; McFarlane, I. R.; Zuckermann, R. N.; Landry, M. P. *Nano Letters* **2019**, *19*, 7563–7572.

(144) Bisker, G.; Ahn, J.; Kruss, S.; Ulissi, Z. W.; Salem, D. P.; Strano, M. S. *The Journal of Physical Chemistry C* **2015**, *119*, 13876–13886.

(145) Williams, R. M.; Lee, C.; Heller, D. A. *ACS Sensors* **2018**, *3*, 1838–1845.

(146) Roxbury, D.; Jena, P. V.; Shamay, Y.; Horoszko, C. P.; Heller, D. A. *ACS Nano* **2016**, *10*, 499–506.

(147) Oh, J. Y.; Kim, H. S.; Palanikumar, L.; Go, E. M.; Jana, B.; Park, S. A.; Kim, H. Y.; Kim, K.; Seo, J. K.; Kwak, S. K.; Kim, C.; Kang, S.; Ryu, J.-H. *Nature Communications* **2018**, *9*, 4548.

(148) Mann, F. A.; Lv, Z.; Grosshans, J.; Opazo, F.; Kruss, S. *Angewandte Chemie* **2019**, *58*, 11469–11473.

(149) Zubkovs, V. Protein Bioconjugation to Carbon Nanotubes for Near-Infrared Sensing, Ph.D. Thesis, Lausanne: Lausanne : Ecole Polytechnique Fédérale de Lausanne, 2019.

(150) Seow, Y.; Wood, M. J. *Molecular Therapy* **2009**, *17*, 767–777.

(151) McNicol, A. M.; Farquharson, M. A. *Journal of Pathology* **1997**, *182*, 250–261.

(152) Hong, F.; Zhang, F.; Liu, Y.; Yan, H. *Chemical Reviews* **2017**, *117*, 12584–12640.

(153) Famulok, M.; Mayer, G. *Accounts of Chemical Research* **2011**, *44*, 1349–1358.

(154) Cunningham, F. J.; Goh, N. S.; Demirer, G. S.; Matos, J. L.; Landry, M. P. *Trends in Biotechnology* **2018**, *36*, 882–897.

(155) Mout, R.; Ray, M.; Yesilbag Tonga, G.; Lee, Y.-W.; Tay, T.; Sasaki, K.; Rotello, V. M. *ACS Nano* **2017**, *11*, 2452–2458.

(156) Godin, A. G.; Varela, J. A.; Gao, Z.; Danne, N.; Dupuis, J. P.; Lounis, B.; Groc, L.; Cognet, L. *Nature Nanotechnology* **2017**, *12*, 238–243.

(157) Jena, P. V.; Roxbury, D.; Galassi, T. V.; Akkari, L.; Horoszko, C. P.; Iaea, D. B.; Budhathoki-Uprety, J.; Pipalia, N.; Haka, A. S.; Harvey, J. D.; Mittal, J.; Maxfield, F. R.; Joyce, J. A.; Heller, D. A. *ACS Nano* **2017**, *11*, 10689–10703.

(158) Tu, X.; Manohar, S.; Jagota, A.; Zheng, M. *Nature* **2009**, *460*, 250–253.

(159) Jena, P. V.; Safaee, M. M.; Heller, D. A.; Roxbury, D. *ACS Applied Materials and Interfaces* **2017**, *9*, 21397–21405.

(160) Ao, G.; Streit, J. K.; Fagan, J. A.; Zheng, M. *Journal of the American Chemical Society* **2016**, *138*, 16677–16685.

(161) Wu, Y.; Phillips, J. A.; Liu, H.; Yang, R.; Tan, W. *ACS Nano* **2008**, *2*, 2023–2028.

(162) Ghosh, S.; Patel, N.; Chakrabarti, R. *Journal of Physical Chemistry B* **2016**, *120*, 455–466.

(163) Wang, C.; Meany, B.; Wang, Y. *Angewandte Chemie* **2017**, *56*, 9326–9330.

(164) Yamamoto, Y.; Fujigaya, T.; Niidome, Y.; Nakashima, N. *Nanoscale* **2010**, *2*, 1767–1772.

(165) Ao, G.; Nepal, D.; Aono, M.; Davis, V. A. *ACS Nano* **2011**, *5*, 1450–1458.

(166) Chen, R. J.; Zhang, Y. *Journal of Physical Chemistry B* **2006**, *110*, 54–57.

(167) Jung, S.; Cha, M.; Park, J.; Jeong, N.; Kim, G.; Park, C.; Ihm, J.; Lee, J. *Journal of the American Chemical Society* **2010**, *132*, 10964–10966.

(168) Alegret, N.; Santos, E.; Rodríguez-Fortea, A.; Rius, F. X.; Poblet, J. M. *Chemical Physics Letters* **2012**, *525-526*, 120–124.

(169) Santosh, M.; Panigrahi, S.; Bhattacharyya, D.; Sood, A. K.; Maiti, P. K. *Journal of Chemical Physics* **2012**, *136*, 065106.

(170) Pingoud, A.; Fuxreiter, M.; Pingoud, V.; Wende, W. *Cellular and Molecular Life Sciences* **2005**, *62*, 685–707.

(171) Azorin, F.; Hahn, R.; Rich, A. *Proceedings of the National Academy of Sciences of the United States of America* **1984**, *81*, 5714–5718.

(172) Shouche, Y. S.; Ramesh, N.; Brahmachari, S. K. *Nucleic Acids Research* **1990**, *18*, 267–275.

(173) Bergler, F. F.; Stahl, S.; Goy, A.; Schöppler, F.; Hertel, T. *Langmuir* **2016**, *32*, 9598–9603.

(174) Conlan, L. H.; Jose, T. J.; Thornton, K. C.; Dupureur, C. M. *Biotechniques* **1999**, *27*, 955–960.

(175) Muddana, H. S.; Morgan, T. T.; Adair, J. H.; Butler, P. J. *Nano Letters* **2009**, *9*, 1559–1566.

(176) Rahul, C.; Jaswinder, S.; Haining, W.; Shengli, Z.; Su, L.; Hao, Y.; Stuart, L.; Yan, L. *Nanotechnology* **2009**, *20*, 485201.

(177) Jen-Jacobson, L. *Biopolymers* **1997**, *44*, 153–180.

(178) Krissinel, E.; Henrick, K. *Journal of Molecular Biology* **2007**, *372*, 774–797.

(179) Kostrewa, D.; Winkler, F. K. *Biochemistry* **1995**, *34*, 683–696.

(180) Winkler, F. K.; Banner, D. W.; Oefner, C.; Tsernoglou, D.; Brown, R. S.; Heathman, S. P.; Bryan, R. K.; Martin, P. D.; Petratos, K.; Wilson, K. S. *EMBO Journal* **1993**, *12*, 1781–1795.

(181) Van den Broek, B.; Noom, M. C.; Wuite, G. J. L. *Nucleic Acids Research* **2005**, *33*, 2676–2684.

(182) Viadiu, H.; Aggarwal, A. K. *Molecular Cell* **2000**, *5*, 889–895.

(183) Ghosh, S.; Chakrabarti, R. *The Journal of Physical Chemistry B* **2016**, *120*, 3642–3652.

(184) Jeltsch, A.; Alves, J.; Wolfes, H.; Maass, G.; Pingoud, A. *Biochemistry* **1994**, *33*, 10215–10219.

(185) Yi, C.; Fong, C.-C.; Chen, W.; Qi, S.; Tzang, C.-H.; Lee, S.-T.; Yang, M. *Nanotechnology* **2007**, *18*, 025102.

(186) Ordinario, D. D.; Burke, A. M.; Phan, L.; Jocson, J. M.; Wang, H.; Dickson, M. N.; Gorodetsky, A. A. *Analytical Chemistry* **2014**, *86*, 8628–33.

(187) Li, B.; Wang, L.; Su, L.; Chen, S.; Li, Z.; Chen, J.; Wu, J. *Biotechnology and Bioprocess Engineering* **2012**, *17*, 1128–1134.

(188) Roxbury, D.; Jena, P. V.; Williams, R. M.; Enyedi, B.; Niethammer, P.; Marcet, S.; Verhaegen, M.; Blais-Ouellette, S.; Heller, D. A. *Scientific Reports* **2015**, *5*, 14167.

(189) Green, M. R., *Molecular cloning : a laboratory manual / Michael R. Green, Joseph Sambrook*; Sambrook, J., Ed.; Cold Spring Harbor Laboratory Press: Cold Spring Harbor, N.Y, 2012.

(190) Roxbury, D.; Tu, X.; Zheng, M.; Jagota, A. *Langmuir* **2011**, *27*, 8282–8293.

(191) Sugita, Y.; Okamoto, Y. *Chemical Physics Letters* **1999**, *314*, 141–151.

(192) Bonomi, M.; Parrinello, M. *Physical Review Letters* **2010**, *104*, 190601.

(193) Martínez, L.; Andrade, R.; Birgin, E. G.; Martínez, J. M. *Journal of Computational Chemistry* **2009**, *30*, 2157–2164.

(194) Berendsen, H. J. C.; van der Spoel, D.; van Drunen, R. *Computer Physics Communications* **1995**, *91*, 43–56.

(195) Van Der Spoel, D.; Lindahl, E.; Hess, B.; Groenhof, G.; Mark, A. E.; Berendsen, H. J. C. *Journal of Computational Chemistry* **2005**, *26*, 1701–1718.

(196) Abraham, M. J.; Murtola, T.; Schulz, R.; Páll, S.; Smith, J. C.; Hess, B.; Lindahl, E. *SoftwareX* **2015**, *1-2*, 19–25.

(197) Bussi, G.; Donadio, D.; Parrinello, M. *Journal of Chemical Physics* **2007**, *126*, 014101.

(198) Hess, B.; Bekker, H.; Berendsen, H. J. C.; Fraaije, J. G. E. M. *Journal of Computational Chemistry* **1997**, *18*, 1463–1472.

(199) Boghossian, A. A.; Sen, F.; Gibbons, B. M.; Sen, S.; Faltermeier, S. M.; Giraldo, J. P.; Zhang, C. T.; Zhang, J.; Heller, D. A.; Strano, M. S. *Advanced Energy Materials* **2013**, *3*, 881–893.

(200) Boghossian, A. A.; Zhang, J.; Barone, P. W.; Reuel, N. F.; Kim, J.-H.; Heller, D. A.; Ahn, J.-H.; Hilmer, A. J.; Rwei, A.; Arkalgud, J. R.; Zhang, C. T.; Strano, M. S. *ChemSusChem* **2011**, *4*, 848–863.

(201) Jeng, E. S.; Nelson, J. D.; Prather, K. L. J.; Strano, M. S. *Small* **2010**, *6*, 40–43.

(202) Star, A.; Tu, E.; Niemann, J.; Gabriel, J.-C. P.; Joiner, C. S.; Valcke, C. *Proceedings of the National Academy of Sciences of the United States of America* **2006**, *103*, 921–926.

(203) Olmsted, J.; Kearns, D. R. *Biochemistry* **1977**, *16*, 3647–3654.

(204) Dragan, A.; Casas-Finet, J.; Bishop, E.; Strouse, R.; Schenerman, M.; Geddes, C. *Biophysical Journal* **2010**, *99*, 3010–3019.

(205) Dragan, A. I.; Pavlovic, R.; McGivney, J. B.; Casas-Finet, J. R.; Bishop, E. S.; Strouse, R. J.; Schenerman, M. A.; Geddes, C. D. *Journal of Fluorescence* **2012**, *22*, 1189–1199.

(206) Mao, P.; Ning, Y.; Li, W.; Peng, Z.; Chen, Y.; Deng, L. *Enzyme and Microbial Technology* **2014**, *54*, 15–19.

(207) Cavuslar, O.; Unal, H. *RSC Advances* **2015**, *5*, 22380–22389.

(208) Vogt, V. M. *European Journal of Biochemistry* **1973**, *33*, 192–200.

(209) Guan, Z.; Liu, J.; Bai, W.; Lv, Z.; Jiang, X.; Yang, S.; Chen, A.; Lv, G. *PLOS ONE* **2014**, *9*, e108401.

(210) Yin, Y.; Zhao, X. S. *Accounts of Chemical Research* **2011**, *44*, 1172–1181.

(211) Harvey, J. D.; Zerze, G. H.; Tully, K. M.; Mittal, J.; Heller, D. A. *The Journal of Physical Chemistry C* **2018**, *122*, 10592–10599.

(212) Fuchs, J.; Fiche, J. B.; Buhot, A.; Calemczuk, R.; Livache, T. *Biophysical Journal* **2010**, *99*, 1886–95.

(213) Hurst, S. J.; Lytton-Jean, A. K. R.; Mirkin, C. A. *Analytical Chemistry* **2006**, *78*, 8313–8318.

(214) Schwarz, F. *Nucleic Acids Research* **1999**, *27*, 4792–4800.

(215) Yang, R.; Jin, J.; Chen, Y.; Shao, N.; Kang, H.; Xiao, Z.; Tang, Z.; Wu, Y.; Zhu, Z.; Tan, W. *Journal of the American Chemical Society* **2008**, *130*, 8351–8358.

(216) Horii, Y.; Ohura, S.; Umemura, K. *Analytical Biochemistry* **2020**, *601*, 113776.

(217) Gillen, A. J.; Siefman, D. J.; Wu, S.-J.; Bourmaud, C.; Lambert, B.; Boghossian, A. A. *Journal of Colloid and Interface Science* **2020**, *565*, 55–62.

(218) Kato, Y.; Inoue, A.; Niidome, Y.; Nakashima, N. *Scientific Reports* **2012**, *2*, 733.

(219) Salem, D. P.; Gong, X.; Liu, A. T.; Koman, V. B.; Dong, J.; Strano, M. S. *Journal of the American Chemical Society* **2017**, *139*, 16791–16802.

(220) Gillen, A. J.; Boghossian, A. A. *Frontiers in Chemistry* **2019**, *7*, 612.

(221) Wu, S.-J.; Boghossian, A. A. *Chimia* **2019**, *73*, 283.

(222) Packer, M. S.; Liu, D. R. *Nat Rev Genet* **2015**, *16*, 379–394.

(223) Zubkovs, V.; Wu, S.-J.; Rahnamaee, S. Y.; Schuergers, N.; Boghossian, A. A. *Chem. Mater.* **2020**, *32*, 8798.

(224) Chio, L.; Pinals, R. L.; Murali, A.; Goh, N. S.; Landry, M. P. *Advanced Functional Materials* **2020**, *30*, 1910556.

(225) Sternberg, S. H.; Redding, S.; Jinek, M.; Greene, E. C.; Doudna, J. A. *Nature* **2014**, *507*, 62–67.

(226) O'Connell, M. R.; Oakes, B. L.; Sternberg, S. H.; East-Seletsky, A.; Kaplan, M.; Doudna, J. A. *Nature* **2014**, *516*, 263–6.

(227) Lapiene, V.; Kukolka, F.; Kiko, K.; Arndt, A.; Niemeyer, C. M. *Bioconjugate Chemistry* **2010**, *21*, 921–927.

(228) Zubkovs, V.; Antonucci, A.; Schuergers, N.; Lambert, B.; Latini, A.; Ceccarelli, R.; Santinelli, A.; Rogov, A.; Ciepielewski, D.; Boghossian, A. A. *Scientific Reports* **2018**, *8*, 13770.

(229) Manders, E. M. M.; Verbeek, F. J.; Aten, J. A. *Journal of Microscopy* **1993**, *169*, 375–382.

(230) Aaron, J. S.; Taylor, A. B.; Chew, T.-L. *Journal of Cell Science* **2018**, *131*, jcs211847.

(231) Kurzban, G. P.; Bayer, E. A.; Wilchek, M.; Horowitz, P. M. *Journal of Biological Chemistry* **1991**, *266*, 14470–14477.

(232) Kim, J.-H.; Patra, C. R.; Arkalgud, J. R.; Boghossian, A. A.; Zhang, J.; Han, J.-H.; Reuel, N. F.; Ahn, J.-H.; Mukhopadhyay, D.; Strano, M. S. *ACS Nano* **2011**, *5*, 7848–7857.

(233) Xu, Y.; Pehrsson, P. E.; Chen, L.; Zhang, R.; Zhao, W. *The Journal of Physical Chemistry C* **2007**, *111*, 8638–8643.

(234) Xu, Y.; Pehrsson, P. E.; Chen, L.; Zhao, W. *Journal of the American Chemical Society* **2008**, *130*, 10054–10055.

(235) Narayanaswamy, N.; Narra, S.; Nair, R. R.; Saini, D. K.; Kondaiah, P.; Govindaraju, T. *Chemical Science* **2016**, *7*, 2832–2841.

(236) Brege, J. J.; Gallaway, C.; Barron, A. R. *The Journal of Physical Chemistry C* **2009**, *113*, 4270–4276.

(237) Rodríguez-López, J. N.; Lowe, D. J.; Hernández-Ruiz, J.; Hiner, A. N. P.; García-Cánovas, F.; Thorneley, R. N. F. *Journal of the American Chemical Society* **2001**, *123*, 11838–11847.

(238) Guo, Q.; He, Y.; Lu, H. P. *Proceedings of the National Academy of Sciences* **2015**, *112*, 13904–13909.

(239) Krainer, F. W.; Glieder, A. *Applied Microbiology and Biotechnology* **2015**, *99*, 1611–1625.

(240) Hayashi, Y.; Yamazaki, I. *Journal of Biological Chemistry* **1979**, *254*, 9101–9106.

(241) Tanaka, Y.; Hirana, Y.; Niidome, Y.; Kato, K.; Saito, S.; Nakashima, N. *Angewandte Chemie International Edition* **2009**, *48*, 7655–7659.

(242) Allen, B. L.; Kotchey, G. P.; Chen, Y.; Yanamala, N. V. K.; Klein-Seetharaman, J.; Kagan, V. E.; Star, A. *Journal of the American Chemical Society* **2009**, *131*, 17194–17205.

(243) Nishimasu, H.; Ran, F. A.; Hsu, P. D.; Konermann, S.; Shehata, S. I.; Dohmae, N.; Ishitani, R.; Zhang, F.; Nureki, O. *Cell* **2014**, *156*, 935–949.

(244) Hu, M.; Yuan, C.; Tian, T.; Wang, X.; Sun, J.; Xiong, E.; Zhou, X. *Journal of the American Chemical Society* **2020**, *142*, 7506–7513.

(245) Hajian, R. et al. *Nature Biomedical Engineering* **2019**, *3*, 427–437.

(246) English, M. A.; Soenksen, L. R.; Gayet, R. V.; de Puig, H.; Angenent-Mari, N. M.; Mao, A. S.; Nguyen, P. Q.; Collins, J. J. *Science* **2019**, *365*, 780–785.

(247) Khripin, C. Y.; Manohar, S.; Zheng, M.; Jagota, A. *The Journal of Physical Chemistry C* **2009**, *113*, 13616–13621.

(248) Monera, O. D.; Kay, C. M.; Hodges, R. S. *Protein Science* **1994**, *3*, 1984–1991.

(249) Lim, W. K.; Rösgen, J.; Englander, S. W. *Proceedings of the National Academy of Sciences* **2009**, *106*, 2595–2600.

(250) Son, I.; Shek, Y. L.; Tikhomirova, A.; Baltasar, E. H.; Chalikian, T. V. *Journal of Physical Chemistry B* **2014**, *118*, 13554–63.

(251) Corona, R. I.; Guo, J.-t. *Proteins: Structure, Function, and Bioinformatics* **2016**, *84*, 1147–1161.

(252) Stancik, A. L.; Brauns, E. B. *Vibrational Spectroscopy* **2008**, *47*, 66–69.

(253) Bonet, J.; Wehrle, S.; Schriever, K.; Yang, C.; Billet, A.; Sesterhenn, F.; Scheck, A.; Sverrisson, F.; Veselkova, B.; Vollers, S.; Lourman, R.; Villard, M.; Rosset, S.; Krey, T.; Correia, B. E. *PLOS Computational Biology* **2018**, *14*, ed. by Fleishman, S. J., e1006623.

(254) Sesterhenn, F. et al. *Science* **2020**, *368*, eaay5051.

(255) Bouilly, D.; Hon, J.; Daly, N. S.; Trocchia, S.; Vernick, S.; Yu, J.; Warren, S.; Wu, Y.; Gonzalez, R. L.; Shepard, K. L.; Nuckolls, C. *Nano Letters* **2016**, *16*, 4679–4685.

(256) Vernick, S.; Trocchia, S. M.; Warren, S. B.; Young, E. F.; Bouilly, D.; Gonzalez, R. L.; Nuckolls, C.; Shepard, K. L. *Nature Communications* **2017**, *8*, 15450.

(257) Cuervo, A.; Dans, P. D.; Carrascosa, J. L.; Orozco, M.; Gomila, G.; Fumagalli, L. *Proceedings of the National Academy of Sciences* **2014**, *111*, E3624.

(258) He, X.; Velizhanin, K. A.; Bullard, G.; Bai, Y.; Olivier, J.-H.; Hartmann, N. F.; Gifford, B. J.; Kilina, S.; Tretiak, S.; Htoon, H.; Therien, M. J.; Doorn, S. K. *ACS Nano* **2018**, *12*, 8060–8070.

Abbreviations

A	Adenine
a.a.	amino acid
ABTS	2,2'-Azino-bis(3-ethylbenzthiazoline-6-sulfonic acid)
AFM	Atomic Force Microscopy
Ala	Alanine
ALDH	aldehyde dehydrogenase
Arg	Arginine
Asp	Aspartate
bp	base pair
BSA	Bovine Serum Albumin
C	Cytosine
Cas	CRISPR-Associated Protein
CCVD	Catalytic Chemical Vapor Deposition
CD	Circular Dichroism
cDNA	Complementary DNA
CoMoCAT	Cobalt Molybdenum CATalyzed process
CRISPR	Clustered Regularly Interspaced Short Palindromic Repeats
Cys	Cysteine
DBCO	DiBenzoCycloOctyne
DFT	Density Functional Theory
DI	DeIonised Water
DNA	DeoxyriboNucleic Acid
DOS	Density Of States
dsDNA	double-stranded DeoxyriboNucleic Acid
DNAzyme	Deoxyribozyme
DTT	DiThioThreitol
EDTA	EthyleneDiamineTetraAcetic acid
ELISA	Enzyme-Linked ImmunoSorbent Assay
EMSA	Electrophoretic Mobility Shift Assay
EtBr	Ethidium Bromide
eV	electron Volt
exc.	excitation

eYFP	Enhanced Yellow Fluorescence Protein
FAM	Fluorescein
FBS	Fetal Bovine Serum
FET	Field-Effect Transistor
FISH	Fluorescence In Situ Hybridization
FRET	Förster Resonance Energy Transfer
FWHM	Full-Width at Half-Maximum
G	Guanine
GFP	Green Fluorescent Protein
Glu	Glutamate
Gly	Glycine
GOx	Glucose Oxidase
GdmCl	Guanidium Hydrochloride
HEPES	4-(2-hydroxyethyl)-1-piperazineethanesulfonic acid
HiPCO	High-Pressure Carbon monOxide process
His	Histidine
HRP	HorseRadish Peroxidase
IEP	IsoElectric Point
InGaAs	Indium Gallium Arsenide
Leu	Leucine
LP	Long-Pass
MAO	MonoAmine Oxidase
MCC	Manders Co-localization Coefficient
MD	Molecular Dynamics
MeOH	Methanol
microRNA	micro-RiboNucleic Acid
MS	Mass Spectrometry
MW	Molecular Weight
MWCO	Molecular Weight Cut-Off
nt	nucleotide
NGS	Next-Generation Sequencing
Ni-NTA	Nickel-Nitrilotriacetic Acid
NIR *or* near-IR	Near-InfraRed
NO	Nitric Oxide
OD	Optical Density
PAM	Protospacer Adjacent Motif
PAGE	PolyAcrylamide Gel Electrophoresis
PBS	sodium Phosphate-Buffered Saline
PCI	Phenol-Chloroform-Isoamyl alcohol
PCR	Polymerase Chain Reaction
PDB	Protein DataBank
PEG	Poly(Ethylene Glycol)

Phe	Phenylalanine
PL	PhotoLuminescence
PTM	Post-Translational Modification
QF	QuantiFluor
RE	Restriction Enzyme
RFU	Relative Fluorescence Unit
RSA	Relative Solvent Accessibility
RT	Room Temperature
SA	StreptAvidin
SABER	Signal Amplification By Exchange Reaction
SASA	solvent accessible surface area
SAXS	Small-Angle X-ray Scattering
SC	Sodium Cholate
SCOP	Structural Classification of Proteins
S.D.	Standard Deviation
SDC	Sodium DeoxyCholate
SDBS	Sodium DodecylBenzene Sulfate
SDS	Sodium Dodecyl Sulfate
SELEX	Systematic Evolution of Ligands by EXponential enrichment
sgRNA	Scaffold Guide RNA
SPR	Surface Plasmon Resonance
SSB	single-stranded DNA binding proteins
SSC	Saline Sodium Citrate
ssDNA	single-stranded DeoxyriboNucleic Acid
SWCNT	Single-Walled Carbon Nanotube
T	Thymine
TALEN	Transcription Activator-Like Effector Nuclease
TBE	Tris/Borate/EDTA
TIRF	Total Internal Reflection Fluorescence
Trp	Tryptophan
Tyr	Tyrosine
UV	UltraViolet
vdw	van der Waals
VHS	Van Hove singularity
Vis	Visible

Shang-Jung **Wu**

Material Scientist · Biochemist

Impasse de Enfant-Prodigue 10, Morges 1110, Switzerland

(+41) 78 692 46 85 | shang-jung.wu@epfl.ch, neil.sjwu@gmail.com | live:neil.sjwu | orcid: 0000-0003-0097-1774

Education

École polytechnique fédérale de Lausanne (EPFL) — *Lausanne, Switzerland*

Doctoral assistant in Chemical Science and Engineering — *Sept. 2015 - Nov. 2020*

- Dissertation: Establishing a Ternary System for Optical Monitoring of DNA–Protein Interactions with Single-Walled Carbon Nanotubes
- Dissertation advisor: Prof. Ardemis Anoush Boghossian
- Relevant Coursework: Nanobiotechnology and biophysics, Biomolecular structure and mechanics

National Taiwan University (NTU) — *Taipei, Taiwan*

M.S. in Materials Science and Engineering — *Feb. 2012 - Jan. 2014*

- Thesis: Facile approach for rapid and tunable self-assembly of rod-coil block copolymers
- Thesis advisor: Prof. Wei-Fang Su

National Taiwan University — *Taipei, Taiwan*

B.E. in Materials Science and Engineering — *Sept. 2008 - Jan. 2012*

- Project: Side chain effect on self-assembly behaviors of poly(3-alkylthiophene) based rod-coil block copolymer
- Project supervisor: Prof. Wei-Fang Su

Professional Experience

Laboratory of Nanobiotechnology, EPFL — *Lausanne, Switzerland*

Doctoral assistant — *Sept. 2015 - present*

- Developed restriction enzyme assay to analyze DNA conformation and protein accessibility on nanoparticles.
- Established nuclease-assisted fluorescence assay to study DNA hybridization on the surface of nanoparticles.
- Designed novel materials composed of DNA-protein-carbon nanotube ternary hybrid, investigated the system by fluorescence microscope.
- Designed and studied CRISPR-Cas9 system on nanoparticle.
- Expressed membrane protein (microbial rhodopsin) and applied site-directed mutagenesis to construct mutants, reconstituted in nanodisc and self-assembled with carbon nanotube.
- Collaborated with colleagues to develop various new projects related to neurotransmitter detection, directed evolution of nanoparticles, and eYFP bioconjugation.
- Collaborated with Prof. Bruno Correia and Prof. David Baker to investigate protein-nanoparticles interaction and the self-assembly behaviors using protein engineering strategy.
- Tutored junior PhD and exchange PhD students to develop new projects related to micropreparative PAGE, plasmonic nanoparticles, and graphene quantum dot.
- Supported Master level courses (Electrochemical Engineering and Transport Phenomena) for 5 semesters.

Frontier Materials Research Group, NTU — *Taipei, Taiwan*

Research assistant — *Jan. 2010 - Jun. 2014*

- Designed and synthesized conducting polymer based block copolymers, resolved the self-assembly behaviors of rod-coil block copolymers by X-ray scattering and electron microscope.
- Established and administered new operating system, Bruker Nanostar for X-ray scattering, designed new apparatus for specific experiment and trained new users.

Center of Nanoscale Materials, Argonne National Laboratory — *Lemont, U.S.*

Research assistant — *Jun. 2013 - Sept. 2013*

- Collaborated with Dr. Seth Darling to synthesize titanium dioxide nanotube for organic/inorganic hybrid solar cell by anodization.

Taiwan Light Source, National Synchrotron Radiation Research Center (NSRRC) — *Hsinchu, Taiwan*

Research assistant — *July. 2011 - Jan. 2014*

- Conducted small-angle/wide-angle X-ray scattering on block copolymer.

Honors & Awards

- Electrochemical Society (ECS) Travel Grant, 2016 and 2018.
- Swiss Chemical Society Fall Meeting Best Poster Award (with travel grant), 2018.
- Research Creativity Award, National Science Council, Taiwan, 2012.
- College Student Research Scholarship, National Science Council, Taiwan, 2011.
- Academic Excellence Award, National Taiwan University, 2010.

Publications

Published manuscript

- V. Zubkovs, **S.-J. Wu**, S. Y. Rahnamaee, N. Schuergers, and A. A. Boghossian. Site-specific protein conjugation onto fluorescent single-walled carbon nanotubes. *Chem. Mater.* 2020, 32, 8798.
- A. J. Gillen, D. Siefman, **S.-J. Wu**, C. Bourmaud, B. Lambert, A. A. Boghossian. Templating colloidal sieves for tuning nanotube surface interactions and optical sensor responses. *J. Colloid Interf. Sci.*, 2019, 565, 55.
- **S.-J. Wu**, A. A. Boghossian. Analytical approaches for monitoring DNA–protein interactions. *CHIMIA*, 2019, 73, 282.
- B. Lambert, A. J. Gillen, N. Schuergers, **S.-J. Wu**, A. A. Boghossian. Directed evolution of the optoelectronic properties of synthetic nanomaterials. *Chem. Comm.*, 2019, 55, 3239.
- **S.-J. Wu**, N. Schuergers, K.-H. Lin, A. J. Gillen, C. Corminboeuf, A. A. Boghossian. Restriction enzyme analysis of double-stranded DNA on pristine single-walled carbon nanotubes. *ACS Appl. Mater. Interfaces*, 2018, 10, 37386.
- **S.-J. Wu**, A. A. Boghossian. Living on the edge: re-shaping the interface of synthetic biology and nanotechnology. *CHIMIA*, 2016, 70, 773.
- C.-C. Ho, **S.-J. Wu**, S.-H. Lin, S. B. Darling, W.-F. Su. Kinetically enhanced approach for rapid and tunable self-assembly of rod-coil block copolymers. *Macro. Rapid Comm.*, 2015, 36, 1329. (cover)
- S.-H. Lin, **S.-J. Wu**, C.-C. Ho, W.-F. Su. Rational design of versatile self-assembly morphology of rod–coil block copolymer. *Macromolecules*, 2013, 46, 2725.
- H. Lim, C.-C. Ho, **S.-J. Wu**, H.-C. Tsai, W.-F. Su, C.-Y. Chao. A poly(3-hexylthiophene) block copolymer with macroscopically aligned hierarchical nanostructure induced by mechanical rubbing. *Chem. Comm.*, 2013, 49, 9146.

In preparation

- **S.-J. Wu**, B. Lambert, A. A. Boghossian. Analysis of dsDNA-SWCNT through S1-nuclease assisted fluorescence assay. In preparation.
- **S.-J. Wu**, A. A. Boghossian. Ternary hybrid system: protein-DNA-SWCNT interaction and applications. In preparation.
- **S.-J. Wu**, C. Yang, M. Mouhib, B. Correia, A. A. Boghossian. Chemical Determinants of DNA-SWCNT/Protein Interaction. In preparation.
- A. Amirjani, T. Tsoulos, A. Antonucci, **S.-J. Wu**, G. Tagliabue, D. F. Haghshenas, A. A. Boghossian. Plasmon induced near-infrared fluorescence enhancement of single-walled carbon nanotubes. In preparation.
- S. Hashem Sajjadi, **S.-J. Wu**, E. K. Goharshadi, H. Ahmadzadeh, A. A. Boghossian. A simple micropreparative gel electrophoresis technique for purification of proteins and nucleic acids. Submitted.

Presentations

Oral

- Presented "Characterization of Double-Stranded DNA (dsDNA) on Single-Walled Carbon Nanotubes (SWCNTs)". *ECS 233rd*, May 2018, Seattle, U.S.
- Presented "Single-Walled Carbon Nanotubes (SWCNTs) for Protein Engineering Applications". *ECS 229th*, May 2016, San Diego, U.S.

Poster

- Presented "Characterization of Double-Stranded DNA (dsDNA) on Single-Walled Carbon Nanotubes (SWCNTs)". *NT19*, July 2019, Würzburg, Germany.
- Presented "Characterization of Double-Stranded DNA (dsDNA) on Single-Walled Carbon Nanotubes (SWCNTs)". *Swiss Chemical Society (SCS) Fall Meeting*, September 2018, Lausanne, Switzerland. (Best Poster Award)
- Presented "Facile Approach for Rapid and Tunable Self-assembly of Rod-coil Block Copolymers" at *Pacific Polymer Conference (PCC)*, November 2013, Kaohsiung, Taiwan.
- Presented "Rational Design of Versatile Self-Assembly Morphology of Rod–Coil Block Copolymer" at *Polymer Conference*, January 2013, Chiayi, Taiwan. (with Excellent Poster Award)
- Presented "Rational Design of Versatile Self-Assembly Morphology of Rod–Coil Block Copolymer" at *Materials Research Society (MRS) Fall Meeting*, November 2012, Boston, U.S.

Skills

Biotechnique	Cloning, PCR, site-directed mutagenesis, cell culture, protein overexpression in bacteria/yeast, column chromatography, gel electrophoresis, bioconjugation, in vitro transcription and RNA handling
Material Synthesis	Nanoparticle functionalization, surface modification, click chemistry, polymer synthesis, glove box
Characterization	Fluorescence microscope, circular dichroism, UV-Vis-NIR absorption spectrum, Nanodrop, microplate reader, zeta potential, density gradient centrifugation, small-angle/wide-angle X-ray scattering (SAXS/WAXS), FT-IR, NMR, AFM, DSC, contact angle
Data Analysis	Image processing, non-linear fitting, spectrum deconvolution
Software	MS Office, OriginPro, ImageJ, VMD, PhotoShop, SketchUp, Blender
Programming	Python, MatLab, LaTeX
Language	Mandarin (native), English (fluent), French (basic)